UNIVERSITÄT HAMBURG

DOCTORAL THESIS

Single Nanoparticle Sensing in Fluidic Chips at Gigahertz Frequencies

Author:
Lucjan GRZEGORZEWSKI

Supervisor:
Prof. Dr. Robert H. BLICK

A thesis submitted in fulfillment of the requirements for the degree of Doctor rerum naturalium

in the

Faculty of Mathematics, Informatics and Natural Sciences (MIN)
Department of Physics at the Universität Hamburg

Hamburg, January 15, 2024

Gutachter/innen der Dissertation:	Prof. Dr. Robert H. Blick Prof. Dr. Mehmet Bayindir
Zusammensetzung der Prüfungskommission:	Prof. Dr. Robert H. Blick Prof. Dr. Mehmet Bayindir Prof. Dr. Gabriel Bester Prof. Dr. Wolfgang Parak Dr. Robert Zierold
Vorsitzende/r der Prüfungskommission:	Prof. Dr. Wolfgang Parak
Datum der Disputation:	26.04.24
Vorsitzender des Fach-Promotionsausschusses PHYSIK:	Prof. Dr. Markus Drescher
Leiter des Fachbereichs PHYSIK:	Prof. Dr. Wolfgang J. Parak
Dekan der Fakultät MIN:	Prof. Dr.-Ing. Norbert Ritter

Declaration of Authorship

I, Lucjan GRZEGORZEWSKI, declare in lieu of an oath that this thesis titled, "Single Nanoparticle Sensing in Fluidic Chips at Gigahertz Frequencies" and the work presented in it are my own. I confirm that:

- Where I have consulted the published work of others, this is always clearly attributed.
- Where I have quoted from the work of others, the source is always given. With the exception of such quotations, this thesis is entirely my own work.
- I have acknowledged all main sources of help.
- Where the thesis is based on work done by myself jointly with others, I have made clear exactly what was done by others and what I have contributed myself.

Signed: Lucjan G

Date: 15.01.2024

This page has been intentionally left blank.

"There's Plenty of Room at the Bottom"

Richard Feynman (1959)

This page has been intentionally left blank.

Preface

The purpose of the preface is to provide context and navigate the reader through the structure of this thesis, clarifying the required background knowledge and thereby setting expectations. My thesis delves into the field of inflow, all-electric, label-free single-particle detection. Within this field, a diverse spectrum of detection methods exists in the literature. These methods have subtle differences that initially led to some confusion. Therefore, I want to contextualize the detection method described in this thesis and pinpoint the developments I have contributed to the intricate landscape of inflow electrical single-particle sensing.

This landscape can be untangled by the measurement frequency of the detection method starting with direct current (DC), which is used by resistive pulse sensing (RPS), also known as the Coulter Counter principle. It is the most popular all-electric and label-free single-particle detection method. It consists of two reservoirs connected by an orifice. A DC voltage applied across the reservoirs creates a constant flow of ions through the orifice. As particles move through the orifice, they displace their volume of conductive fluid, causing a change in electrical resistance, detected as a pulse in the electrical current.

Electrical impedance spectroscopy (EIS) is a widely utilized technique at higher frequencies for characterizing materials. When EIS is specifically applied to the detection or characterization of particles in a fluidic channel, it is often termed Electrical Impedance Flow Spectroscopy (EIFS). It involves suspending particles in a conductive liquid, which flows through a microfluidic channel. Electrodes are embedded within or in close proximity to this channel, which apply an alternating voltage across the channel. This induces a current flow through the fluid, which can be measured subsequently.

The channel impedance is the ratio between the applied voltage and the measured current. When particles translocate close to the electrodes, they induce variations in this impedance. The differences in impedance are related to the particle's size, shape, and material properties. Different particle attributes can be explored by altering the frequency of the applied alternating voltage. The most popular application of that method is the detection of cells, called electrical impedance flow cytometry (EIFC). However, in literature, the expression EIFC is not exclusively used for detecting cells, and the three expressions EIS, EIFS, and EIFC are used interchangeably. To maintain terminological consistency, I will only use the expression EIFC throughout this thesis.

The EIFC method utilizes a trans-impedance amplifier (TIA), which converts a current into a voltage. TIAs inherently restrict the bandwidth of EIFCs. A maximum bandwidth of 450 MHz can be achieved with the most advanced EIFC setups. Moreover, the gap between electrodes becomes purely capacitive at high frequencies, resulting in a high impedance, which converts the applied voltage into a small current,

resulting in a less sensitive EIFC setup. Consequently, conventional EIFC architectures are not capable of measuring at GHz frequencies.

At GHz frequencies and for inflow all-electric single particle detection methods, abbreviations have not been established. They are commonly termed microwave sensors, microwave reflectometry, and sometimes microwave impedance spectroscopy. A reflectometric approach is most commonly used at these frequencies. In such a measurement, similar to the EIFC setup, electrodes are placed in close proximity to a fluidic channel. Microwave signals are reflected at the gap between the electrodes, caused by an impedance mismatch on the transmission line. Particles that translocate through the channel modulate the gap impedance, which results in a modulation of the reflected signal intensity and phase. The reactive components of impedance (inductance and capacitance) vary more significantly with increasing frequency, which enhances the sensitivity of the reflectometric approach at high frequencies.

In this thesis, microwave resonators have been implemented to enhance the sensitivity of the reflectometric approach in particle sensing. Conceptually, a resonator operates like an electrical tank circuit (TC), where the sensing volume acts as a capacitance integrated into the resonant circuit. The presence of particles within this sensing volume alters the circuit's capacitance, leading to a shift in the resonance frequency. There are many different resonator types: ring, split ring (SRRs), coplanar waveguide (CPW), hairpin, microstrip, and many more. A summary of resonators used for microfluidic particle detection is presented in section 3.3. This thesis discusses the development of a new type of resonator which is called coupling-based coplanar waveguide resonator (cCPW). The geometry is based on a $\lambda/2$ CPW resonator with some adjustments that improve sensitivity. However, the main innovation relies on a coupling-based approach. This approach adds a coupling component that increases sensitivity. Indeed, this coupling approach can be universally added to any resonator type. The development of the cCPW sensor resulted in the publication: *Coupling-Based Sensing with a Microwave Resonator for Single Nanoscale Particles Detection* [1].

Another challenge has been to get a good overview of the advancements in microwave reflectometry, which were outside the field of particle detection and part of the much more extensive field of reflectometric techniques like scanning microwave microscopy (SMM) or microwave resonators sensors for dielectric characterization of liquids, not single particles. This interdisciplinary aspect was a challenge but also a chance to learn from these fields and incorporate their solutions to the sensing of particles. Benefiting from this interdisciplinary approach, I introduced an interferometric impedance matching circuit commonly used in SMM setups. I also proposed a figure-of-merit (FOM) inspired by the field of resonator-based liquid characterization.

The structure of this thesis is organized into eight main chapters: Introduction, Theory, Sensor Development, Fabrication, Setup, Interferometer & Data Analysis, High Frequency Particle Detection, and Conclusion.

The introduction aims to motivate why high-frequency nanoparticle sensing has great potential. After the introduction, the following chapter presents the theory. It includes a comprehensive discussion of the theoretical fundamentals, focusing on the transmission line (TL) theory and its application to TL resonators. Furthermore,

the coupling theory is derived, which describes the operation of the novel coupling-based sensor type. Then, the geometric optimization process of the sensor is explained in detail. This phase is guided by theoretical principles and finite element method (FEM) simulations. Finally, the theoretical coupling concept is validated by characterizing a fabricated sensor and comparing its sensitivity with existing literature. In the next chapter, I describe the fabrication process of the sensor, followed by a forward-looking perspective on future fabrication approaches, in particular one that utilizes sacrificial layer fluidics (SLF), which has the potential to create fluidic channels that are strictly confined between the sensing electrodes. The following chapter presents the measurement setup using an interferometric impedance matching approach. Actually, it is the first demonstration of interferometric impedance matching for inflow microwave particle sensing. The use of an interferometer and general impedance matching presents unique challenges in data analysis and reproducibility, which are explored in the following chapter. The final chapter of the thesis demonstrates the inflow detection of single particles such as polystyrene beads, cells, droplets, and liposomes with unprecedented sensitivities.

This page has been intentionally left blank.

UNIVERSITÄT HAMBURG

Abstract

Center for Hybrid Nanostructures

Institute of Nanostructure and Solid State Physics

Doctor rerum naturalium

Single Nanoparticle Sensing in Fluidic Chips at Gigahertz Frequencies

by Lucjan GRZEGORZEWSKI

State-of-the-art microfluidic devices face challenges in detecting and characterizing the dielectric properties of individual nanoscale objects due to their limited sensitivity. To overcome this issue, a new coupling-based coplanar waveguide (cCPW) sensor was proposed and demonstrated. This sensor features a capacitively coupled $\lambda/4$ resonator with improved sensitivity owing to its reduced electrical length and finely tuned characteristic impedance. Additionally, the innovative design extends the established tank circuit configuration with a coupling component, significantly improving sensitivity. The performance of this system is evaluated against conventional sensors by introducing a new figure-of-merit (FOM). The sensor's FOM is 1300, indicating a 15-fold sensitivity enhancement over the most sensitive microwave sensors to date.

A wafer-level manufacturing process was developed that integrates 16 individual sensor chips onto a single two-inch wafer. Each chip occupies a compact footprint of 8 x 12 mm. Additionally, a setup was established that interfaces these chips with a radio frequency (RF) circuit, a fluorescent microscope, and a fluidic system. This arrangement permits the simultaneous electrical sensing and optical monitoring of particles while maintaining control over the fluidic flow.

The RF circuit consists of a new interferometric impedance matching configuration, demonstrating unprecedented sensitivity and ultra-fast sensing capabilities by in-flow detection of polystyrene beads, cells, droplets, and liposomes. In particular, for the detection of polystyrene beads as small as 200 nm, a signal-to-noise ratio of up to 417 has been achieved. To our best knowledge, these are the smallest single particles detected at RF with the highest signal-to-noise ratio. Furthermore, a peak processing algorithm was developed to ensure reproducible data by correcting the impedance-match quality and the drift in the amplitude and phase values.

Our research represents a significant advancement towards the high-throughput classification of virions, proteins, and DNA utilizing their high-frequency dielectric properties. Since RF characterization is still an under-explored field, especially for the dielectric characterization of single nanoparticles, it opens up vast opportunities for advances in both scientific and diagnostic applications.

This page has been intentionally left blank.

Zusammenfassung

Detektieren von einzelnen Nanopartikeln mit einem Mikrofluidik-Sensor bei Gigahertz-Frequenzen

von Lucjan GRZEGORZEWSKI

Bisher etablierte mikrofluidische dielektrische Messsysteme sind nicht sensitiv genug, um einzelne nanoskopische Partikel zu detektieren/charakterisieren. Um dieses Hindernis zu überwinden, wurde ein neuartiger kopplungsbasierter koplanarer Wellenleitersensor entwickelt. Dieser Sensor besteht aus einem $\lambda/4$-Resonator, der über eine Kapazität mit der Zuleitung verbunden ist. Das Messprinzip dieses Sensors beruht auf der Modulation dieser Kopplungskapazität. Diese Anordnung beruht also nicht nur auf der konventionellen Modulation der Eigenfrequenz eines elektrischen Schwingkreises, sondern auch auf der Modulation der Kopplung. Die Leistungsfähigkeit des Sensors wird im Vergleich zu konventionellen Sensoren durch die Einführung einer neuen Metrik, der Figure-of-Merit (FOM), bewertet. Die FOM des Sensors beträgt 1300, was eine 15-fache Verbesserung der Sensitivität gegenüber den bisher sensitivsten Mikrowellensensoren bedeutet.

Darüber hinaus wurde ein Herstellungsverfahren auf Wafer-Ebene entwickelt, mit dem 16 Sensoren mit einer Größe von 8 x 12 mm auf einem einzigen 2-Zoll-Wafer hergestellt werden können. Außerdem wurde ein Aufbau entwickelt, der die Sensoren in einen Hochfrequenzschaltkreis, ein Fluoreszenzmikroskop und ein Fluidiksystem integriert. Diese Anordnung ermöglicht die gleichzeitige elektrische und optische Beobachtung von Partikeln bei paralleler Kontrolle des Partikelflusses. Eine Besonderheit des Hochfrequenzschaltkreises ist die Impedanzanpassung des Mikrowellensensors, die interferometrisch realisiert wurde. Dies ist die erste Anwendung einer solchen Impedanzanpassung in einem mikrofluidischen Sensor. Mit dem neuartigen Sensor und der Impedanzanpassung konnte die bisher höchste Sensitivität bei ultraschneller Messgeschwindigkeit demonstriert werden. Mit dem neuen Aufbau wurden Polystyrolkügelchen, Zellen, Tröpfchen und Liposomen detektiert. Bei der Detektion von Polystyrolkügelchen mit einer Größe von 200 nm wurde ein Signal-Rausch-Verhältnis von bis zu 417 erreicht. Dies sind nach unserem Kenntnisstand die kleinsten Partikel mit dem höchsten Signal-Rausch-Verhältnis, die mit Mikrowellen detektiert wurden. Darüber hinaus wurde ein Algorithmus zur Peakverarbeitung entwickelt, der die Impedanzanpassung sowie Amplituden- und Phasendrift korrigiert und somit reproduzierbare Messungen gewährleistet.

Unsere Forschung stellt einen bedeutenden Fortschritt auf dem Weg zur Hochdurchsatz-Charakterisierung von Virionen, Proteinen und DNA anhand ihrer dielektrischen Eigenschaften dar. Da die Charakterisierung mit Mikrowellen ein noch wenig erforschtes Gebiet ist, insbesondere die dielektrische Charakterisierung von einzelnen Nanopartikeln, eröffnet sie vielfältige Möglichkeiten sowohl für wissenschaftliche als auch für diagnostische Anwendungen.

This page has been intentionally left blank.

Acknowledgements

I want to thank Prof. Robert Blick for his guidance throughout my research journey. His input and encouragement helped me, especially in the early stages of my studies. Also, I am grateful for the academic infrastructure (CHyN Building) he was so significantly involved in.

A special mention goes to Prof. Dr. Mehmet Bayindir. He gave me invaluable scientific feedback, and his interest in my research was both motivating and inspiring. The discussions with him enriched my academic perspective and made me reflect on my life goals.

Furthermore, I extend my gratitude to Paul Gwozdz, who tutored me in the initial phases of my Ph.D. journey. His mentorship equipped me with the necessary skills and confidence to navigate independently through my research field.

Additionally, I would like to thank Maxim Heinrichs and Steven Ma for their contributions to this research, particularly in measuring the contrast curves of polycarbonate resists. Jann Harberts provided human-induced pluripotent stem cells, and Lars Bocklage assisted me with the etching of metal layers.

The love of my family smoothed the downs of my PhD journey, and I owe each member of my family a world of gratitude. In particular, my twin brother, Jan Grzegorzewski, has been a source of support and encouragement.

My deepest thanks go to my partner, Inga. Thank you for your patience, understanding, and love, even in the most challenging times.

Finally, my sincere thanks go to the reviewers of my thesis. Their meticulous scrutiny and constructive criticism have significantly contributed to the refinement and precision of this thesis.

This page has been intentionally left blank.

Contents

List of Figures

List of Tables

This page has been intentionally left blank.

List of Abbreviations

AC	**A**lternating **C**urrent
BW	**B**and**w**idth
CPW	**C**o**P**lanar **W**aveguide
cCPW	**c**oupling-based **C**o**P**lanar **W**aveguide
DC	**D**irect **C**urrent
DNA	**D**eoxyribo**N**ucleic **A**cid
DLS	**D**ynamic **L**ight **S**cattering
EBL	**E**lectron **B**eam **L**ithography
EIFC	**E**lectrical **I**mpedance **F**low **C**ytometer
FEM	**F**inite **E**lement **M**ethod
FWHM	**F**ull **W**idth **H**alf **M**aximum
HTS	**H**igh-**T**hroughput **S**creening
IQ	**I**n-phase and **Q**uadrature
LIA	**L**ock-**I**n **A**mplifier
LNA	**L**ow **N**oise **A**mplifier
LOD	**L**imit **o**f **D**etection
iPSC	**i**nduced **P**luripotent **S**tem **C**ell
NMP	**N**-**M**ethyl-2-**P**yrrolidon
PC	**P**oly**c**arbonate
PEEK	**P**oly**e**ther**e**ther**k**etone
PECVD	**P**lasma- **E**nhanced **C**hemical **V**apor **D**eposition
PTFE	**P**oly**t**etra**f**luoro**e**thylene
RF	**R**adio **F**requency
RIE	**R**eactive **I**on **E**tching
RPS	**R**esistive **P**ulse **S**ensing
S/N	**S**ignal-to-**N**oise ratio
SEM	**S**canning **E**lectron **M**icroscope
SLF	**S**acrificial **L**ayer **F**luidics
SOLT	**S**hort-**O**pen-**L**oad-**T**hru
TC	**T**ank **C**ircuit
TIA	**T**rans **I**mpedance **A**mplifier
TL	**T**ransmission **L**ine
TEM	**T**ransverse **E**lectro**m**agnetic
VNA	**V**ector **N**etwork **A**nalyzer
RT-PCR	**R**everse **T**ranscription-**P**olymerase **C**hain **R**eaction
SARS-CoV-2	**S**evere **A**cute-**R**espiratory **S**yndrome- **Co**rona **V**irus-**2**

This page has been intentionally left blank.

Physical Constants

Speed of Light	$c_0 = 2.997\,924\,58 \times 10^{8}\,\mathrm{m\,s^{-1}}$
Vacuum Permittivity	$\varepsilon_0 = 8.854\,187\,81 \times 10^{-12}\,\mathrm{F\,m^{-1}}$
Vacuum Permeability	$\mu_0 = 1.256\,637\,06 \times 10^{-6}\,\mathrm{H\,A^{-1}}$

This page has been intentionally left blank.

List of Symbols

a	distance	m
b	distance	m
b_c	normalized susceptance	$\Omega\,\mathrm{rad}\,\mathrm{F}$
C	capacitance	F
d	distance	m
E	electric field	$\mathrm{V\,m^{-1}}$
f	frequency	Hz
FOM	figure of merit	$\mathrm{L^{-1}}$
G	conductance	S
g	coupling coefficient	
h	height	m
h_p	particle translocation height	m
I	current	A
l	distance	m
L	inductance	H
L	channel length	m
P	polarization	$\mathrm{C\,m^{-2}}$
p	pressure	Pa
Q	quality factor	
Q	flow rate	$\mathrm{m^2\,s^{-1}}$
R	resistance	Ω
R	signal amplitude	V
R_{hyd}	hydraulic resistance	$\mathrm{Pa\,s\,m^{-3}}$
ΔR_{T}	peak amplitude (Transformed)	V
S	scattering parameter	
s	distance	m
U	potential	V
V	voltage	V
V_{eff}	effective volume	L
v_p	particle flow velocity	$\mathrm{m\,s^{-1}}$
w	distance	m
W	stored energy	J
w_p	peak width	s
X	in-phase component	V
Y	quadrature component	V
Z	impedance	Ω
z	distance	m
α	attenuation constant	$\mathrm{Np\,m^{-1}}$
$\alpha_{1,2}$	normalization factors	
β	phase constant	$\mathrm{rad\,m^{-1}}$
δ	skin depth	m

γ	propagation constant	$\mathrm{Np\,m^{-1}} + j\,\mathrm{rad\,m^{-1}}$
Γ	reflection coefficient	
λ_0	free space wavelength	m
η	viscosity	Pa s
ω	angular frequency	$\mathrm{rad\,s^{-1}}$
ρ	resistivity of the conductor	$\Omega\,\mathrm{m}$
σ	conductivity	$\mathrm{S\,m^{-1}}$
σ_{noise}	noise as standard deviation	$\mathrm{V\,S\,m^{-1}}$
$\tan\delta_{\mathrm{e}}$	dielectric loss tangents	
τ	relaxation time	s
ϕ	angle	$^\circ$
Θ	phase	$^\circ$
Θ_{T}	peak phase (transformed)	$^\circ$
Θ_{n}	peak phase (drift corrected)	$^\circ$
ε	permittivity	
$\varepsilon_{\mathrm{eff}}$	effective permittivity	
ξ	volume	$\mathrm{m^3}$

Chapter 1

Introduction

The opening words of my thesis quote Richard Feynman's famous 1959 lecture: "There is plenty of room at the bottom". Feynman aimed to establish a new field of physics at the atomic level of matter. He used the word *bottom* to refer to the ability to manipulate matter on an atomic scale. In contrast, this thesis focuses on detecting and characterizing individual nanoscopic particles in fluid. Here, *bottom* refers to objects at the nanoscale, significantly smaller than the biological cell, which is around ten micrometers and already thoroughly explored. This nanoscale is significant because many crucial processes occur at the subcellular level involving nanoscopic entities such as bacteria, viruses, proteins, or DNA. Consequently, these entities often play direct or indirect roles in human diseases, and therefore, detecting these particles is the subject of many scientific and clinical endeavors. However, detecting and characterizing such small objects in fluids remains a challenging task.

Evolution of Resistive Pulse Sensing: A Blueprint for High-Frequency Sensing?

In 1996, Kasianowicz et al. demonstrated a remarkably high sensitivity of the resistive pulse sensing (RPS) method, also known as the Coulter counter, by detecting single strands of RNA [2]. RPS is an all-electric, label-free method for detecting single particles in a fluid. It consists of two reservoirs connected by a pore. A voltage applied across the reservoirs creates a constant flow of ions through the pore. As particles translocate through the pore, they cause a modulation in the ion current. The strength of this modulation depends on the size of the translocating particles. Thus, the Coulter counter provides information on particle size in a label-free and non-invasive manner.

Fig. 1.1 illustrates the findings of Kasianowicz et al. in their detection of individual RNA strands. The first arrow indicates applying a -120 mV potential across a membrane, resulting in a stable -120 pA current. A second arrow indicates the addition of poly[U] oligomers, averaging 210 bases in length. The translocation of RNA molecules through a channel blocks the ionic current. An expanded time scale in the lower graph illustrates two exemplary blockade events. The detection of individual RNA strands opened a new field of electrical nanoparticle sensing and led to the revival of a technology that Wallace H. Coulter had established already in 1953 [3].

Within 15 years after the detection of single RNA strands by RPS for the first time, numerous companies, including Oxford Nanopore Technologies, Ionera, Nanopore Solutions, and Goeppert, have successfully commercialized RPS-based devices [4]. Because of their all-electric nature, the instruments have been miniaturized into portable, handheld devices. These modern RPS devices can detect single nucleic acids (e.g., gene sequencing), proteins, and polymer species [5, 6, 7, 8, 6, 9]. These

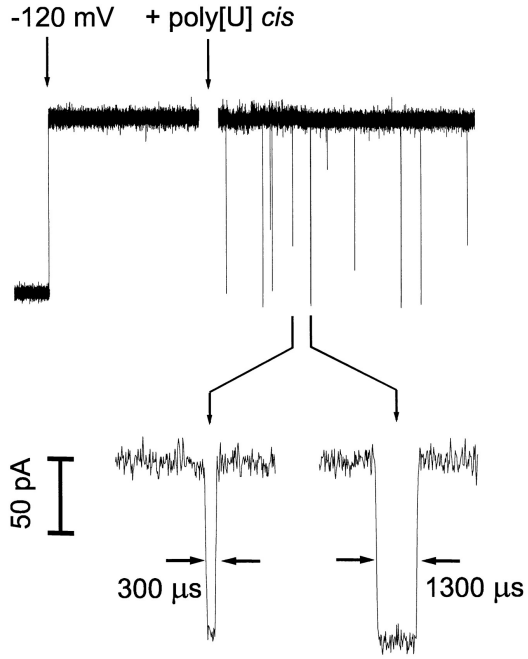

FIGURE 1.1: **Single RNA strand detection via resistive pulse sensing (RPS):** At the first arrow, a -120 mV potential was applied across the membrane, generating a steady -120 pA current. The second arrow points to when poly[U] oligomers (mean length: 210 bases) were added, causing short-lived current interruptions indicative of RNA translocation events. The lower graph, with an expanded time scale, depicts two representative blockade events. This experiment, conducted by Kasianowicz et al. (1996), demonstrates the exceptional sensitivity of RPS in detecting nanoscale objects. Adapted from "Characterization of individual polynucleotide molecules using a membrane channel," Kasianowicz et al., 1996, in Proceedings of the National Academy of Sciences of the United States of America. Vol. 93., pp. 13770-13773 [2], © 1996 National Academy of Sciences.

developments have made the RPS the most successful all-electric inflow single particle detection system. Clinical applications range from human genomics to cancer diagnostics and virus detection [10]. The scientific community has also recognized the potential of RPS. Since the year 2000, the number of publications (PubMed entries) on the topics of *resistive pulse sensing*, *nanopore*, and *coulter counter* has increased dramatically. In particular, since 2010, this number has doubled approximately every 4.3 years, as detailed in the Appendix A.1.

In summary, since the establishment of nanoscopic sensing capabilities by detecting single RNA strands, RPS has experienced an unprecedented success story. RPS's trajectory may provide a path forward for AC sensing techniques, which are still in an earlier stage of development.

However, RPS also has its limitations. In particular, they are unable to discriminate between particles of the same size, and their measurement speed is typically limited to a bandwidth (BW) of about 10 kHz, with a maximum value of 10 MHz [4, 11, 7, 12]. At higher BWs, the f^2 noise component limits the maximum measurement speed. This noise originates from the system's total capacitance and amplifier input-referred voltage noise [7]. These limitations necessitate an alternative approach to

ultra-fast inflow single-particle sensing.

High-Frequency Single Particle Sensing

Electrical impedance flow sensing is a compelling alternative to RPS. It is an all-electric label-free approach with ultra-fast sensing capabilities. This method relies on the interaction of objects with alternating electric fields created by electrodes placed in close proximity to a fluidic channel. In 1999, Ayliffe et al. first introduced such a sensor [13]. Fig. 1.2a illustrates the original design of Ayliffe's sensor, featuring microchannels with integrated gold electrodes. Fig. 1.2b and c present the sensor's magnitude and phase response to human polymorphonuclear leukocytes (PMNs) and teleost fish red blood cells (RBSs) at four selected frequencies. This pioneering work achieved the first detection of individual cells and demonstrated the potential of electrical impedance flow cytometry (EIFC) in differentiating between cell types.

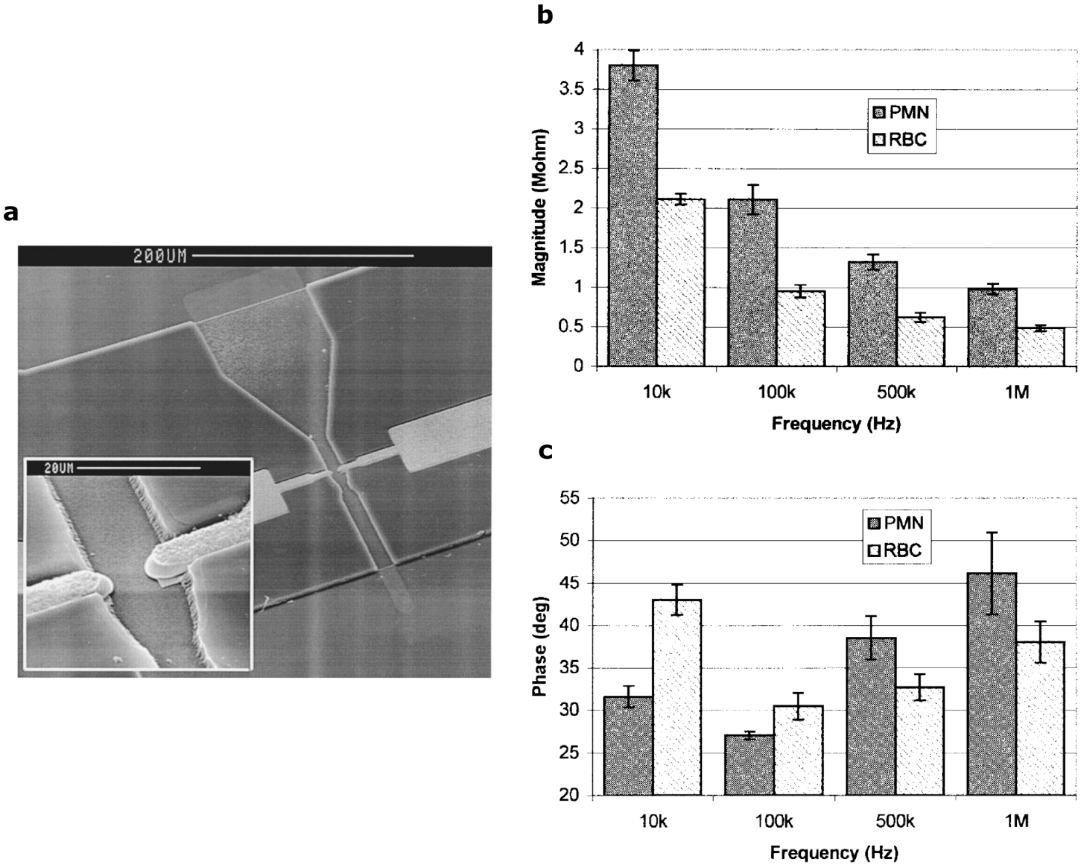

FIGURE 1.2: **Electrical impedance flow sensing of individual cells: a**, SEM image of microchannels with integrated gold electrodes, depicting the first chip used for electrical impedance flow sensing of individual cells. The magnitude **b** and phase **c** of the impedance measured for two cell types, for human polymorphonuclear leukocytes (PMNs) and teleost fish red blood cells (RBS) at four selected frequencies. Error bars depict one standard deviation. Adapted from "Electric Impedance Spectroscopy Using Microchannels with Integrated Metal Electrodes," Ayliffe et al., 1999, in IEEE Journal of Microelectromechanical Systems, Vol. 8. No.1, pp. 50-57 [13], © 1999 IEEE.

The AC signals change the nature of the measurement, making it a complementary method to RPS. Compared to RPS, which measures particle size, the electric fields

of the EIFC interact directly with the particle, probing its dielectric properties, and different measurement frequencies provide information about different properties of the particle under test. For example, at frequencies between 10 kHz and 10 MHz, the EIFC is most sensitive to the properties of the cell membrane [14]. The membrane capacitance is short-circuited at frequencies above 10 MHz, allowing the intracellular parts of the cell to be probed [15]. A cell circuit model can be used to infer cell properties such as cell size, membrane potential, capacitance, or cytoplasmic conductivity.

Conventional EIFCs have two major limitations: (1) they lack sensitivity compared to RPS, and (2) their measurement frequency is limited to the MHz range. Recently, Xie et al. [16] used EIFC to detect 200 nm particles with a maximum signal-to-noise ratio (S/N) of ≈ 6, currently the smallest single particles detected with AC signals. The other major limitation is bandwidth, as conventional EIFCs operate primarily in the low MHz range [17], typically limited by the trans-impedance amplifier (TIA). The maximum reported measurement frequency for such a setup is 450 MHz [18]. Thus, the EIFC has yet to achieve measurements at GHz frequencies.

Reflectometry and the GHz Regime for Biomolecules

As mentioned in the previous section, EIFC does not operate in the GHz regime. Consequently, the GHz regime has been less studied than the kHz and MHz regimes. Nevertheless, the GHz regime is highly relevant, as recent research in cell studies has shown. At these frequencies, different cell states and types can be identified [19, 20, 21]. Hussein et al. discovered a unique dielectric signature for breast cancer cells in this regime [22]. These discoveries underscore the potential of GHz frequencies to discriminate between different cell types and states, including the identification of cancer cells. Given the structural and functional similarities between cells, bacteria, and viruses, it is plausible that the GHz regime may also provide insights into smaller biological objects.

Reflectometry offers another detection architecture that differs from traditional EIFCs, allowing it to operate and probe particles in the GHz regime without relying on a TIA. This architecture was first demonstrated by Schoelkopf et al. [23]. They measured the reflected signal intensity from a tank circuit (TC) connected to a high impedance single electron transistor at 1.7 GHz. Unlike the RPS, such a configuration is not limited by f^2 noise, allowing super-fast particle detection with measurement bandwidths exceeding 100 MHz. Schoelkopf's work inspired the development of similar detection architectures. These have been used for inflow particle detection and have achieved measurement bandwidths exceeding 30 MHz [24, 25, 26]. Reflectometric methods currently offer advantages over RPS in some areas. However, their sensitivity needs further improvement, as the smallest detected object is a 500 nm polystyrene bead [24].

In summary, both the EIFC and TC-based reflectometric approaches share the same attributes that have contributed to the success of RPS. They are label-free, non-destructive, all-electric, and reflectometry has an increased measurement BW compared to RPS, making it suitable for high throughput screening (HTS) of particles. The non-destructive nature allows analyzed or sorted samples to remain viable for subsequent scientific or medical applications. An advantage of AC sensing is the

ability of electric fields to interact directly with a particle. Unlike RPS, this interaction allows for an internal view of a particle, differentiating particles of similar size based on their dielectric properties.

However, AC-based techniques fall short of RPS in terms of sensitivity. Further improvements in sensitivity will enable the detection of sub-cellular objects such as bacteria, viruses, proteins, or DNA. Such advancements might propel electrical impedance flow sensing to a success similar to that achieved by RPS.

The limitations of AC-based techniques have led to the primary goal of this thesis: **Enhance sensitivity for the detection of nanoscopic particles at GHz frequencies**. To accomplish this, I have developed, optimized, and fabricated an ultra-sensitive, finely-tuned novel sensor type that operates in a coupling-based configuration. A distinctive feature of this configuration is the modulation of coupling strength between the feedline and resonator as particles translocate through the sensing volume. The development process of the novel sensor, included deriving an analytical model that describes the working principle and finite element method (FEM) simulations which guided the geometrical optimization process that drastically improved sensitivity and adjusted the sensor for the operation frequency of approximately 20 GHz. Concluding the developmental phase, the sensor was manufactured and thoroughly characterized, and its performance was compared with analytical and simulation results. Altogether, the analytical models, the FEM simulations, and the empirical measurements provide a complete picture of the novel coupling-based resonator type. Incorporating that sensor in a new interferometric impedance-matching circuit detected 200 nm-sized polystyrene beads, the up-to-date smallest particles detected at RF, with unprecedented signal-to-noise ratios. These advancements represent significant progress towards the dielectric classification nanoscopic particles like virions, proteins, and DNA.

This page has been intentionally left blank.

Chapter 2

Theory

This chapter provides a comprehensive introduction to transmission line (TL) theory, which is essential for the analytical modeling of the novel coupling-based sensor. This model is used in section 3.7 to compare analytical results with simulations and experiments. Moreover, the insights gained from the TL theory enabled the derivation of the coupling-based theory. Specifically, I derived an equation that illustrates how the coupling coefficient changes in response to the modulation of the capacitance with respect to the sensing area and relates the coupling coefficient with circuit parameters. This relation provides a framework for systematically tuning the sensor geometry, as explored in section 3.5.

2.1 Transmission Line Theory

Transmission line theory describes the propagation of electrical signals in circuits with a length smaller than the electrical wavelength. It is commonly applied to radio frequencies ranging from about 3 kHz, corresponding to a wavelength of several kilometers, to 300 GHz, corresponding to a wavelength of 1 mm. At lower frequencies, circuit analysis is used, approximating a circuit's behavior by lumped elements such as resistors, inductors, and capacitors. This method assumes that both the magnitude and phase of the voltage and current in a circuit are approximately constant across the lumped elements.

However, the constant magnitude and phase assumptions are no longer valid when the electrical wavelength is shorter than the circuit approximated by the lumped elements. In such cases, a more accurate representation can be achieved by using a distributed element model of the TL. This distributed model is the starting point for deriving the famous telegrapher equations.

2.1.1 Telegrapher Equations

In this section, I derive the *Telegrapher Equations*, which provide a mathematical framework to describe wave propagation on TL. The derivation follows the textbook *Microwave Engineering* by *D. Pozar* [27].

Fig. 2.1a illustrates Δz, an infinitesimally long TL segment. The current and voltage along the line are described by $i(z,t)$ and $v(z,t)$, respectively. Two parallel lines schematically represent the TL. The representation of two parallel lines is essential, especially at high frequencies, where the electric wave requires a return path, typically between two conductors. These lines can be represented with lumped element components as shown in Fig. 2.1b. A lumped element is valid under the condition

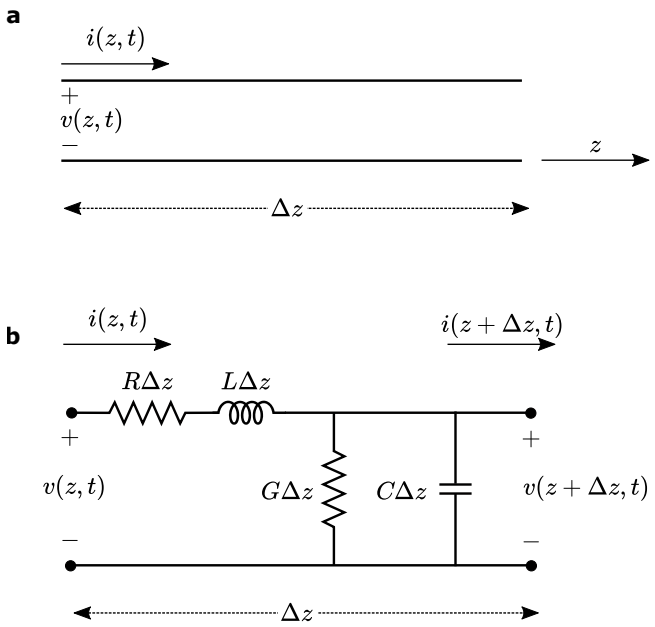

FIGURE 2.1: **Schematic illustrations of an infinitesimal length segment Δz in a transmission line (TL): a**, Standard representation depicted by two parallel lines symbolizing the conductive paths. **b**, Lumped element representation showing the simplification into discrete components.

that the phase and amplitude components of the voltage and current remain approximately constant over an infinitesimal length of the TL. This assumption is especially true when the signal's wavelength is much larger than the segment of the TL under consideration.

These lumped elements are a series resistance and inductance per unit length, R and L, respectively, and a shunt conductance and shunt capacitance, G and C, respectively. A given length of a TL can be viewed as an interconnection of many infinitesimally small sections.

Applying Kirchoff's voltage law to the circuit in Fig. 2.1b yields the following relationship between voltage and current along the TL:

$$v(z,t) - R\Delta z i(z,t) - L\Delta z \frac{\partial i(z,t)}{\partial t} - v(z+\Delta z,t) = 0 \tag{2.1}$$

and Kirchoff's current law leads to

$$i(z,t) - G\Delta z v(z+\Delta z,t) - C\Delta z \frac{\partial v(z+\Delta z,t)}{\partial t} - i(z+\Delta z,t) = 0 \tag{2.2}$$

Both equations are divided by Δz and the limit $\Delta z \to 0$ leads to the *Telegrapher Equations*

$$\begin{aligned} \frac{\partial v(z,t)}{\partial z} &= -Ri(z,t) - L\frac{\partial i(z,t)}{\partial t}, \\ \frac{\partial i(z,t)}{\partial z} &= -Gi(z,t) - C\frac{\partial v(z,t)}{\partial t}. \end{aligned} \tag{2.3}$$

These differential equations can be investigated in a standard sinusoidal steady-state

condition. In that condition, the current and voltage can be represented as phasors with:

$$\begin{aligned} v(z,t) &= V(z)\mathrm{e}^{j\omega t}, \\ i(z,t) &= I(z)\mathrm{e}^{j\omega t} \end{aligned} \tag{2.4}$$

with ω being the angular frequency of the sinusoidal source.

Substituting these representations into the *Telegrapher's Equations* (2.3) and using $\partial \mathrm{e}^{j\omega t}/\partial t = j\omega \mathrm{e}^{j\omega t}$, we can transform the Telegrapher's equations into the following steady-state phasor form:

$$\begin{aligned} \frac{dV(z)}{dz} &= -(R + j\omega L)I(z), \\ \frac{dI(z)}{dz} &= -(G + j\omega C)V(z). \end{aligned} \tag{2.5}$$

2.1.2 Waves on a Transmission Line

The steady-state *Telegrapher Equations* 2.3 are two dependent differential equations. If a second derivative with respect to z is taken for Eqs. 2.5, we get

$$\begin{aligned} \frac{d^2V(z)}{d^2z} &= \gamma V(z), \\ \frac{d^2I(z)}{d^2z} &= \gamma I(z), \end{aligned} \tag{2.6}$$

with $\gamma = \alpha + j\beta = \sqrt{(R + j\omega L)(G + j\omega C)}$. γ is called the complex propagation constant with α the attenuation constant and β the phase constant. Eqs. 2.6 indicate that $V(z)$ and $I(z)$ have structurally similar solution. By substitution, it can be seen that each Eq. 2.6 has two independent solutions of the form

$$\begin{aligned} V(z) &= V_0^+\mathrm{e}^{-\gamma z} + V_0^-\mathrm{e}^{\gamma z}, \\ I(z) &= I_0^+\mathrm{e}^{-\gamma z} + I_0^-\mathrm{e}^{\gamma z}. \end{aligned} \tag{2.7}$$

The term $\mathrm{e}^{-\gamma z}$ describes a wave that propagates in positive z direction with an amplitude of V_0^+ and correspondingly, the term $\mathrm{e}^{\gamma z}$ describes a wave that propagates in negative $-z$ direction with an amplitude of V_0^-.

Applying the wave solutions to the current Eq. 2.5 (can be derived analogously for $V(z)$), we get

$$\begin{aligned} I(z) &= -\frac{1}{(R + j\omega L)}\frac{dV(z)}{dz} \\ I(z) &= -\frac{1}{(R + j\omega L)}\frac{d(V_0^+\mathrm{e}^{-\gamma z} + V_0^-\mathrm{e}^{\gamma z})}{dz} \\ I(z) &= \frac{1}{(R + j\omega L)}(V_0^+\gamma\mathrm{e}^{-\gamma z} - V_0^-\gamma\mathrm{e}^{\gamma z}) \\ I(z) &= \frac{\gamma}{R + j\omega L}(V_0^+\mathrm{e}^{-\gamma z} - V_0^-\mathrm{e}^{\gamma z}). \end{aligned} \tag{2.8}$$

The quotient of $I(V)$ and $I(z)$ from Eq. 2.7 and Eq. 2.8,results in

$$\begin{aligned} Z_0 &= \frac{V(z)}{I(z)} \\ &= \frac{R + j\omega L}{\gamma} \\ &= \sqrt{\frac{R + j\omega L}{G + j\omega C}}. \end{aligned} \tag{2.9}$$

The derived equation is independent of the position z on the TL and is called the line's characteristic impedance Z_0.

The characteristic impedance relates the current and voltage on a TL as follows

$$\frac{V_0^+}{I_0^+} = Z_0 = \frac{-V_0^-}{I_0^-} \tag{2.10}$$

The current and voltage can be written in terms of their characteristic impedance of the TL as:

$$\begin{aligned} I(z) &= \frac{V_0^+}{Z_0} e^{-\gamma z} - \frac{V_0^-}{Z_0} e^{\gamma z}, \\ V(z) &= I_0^+ Z_0 \, e^{-\gamma z} - I_0^- Z_0 \, e^{\gamma z}. \end{aligned} \tag{2.11}$$

2.1.3 Transmission Line Terminated with a Load Impedance

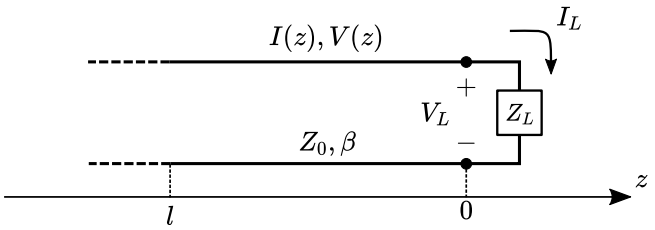

FIGURE 2.2: **Transmission line terminated with a load impedance** Z_L: This schematic illustrates the connection between a TL and a load, characterized by a load impedance value of Z_L.

As demonstrated in the previous section, the characteristic impedance Z_0 is constant over the entire TL, ensuring no reflection of an electric wave. This relation changes once a load impedance Z_L terminates the line. Fig. 2.2 displays a TL terminated with a load impedance. The load impedance induces a boundary condition at $z = 0$. At that boundary condition, the ratio between the voltage and current has to be Z_L. If the load impedance differs from the line's characteristic impedance ($Z_0 \neq Z_L$), the boundary condition can only be satisfied if an additional backward traveling wave is excited. A voltage wave on a TL is mathematically described as $V_0^+ e^{-j\gamma z}$, with $\gamma = \alpha + j\beta$ the propagation constant. The voltage at each point of the TL is a superposition of the incident and reflected waves with

$$V(z) = V_0^+ e^{-j\gamma z} + V_0^- e^{j\gamma z}. \tag{2.12}$$

The incoming and reflected voltage waves have corresponding current waves given by Eq. 2.11.

$$I(z) = \frac{V_0^+}{Z_0} e^{-j\gamma z} + \frac{V_0^-}{Z_0} e^{j\gamma z}. \tag{2.13}$$

The load impedance at $z = 0$ is

$$Z_L(0) = \frac{V(0)}{I(0)} = \frac{V_0^+ + V_0^-}{V_0^+ - V_0^-} Z_0 \tag{2.14}$$

Eq. 2.14 can be solved for the reflected wave V_0^-

$$V_0^- = V_0^+ \frac{Z_0 - Z_L}{Z_0 + Z_L}. \tag{2.15}$$

As expected, this equation shows that the reflected wave becomes zero for $Z_0 = Z_L$. The ratio between the reflected and incoming wave is called the *reflection coefficient* Γ given by

$$\underline{\underline{\Gamma = \frac{V_0^-}{V_0^+} = \frac{Z_L - Z_0}{Z_L + Z_0}}}. \tag{2.16}$$

The reflection coefficient is an important quantity that can be measured with a vector network analyzer (VNA) and is used extensively in this thesis. It can be used to characterize circuits and, for example, describe the quality of an impedance match between a load and the feedline.

It is generally desirable to have zero back reflections on TLs in order to transfer the maximum power to a circuit (e.g., a sensor). This condition is achieved when the load impedance matches the feedline impedance $Z_L = Z_0$. If the load impedance is much lower or higher, the reflection coefficient becomes one, and the total power is reflected $|\Gamma| \to 1$.

Next, the current and voltage waves on a not-perfectly-matched TL are investigated. For such a condition, Eqs. (2.12) & (2.13) can be rewritten with the definition of Γ from Eq. 2.16 as

$$\begin{aligned} V(z) &= V_0^+ (e^{-j\gamma z} + \Gamma e^{j\gamma z}), \\ I(z) &= \frac{V_0^+}{Z_0} (e^{-j\gamma z} - \Gamma e^{j\gamma z}), \end{aligned} \tag{2.17}$$

The reflection of waves at a not perfectly impedance-matched load leads to standing waves. For special applications, standing waves can be utilized to build resonators. Such resonators will be discussed in section 2.2. These waves alter the impedance at each point of the TL. From Eq. 2.17, the input impedance at a distance $l = -z$ in the direction of the load is

$$Z_{\text{in}} = \frac{V(-l)}{I(-l)} = Z_0 \frac{e^{j\gamma l} + \Gamma e^{-j\gamma l}}{e^{j\gamma l} - \Gamma e^{-j\gamma l}} \tag{2.18}$$

In the following, two load impedance cases are discussed. The first case is a short-circuited load. A shorted load has an impedance of $Z_L = 0$, and from Eq. 2.16 we get $\Gamma = -1$. The corresponding input impedance can be calculated with Eq. 2.18, and

by applying the trigonometric identities, the input impedance becomes

$$\begin{aligned} Z_{\text{short}} &= Z_0 \frac{e^{j\gamma l} - e^{-j\gamma l}}{e^{j\gamma l} + e^{-j\gamma l}} \\ &= Z_0 \tanh \gamma l. \end{aligned} \tag{2.19}$$

The second case is an open load. The calculation of an open load is similar to the shorted load. The only difference is the reflection coefficient, which becomes $\Gamma = 1$. To reduce the length of calculation, we observe that Eq. 2.18 becomes the inverse with respect to the shorted load with

$$Z_{\text{open}} = Z_0 \coth \gamma l. \tag{2.20}$$

The similarity between the input impedance of an open and shorted load allows the use of either termination to build a TL resonator. The following section will discuss such resonators and the differences between an open or shorted TL termination.

2.2 Transmission Line Resonator

This section discusses TL resonators and compares them with conventional *RLC*-resonant circuit models. This comparison allows us to derive relationships between TL parameters and *RLC*-resonant circuit parameters. Furthermore, the differences between a $\lambda/2$- and $\lambda/4$-resonator are demonstrated. The theory of both resonators is used in section 3.7 to highlight the advantages of a coupled $\lambda/4$ resonator over a $\lambda/2$ resonator for capacitive sensing. These resonators can be obtained by terminating a TL with an open or short circuit. The terminations of a TL were discussed in the previous section 2.1.3.

In Fig. 2.3a, TL models for both open- and short-circuited TLs are presented in black and blue, respectively. The corresponding voltage profiles along these TLs are illustrated in Fig. 2.3b. The open TL has a length of $l_{\lambda/2}$, while the shorted TL measures $l_{\lambda/4}$. These TLs are characterized by an attenuation constant α, a phase constant β, and a characteristic impedance Z_0. Both TLs receive a signal with a wavelength of λ. They are positioned such that the termination point of the shorted TL is offset by a distance of $\lambda/4$ relative to the open termination. This configuration ensures that the reflected voltage waves from both TLs are identical in magnitude and phase. This illustration reinforces the idea that different TL lengths can produce identical standing waves when properly terminated, resulting in resonators with equivalent resonant conditions.

At resonance, both resonators can be modeled as a parallel *RLC*-resonant circuit [27], as shown in Fig. 2.3c. The input impedance Z_{RLC} into a parallel *RLC*-resonant circuit is

$$Z_{RLC} = \left(\frac{1}{R} + \frac{1}{j\omega L_R} + j\omega C_R \right)^{-1} \tag{2.21}$$

with R the resistance, L_R the magnetic inductance, and C_R the capacitance of the resonant circuit.

In the book *Microwave Engineering* by Pozar [27], relationships are established between the parameters of a parallel *RLC* resonant circuit and the TL resonator. These relationships can be derived by rearranging the input impedance equations Eq. 2.21 of the *RLC* circuit and those of the open Eq. 2.19 and short-circuited Eq. 2.20 TL

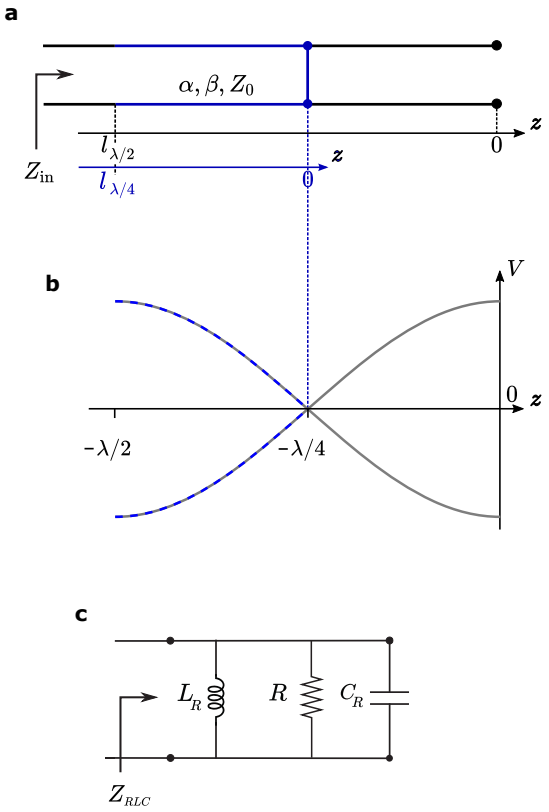

FIGURE 2.3: **Distributed circuit models of shorted and open transmission lines (TL): a**, Diagram contrasting the TL model for a shorted $\lambda/4$-line (shown in blue) with an open $\lambda/2$-line (in black). **b**, Graphical representation of the voltage variation along both short- and open-circuited TL, depicted in blue and black, respectively. **c**, The equivalent parallel *RLC*-circuit showing how these TLs at resonance can be modeled using standard lumped components.

resonators into a similar form. By comparing these equations, one can deduce the relationships between the parameters of both circuits. Table 2.1 summarizes these relationships.

By comparison, we can conclude that for the same resonance frequency ω_0, the capacitance of shorted $\lambda/4$-TL is half the capacitance of an open $\lambda/2$-TL. The inductance is inversely proportional to the capacitance. The inductance of a shorted $\lambda/4$-TL is, therefore, twice as high as that of an open $\lambda/2$-TL.

The resonance frequency for both resonators is given by

$$w_0 = \frac{1}{\sqrt{L_R C_R}}. \tag{2.22}$$

A resonant circuit's quality factor Q is defined as the ratio between the average stored energy and the energy dissipated per unit time. The quality factor can be divided into the resonator's quality factor, called the unloaded or internal quality factor Q_0, and the quality factor of an external load resistance Q_e. The loaded quality factor is given by

$$\frac{1}{Q_L} = \frac{1}{Q_e} + \frac{1}{Q_0}. \tag{2.23}$$

In the realm of time-resolved particle detection, bandwidth (BW) plays an important

TABLE 2.1: **Comparison of *RLC* tank circuit parameters with $\lambda/4$ and $\lambda/2$ transmission line (TL) models:** This table illustrates the relationship between the *RLC* tank circuit parameters shown in Fig. 2.3c and the parameters specific to the $\lambda/4$ and $\lambda/2$ TL models presented in Fig. 2.3a. It serves as a reference for understanding the correlation between these equivalent circuit representations.

RLC-circuit parameter	shorted $\lambda/4$-TL	open $\lambda/2$-TL
C_R	$\frac{\pi}{4\omega_0 Z_0}$	$\frac{\pi}{2\omega_0 Z_0}$
L_R	$\frac{1}{\omega_0^2 C_R}$	$\frac{1}{\omega_0^2 C_R}$
Q_0	$\frac{\pi}{4\alpha l}$	$\frac{\pi}{2\alpha l}$
R	$\frac{Z_0}{\alpha l}$	$\frac{Z_0}{\alpha l}$

role, especially when the goal is to achieve ultra-fast detection. The quality factor is inherently related to the bandwidth. This relationship can be expressed mathematically as

$$Q_L = \frac{f_0}{\mathrm{BW}}. \tag{2.24}$$

In the experimental part of this dissertation, I use a resonator for the time-resolved detection of particles in a microfluidic setup. The loaded quality factor of our sensor was about 100 at a resonance frequency of ≈ 20 GHz. This specification results in a resonator with a limited bandwidth of 200 MHz, allowing a temporal resolution of about five nanoseconds.

2.2.1 Coupling to a $\lambda/4$ - Resonator

The operating principle of the innovative inflow particle microwave sensor, detailed in section 3.4, is based on the particle-induced modulation of the coupling strength between a circuit and a resonator. In detail, a fluidic channel is positioned between the feedline and a resonator, forming a capacitance that links both circuits. As particles move through the channel, they modulate the coupling between the circuits.

Understanding the relationship between the measured signal and the modulation of the coupling strength is essential. Therefore, in the following section, I derive the coupling theory. Although the derivation has similarities with the capacitively coupled $\lambda/2$ resonator described in the book *Microwave Engineering* [27], I have made original contributions to the derivation of a capacitively coupled $\lambda/4$ resonator.

The coupling coefficient g quantifies the coupling strength between a resonator and an attached circuit. It is defined by the ratio of the internal to the external quality factor

$$g = \frac{Q_0}{Q_e}. \tag{2.25}$$

A resonator can be either loosely coupled to maintain a high loaded quality factor or strongly coupled to ensure good power transfer. For the sensor developed in this

thesis, the coupling strength must be fine-tuned to achieve optimal performance.

In the following, I derive the dependence between the coupling coefficient g and the circuit parameters of the coupling-based sensor, represented by a distributed circuit model as shown in Fig. 2.4. The model consists of a feedline with the char-

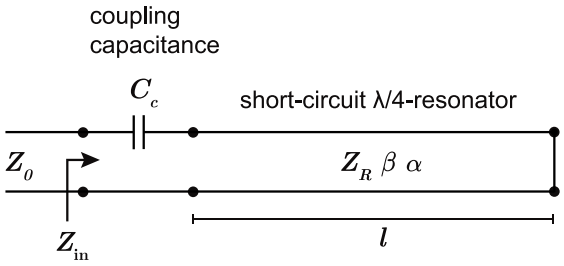

FIGURE 2.4: **Distributed circuit model of the novel coupling-based sensor:** This model represents the coupling approach of the sensor, where the capacitance C_c acts as a coupling element between the feedline and a $\lambda/4$-TL resonator. Particles within the sensing volume modulate this capacitance.

acteristic impedance Z_0 coupled with the coupling capacitance C_c to a short-circuit $\lambda/4$-resonator. This resonator consists of a TL with length l, attenuation constant α, phase constant β, and characteristic impedance Z_R. The derivation will relate these circuit parameters with the coupling coefficient g.

At the beginning of the derivation, the TL losses ($\alpha = 0$) are neglected ($\gamma = j\beta$). These losses will be reintroduced later. The normalized input impedance $\tilde{Z}_{\text{in}}$ from a feedline to a capacitively coupled lossless $\lambda/4$ TL resonator is given by

$$\begin{aligned}\tilde{Z}_{\text{in}}(\omega) &= \frac{Z_{\text{in}}}{Z_0}, \\ &= -j\frac{1}{\omega C_c Z_0} + \frac{Z_R}{Z_0}\tanh(j\beta l), \\ &= -j\left(\frac{1}{b_c} - \frac{Z_R}{Z_0}\tan(\beta l)\right),\end{aligned} \tag{2.26}$$

where $b_c = Z_0\omega C_c$ is the normalized susceptance of the coupling capacitance.

The input impedance varies along the length of the resonator, similar to the impedance of a blank shorted $\lambda/4$ TL. Resonance occurs at frequencies where the length satisfies $\tilde{Z}(\omega) = 0$. Applying this resonance condition to Eq. 2.26 and incorporating the phase velocity defined as $v_p = \omega/\beta$, we obtain the following transient equation

$$(C_c\omega Z_R)^{-1} = \tan\left(\frac{\omega l}{v_p}\right). \tag{2.27}$$

The left part of the equation introduces a resonance frequency shift due to a capacitive load of the resonator.

To get an intuitive understanding of the coupling between the feedline and the circuit, Eq. 2.26 is transformed into an equivalent series *RLC*-circuit, which is done by a Taylor series expansion around the resonance frequency ω_1. At resonance, the input

impedance becomes $\tilde{Z}(\omega_1) = 0$:

$$\begin{aligned}\tilde{Z}(\omega) =& \tilde{Z}(\omega_1) + (\omega - \omega_1) \left.\frac{d\tilde{Z}(\omega)}{d\omega}\right|_{\omega_1} + \dots , \\ =& (\omega - \omega_1) \left.\frac{d\tilde{Z}(\omega)}{d\beta l}\frac{d\beta l}{d\omega}\right|_{\omega_1} + \dots .\end{aligned} \tag{2.28}$$

From Eq. 2.27 and the assumption that $b_c^2 \ll 1$ follows:

$$\begin{aligned}\left.\frac{d\tilde{Z}(\omega)}{d\beta l}\right|_{\omega_1} &= j\frac{Z_R}{Z_0}\left(1 + \tan^2(\beta l)\right) \\ &= j\frac{Z_R}{Z_0}\left(1 + \frac{Z_0^2}{Z_R^2}\frac{1}{b_c^2}\right) \\ &\approx j\frac{Z_0}{Z_R}\frac{1}{b_c^2}\end{aligned} \tag{2.29}$$

For a weakly coupled resonator, no capacitive loading and a negligible reduction of the resonance frequency is assumed. In this case, the length of the resonator is $l \approx \lambda_1/4$ with the wavelength λ_1 given by $\lambda = 2\pi v_p/\omega$. A transverse electromagnetic (TEM) wave on the TL results in

$$\frac{d(\beta l)}{d\omega} = \frac{l}{v_p} \approx \frac{\pi}{2\omega_1}. \tag{2.30}$$

This function is put into to Eq. 2.29 which reduces to

$$\tilde{Z}(\omega) \approx j\frac{Z_0(\omega - \omega_1)}{Z_R b_c^2}\frac{\pi}{2\omega_1}. \tag{2.31}$$

In the case of low loss resonators, the losses due to TL attenuation α can be reintroduced by substituting the resonance frequency with its complex effective frequency $\omega_1 \rightarrow \omega_1\,(1 + j1/2Q_0)$, with Q_0 the internal quality factor of the resonator. This leads to a normalized input impedance of a lossy capacitively coupled $\lambda/4$-resonator

$$\tilde{Z}(\omega) = \frac{\pi Z_0}{4b_c^2 Z_R Q_0} + j\frac{(\omega - \omega_1)}{b_c^2 Z_R}\frac{Z_0\pi}{2\omega_1}. \tag{2.32}$$

In contrast to the initial Eq. 2.26, the Eq. 2.32 can be related to a series *RLC*-circuit near resonance, which has the following form

$$Z_{\text{in}} = R + j\frac{2RQ_0(\omega - \omega_1)}{\omega_1}. \tag{2.33}$$

The real term $R = \pi Z_0^2/4b_c^2 Z_R Q_0$ of Eq. 2.33 corresponds to the input resistance. At resonance, the input impedance is purely real $(\omega - \omega_1) = 0$. For critical coupling, the input impedance has to be matched to the feedline impedance $R = Z_0$. The coupling coefficient of a series *RLC*-circuit is defined as $g = Z_0/R$, which leads to the following relationship:

$$\boxed{g = \frac{4Z_R Z_0 Q_0 \omega^2 C_c^2}{\pi}} \tag{2.34}$$

This equation links the circuit parameters with the coupling coefficient and allows for a systematic adjustment of the coupling coefficient.

2.2.2 Coplanar Waveguide

Transmission lines come in various forms, including coaxial, strip, microstrip, slot, coplanar, and single conductor lines, such as rectangular waveguides. Each type of TL has a theory describing the relationship between its geometric characteristics and electrical properties. These properties include characteristic impedance, effective permittivity, unit-length inductance and conductance, and losses. For more details on different types of coplanar waveguide structures, I recommend the book *Coplanar Waveguide Circuits, Components, and Systems* by R. Simons [28]. In the following, I will introduce the theory of coplanar waveguides (CPW) with finite substrate thickness, a TL discussed in detail in this thesis.

Cheng P. Wen invented CPWs in 1969 [29]. A typical CPW consists of a central signal line and two ground planes on either side. These are fabricated on the top surface of a dielectric substrate. CPWs are particularly suited for the sensor developed in this thesis. The CPWs can be fabricated by standard lithographic methods, including photolithography and electron beam lithography. The precision of e-beam lithography allows the fabrication of electrodes with nanoscale dimensions. In addition, CPWs do not require a conductive backside. Instead, the electric field is localized between the signal and ground lines on the top of the chip. In the case of the sensor presented in this thesis, this arrangement enhances the confinement of the electric field to the microfluidic channel, which is also located on the top of the chip. Furthermore, the characteristic impedance of a CPW can be fine-tuned, e.g., to the most commonly used 50 Ω, making CPW probe tips ideal for ensuring fast, reversible, and impedance-matched connections between the CPW sensor and the measurement circuit.

Fig. 2.5 displays a schematic model of a CPW. The width of the signal line is w, the distance from the signal line to the ground is s, and a finite dielectric substrate thickness is h. For simplicity, the ground plane width is assumed to be infinite. The red

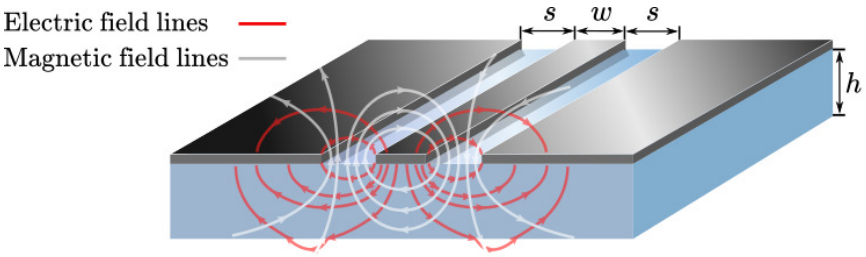

FIGURE 2.5: **Schematic sketch of a coplanar waveguide (CPW):** The central line width w, the distance s between the central line and the ground planes, and the substrate height h define the CPW geometry. These parameters are linked to electrical characteristics like impedance and attenuation of the CPW.

and gray lines schematically represent the electric and magnetic field lines, respectively. The field lines represent the solution of Laplace's equations in two dimensions. These solutions are difficult to find because they are nonuniform fields in the natural coordinate system. The electric field and the permittivities of the dielectrics

are essential properties because they are directly related to the TL's capacitance and inductance per unit length, characteristic impedance, and effective permittivity.

An elegant workaround to solve Laplace's equations is the quasi-static analysis based on the conformal mapping method. It transforms the TL boundaries into a simpler coordinate system, such as a parallel plate configuration. Laplace's equations for a parallel plate configuration are easy to solve because the solution is a uniform field. The transformation is based on the assumption that magnetic walls can replace all dielectric boundaries. This assumption is only valid if the electric field lines are parallel to the dielectric boundaries [30]. Such a transformation was first performed for an infinitely thick substrate [29]. The following section demonstrates the transformation for a finite thickness. The transformation follows the book by I. Bahl, M. Bozzi, and R. Garg called *Microstrip Lines and Slotlines, Third Edition* [31].

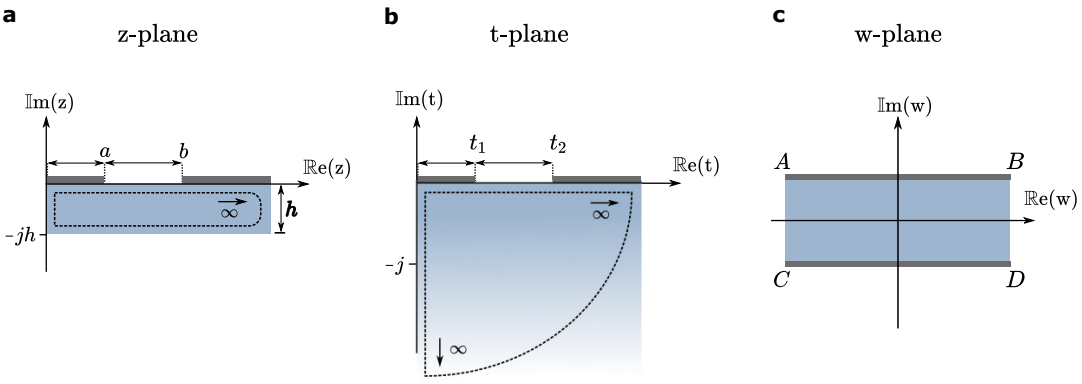

FIGURE 2.6: **Conformal mapping transformations: a**, Z-plane with a finite thickness substrate. **b**, Transformation of the finite substrate thickness in the z-plane to the infinite thickness t-plane. **c**, The Schwarz-Christoffel transformation from nonuniform fields into a parallel plate structure with uniform fields.

Fig. 2.6a shows the cross-section of a CPW in a complex plane. A CPW has an axis of symmetry at the center of the signal line. Because of the symmetry, only half of the cross-section needs to be evaluated. The distance $a = w/2$, $b = w/2 + s$, and h is the thickness of the substrate. The area without dielectric has the permittivity of free space, and the dielectric has a permittivity of ε_r.

In the following, I calculate the capacitance per unit length for the CPW. For simplicity, I divide the capacitance into two contributions: the free-space contribution and the dielectric contribution in the second step. Therefore, in the first step, the permittivities in the upper and lower half-planes are assumed to be the same as the permittivity of free space.

The capacitance of the free space is calculated as follows: The Schwarz-Christoffel transformation maps the upper half of the z-plane in (a) to the interior of the rectangle, as shown in (c). The Schwarz-Christoffel transformation is given by

$$w = \int_{z_0}^{z} \frac{dz}{\sqrt{(z-a)(z-b)}} \tag{2.35}$$

The conductor strips in the z-plane transform into the strips $\overline{AB}$ and $\overline{CD}$ in the w-plane. The size of the rectangle between the conductors can be calculated by evaluating the integral in the above equation, which is given by

$$\frac{\overline{AB}}{\overline{BD}} = \frac{K(k_1)}{K'(k_1)} \tag{2.36}$$

with $K(k)$ and $K'(k)$ the complete elliptic integral of the first kind and the complementary elliptical integral of the first kind, respectively. These integrals are related by $K'(k_1) = K(k_1')$ with $k_1' = \sqrt{1-k_1^2}$. The argument k is given by

$$k_1 = \frac{a}{b} = \frac{w}{w+2s} \tag{2.37}$$

A simple approximation for K/K' can be found in the literature [32] :

$$\begin{aligned} \frac{K(k)}{K'(k)} &= \frac{\pi}{\ln\left(2(1+\sqrt{k'})/(1-\sqrt{k'})\right)} \quad \text{for } 0 \le k \le 0.707 \\ \frac{K(k)}{K'(k)} &= \frac{\pi}{\ln\left(2(1+\sqrt{k'})/(1-\sqrt{k'})\right)} \quad \text{for } 0.707 \le k \le 1 \end{aligned} \tag{2.38}$$

The free-space contribution to the total capacitance per unit length is given by

$$C_{\text{air}} = 4\varepsilon_0 \frac{K(k_1)}{K'(k_1)} \tag{2.39}$$

The factor four originates from the assumption that the upper and lower half plane contributes the same amount to the free-space capacitance.

In the second part of the derivation, the dielectric contributions are derived. First, the finite thickness of the substrate in the z-plane is converted into a conventional infinite thickness substrate. This transformation is performed by

$$t = \sinh\left(\frac{\pi z}{2h}\right). \tag{2.40}$$

It transforms the z-plane into the t-plane as shown in Fig. 2.6b.

In the second step, the infinite t-plane is transformed by Schwarz-Christoffel into a parallel plate structure (i.e., w-plane). This transformation is identical to the one used for the upper half of the free space plane given by Eq. 2.35. Thus, the capacitance contributions of the dielectric are

$$C_{\text{r}} = 2\varepsilon_0(\varepsilon_r - 1)\frac{K(k_2)}{K'(k_2)}, \tag{2.41}$$

with Eq. 2.37 & 2.40 the transformed argument becomes

$$k_2 = \frac{t_1}{t_2} = \frac{\sinh(\pi a/2h)}{\sinh(\pi b/2h)} \tag{2.42}$$

The total capacitance per unit length is the sum of the air and dielectric capacitance. From Eq. 2.39 & 2.41 follows the total capacitance

$$\begin{aligned} C_l &= C_\mathrm{r} + C_\mathrm{air} \\ C_l &= 2\varepsilon_0(\varepsilon_r - 1)\frac{K(k_2)}{K'(k_2)} + 4\varepsilon_0\frac{K(k_1)}{K'(k_1)} \end{aligned} \tag{2.43}$$

The magnetic inductance per unit length can also be derived by conformal mapping [33] as

$$L_l = \frac{\mu_0}{4}\frac{K(k_1)}{K'(k_1)}. \tag{2.44}$$

For a quasi-static approximation and with Eq. 2.39 & 2.41 the effective permittivity is given as

$$\begin{aligned} \varepsilon_\mathrm{eff} &= \frac{C_l}{C_\mathrm{air}} \\ &= \frac{C_\mathrm{r} + C_\mathrm{air}}{C_\mathrm{air}} \\ &= 1 + \frac{\varepsilon_r - 1}{2}\frac{K(k_2)}{K'(k_2)}\frac{K'(k_1)}{K(k_1)} \end{aligned} \tag{2.45}$$

The impedance of a lossless CPW can be derived from Eq. (2.9) with $R = 0$ and $G = 0$. The phase velocity of such a lossless TL is $v_p = \omega/\beta = 1/\sqrt{LC}$ and the phase velocity for a TEM wave is given by $v_p = c_0/\sqrt{\varepsilon_\mathrm{eff}}$ [27]. These equations can be used to determine the characteristic impedance for a lossless CPW as follows:

$$\begin{aligned} Z_0 &= \sqrt{\frac{L_l}{C_l}} = \frac{\sqrt{L_l C_l}}{C_l} = \frac{1}{C v_p} \\ &= \frac{\sqrt{\varepsilon_\mathrm{eff}}}{c_0 C_l} = \frac{1}{c_0\sqrt{\varepsilon_\mathrm{eff}} C_\mathrm{air}} \\ &= \frac{1}{4\varepsilon_0 c_0\sqrt{\varepsilon_\mathrm{eff}}}\frac{K'(k_1)}{K(k_1)} \\ &\approx \frac{30\pi}{\sqrt{\varepsilon_\mathrm{eff}}}\frac{K'(k_1)}{K(k_1)} \end{aligned} \tag{2.46}$$

2.2.3 CPW Attenuation

The attenuation of a CPW can be divided into at least three types: the attenuation due to dielectric loss α_d, the attenuation due to conductor loss α_c, and the attenuation due to radiation loss α_r. The total attenuation is the sum of all contributions with $\alpha_\mathrm{t} = \alpha_d + \alpha_c + \alpha_r$. The relative contribution of each type of attenuation depends on the frequency and the geometry of the CPW. In the following, I present theoretical models that describe each attenuation type. In addition, I calculate the theoretical attenuation for a CPW identical to the one used in this thesis (section 3.6).

Dielectric Loss

The attenuation due to dielectric loss is given by [34]

$$\alpha_d = \frac{\pi}{\lambda_0}\frac{\varepsilon_r}{\sqrt{\varepsilon_{\text{eff}}}} q \tan\delta_{\text{e}} \qquad \text{Nepers/meter,} \tag{2.47}$$

with λ_0 the free space wavelength, ε_r is the relative permittivity of the substrate, ε_{eff} is the effective permittivity given by Eq. (2.45) and $\tan\delta_{\text{e}}$ is the dielectric loss tangent of the substrate. The filling factor q is given by

$$q = \frac{1}{2}\frac{K(k_1)}{K'(k_1)}\frac{K'(k_0)}{K(k_0)}. \tag{2.48}$$

It is calculated with the complete elliptic integrals $K(k_1)$ and $K(k_0)$, and the moduli k_1 and k_0 are determined as outlined in Eq. 2.38.

Conductor Loss

At high frequencies, the skin effect is a major contributor to the attenuation of a conductor. The skin effect describes the concentration of AC currents at the surface of a conductor. As the frequency increases, the currents become more concentrated at the surface. The skin depth δ describes the distance from the surface of the conductor to the point where the current density decreases to $1/\text{e}$ of the surface value. Below the skin depth, the conductor does not contribute significantly to the conductivity. For microwave frequencies, the skin depth is defined as

$$\delta = \sqrt{\frac{2\rho}{\omega\mu_c}}, \tag{2.49}$$

where ρ is the resistivity of the conductor, ω is the angular frequency, and μ_c is the permeability of the conductor. For minimum attenuation, it is essential that the thickness of the metal exceeds the calculated skin depth. The resonators described in this thesis have a metal thickness between 1 - 1.3 µm and a resonance frequency around 19 GHz with a conductivity of the metal layer of $\sigma_c = 5.65 \cdot 10^7\,\text{S}\,\text{m}^{-1}$. These values give a ratio of metal thickness to skin depth of approximately $t/\delta \approx 2.7$.

A second major determining factor of the conductor losses is the geometry of the CPW. More surface area (i.e., wider CPW signal line and ground) generally results in better conductivity. Several different models, such as the Collin (i.e., conformal mapping method) [35], Holloway-Kuester (i.e., matched asymptotic technique) [36], Heinrich (i.e., mode-matching method and quasi-TEM model) [37] and Ponchak et al. (i.e., measurement-based design equations) [38] exist for the calculation of the CPW conductor attenuation constant. Some of these models are accurate only within a range of the CPW width and ratio of the metal layer thickness to the skin depth.

I chose the Holloway-Kuester model because it has the least restrictions. In particular, the thickness t of the metal layer can be close to the skin depth δ, and the model is accurate in the GHz range. For this model, the attenuation constant due to conductor loss is [36]

$$\alpha_c = \frac{R_{\text{sm}} b^2}{16 Z_0 K^2(k)(b^2-a^2)}\left(\frac{1}{a}\ln\left(\frac{2a}{\Delta}\frac{(b-a)}{(b+a)}\right) + \frac{1}{b}\ln\left(\frac{2b}{\Delta}\frac{(b-a)}{(b+a)}\right)\right) \text{ Nepers/meter,} \tag{2.50}$$

with the characteristic impedance Z_0 given by Eq. (2.46), $a = w/2$ and $b = w/2 + s$ (described in the previous section), $K(k)$ is the complete elliptical integral of the first kind with the modulus $k = a/b$.

Δ is the so-called stopping distance. It is numerically calculated for a given metal thickness t and skin depth δ. The value can be extracted from reference [36]. For $t/\delta \approx 2$ the $\Delta \approx 4.01 \cdot 10^{-9}$.

R_{sm} is the resistance in the modified Horton impedance boundary condition given by

$$R_{\mathrm{sm}} = \omega \mu_c t \,\mathrm{Im}\left(\frac{\cot(k_c t) + \csc(k_c t)}{k_c t}\right), \tag{2.51}$$

where is $k_c = \omega\sqrt{\mu_0 \varepsilon_0}\sqrt{1 - j\sigma_c/\omega\varepsilon_0}$ and $\mu_c = \mu_r \mu_0$.

Radiation Loss

The radiation loss originates from the leakage from the CPW propagation mode and the substrate modes. The leakage increases as the TL's phase velocity exceeds the substrate's phase velocity. It has been shown that the amount of radiation depends on the velocity mismatch between the CPW modes and the surface modes [39]. The frequency-dependent radiation loss factor was derived by Frankel et al. [40] as

$$\alpha_{\mathrm{r}} = \left(\frac{\pi}{2}\right)^5 2 \left(\frac{\left(1 - \frac{\varepsilon_{\mathrm{eff}}}{\varepsilon_r}\right)^2}{\sqrt{\frac{\varepsilon_{\mathrm{eff}}}{\varepsilon_r}}}\right) \frac{(s + 2w)^2 \varepsilon_r^{3/2}}{c_0^3 K'(k) K(k)} f^3 \qquad \text{Nepers/meter,} \tag{2.52}$$

where c_0 is the speed of light, $K(k)$ is the complete elliptic integral of the first kind, the parameter $k = w/(w + 2s)$, and $K'(k) = K(\sqrt{1 - k^2})$ (see section 2.2.2). ε_r is the permittivity of the substrate and $\varepsilon_{\mathrm{eff}}$ is the effective permittivity given by Eq. (2.45). The effective permittivity has a dispersion as it decreases with increasing frequency. In the radiation model, this effect is neglected because the dispersion is small in the 10 - 100 GHz range [40].

Fig. 2.7 summarizes the previously described attenuation types for different CPW widths ($w + 2s$) (i.e., ground-to-ground distance). The relative contributions of the different attenuation types are given for a frequency of 19.74 GHz and a characteristic impedance of about 80 Ω. These values correspond to the CPW used in the thesis. The characteristic impedance is obtained by adjusting the signal line width w and the signal line to ground distance s to remain between $79 \pm 3\ \Omega$. The substrate is quartz glass with a real permittivity of $\varepsilon_r = 4.05$ and a loss tangent of $\delta_{\mathrm{quartz}} = 0.0002$ [41, 42]. The height of the substrate is 500 µm, and the thickness of the metal is 1.3 µm, with a conductivity of $\sigma_c = 5.65 \cdot 10^7\ \mathrm{S\,m^{-1}}$. For narrow widths, conductor losses primarily contribute to the total attenuation. However, when the width exceeds 800 µm, radiation losses become the dominant factor. The minimum attenuation is 15.22 dB/m at a width of 603 µm.

A dotted line at 800 µm marks the sensor width developed in this thesis, which has a theoretical attenuation of 16.17 dB/m.

It is worth noting that radiation losses were not taken into account during the design phase of the sensor. This resulted in a wider than optimal CPW width. Nevertheless, the total attenuation remains close to the ideal value.

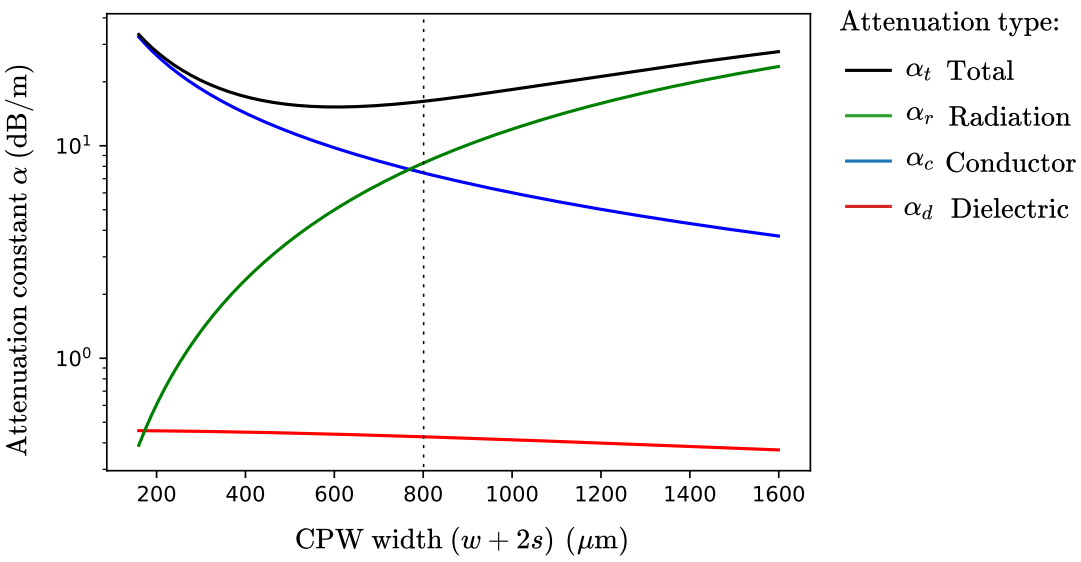

FIGURE 2.7: **Graph of attenuation constants in a coplanar waveguide (CPW) at 19.74 GHz:** The attenuation constants: dielectric (α_d), conductor (α_c), radiation (α_r), and total loss (α_t), as functions of the ground-to-ground distance (width of the CPW line, $w + 2s$). The s and w parameters were scaled to maintain the characteristic impedance within the range of $79 \pm 3\ \Omega$. The visualization provides insight into how different losses contribute to the attenuation at a specific frequency and geometry. The dotted line at 800 µm marks the sensor width developed in this thesis, which has a theoretical attenuation of 16.17 dB/m.

2.3 Permittivity

An electric field applied to a dielectric displaces positive charges in the direction of the electric field and negative charges in the opposite direction. This separation of charges under an applied electric field is called polarization. The polarizability of a material is described by the permittivity ε of a dielectric. It is usually represented by the relative permittivity ε_r, which is the ratio of the absolute permittivity to the vacuum permittivity ε_0.

$$\varepsilon_r = \frac{\varepsilon}{\varepsilon_0} \tag{2.53}$$

However, this formula does not consider the losses caused by the movement of charges in a dielectric. A complex representation of permittivity can account for these losses

$$\varepsilon(\omega) = \varepsilon'(\omega) - j\varepsilon''(\omega) \tag{2.54}$$

with the real part ε' representing the polarizability (i.e., the stored energy) and the imaginary part ε'' representing the dielectric loss. Both quantities are frequency dependent, denoted by ω, and the angular frequency is given by $2\pi f$.

An alternating field periodically displaces the electrical charges. The alternating field is reversed after reaching the maximum electric field and polarization. This initiates the relaxation of the dielectric to its equilibrium state. The relaxation mechanism is limited in speed. In general, large structures relax to their equilibrium state more slowly than smaller structures. At high frequencies, the electric fields alternate rapidly, so the polarization of slow processes cannot follow. As a result, with increasing frequency, slow processes successively do not contribute to the permittivity.

In 1914, P. Debye was the first to discuss such relaxation processes of dipoles in dielectrics [43]. He introduced a relationship between permittivity and frequency as

$$\varepsilon(\omega) = \varepsilon_\infty + \frac{\varepsilon_s - \varepsilon_\infty}{1 + j\omega\tau} = \varepsilon_\infty + \frac{\Delta\varepsilon}{1 + j\omega\tau}. \tag{2.55}$$

Here, the relaxation parameters ε_∞ and ε_s represent the permittivity at high frequencies and DC, respectively. The term $\Delta\varepsilon$ denotes the relaxation strength, while τ denotes the relaxation time. This relaxation time is related to the relaxation frequency by $2\pi f_0 = \tau^{-1}$.

Eq. (2.55) can be decomposed into its real and imaginary components [44]

$$\begin{aligned} \varepsilon'(\omega) &= \varepsilon_\infty + \frac{\Delta\varepsilon}{1 + (\omega\tau)^2} \ , \\ \varepsilon''(\omega) &= \frac{\Delta\varepsilon\omega\tau}{1 + (\omega\tau)^2} \ . \end{aligned} \tag{2.56}$$

The real part decreases by $\Delta\epsilon$ during a relaxation process. Half of the relaxation amplitude is reached at the relaxation frequency f_0. The imaginary part peaks at this frequency and decays to zero for frequencies significantly higher or lower than the relaxation frequency.

Dielectrics typically have a variety of polarizable structures. Polarization can range from small charge displacements, such as the reorientation of water molecules, to much larger displacements, such as the movement of ions. Each relaxation process is characterized by its unique relaxation parameters. The overall permittivity is the cumulative effect of all these processes. This cumulative effect can be represented by a relaxation model, such as the classical Debye model, combined with a conductivity term:

$$\varepsilon(\omega) = \varepsilon_\infty + \sum_i \frac{\Delta\varepsilon_i}{1 + j\omega\tau_i} + \frac{\sigma}{j\omega\epsilon_0}. \tag{2.57}$$

Here σ denotes the conductivity resulting from ionic currents. This equation is used to fit permittivity spectra and extract relaxation parameters. It is worth noting that real permittivity spectra often deviate from the Debye model. As a result, numerous empirical models have been formulated, such as the Cole-Cole, Davidson-Cole, Havriliak-Negami, von Schweidler, and others [44].

Fig. 2.8 displays an exemplary real and imaginary permittivity spectrum. It illustrates some common types of polarization. The relaxation parameters of an exemplary polarization type, namely the polarization of ions, are represented by $\Delta\varepsilon_i$ and τ_i. As described by Eq. (2.56), each relaxation process has a maximum in the imaginary permittivity at the relaxation frequency.

In the following, the permittivity spectrum of cells is discussed. It is well suited for a reference system as it is the best-studied biological system, and it contains various polarization types. Several relaxation processes can be observed in cells, often labeled with Greek letters such as α, β, δ and γ [14]. At frequencies between 10 - 10^4 Hz the α dispersion can be observed [45]. It is attributed to counterion diffusion effects and is shown in Fig. 2.8 as the ionic polarization.

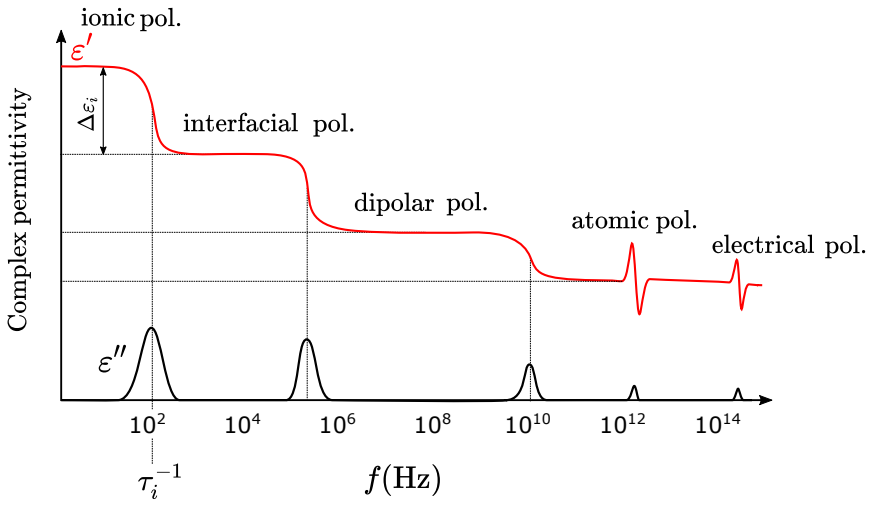

FIGURE 2.8: **Dielectric permittivity spectrum using the classical Debye relaxation model:** This diagram depicts the complex permittivity spectrum, characterized by the real part ε', symbolizing material polarization strength and energy storage, and the imaginary part ε'', representing energy loss. As the Debye model details, key polarization parameters include changes in permittivity ($\Delta\varepsilon_i$) and relaxation times (τ_i).

At frequencies between 10 kHz and 10 MHz the β-dispersion occurs [45]. It is associated with the polarization of interfaces such as the cell membrane. The membrane and intracellular molecules bound to the membrane are charged and act as a capacitance. The capacitance shields the electric field from entering the cell. At frequencies above the β-dispersion, the capacitance is shorted, and current can flow through the interior of the cell. Pauly H. and Schwan H. P. were the first to demonstrate that adding digitonin reduces the β-dispersion and breaks the membrane capacitance and resistance [46]. It is important to note that only frequencies above the β-dispersion can probe intracellular structures.

The effect of electrode polarization (i.e., the formation of an ionic double layer) is in the frequency range between 100 Hz - 500 kHz [47]. Depending on the electrode configuration, the electrode polarization may dominate over the membrane-related relaxation effects, thereby affecting the sensor's ability to detect cells.

In the frequency range of 100 MHz to 5 GHz, the δ-dispersion was first described by Pethig R. [15]. This dispersion is attributed to the polarization of larger molecules, such as proteins, or the polarization of bound water. The term "bound water" refers to water molecules that form more robust bonds with cellular biomolecules than with other water molecules, primarily through hydrogen bonding. This bond restricts their rotational movement compared to free water, causing the reorientation processes to slow down. As a result, there is a noticeable decrease in the relaxation frequency. Sometimes, the δ-dispersion is perceived as an extension of the β-dispersion or as a broadening of the γ-dispersion [45].

The first measurements of γ-dispersion in biological samples were made by Cook et al. (1951) and England et al. (1950) [48, 49]. The origin of the γ-dispersion comes from the polarization of bulk water, which has a relaxation frequency of about 17 GHz at 20°C [50]. Temperature plays a vital role in the rotational freedom of water

molecules. With decreasing temperature, the rotational freedom of water molecules reduces, leading to a corresponding reduction in the relaxation frequency.

Different cell types and states exhibit differences in the water content, protein concentration, nucleus volumetric ratio, or cytoplasm structure. These intracellular properties can only be probed at frequencies above the β-dispersion. Recently, this requirement has increased scientific interest in the γ-dispersion region of cells. Living and dead cell suspensions and bovine serum albumin protein suspensions have been characterized in the GHz frequency range [19, 20]. For both samples, the real permittivity contrast between the suspension medium and the samples was highest around 1 - 5 GHz, and the imaginary permittivity contrast was highest around 20 GHz. In another study by Zedek et al., the complex permittivity at GHz frequencies revealed the biological state of single cells after different stimuli, namely thermal stress and permeabilization [51]. In addition, Hussein et al. discovered that breast cancer cells have a specific dielectric signature in the GHz range [22]. These findings demonstrated that measuring cells at GHz frequencies can facilitate the discrimination between different cell types and states, including the detection of cancerous cells.

At frequencies above the GHz regime, the electric field can excite resonant states (Fig. 2.8 atomic and electrical pol.). Infrared radiation ($\approx 10^{11} - 10^{14}$ Hz) interacts with matter at the molecular level by exciting vibrational and rotational states of chemical bonds. At frequencies from visible light to ultraviolet ($\approx 10^{13} - 10^{15}$ Hz), electrons can be excited to unoccupied states.

2.4 Capacitance of a Particle Between Electrodes

This section calculates the capacitance change ΔC induced by a particle in an electric field. The calculation follows the reference [52].

I assume that the capacitance due to a region of nonuniform electric field within a microfluidic channel filled with a dielectric of permittivity ϵ_l is equivalent to C_0, the stored energy in this region can be expressed as:

$$W_0 = -\frac{1}{2} C_0 U^2. \tag{2.58}$$

The potential at the electrodes is given by U. I assume that a particle is placed between the electrodes, and the capacitance changes to C. The particle has a frequency-dependent permittivity $\varepsilon_p(\omega)$. The stored energy changes to

$$W = -\frac{1}{2} C U^2 = -\frac{1}{2} C_0 U^2 - \frac{1}{2} \int_{\xi} \vec{E}\vec{P} d\xi. \tag{2.59}$$

The integral of Eq. 2.59 describes the change of the stored energy in a nonuniform electric field $\vec{E}$. The electric field polarizes the particle. This polarization $\vec{P}$ stores energy in the electric field and thus changes the capacitance. The integral is over the whole volume ξ between the electrodes. The induced polarization is zero for the whole volume except the volume ξ_p of the particle. To reduce the complexity of the model, the losses and the conductivity of the particle medium are assumed to be zero. In this case, the induced polarization is given by

$$\vec{P} = \varepsilon_0 (\varepsilon_l - \varepsilon_p) \vec{E_p}. \tag{2.60}$$

For simplicity, I assume that the particle is small compared to the sensing volume and spherical with radius a. Therefore, I can assume that the electric field in the particle volume ξ_p is constant with

$$\vec{E_p} = \vec{E}\frac{3\varepsilon_l}{\varepsilon_p + 2\varepsilon_l}. \tag{2.61}$$

Eq. 2.59 can be rearranged for the change of capacitance $\Delta C = C - C_0$.

$$\Delta C = 4\pi\varepsilon_0\varepsilon_l a^3 \,\mathrm{Re}(K_{\mathrm{CM}})\frac{|E^2_{\mathrm{rms}}|}{U^2} \tag{2.62}$$

K_{CM} is the Clausius-Mossotti factor. It describes the electric field of a particle immersed in a dielectric medium. This factor is related to the complex permittivities of the particle and the medium, which are frequency-dependent quantities. For a spherical object, the Clausius-Mossotti factor becomes

$$K_{\mathrm{CM}} = \frac{\tilde{\varepsilon}_p(\omega) - \tilde{\varepsilon}_l(\omega)}{\tilde{\varepsilon}_p(\omega) + 2\tilde{\varepsilon}_l(\omega)}. \tag{2.63}$$

The complex permittivity was described in section (2.3) by $\tilde{\varepsilon}(\omega) = \varepsilon' - j\varepsilon'' - j\sigma/w$, where σ is the conductivity of the suspending medium. For GHz frequencies, the conductivity term can be neglected. In the following, I calculate the capacitance change due to cell-like particles in the GHz range. For simplicity, I neglect the di-

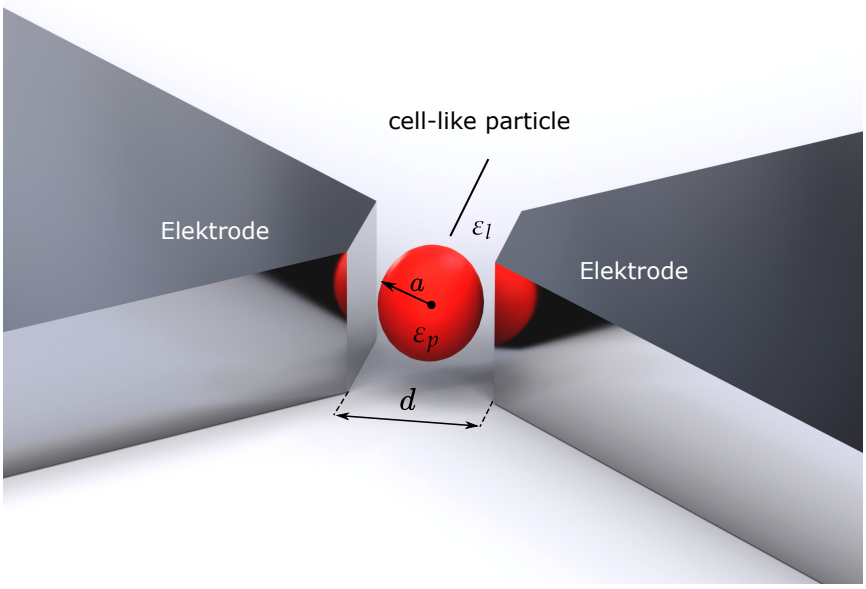

FIGURE 2.9: **Illustration of a cell-like particle between electrodes:** Two electrodes form a plate capacitor. The electrodes are separated by the distance d. A cell-like particle with the radius a and the permittivity ε_p is located between the electrodes. The medium surrounding the particle has the permittivity of ε_l. The particle induces a capacitance change described by Eq. 2.62.

electric loss term and assume $\tilde{\varepsilon}(\omega) = \varepsilon'$. The real permittivity of cells in the GHz regime depends on the state of the cell [51]. For 30 GHz, I assume $\varepsilon'_p = 20$ and the

suspending medium is water with $\varepsilon_l' = 25$. To make a rough estimate of the capacitance change, I assume two electrodes form a plate capacitor. Fig. 2.9 visualizes the particle and electrode configuration. The electric field between a plate capacitor is given by $E = U/d$ where d is the distance between the electrodes. For Eq. 2.62 follows:

$$\Delta C = 4\pi\varepsilon_0\varepsilon_l \,\mathrm{Re}(K_{\mathrm{CM}})\frac{a^3}{d^2}. \tag{2.64}$$

This equation allows us to estimate the change in capacitance for different particle sizes and electrode configurations. In Fig. 2.10, I study the capacitive change ΔC

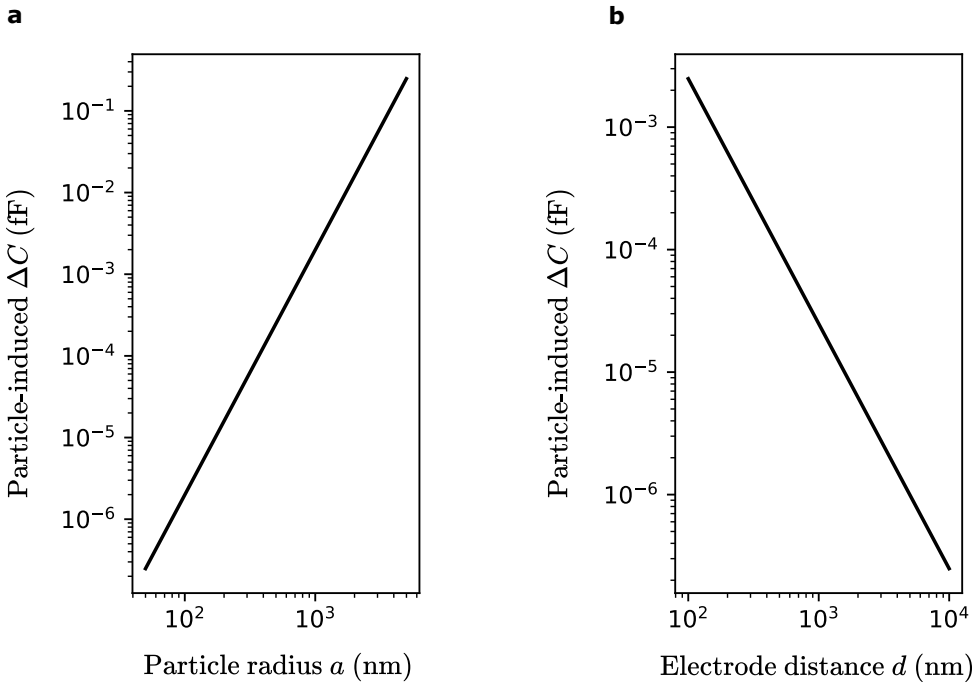

FIGURE 2.10: **Capacitance variation due to a spherical cell-like particle between electrodes:** I explore the phenomenon described by Eq. 2.64 by examining a spherical cell-like particle immersed in water with a permittivity value corresponding to a frequency of 30 GHz. **a**, Changes in capacitance as the particle radius is systematically varied in the range from 50 nm to 5 µm while keeping the electrode spacing constant at 10 µm. **b**, The change in capacitance as the electrode spacing is varied from 10 µm to 100 nm, while keeping the particle radius fixed at 50 nm.

induced by a particle between electrodes. In Fig. 2.10a, the electrode spacing is fixed at d=10 µm, and the particle radius is varied from 5 µm to 50 nm. In this range, the capacitance changes by more than five orders of magnitude. This significant change is due to the cubic relationship between ΔC and the particle radius, represented as $\Delta C \propto a^3$. Conversely, in Fig. 2.10b, the particle is fixed at a radius of 50 nm, and the electrode distance is reduced from 10 µm to 100 nm. Similarly, ΔC increases by four orders of magnitude. The strong influence is caused by the inverse square relationship between ΔC and the electrode distance.

To date, the smallest particle detected by an AC field measures 200 nm. Increasing the current state-of-the-art detection limit can be achieved by adjusting the electrode distance, which effectively amplifies the capacitance response for particles of the

same size. However, minimizing the channel and electrode dimensions presents practical challenges, particularly the risk of clogging.

This page has been intentionally left blank.

Chapter 3

Sensor Development

In this chapter, I present the development and characterization of the coupling-based CPW (cCPW) sensor. I review electrode designs that were applied to AC sensing of individual particles in fluidic systems. As highlighted in the previous chapter, improving the current detection limit depends mainly on modifying the electrode spacing. This modification enhances the capacitance response for similarly sized particles. However, reducing electrode size to nanoscopic sensing volumes presents numerous challenges. First, nanoscopic electrodes form a small series gap capacitance, resulting in a high impedance mismatch that leads to insensitive measurements [53]. Second, the parasitic capacitance increases at higher frequencies, potentially short-circuiting the small sensing capacitance [25]. To better understand the magnitude of these effects, I performed Finite Element Method (FEM) simulations using COMSOL Multiphysics® software to model two electrodes (composed of CPWs) connected to a fluidic channel.
An additional obstacle is the non-uniform electric field distribution between the electrodes. As the electrode dimensions decrease, creating a fluidic channel between them becomes difficult, and ensuring a uniform electric field within the channel becomes increasingly challenging. In the current manufacturing process, these obstacles are a primary challenge. The next chapter discusses one potential solution: sacrificial layer fluidics (SLF).
Next, I review the literature on high-frequency electrical resonators for particle detection. This discussion paves the way for the presentation of our novel coupling-based sensor design. I begin this presentation with an analytical calculation based on transmission line (TL) theory to identify the optimal set of coupling parameters. These calculations and FEM simulations allow me to fine-tune the sensor design. The working principle of the coupling-based method is validated by comparing FEM simulations with a manufactured sensor and comparing the results with the analytical TL model calculations. Altogether, analytical TL models, FEM simulation, and empirical measurements provide a complete picture of the coupling-based approach.
In the final sections of this chapter, I analyze the sensor's response to particles within its sensing volume using an analytical approach and FEM simulation. This research shows that the new coupling-based method outperforms the traditional TC method, and a side-by-side comparison of the sensitivity of the cCPW sensor with TC sensors reported in previous studies highlights its superior capabilities.

3.1 Review: Electrode Configurations

AC particle sensing uses electrode tips positioned near a fluidic channel. These tips are the origin of the electric field. As particles flow through the channel, they move between the electrodes and interact with the electric field.

This interaction modifies the capacitance and resistance between the electrodes, al-

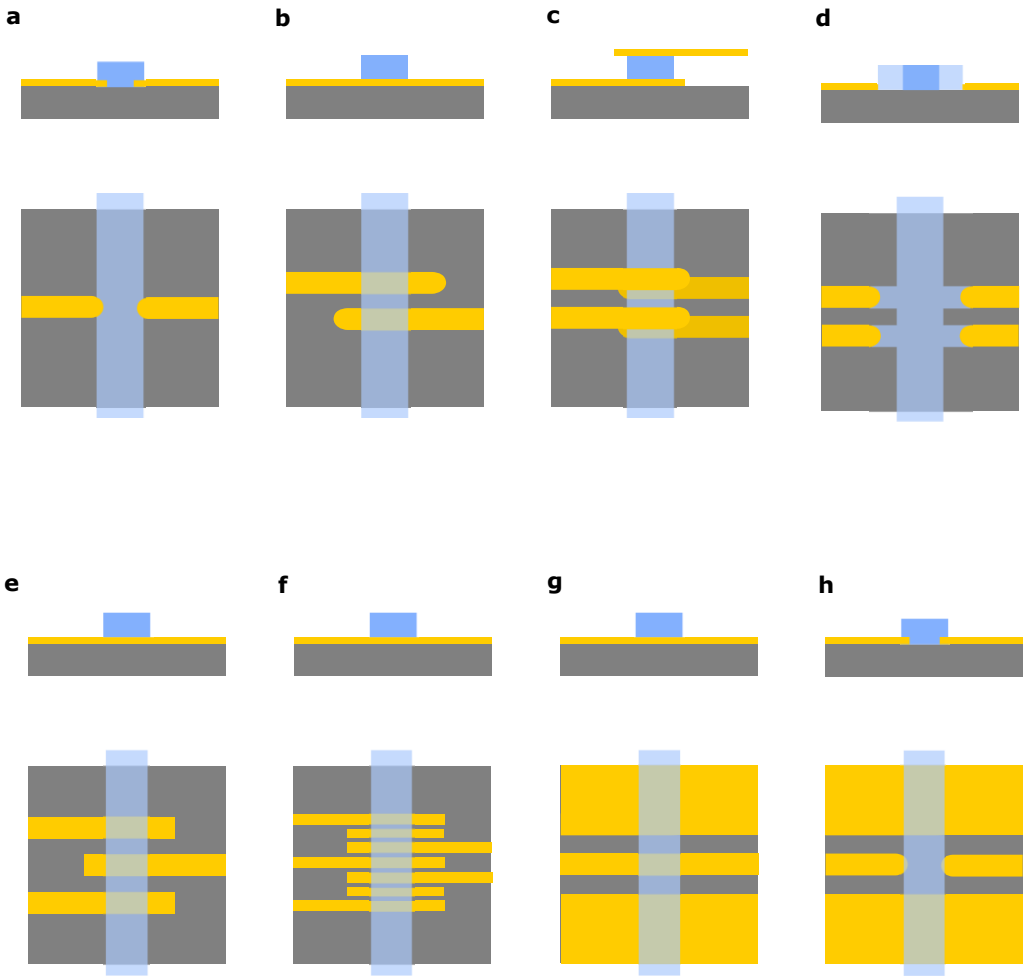

FIGURE 3.1: **Overview of Electrode Sensing Configurations:** These sketches present various configurations from two perspectives: the top sketch provides a cross-sectional view, while the bottom sketch offers a top view. The dark gray color represents the substrate, and the yellow and blue colors illustrate the electrode and fluidic channel design. **a**, Two facing electrodes, as described by Ayliffe et al.[13]. **b**, Coplanar two-electrode arrangement [54]. **c**, Top and bottom facing electrodes configuration [55, 56, 26]. **d**, Liquid electrodes layout [57]. **e**, differential electrode scheme [58]. **f**, Double differential electrode design [59]. **g**, Coplanar waveguide design [25, 60], and **h**, coplanar waveguide gap configuration (this thesis).

tering the sensor's impedance.

In the following, I will provide an overview of electrode configurations and briefly state the primary purpose of each. The examples presented are not a complete list of all published configurations, but most configurations are covered. For the interested reader, I recommend the excellent review by Tao Sun and Hywel Morgan, which covers early electrode developments in electrical impedance flow cytometry [61].

Ayliffe et al. first demonstrated this electrical impedance sensor in 1999, integrating it into a microfluidic chip capable of detecting individual cells [13]. In Ayliffe's design, two electrodes were embedded on both sides of the microfluidic channel, as shown in Fig. 3.1a.

In 2001, Gawad et al. were the first to introduce additional electrodes in the so-called

differential electrode configuration (Fig. 3.1e) [58]. These additional electrodes measure a reference signal without a particle. Such a configuration improves sensitivity and isolates the influence of the particle from the suspending medium. The drifting properties of the medium and electrodes are canceled out. In addition, the added electrodes produce multiple peaks, with the distance between peaks indicating the particle velocity. This differential configuration was later refined into a double differential design, further improving sensitivity [59] (Fig. 3.1f).

A primary challenge in electrode design is the non-uniform electric field within the sensing volume. Such a field leads to a dependence between the detected signal and the particle position in the channel [62], which affects reproducibility. This obstacle can be overcome in many ways.

In 2001, Gawad et al. simulated the non-uniform electric fields of different electrode structures by FEM [58]. Electrodes positioned on the top and bottom of the fluidic channel yield a more homogeneous electric field than coplanar configurations (Fig. 3.1c). Later, the same group built such electrode structures and showed that the opacity (ratio between the impedance at two frequencies) could normalize the data for particle size and position [56].

Alternatively, Mernier et al. used so-called liquid electrodes as shown in Fig. 3.1d [57]. The liquid electrode structure improves the homogeneity of the electric field. However, the increased distance between the liquid electrodes compromises the sensitivity.

In 2005, Wood et al. used a coplanar waveguide (CPW) structure (Fig. 3.1g) in combination with a high-frequency tank circuit (TC) resonant at 169 MHz to measure polystyrene beads [25]. The CPW consists of a ground near the signal line. In such a configuration, the electric field is concentrated in a small gap between the signal and ground lines. This configuration is advantageous because it increases the electric field strength, shields the signal line, and reduces parasitic capacitance. However, as a downside, the design results in a non-uniform electric field throughout the sensing volume.

Similarly, two coplanar electrodes were used by Rodriguez-Trujillo et al. in 2007 (Fig. 3.1b) [54]. Instead of improving the electric field homogeneity, the position of the particles was improved by guiding particles to the same position in the sensing volume with hydrodynamic focusing.

In 2010, Booth et al. used a CPW structure to quantify the complex permittivity of nanoliter fluid volumes for frequencies up to 40 GHz [60]. Later, Bausch et al. used a CPW in a microtube to increase the sensitivity and improve the homogeneity of the electric field [63]. In 2018, Bhat et al. also utilized a CPW design and combined the CPW with a micropore [24]. In this case, the fluidic pore is perpendicular to the metal structure plane. Furthermore, the pore was only 2 µm in diameter, and the CPW electrode tip featured a tapered design aimed at the micropore. The tapered design confines the electric field inside the micropore, which results in significant field enhancements and improved sensitivity. This design enabled Bhat et al. to detect individual 500 nm-sized polystyrene beads. These are the smallest individual particles detected with GHz electric signals.

The sensor developed in this thesis also uses the CPW tip configuration akin to Bhat et al.'s original design. However, it introduces tapered CPW tips on both sides of the fluidic channel (Fig. 3.1h). The electrical properties like capacitance and

impedance of such a tip configuration are explored in the next section with finite element method (FEM) simulations.

3.2 FEM Simulation Electrode-Channel Interface

This section explores the implications and challenges of a shrinking electrode-channel interface. Shrinking the interface (i.e., the sensing volume) is a simple approach to improve the sensitivity for electrical sensing of nanoparticles in a microfluidic channel. It is achieved by bringing the electrode tips closer together. The capacitance per unit volume between the electrodes increases, and thus, particles translocating between the electrodes induce an enhanced capacitive change. However, shrinking electrodes also introduces challenges related to impedance mismatch and the relatively high contributions of parasitic capacitance relative to the sensing capacitance. Therefore, in this section, the interface between the fluidic channel and the nanoelectrodes is studied in detail at GHz frequencies.

As discussed in the previous section, Fig. 3.1 illustrates typical electrode configurations used in inflow high-frequency particle sensing setups. Despite the configuration (g), all these electrode configurations have in common that the gap capacitance is connected in series with the sensing electrodes. If the load consists of a series-connected gap capacitance, the impedance is given by

$$Z_L = \frac{1}{j\omega C_g} \tag{3.1}$$

with $\omega = 2\pi f$ being the angular frequency.

As discussed in section 1, reflectometry is the measurement method of choice at GHz frequencies. In reflectometry, the reflected signal is measured. That signal is related to the load impedance described by the reflection coefficient, which was derived in Eq. 2.16 as

$$\Gamma = \frac{Z_L - Z_0}{Z_L + Z_0}, \tag{3.2}$$

with Z_0 the characteristic impedance derived in Eq. 2.9.

Reducing the sensing volume diminishes the gap capacitance, resulting in a high load impedance. A high load impedance introduces an impedance mismatch between the feedline and the load. Consequently, the mismatch leads to a near-total reflection ($\Gamma \approx 1$) of incoming microwaves and, thereby, to a low contrast and insensitive measurement [53]. In addition, an impedance-matched sensor allows higher input powers without saturating the detector.

In real-world sensors, the gap capacitance C_g is the sum of the sensing volume capacitance C_s and parasitic capacitance C_p given by

$$C_g = C_s + C_p \tag{3.3}$$

The parasitic capacitance is the capacitance that is not part of the sensing capacitance while still interacting with the electrode opposing the fluidic channel. That capacitance is less controlled in electrodes that are not a waveguide, including most of the classical EIFC electrode structures. That is because waveguides confine the electric field between the signal line and the ground in a controlled way. In these structures, the parasitic capacitance is typically higher than the sensing capacitance; thus,

the gap capacitance is short-circuited at high frequencies, limiting the measurement bandwidth [25]. Waveguide structures have the advantage that the characteristic impedance can be adjusted, and they have reduced radiation losses. For these reasons, all TLs of the sensor described in this thesis are constructed from CPW. These CPWs are tapered as they approach the sensing volume, ensuring electric fields are concentrated within the sensing area. A schematic representation, excluding the tapered structure, of the CPW electrode-channel interface can be found in Fig. 3.1 h.

The presented relations are general in nature and do not sufficiently capture the geometric difference in the sensor design, e.g., the tip shape has a major impact on the sensing and parasitic capacitance. Therefore, I use a FEM model (COMSOL Multiphysics® software) to investigate the relationship between the geometry of the electrode-channel interface and the parasitic and sensing capacitance. Simulation of this basic model serves two purposes. First, the parasitic and sensing capacitances can be determined. They contribute to the total gap capacitance, which defines the impedance mismatch by Eqs. (3.1) & (3.2). These capacitance values demonstrate the limitations introduced by a shrinking sensing volume. Second, later sections combine the gap capacitance model with a resonator model. Together, the two models form the model for the novel coupling-based sensor.

Fig. 3.2 displays the geometry of the gap capacitance model. It consists of a CPW where the signal line shrinks towards a nanoscopic gap (i.e., sensing volume). The capacitance of the sensing volume is formed between the electrode tips represented by the dotted lines in Fig. 3.2b. The size of the sensing volume ($V_x = w_x^3$) is parameterized to keep the width, length, and height at the same fixed value of w_x. In this way, the size of the sensing volume is tunable by a single parameter w_x. This parameter will be referred to as the volume unit throughout this thesis.

The permittivity of the sensing volume is $\varepsilon_s = 80$, which corresponds to the permittivity of pure water at room temperature (20°C) and 1 GHz [50]. At 1 GHz, the imaginary permittivity is small. Therefore, it is neglected to reduce the complexity of the model. The substrate is 500 µm thick quartz glass with a dielectric constant of $\varepsilon_{\text{quartz}} = 3.86$ and a loss tangent of $\delta_{\text{quartz}} = 2 \cdot 10^{-4}$ [64, 41, 42]. The conductor is made of metal with a thickness of $d = w_x$ and a conductivity of $\sigma = 5.65 \cdot 10^7\,\text{S}\,\text{m}^{-1}$.

The model's electric field is excited at the air gaps between the signal and ground electrodes. At these ports, the width of the central line w_c is 100 µm, and the distance from the central line to the ground s_c is 13 µm, resulting in a characteristic impedance of 50 Ω. Two separate sensor designs were investigated, with and without a tapered ground plane (see Fig. 3.2 c). The tapered configuration has a ground plane tapering towards the tips with a tip-to-ground distance of $w_x/2$. The signal line tapers at a 45-degree angle towards the electrode tips.

The gap capacitance can be calculated from an S-parameter simulation, which determines the amplitude and phase information of transmitted and reflected microwaves at each port. The S-parameters can be converted to Z- and Y-parameters [65], which are related to the gap capacitance by

$$Y = Z^{-1} = j\omega C_g. \tag{3.4}$$

The sensing capacitance is isolated from the parasitic capacitance by subtracting the corresponding Y-parameters of two simulations with sensing volume permittivity of $\varepsilon_s + 1$ and 1. In this way, the parasitic capacitance, which is not part of the sensing volume, cancels out.

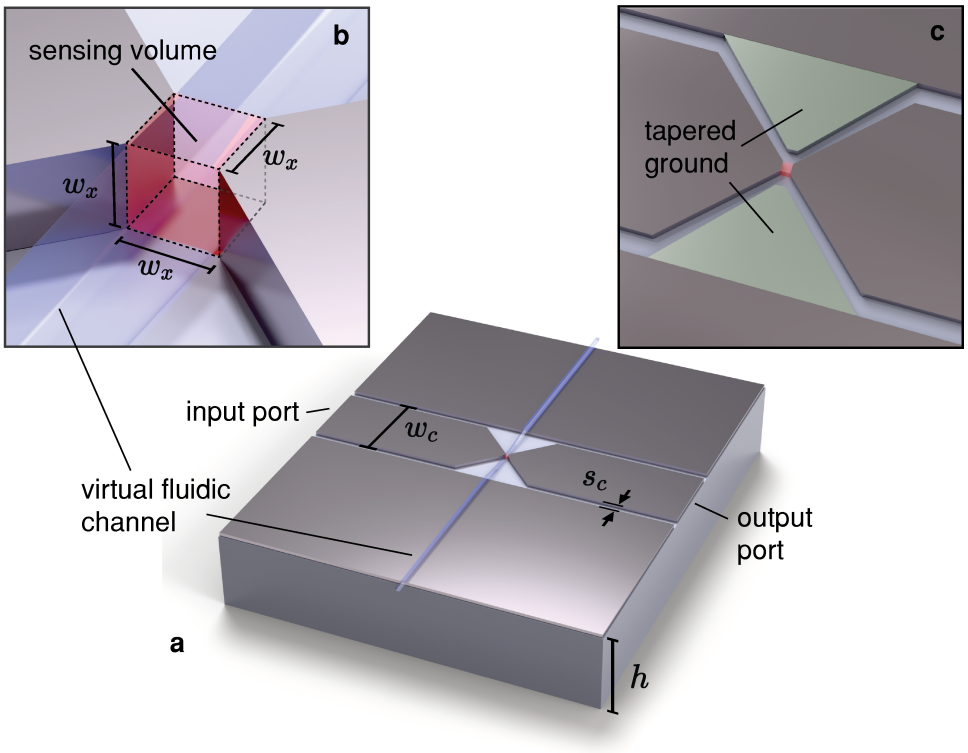

FIGURE 3.2: **Electrode-channel interface FEM model:** This model is designed to analyze the capacitance formed in the gap between the CPW electrode. The model is a two-port network that is excited at 1 GHz. The sensing capacitance C_s is part of the gap capacitance. It originates from the volume between electrode tips. That volume is systematically varied from the micro- to the nano-scale. **a** displays the total FEM model, while **b** shows a magnified view of the sensing volume. The dotted lines illustrate the size of the sensing volume. The sensing volume's width, height, and length are maintained at the same value w_x. That size is reduced from 10 µm to 100 nm. **c** introduces the tapered ground configurations, highlighted in green. Images reproduced from my publication [1], © 2023 IEEE

Fig. 3.3a shows the insertion loss expressed in $|S_{21}|$ and in Fig. 3.3b the capacitance is displayed as the channel shrinks. The simulation is performed at 1 GHz as the volume unit w_x decreases from 10 µm to 200 nm. The sensing capacitance C_s is identical (dotted line) for the straight and tapered configurations. It is linearly related to the gap size and perfectly described by a parallel plate capacitor ($C_s = \varepsilon_0 \varepsilon_s w_x$). The parasitic capacitance C_p is higher for the straight ground configuration and remains relatively constant for both geometries at different gap sizes. At nanoscopic gap sizes, the parasitic capacitance dominates over the sensing capacitance.

Consequently, a tapered gap geometry can be used to adjust the total gap capacitance and reduce the impedance mismatch for nanoscopic gaps. As mentioned, a nanoscopic gap is beneficial for sensing small particles. However, for a 200 nm gap and 1 GHz, the straight and tapered ground configurations have an insertion loss of -57 dB and -63 dB, respectively. In absolute magnitude $|S_{21}|$, this corresponds to 0.14% and 0.07% of the total signal passing through the 200 nm gap. The signal is mainly transmitted via parasitic capacitance. In such a mismatched configuration, changes in the load impedance will result in small changes in the reflected signal and, thus, in an insensitive measurement.

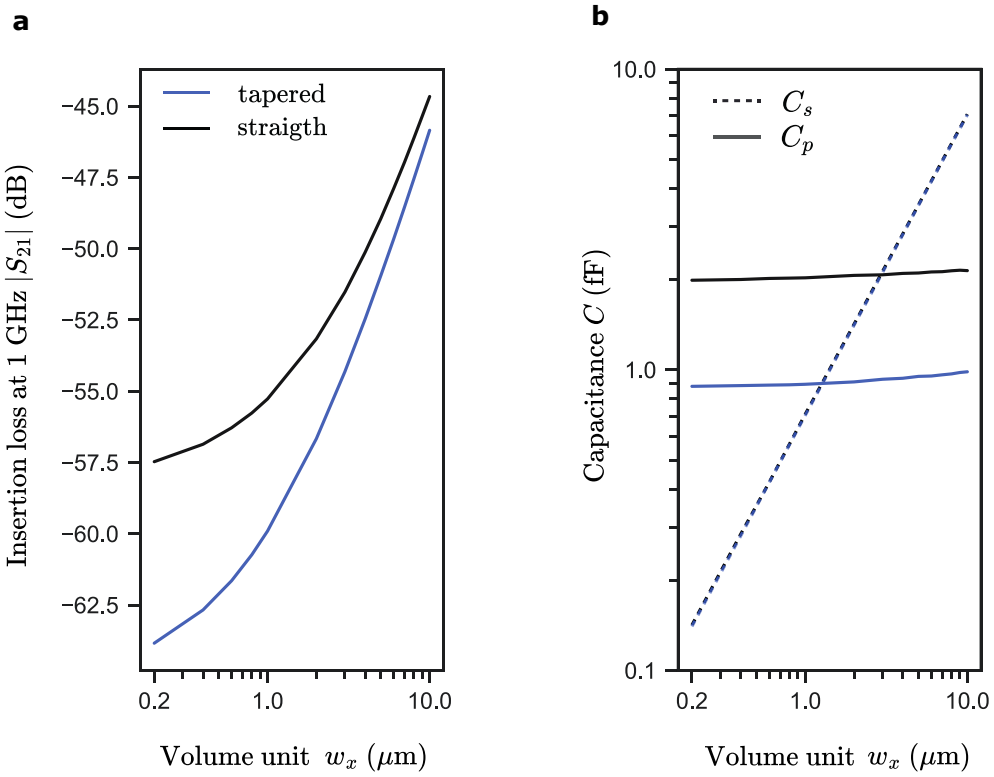

FIGURE 3.3: **Relation between electrode tip size and gap capacitance:** The electrode tip size (i.e, volume unit) w_x is scanned from 10 µm to 200 nm at 1 GHz. **a** plots the insertion loss ($|S_{21}|$-parameter), and **b** displays the corresponding gap capacitance. The gap capacitance C_g consists of the sensing volume capacitance C_s (dotted) and parasitic capacitance C_p (solid line). The straight ground configuration is displayed in black, and the tapered ground plane configuration is displayed in blue. The corresponding geometries are displayed in Fig. 3.2c. Graph reproduced from my publication [1], © 2023 IEEE

These issues, namely impedance mismatch and the influence of parasitic capacitance, are not exclusive to the design chosen for this study. They are fundamental challenges encountered when reducing the size of the sensing volume. Consequently, the reflectometric measurement of individual nanoparticles suffers from diminished sensitivity in configurations where the sensing capacitance is connected in series to the electrodes. Alternative sensing configurations need to be explored to enhance the sensitivity for nanoparticle detection. One such promising alternative involves using resonators, which will be discussed in subsequent sections.

3.3 Review: Resonators for High-Frequency Particle Detection

Electro-Impedance Flow Cytometry (EIFC) is the most common device for measuring individual particles using AC signals. In conventional EIFC setups, signals are applied to electrodes near a channel, creating electric fields between the electrodes. These fields then induce currents that are converted to voltages by a transimpedance amplifier (TIA).

However, TIAs are typically limited in bandwidth, with the most advanced EIFC setups achieving a maximum bandwidth of 450 MHz [18]. Moreover, small sensing volumes (i.e., small sensing capacitance) and low conductive media lead to a high impedance. A high impedance translates the applied voltage into a small current, making the classic EIFC less sensitive. In addition, the inherent high impedance of a small sensing volume and the parasitic capacitance of the sensing electrodes limit the electrical bandwidth of these devices. Consequently, EIFC-based sensing at GHz frequencies has not yet been established.

A promising alternative is the high-frequency TC reflectometer. This configuration bypasses the need for a TIA and instead directly measures the reflected or transmitted voltage signal. In 1998, Schoelkopf et al. demonstrated that such a TC-based reflectometer setup can be used for ultra-sensitive and fast measurement of a single electron transistor at radio frequencies. They integrated a single electron transistor into a TC, enabling the detection of charge state changes at GHz frequencies and bandwidths exceeding 100 MHz [23]. The TC-based reflectometer is also capable of detecting individual particles in fluidic systems. In this setup, electrodes are positioned in or near a channel or pore. The gap between the electrodes forms a capacitance that is part of a capacitive-inductive TC. As particles flow through the channel, they modulate the impedance of the TC, shifting the resonance frequency of the TC. In 2005, Wood et al. pioneered the use of a radio-frequency TC resonating at 169 MHz to measure individual polystyrene beads in a microfluidic channel [25]. Subsequently, Wood and his team improved the tip geometry and integrated electronic tuning into the TC [26]. They used a reflectometer configuration similar to Schoelkopf's to overcome the bandwidth limitations of classical EIFC for ultra-fast particle detection. At that time, the technique improved the throughput (compared to the EIFC [55]) by a factor of 100. Since then, many resonant structures have been used to detect particles and fluids in microfluidic environments.

Fig. 3.4 shows a curated selection of electrical resonators. While TCs have been used in impedance matching for standard EIFC setups [73], this collection focuses on reflectometric configurations. The presented list is an exemplary collection of resonators that incorporate a microfluidic channel but not a complete list of all published designs.

As mentioned above, Wood et al. were the first to use a TC, as shown in Fig. 3.4a. An inductance is connected in series with a CPW signal line. The inductance, together with the capacitance of the CPW line and the capacitance of the sensing region, form a TC resonant at 169 MHz. TCs cancel out the parasitic capacitance of the contact electrodes by the TC inductance and simultaneously impedance-match the sensor. Resonators also increase the electric field strength, ideally in the volume of the fluidic channel. Additionally, a resonator improves the sensitivity due to the resonance peak shift. In 2009, Nikolic- Jaric et al. incorporated a TL resonator ($\lambda/4$-resonator) to detect 5.7 µm sized polystyrene beads and chinese hamster ovary cells at 1.5 - 2 GHz frequencies [52]. It was the first GHz sensing of particles in a microfluidic system, but the resonator had a low quality factor of ≈ 10. The geometry of this sensor is shown in Fig. 3.4b. In 2013, Chretiennot et al. used a CPW with an integrated $\lambda/4$-resonator to determine the complex permittivity of liquid mixtures in a microfluidic channel [68] (Fig. 3.4c). They applied a model to estimate the complex permittivity of media in a microfluidic channel. This is done by a set of linear functions that approximate the relationship between the frequency shift Δf,

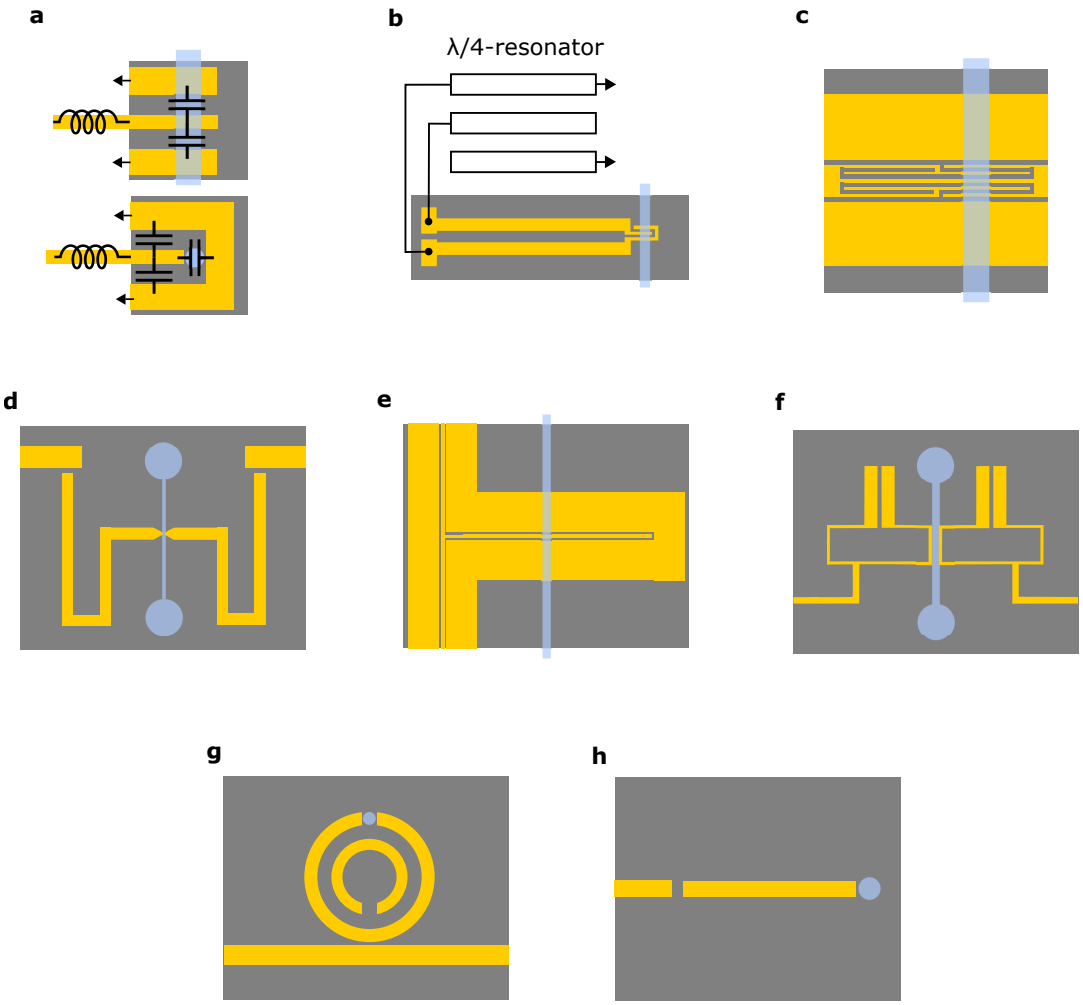

FIGURE 3.4: **Overview of high-frequency resonators for inflow particle sensing: a**, Tank circuit [25, 24, 66, 26]; **b**, Transmission line $\lambda/4$-resonator [52, 67]; **c**, Coplanar waveguide $\lambda/4$-resonator [68]; **d**, Two coupled $\lambda/2$- microstrip resonators [69]; **e**, CPW $\lambda/2$ resonator [70]; **f**, Hairpin resonator [71]; **g**, Double split ring resonator [72]; **h**, Microstrip resonator [72].

the Q factor or peak attenuation $|\Delta S|$, and the complex permittivity [74]. This thesis adopts a similar approach, which is elaborated in detail in section 3.8. In 2015, Leroy et al. used a broadband setup (0.5 - 8 GHz) and resonant structure (5 GHz) to detect trapped cells and polystyrene beads in a microfluidic channel [69]. The resonator improved the sensitivity compared to the broadband application, and the permittivity of cells and polystyrene beads could be extracted. The sensor consists of two coupled $\lambda/2$-microstrip resonators (Fig. 3.4d). In the same year, Watson et al. applied a CPW $\lambda/2$-resonator to sense complex permittivity changes in a nanoliter volume [70] (Fig. 3.4e). The metallization layer had a thickness of 6 µm, which minimized the resistive losses and resulted in a high Q-factor of 177. Liu et al. utilized a hairpin resonator to detect trapped cells, as detailed in their 2018 study [71] (see Fig. 3.4f). However, a notable limitation of this hairpin resonator design is its inability to confine the electric field within a small volume. Tsai et al. used a microstrip (Fig. 3.4g) and a double split ring resonator (Fig. 3.4h) to detect particles in a fluidic channel. The smallest detectable particle was 5 µm at a time resolution of 5 ms [72]. A phase-locked loop circuit was incorporated to track the resonance frequency shift.

3.4 Theory: Coupling-Based Sensor and Sensitivity

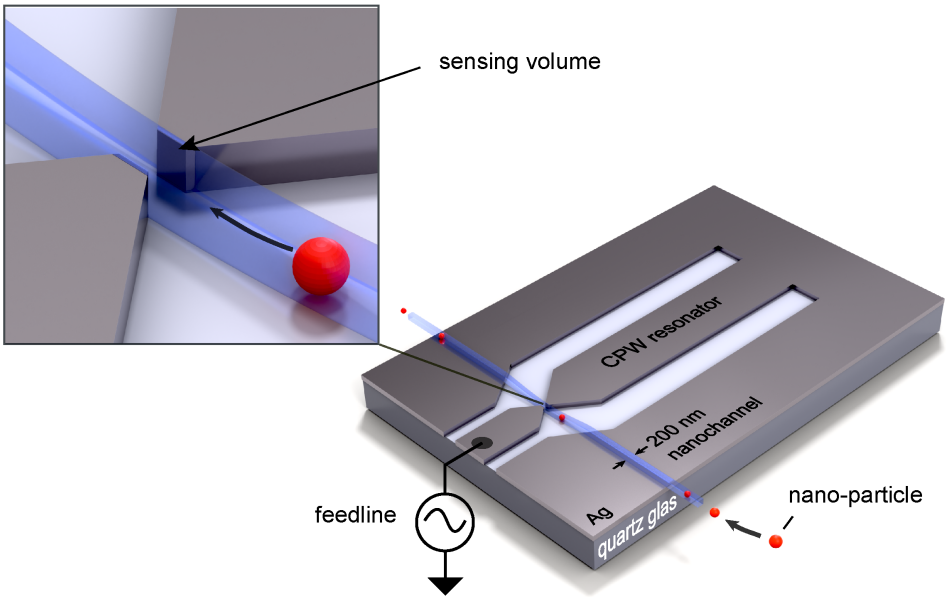

FIGURE 3.5: **Schematic overview of the coupling-based CPW (cCPW) sensor:** A short-circuited CPW $\lambda/4$-resonator couples via a sensing volume to a feedline. A fluidic channel intersects the sensing volume between the electrode tips. The flow of particles through this channel modulates the coupling between the resonator and feedline. Illustration reproduced from my publication [1], © 2023 IEEE

This section presents a novel coupling-based approach, an improved TC-based sensor. The goal of the sensor is to enhance the sensitivity for the detection of nanoscopic particles. The novelty centers around utilizing the sensing volume as the input coupling capacitance to a TC. Fig. 3.5 displays a schematic picture of the novel sensor configuration.

The novel configuration is a coupling-based CPW (cCPW) resonator. It consists of a $\lambda/4$ CPW resonator coupled to the feedline via a femto farad gap capacitance. In the theory chapter, the distributed element model of the coupling-based configuration is introduced and displayed in Fig. 2.4. The gap capacitance forms the coupling capacitance between the feedline and the resonator. In such a configuration, in addition to the conventional peak shift, the input coupling is sensitive to changes in the sensing capacitance. The coupling coefficient affects the intensity of the reflected signal.

The proposed sensing configuration is a series one-port undercoupled resonator ($g < 1$). The reflection coefficient of such a configuration is given by [75]

$$\Gamma = \frac{1-g}{1+g} \tag{3.5}$$

In the theory section 2.2.1, the relationship between the coupling coefficient g and the circuit parameters was derived, and the relationship is described by Eq. 2.34:

$$g = \frac{4Z_R Z_0 Q_0 \omega^2 C_c^2}{\pi} \tag{3.6}$$

Z_R is the characteristic impedance of the resonator, Z_0 is the feedline impedance, ω is the resonance angular frequency, Q_0 is the quality factor of the resonator, and C_c is the coupling capacitance. Substitution of Eq. 3.6 into Eq. 3.5 shows that the reflected signal is sensitive to changes in the coupling capacitance via the coupling mechanism. Importantly, this phenomenon is distinctly different from the modulation of the input coupling caused by losses in the sensing volume that can occur in conventional TC configurations.

3.4.1 Coupling-Based Sensitivity

I define the coupling sensitivity as the change in reflection coefficient divided by the change in coupling capacitance $P_s = \delta\Gamma/\delta C_c$.

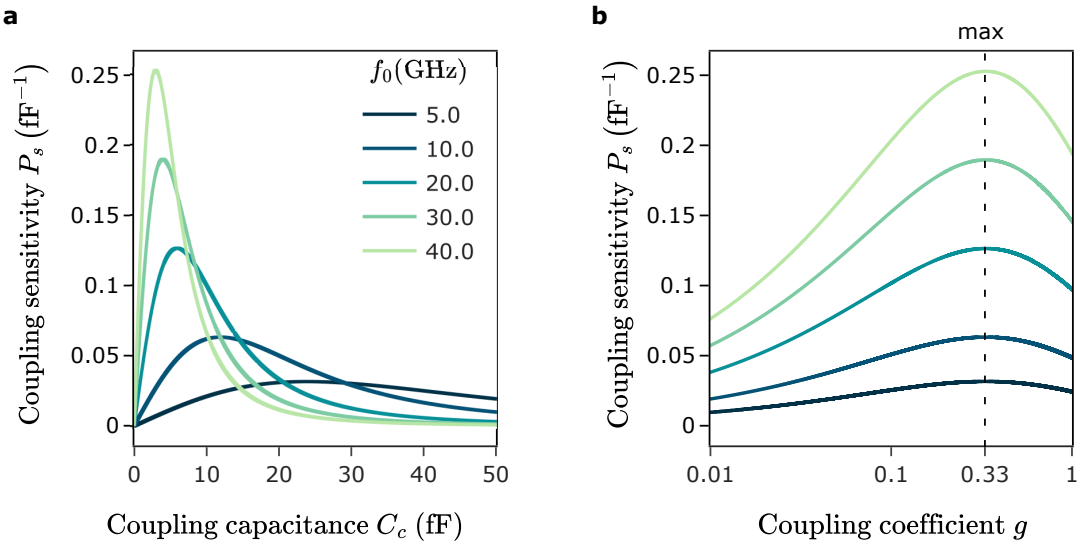

FIGURE 3.6: **Theoretical solutions for the sensor's coupling sensitivity:** This illustration outlines the calculated solutions based on the circuit parameters ($Z_0 = 50\ \Omega$, $Z_R = 80\ \Omega$, and $Q_0 = 117$). **a**, The sensitivity parameter ($P_s = \delta\Gamma/\delta C_c$) is evaluated over a range of coupling capacitances C_c spanning from 0 to 50 fF, and at various resonance frequencies f_0 from 5 to 40 GHz. Graph **b** plots the corresponding coupling coefficient g for the same frequencies and coupling capacitances. Graphs reproduced from my publication [1], © 2023 IEEE

It is calculated by substituting (3.6) into (3.5) followed by the derivative with respect to C_c. Fig. 3.6 shows the relationship between coupling-based sensitivity and coupling capacitance for various resonant frequencies between 5 - 40 GHz. The sensitivity is calculated for the coupling parameters ($Z_0 = 50\ \Omega$, $Z_R = 80\ \Omega$, and $Q_0 = 117$), which corresponds to one of the manufactured sensors described in section 3.6. Each set of coupling parameters translates into a range of coupling capacitances at which the sensor is most sensitive. This range shifts to lower coupling capacitances as the resonance frequency increases. Fig. 3.6b shows the relationship between sensitivity and coupling coefficient. The sensor is most sensitive at a coupling coefficient of $g = 0.33$, which results in a reflection coefficient of $\Gamma = 0.5$.

The coupling coefficient can be fine-tuned by adjusting the geometry of the sensor. The most coupling-sensitive configuration does not produce a perfectly impedance-matched sensor. An interferometer is incorporated to account for the mismatch (see

section 5.2.1). In the following section, the relationship between the circuit parameters, the coupling coefficient, and the geometry of the sensor is investigated using FEM simulations. These simulations help to determine the geometry with the highest coupling sensitivity.

3.5 FEM Simulation: Optimizing Geometry for Coupling

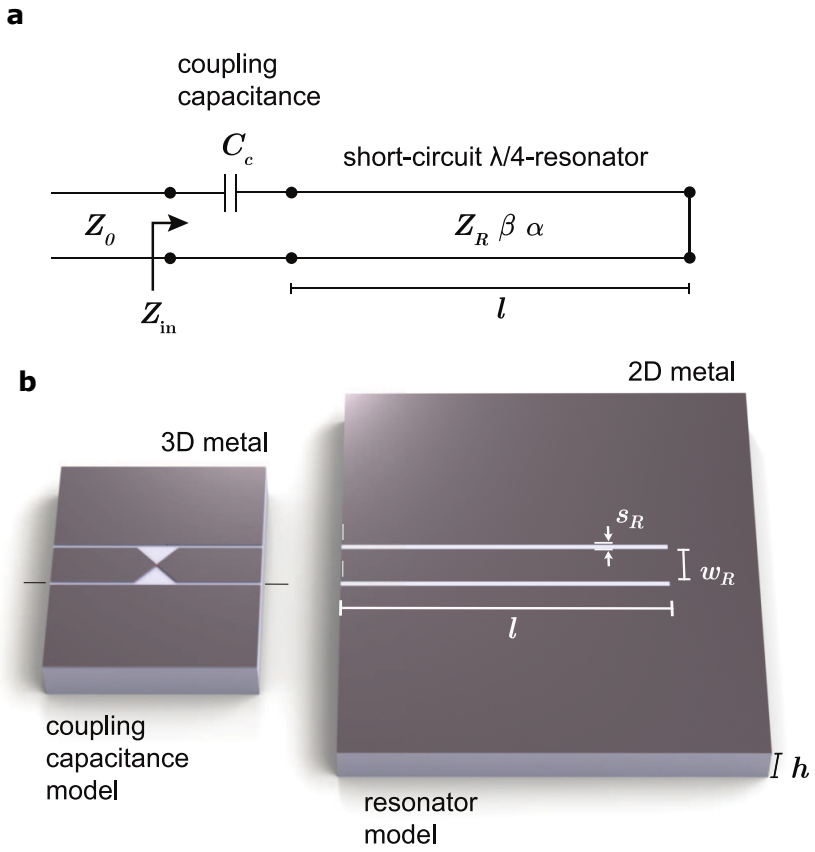

FIGURE 3.7: **Distributed circuit model and FEM simulation: a**, The distributed circuit model of the coupling-based sensor. It is a gap-coupled short-circuit CPW $\lambda/4$-resonator. **b**, The corresponding FEM simulation consists of two sub-models: the coupling capacitance model and the CPW $\lambda/4$-resonator model. Both models are cascaded to obtain the total sensor model. The metal layer of the coupling capacitance model is simulated in 3D, while the resonator's metal layer is modeled in 2D. Image reproduced from my publication [1], © 2023 IEEE

FEM simulations investigate the sensor geometry and determine the optimal coupling configuration. The circuit parameters, such as the resonator characteristic impedance Z_R, the feed line characteristic impedance Z_0, the unloaded quality factor Q_0, and the angular frequency ω, are all closely related to the sensor geometry and the coupling coefficient g, as can be seen from Eq. 3.6.

By modifying the resonator geometry and the gap region, it is possible to fine-tune the coupling coefficient g. The resonator consists of a short-circuited CPW, which allows for the modification of the circuit parameters. The characteristic impedance can be effectively adjusted by changing the ratio between the center line width w_r

and the center line to ground distance s_r. In addition, the length l of the CPW resonator can be changed to control the resonance frequency. Furthermore, the distance between the sensing electrodes and the transition between the feedline CPW ground and the resonator CPW ground determine the coupling capacitance C_c.

The overall sensor model consists of two separate sub-models: the coupling capacitance model and the resonator model, shown in Fig. 3.7b. Separating the geometry into two FEM sub-models drastically reduces the computational cost. It allows 3D simulation of the gap region while simplifying the resonator modeling to 2D. The simulation of the entire sensor in 3D exceeded the available computational resources. The coupling capacitance model has been discussed in detail in section 3.2. It is a two-port network with the metal layer and the sensing volume modeled in 3D. The gap region has a straight ground configuration to increase the coupling capacitance. The sensing volume is assumed to be cubic with the same width, height, and length as w_x, the volume unit. Unless otherwise specified, the volume unit is 1 µm.

The second submodel represents the $\lambda/4$ short-circuit resonator. The input port of the resonator is located between the signal line and the ground on the left side of the resonator. This port creates a one-port network. The resonator submodel is cascaded with the coupling capacitance submodel at this port. The metal is represented in 2D, with a thickness of 1 µm. The substrate is made of 500 µm quartz glass. The resonator model has the same metal conductivity $\sigma = 5.65 \cdot 10^7\ \mathrm{S\,m^{-1}}$ and dielectric constant values ($\varepsilon_{\mathrm{quartz}} = 3.86$, $\delta_{\mathrm{quartz}} = 2 \cdot 10^{-4}$) as the gap model [64, 41, 42]. The width of the signal line w_r is kept at 400 µm. If not explicitly stated, the signal line to ground distance s_r is 44 µm for a characteristic impedance of about 50 Ω. The S-parameters are simulated separately for each model. A simulation of the gap region's S-parameters allows the calculation of the coupling capacitance. The total S-parameter solution is obtained by cascading the S-parameters of both networks.

Resonance Frequency

I start the geometric optimization by studying the effect of the resonator length l on the resonance frequency and the coupling coefficient. For each geometry, the theoretical results are compared with the simulation results. The resonator length is related to the resonance frequency f_0 by the transient equation provided by Eq. 2.27 in the theory chapter. The left part of the equation approaches infinity for a weakly coupled resonator ($C \to 0$). In this case, the transient equation is solved by

$$\frac{\omega l}{v_p} = \frac{n\pi}{2}. \tag{3.7}$$

The phase velocity is given by $v_p = c_0/\sqrt{\varepsilon_{\mathrm{eff}}}$. The effective dielectric constant $\varepsilon_{\mathrm{eff}} = 2.36$ has been determined by the quasi-static conformal mapping approach [31]. The fundamental resonance frequency of Eq. 3.7 is

$$f_0 = \frac{c_0}{\sqrt{\varepsilon_{\mathrm{eff}}}} \frac{1}{4l} \tag{3.8}$$

For the FEM simulations, the length l of the resonator varies between 1 - 6 mm. The real permittivity of the sensing volume is 40, which is an approximate average value of water over the investigated frequency range [50]. This is a rough approximation of water, as it has a relaxation frequency of about 17 GHz at room temperature, which causes the real permittivity to drop from 80 to 10 in the investigated frequency range.

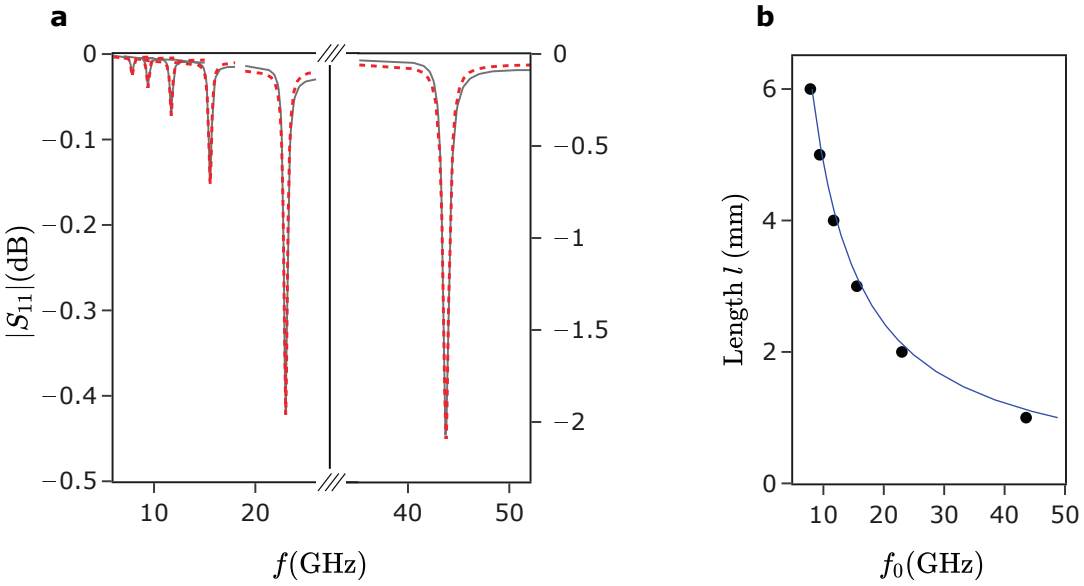

FIGURE 3.8: **Coupling strength and resonance frequency dependence on resonator length l: a**, The simulated $|S_{11}|$-parameter as the resonator length l varies from 1 - 6 mm. A dotted red line represents the Lorentzian peak fit. **b**, The relationship between the resonator length and the resonance frequency f_0. The black dots denote the resonance frequencies derived from the Lorentzian fits, while the blue line presents the analytical solution from Eq. 3.8. Graphs reproduced from my publication [1], © 2023 IEEE

A fixed permittivity value allows us to isolate the influence of the resonator length on the coupling.

Fig. 3.8a shows the fundamental resonance peaks for different resonator lengths l (black). I computed the S-parameter solution by cascading the resonator networks of different lengths with the gap network. Each solution is fitted with a Lorentz shape (dashed red line) to obtain the resonance frequency f_0, reflection coefficient Γ, and loaded quality factor Q_L. Fig. 3.8b plots the resonance frequencies f_0 at different lengths l obtained from FEM simulations and theory Eq. 3.8 in black and blue, respectively. As expected, the resonance frequency shifts to higher values as the resonator length decreases. Except for a frequency offset, the simulation agrees with the theoretical values. The offset is due to the capacitive loading of the resonator by the gap capacitance, imperfect impedance matching at the cascaded simulation ports, and the shorted region of the resonator, which extends the effective length of the resonator. The coupling coefficient is determined by Eq. 3.2 and subsequently compared with the theoretical value obtained from Eq. 3.6. The theoretical coupling capacitance is extracted from the capacitive gap model (discussed in part 3.2).

Fig. 3.9a shows a quadratic increase of the coupling coefficient g towards higher resonance frequencies ($g \propto f_0^2$). For lengths l between 1 mm - 6 mm, the coupling coefficient spans two orders of magnitude, suggesting that a shorter length effectively shifts the coupling coefficient toward the optimal value of 0.33. The choice of the optimal resonance frequency must consider the permittivity contrast between the medium and the particle. Water is a particularly suitable medium due to its exceptionally high real permittivity.

The following simulations use a 2 mm long resonator with a resonance frequency

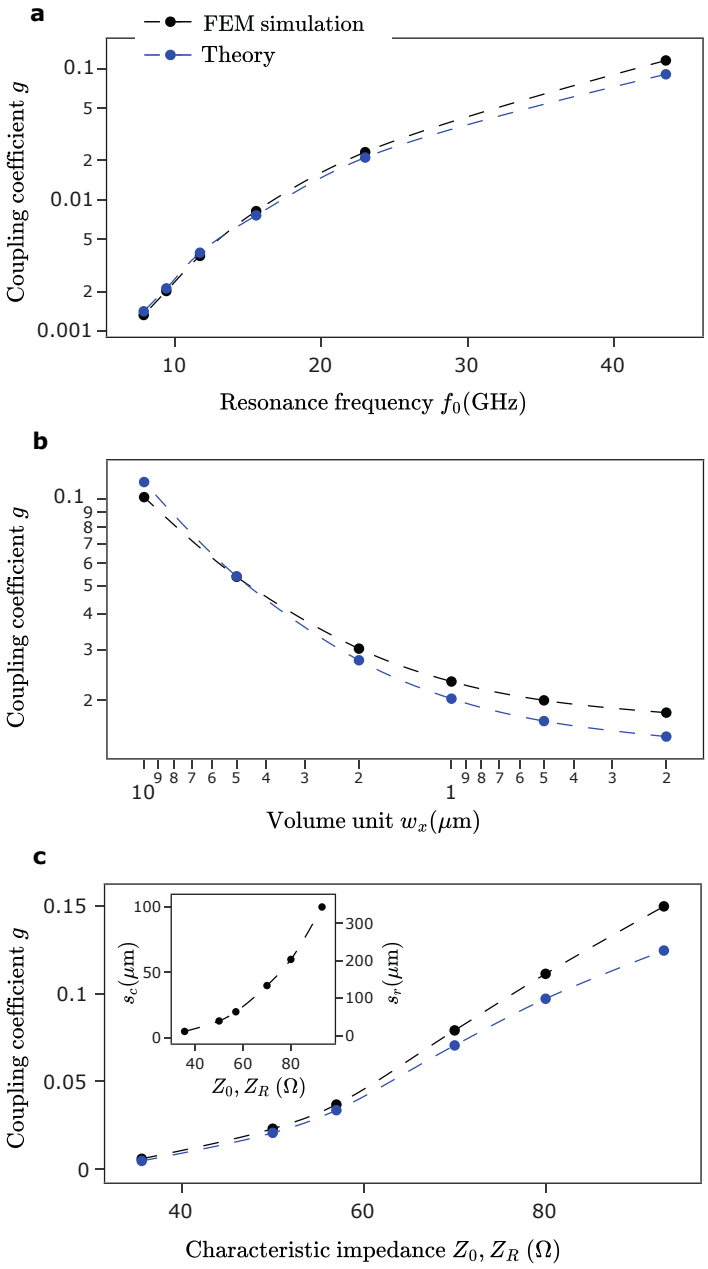

FIGURE 3.9: **Dependence of circuit parameters on coupling coefficient g:** Black dotted lines represent FEM simulation results, while blue lines indicate theoretical solutions derived from Eq. (3.8). **a**, Resonator length ranges from 1 mm to 6 mm. **b**, Volume unit w_x reduces from 10 µm to 200 nm. **c**, The dependence between the CPW characteristic impedances of the resonator Z_R and feedline Z_0 and the coupling coefficient. Inset: Correlation between the characteristic impedance of the resonator Z_R and the feedline Z_0, and the CPW signal-to-ground distances of the resonator s_r, and feedline s_c, respectively. Adjustments of the CPW geometry result in a characteristic impedance between 35 Ω to 93 Ω. Graphs reproduced from my publication [1], © 2023 IEEE

of about 23 GHz. I choose a real permittivity of $\varepsilon = 40$. This choice is a balance between the increased coupling at higher frequencies and the counteracting decrease in coupling capacitance due to the decreasing real permittivity of water at higher

frequencies.

Sensing Volume Size

In Fig. 3.9b, I examine the effect of the size of the sensing volume on the coupling coefficient g. The volume unit w_x changes from 10 µm to 200 nm. As described in section 3.2, the sensing capacitance C_s decreases linearly with shrinking electrode tips, while the parasitic capacitance C_p remains approximately constant. Thus, as the tip size decreases, the coupling capacitance C_c approaches the value of C_p. This aspect leads to a saturation of the coupling coefficient at nanoscopic sensing volumes. Between 10 µm and 1 µm, the coupling coefficient decreases significantly to 0.25% of its initial value. From 1 µm - 200 nm, the coupling coefficient approaches a limit of 0.02. The geometry of the gap region is responsible for the gap region parasitic capacitance C_p. This parasitic capacitance defines the coupling coefficient for nanoscopic sensing volumes. Conversely, the gap geometry can be used to adjust the coupling capacitance and, thus, the coupling coefficient.

Characteristic Impedance

The characteristic impedance of the feedline Z_0 and the resonator Z_R are also relevant coupling parameters. The characteristic impedance is related to the geometry of the CPW by the ratio of the signal line width w to the signal line to ground distance s. For the gap model, the signal line width w_c is fixed at 100 µm, while the signal line to ground distance s_c varies from 5 to 100 µm. For the resonator model, the signal line width w_r is fixed at 400 µm, and the signal line to ground distance s_r varies between 10 - 440 µm. These parameters correspond to characteristic impedances of 35 - 93 Ω (inset Fig. 3.9c).

Fig. 3.9c shows the relationship between the coupling coefficient g and the characteristic impedance of the feedline and resonator. The coupling coefficient increases from 0.02 at 50 Ω to 0.15 at 93 Ω. As expected, the resonator impedance can optimize the coupling by shifting the coupling coefficient toward the optimal value of 0.33. In addition, the signal line width w_r and the signal line to ground distance s_r affect not only the characteristic impedance but also the attenuation of the line, which in turn affects the internal quality factor of the resonator. At $Z_R = 75$ Ω, the resonator had the highest loaded quality factor of 65.

The characteristic impedance also affects the conventional TC resonance peak shift. The total capacitance at 80 Ω is 69% of the capacitance at 50 Ω calculated by the conformal mapping approach. As discussed earlier, minimal capacitance maximizes the resonance peak shift. Therefore, an increased characteristic impedance benefits the input coupling and the conventional resonance frequency shift.

Based on this, the coupling coefficient can be optimized for sub-fF sensing capacitances by adjusting the resonator and tip geometry to achieve an optimal value of g = 0.33.

3.6 Experiment: Validation of the Optimized Sensor

In the previous FEM simulations, the dependence between the sensor geometry and the coupling coefficient was studied. In the following, I use this knowledge by combining all optimization aspects to achieve a coupling coefficient close to the optimal

value of g = 0.33. Therefore, I choose a resonator length of 2.2 mm, which results in a resonance frequency of 19.74 GHz, a signal line width of 400 µm, and a signal line to ground distance of 200 µm, resulting in a characteristic impedance of 80 Ω. The feedline is matched to a characteristic impedance of 50 Ω (determined by conformal mapping) with a signal line width of 200 µm and a signal-to-ground distance of 21 µm. In this way, the feedline matches the CPW probe tip with the same characteristic impedance of 50 Ω. The ground plane has a straight transition from the feedline to the resonator, which increases the parasitic coupling of the resonator to the feedline and shifts the sensor into the capacitively sensitive regime. A wafer with 16 resonators was manufactured (see Fig. 4.3). The fabrication process is described in chapter 4. 8 of these 16 resonators are defect-free and have the same tip geometry with a tip width and tip-to-tip distance of 2 - 3 µm, confirmed by scanning electron microscopy (SEM).

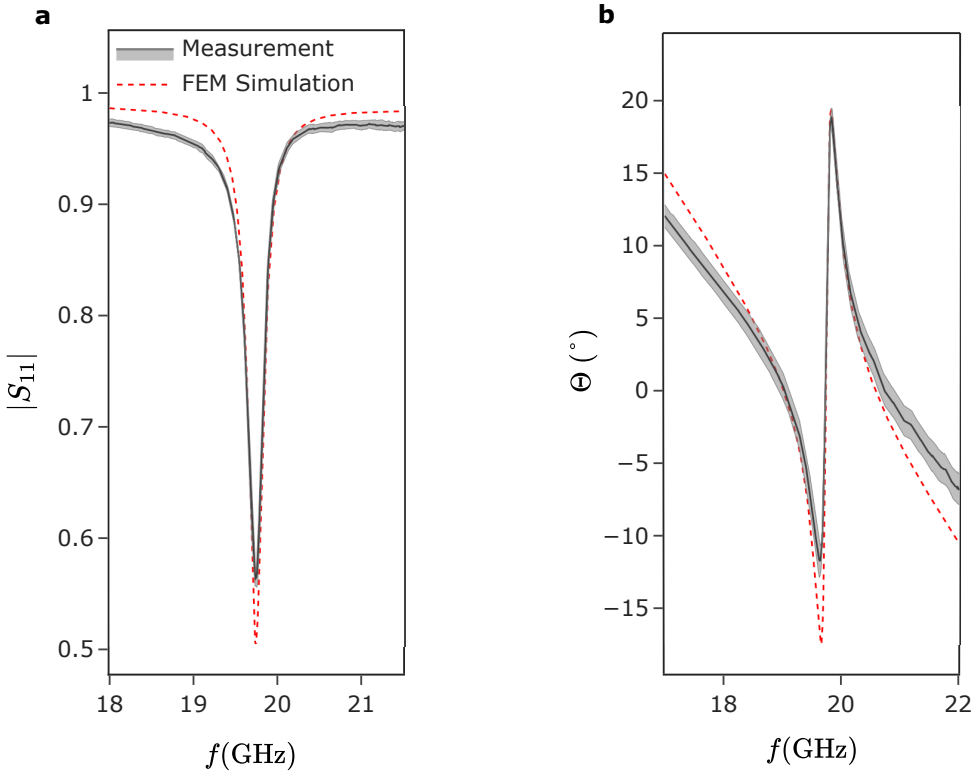

FIGURE 3.10: **Experimental validation of the coupling-based concept: a**, The characterization of the sensor's $|S_{11}|$-parameter (i.e., reflection coefficient), and **b** the sensor's phase. The red dashed line represents FEM simulation results. The average $|S_{11}|$-parameter and phase from 8 resonators are shown in black, with error bounds calculated as the standard deviation indicated by the shaded gray region. Graphs reproduced from my publication [1], © 2023 IEEE

A vector network analyzer (VNA) (N5222A, *Keysight / Agilent*) measured the S-parameters of 8 different resonators. Prior to the measurement, the reference plane was shifted to the CPW probe tips (FPC-GSG-250, *Cascade Microtech*) using the short-open-load-thru (SOLT) method performed on a calibration substrate (AC-2, *MPI*). Fig. 3.10a shows the average amplitude response (i.e., $|S_{11}|$-parameter), and Fig. 3.10b displays the average phase response of the eight sensors. The black line represents the VNA measurement, and the dashed red line represents the corresponding FEM simulation. The offset between the measured and simulated phase

spectra is removed for better comparison. All eight manufactured sensors have a similar amplitude and phase response. The standard deviation of all sensors at each frequency is shown in gray.

The gap region and the CPW resonator are simulated in a single FEM model with a 2D metal layer. Such an approach is feasible if the metal layer is thin relative to the size of the gap. A good fit to the simulation was obtained for $\varepsilon_{\text{quartz}} = 4.05$ and $\tan\delta_{\text{quartz}} = 0.003$. The measured S_{11} parameter has a resonance frequency of 19.74 GHz with a loaded quality factor of 86. The reflection coefficient is 0.59, close to the optimal value of 0.5, with a coupling coefficient of 0.26 calculated by Eq. 3.6. The internal quality factor is $Q_0 = Q_L(1+g) = 108$.

In conclusion, the dependence between the coupling coefficient and the sensor's geometry guided the optimization of the sensor. An optimized sensor was fabricated and compared with FEM simulations. The excellent agreement between simulated and measured data validates the novel coupling-based sensor approach.

Attenuation

The total attenuation constant at resonance is calculated as $\alpha = \frac{\pi}{4Q_0 l} = 28.66\,\text{dB/m}$. This attenuation can be compared with the theoretical contributions of dielectric and conductor (i.e., resistive) loss and radiation loss discussed in the theory section 2.2.3. For the theoretical calculation I assume $\varepsilon_{\text{quartz}} = 4.05$ and $\tan\delta_{\text{quartz}} = 0.0002$. The theoretical dielectric loss is $\alpha_d = 0.43\,\text{dB/m}$ (Eq. 2.47), the conductor loss is $\alpha_c = 7.46\,\text{dB/m}$, and the radiation loss is $\alpha_r = 8.29\,\text{dB/m}$. The total attenuation is $\alpha_t = 16.17\,\text{dB/m}$. Interestingly, this theoretical value is significantly lower than the observed experimental attenuation. The reason for this discrepancy is not fully understood. While some differences can be attributed to losses from the tapered gap region and ground termination (elements not captured in our theoretical model), this does not account for the entire variance. Even when these factors are included in a Finite Element Method (FEM) simulation, the predicted attenuation remains lower than the experimental results.

One possible explanation is the dielectric loss tangent of the fused silica substrate. Adjusting its value to $\tan\delta_{\text{quartz}} = 0.003$ yields a theoretical dielectric loss of $\alpha_d = 6.4\,\text{dB/m}$. This gives a total theoretical attenuation of $\alpha_t = 22.14\,\text{dB/m}$.

This revised value is more in line with our experimental observations, with a difference of 6.52 dB/m due to losses from the aforementioned tapered gap region and ground termination. The fabrication process, particularly the Ar-ion milling, may have affected the quality of the quartz glass. Alternatively, the available quartz glass may have a loss tangent that deviates from typical literature values.

3.7 TL Theory: Validation and Capacitive Response

In the previous section, I compared a manufactured cCPW sensor with FEM simulations. In this section, I contrast the experimental results with the TL theory. Furthermore, I model the theoretical response of the cCPW sensor to a capacitance change in the sensing volume. This response is then compared to the capacitance change of a conventional TC sensor that does not use a coupling-based approach. This comparison serves two purposes:

- It quantifies the advantages of using a short-circuited CPW, which reduces the length of the resonator from $\lambda/2$ to $\lambda/4$. To my knowledge, such a shorted CPW configuration has not been used for particle detection in the existing literature.
- It demonstrates the advantages of a coupling-based approach over conventional TC sensors.

Circuit Models and Input Impedance

The response of both circuits is analyzed in terms of the modulation of the reflection coefficient Γ (i.e., the scattering parameter S_{11}). This parameter can be calculated with the use of the input impedance. In the following, I present circuit models and derive the theoretical input impedances for the cCPW sensor, as well as the open circuit $\lambda/2$-resonator and its equivalent *RLC*-circuit model.

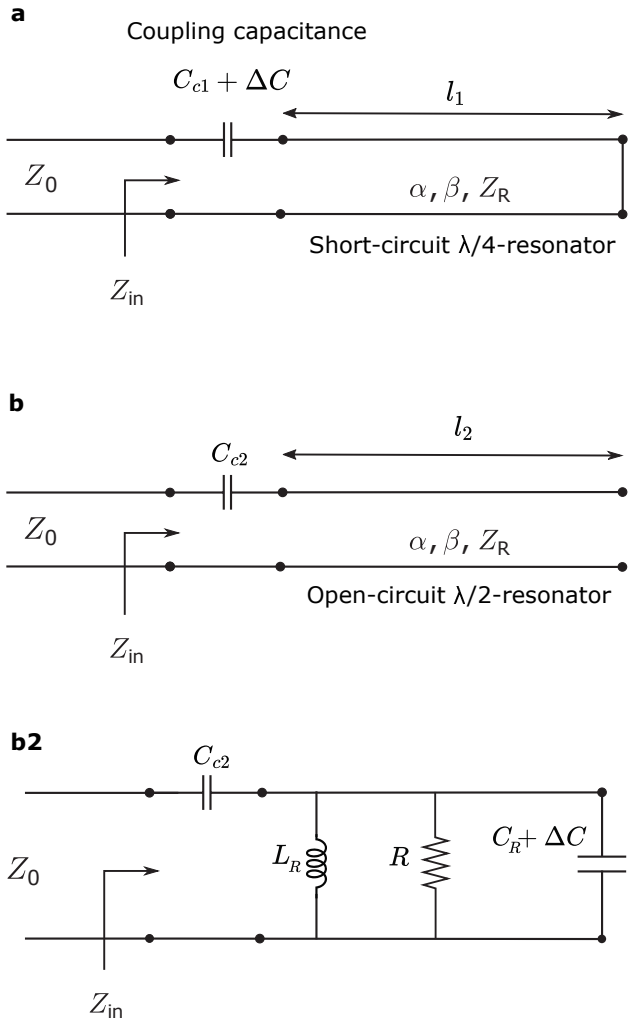

FIGURE 3.11: **Comparison of coupling-based $\lambda/4$-sensor and conventional tank circuit sensor: a**, Coupling-based short-circuit $\lambda/4$-resonator model. **b**, Open-circuit $\lambda/2$-resonator model, and **b2**, Equivalent *RLC*-resonant circuit representation. The capacitive response is investigated by modulating ΔC.

Fig. 3.11a depicts the distributed circuit model of the cCPW sensor. It consists of a short-circuit $\lambda/4$-resonator, which couples via a series capacitance C_{c1} to the feedline. The input impedance of this circuit is given by

$$Z_{\text{in}_{\lambda/4}} = -\frac{j}{\omega(C_{c1}+\Delta C)} + Z_0 \tanh(\alpha l_1 + j\beta l_1), \tag{3.9}$$

where α is the attenuation constant, β is the phase constant, and l_1 is the length of the TL. The coupling capacitance C_{c1} is also the sensing capacitance. During a microfluidic flow measurement, this capacitance is modulated by particles in the sensing volume. In a later section, I analyze the capacitive response of the coupling-based sensor by modulating the coupling capacitance by ΔC.

Fig. 3.11b shows a distributed model of the open-circuit $\lambda/2$-resonator. The resonator is coupled to the feedline via a capacitance C_{c2}. The impedance of this configuration is

$$Z_{\text{in}_{\lambda/2}} = -\frac{j}{\omega C_{c2}} + Z_0 \coth(\alpha l_2 + j\beta l_2). \tag{3.10}$$

Unlike the first configuration, the coupling capacitance is constant. An equivalent *RLC*-circuit model can be used to model that resonator configuration (Fig. 3.112b). In fact, an *RLC* circuit can also model all kinds of conventional TC sensors. An overview of various TC sensors used for inflow particle sensing that could be modeled with a *RLC* circuit is presented in section 3.3. Unlike the coupling-based configuration, in these sensors, the modulated capacitance is part of the resonant circuit, not the coupling capacitance. The *RLC*-circuit model provides a systematic framework for studying variations in this capacitance. ΔC represents the variation of this capacitance.

The input impedance is calculated as a series capacitance connected to a parallel *RLC* circuit as

$$Z_{\text{in}_{RLC}} = -j\frac{1}{\omega C_{c2}} + \left(\frac{1}{R} + \frac{1}{j\omega L_R} + j\omega(C_R+\Delta C)\right)^{-1} \tag{3.11}$$

The equivalents between a distributed model and the *RLC*-circuit model was described in section 2.2. Table 2.1 describes the relationship between the *RLC*-circuit parameters and the TL parameters. This allows the adjustment of the *RLC*-circuit parameters to represent the manufactured sensor.

Adjusting Circuit Parameters to Represent the Manufactured Sensor

The circuit parameters of the cCPW sensor and the $\lambda/2$-resonator are adjusted in a way that they accurately represent the manufactured sensor described in the previous section 3.6. To achieve this, the TLs of both theoretical models are represented with CPWs. Therefore, TL parameters: attenuation constant α, phase constant β, and characteristic impedance Z_R are adjusted to the same values as the manufactured sensor. Furthermore, The length l_1 of the $\lambda/4$ cCPW resonator is adjusted to the same value as the manufactured sensor. The length of the $\lambda/2$ resonator is twice the length of the $\lambda/4$ resonator to achieve the same resonance frequency f_0 for both sensors. Furthermore, the coupling capacitances C_{c1} and C_{c2} are adjusted so that both circuits have an identical impedance match to the feedline. The phase constant is calculated by

$$\beta = \omega\sqrt{\varepsilon_{\text{eff}}}/c_0. \tag{3.12}$$

The effective permittivity ε_{eff} is obtained via the conformal mapping approach described in section 2.2.2. For a 500 µm thick quartz glass with a permittivity of $\varepsilon_r = 4.05$, the effective permittivity is $\varepsilon_{\text{eff}} = 2.38$.

For an open-circuit $\lambda/2$-resonator, it is essential to determine the parameters of its equivalent RLC-circuit. The total capacitance, denoted as C_R, can be calculated using the equation

$$C_R = \frac{C_l l}{2},$$

where C_l is the capacitance per unit length of a coplanar waveguide, as given by Eq. 2.43 [76].

Similarly, the inductance, L_R, can be obtained through the following equation:

$$L_R = \frac{2L_l l}{\pi^2}.$$

Here, L_l is the inductance per unit length, as defined in Eq. 2.44 [76].

The resistance R can be calculated using the formula:

$$R = \frac{Z_R}{\alpha l_2},$$

where $Z_R = 78.1\ \Omega$ represents the characteristic impedance of the resonator. A comparison of the RLC-circuit model with the original distributed model, which is described by Eq. 3.10, yielded identical amplitude and phase responses for both models (not shown). This comparison validates the equivalence of both models and justifies using the RLC-circuit model for further calculations. The *RLC*-circuit model is beneficial because it provides a framework for studying variations in the sensing capacitance represented by ΔC in Fig. 3.11b2.

Adjusting the parameters allows, on the one hand, comparing the theoretical with the experimental results and, on the other side, comparing both theoretical models. A summary of the used parameters can be found in table (3.1).

TABLE 3.1: **Circuit parameters for the $\lambda/4$ - & $\lambda/2$ - resonators.** The corresponding circuit is depicted in Fig. 3.11.

shorted $\lambda/4$ - resonator	open $\lambda/2$ - resonator
$C_{c1} = 5.5$ fF	$C_{c2} = 8$ fF
$l = 2.2$ mm	$l = 4.4$ mm
$Z_0 = 50\ \Omega$	$Z_0 = 50\ \Omega$
$Z_R = 80\ \Omega$	$Z_R = 80\ \Omega$
$\alpha = 28.66$ dB/m	$\alpha = 28.66$ dB/m

Characterization of Theoretical Models

Microwave sensors are usually characterized by the complex scattering parameter S_{11}, also called the reflection coefficient. The complex scattering parameter can be

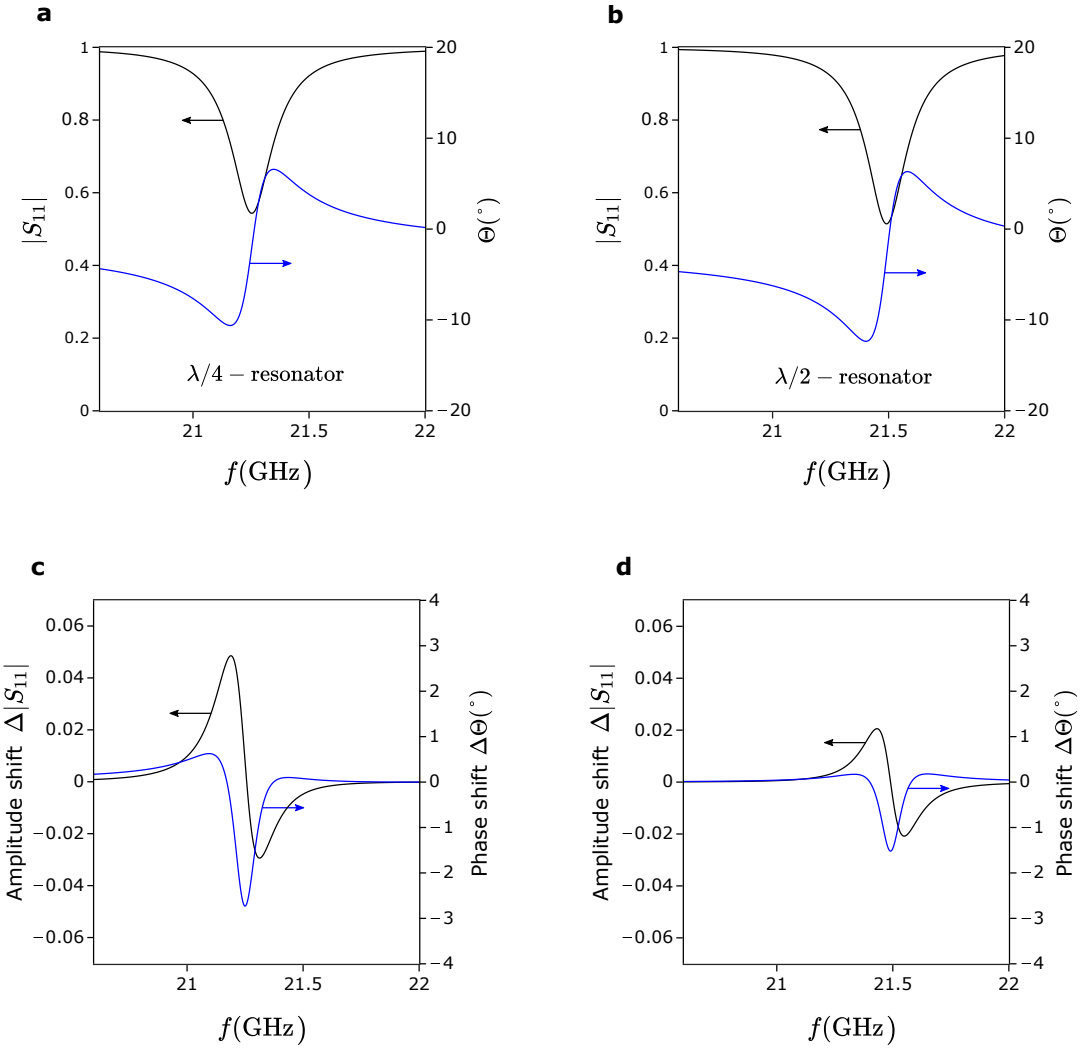

FIGURE 3.12: **Comparison of responses between a coupling-based sensor and a conventional TC sensor:** The graphs depict the theoretical amplitude (black) and phase (blue) responses of **a**, a short-circuit $\lambda/4$-resonator (coupling-based) and **b**, an open-circuit $\lambda/2$-resonator (conventional). The depicted data corresponds to the circuits illustrated in Fig. 3.11, with the circuit parameters detailed in Table 3.1. Difference spectra, arising from a capacitive change of $\Delta C = 0.1$ fF, are presented for **c**, the short-circuit $\lambda/4$-resonator and **d**, the open-circuit $\lambda/2$-resonator. The coupling-based $\lambda/4$ configuration exhibits a higher response to the identical capacitive change.

represented by the amplitude $|S_{11}|$ and the phase parameter θ: $S_{11} = |S_{11}|\exp^{j\Theta}$. It can be measured experimentally with a vector network analyzer (VNA). Theoretically, it can be calculated using Eq. 2.16 and using the previously derived input impedances Z_{in} as the load impedance.

The theoretical scattering parameter (amplitude and phase) of the coupling-based $\lambda/4$ resonator and the conventional $\lambda/2$ resonator are shown in Fig. 3.12a and 3.12b, respectively. The amplitude $|S_{11}|$ is black, and the phase Θ is blue. The length of the $\lambda/2$ resonator is double that of the $\lambda/4$ resonator. Such an arrangement results in approximately the same resonance frequency with $f_{0_{\lambda/4}} = 21.25$ GHz and $f_{0_{\lambda/2}} = 21.49$ GHz.

The resonance frequencies are not identical because both resonators are connected to different coupling capacitances of $C_{c1} = 5.5$ fF and $C_{c2} = 8$ fF. For comparison purposes, the input coupling capacitances have been adjusted so that both resonators have the same input coupling of $|S_{11}| = 0.5$ at resonance. A coupling capacitance loads the resonator capacitively and thus shifts the resonator to lower frequencies. Besides the peak shift, both resonator's amplitude and phase curves are very similar. The phase has a Fano shape with a zero crossing at resonance.

Comparison to Experimental Results

The resonance frequency of the cCPW is 1.5 GHz higher than the experimental value presented in the last section. That difference can be explained by several effects which are not accounted for in the theoretical model. The main effects stem from the inductance of the shorted CPW and the capacitance of the open segment of the CPW. The inductance of the shorted line can be approximated by an equivalent length extension Δl [77]. The length extension can be approximated by

$$\Delta l_{\text{short}} = \frac{L_{\text{short}}}{L_l} \approx \frac{s + 2w}{8}. \tag{3.13}$$

The increased inductance reduces the resonance frequency. The capacitance of an open CPW can also be approximated by an equivalent length extension Δl, which results from the fringing fields [77] by

$$\Delta l_{\text{open}} = \frac{C_{\text{open}}}{C_l} \approx \frac{s + 2w}{4}. \tag{3.14}$$

The metallization thickness t is also not implemented in the theoretical model. The metallization thickness influences the characteristic impedance and effective permittivity. The effective permittivity is given by [31]

$$\varepsilon'_{\text{eff}} = \frac{0.7(\varepsilon_{\text{eff}} - 1)t/w}{K'(k)/K(k) + 0.7t/w}. \tag{3.15}$$

For a thickness of $t = 1$ µm, the effective permittivity changes by 0.25%. Thus, the influence of the thickness can be neglected. Finally, the theoretical model also does not account for the losses introduced by the tapered electrodes. Such a non-standard CPW configuration is difficult to describe accurately by theory. FEM simulations are an excellent way to account for non-standard CPW configurations. Therefore, in the subsequent section 3.8, I additionally analyze permittivity variations in the sensing volume by FEM simulations.

Capacitive Response

Fig. 3.12c and d contrast both the circuit's amplitude and phase responses to a capacitance change. As discussed in section 2.4, the capacitance change induced by a particle depends on the geometry of the sensing electrodes, the position of the particle in the electric field, and the permittivity contrast between the suspending medium and the particle. A capacitance change of ΔC = 0.1 fF is chosen. It corresponds to a 7 µm sized cell-like particle between 10 µm separated electrodes (see Fig. 2.10).

Fig. 3.12c and 3.12d display difference-spectra induced by a 0.1 fF capacitance change for both resonators. The magnitude and phase difference spectra are calculated by

$$\begin{aligned} \Delta|S_{11}| &= |S_{11}(\Delta C = 0.1\ \text{fF})| - |S_{11}(\Delta C = 0)| \\ \Delta\Theta &= \Theta(\Delta C = 0.1\ \text{fF}) - \Theta(\Delta C = 0). \end{aligned} \tag{3.16}$$

Although the initial resonance curves of both theoretical models are very similar, the induced difference curves differ significantly. The amplitude difference curves have a fano-shape with a maximum and minimum located right and left of the original resonance frequency. In the case of the cCPW $\lambda/4$ configuration, the peaks are significantly higher than the $\lambda/2$ configuration. The fano-shape results from the capacitively induced resonance peak shift. That peak shift is stronger for the $\lambda/4$ configuration. Furthermore, in the $\lambda/4$ configuration, ΔC also modulates the coupling coefficient. This modulation induces a change in the peak amplitude, leading to an asymmetry of the fano-shape difference curve. Both effects, an increased resonance-peak shift, and the coupling-induced amplitude change result in an increased sensitivity of the $\lambda/4$ configuration. The amplitude sensitivity is 2.3 times higher for the $\lambda/4$ configuration. The phase difference spectrum has a negative peak at the resonance frequency. The phase sensitivity is up to 1.8 times higher for the $\lambda/4$ configuration. The amplitude is most sensitive at the flanks of the resonance curve. At that frequency, the phase difference spectra become zero. Reversely, the phase difference spectra are maximal at the resonance frequency; the amplitude becomes zero.

During the time-resolved application of the sensor, a discrete measurement frequency on the resonance curve is chosen, and a time trace of the reflected signal and phase is monitored. The position of the measurement frequency on the resonance curve will decide whether the sensor is phase or amplitude-sensitive.

3.8 FEM Simulation: Permittivity Variations in the Sensing Volume

In the preceding section, I examined the sensor's response to particles in the sensing volume using TL models, which exclusively explored the sensor's capacitive behavior. That analysis is extended by FEM simulations which investigate both the capacitive and loss responses of the optimized cCPW sensor when particles are present in the sensing volume.

The dual nature of these responses can be mathematically represented by the complex permittivity, denoted as ε, which was introduced in a previous section 2.3. The equation for complex permittivity is given by:

$$\varepsilon = \varepsilon' - j\varepsilon'', \tag{3.17}$$

This mathematical construct captures the material's interaction with an oscillating electric field. The real part of the complex permittivity, ε', describes the dielectric polarizability, which is responsible for the sensor's capacitive response. On the other hand, the imaginary part, ε'', accounts for energy loss within the sensing system.

Biological objects are commonly stored in water-based solutions. The permittivity of such media depends on various parameters like temperature, frequency, or ionic concentration. To account for most of the potential media, I investigate a ε' range between 1 - 100 and ε'' between 0 - 50 by FEM simulations [78, 79]. Based on prior simulations, I chose an optimized sensor geometry with a resonator length of 2 mm and a characteristic impedance of 80 Ω. The sensing volume is chosen to be 1 µm.

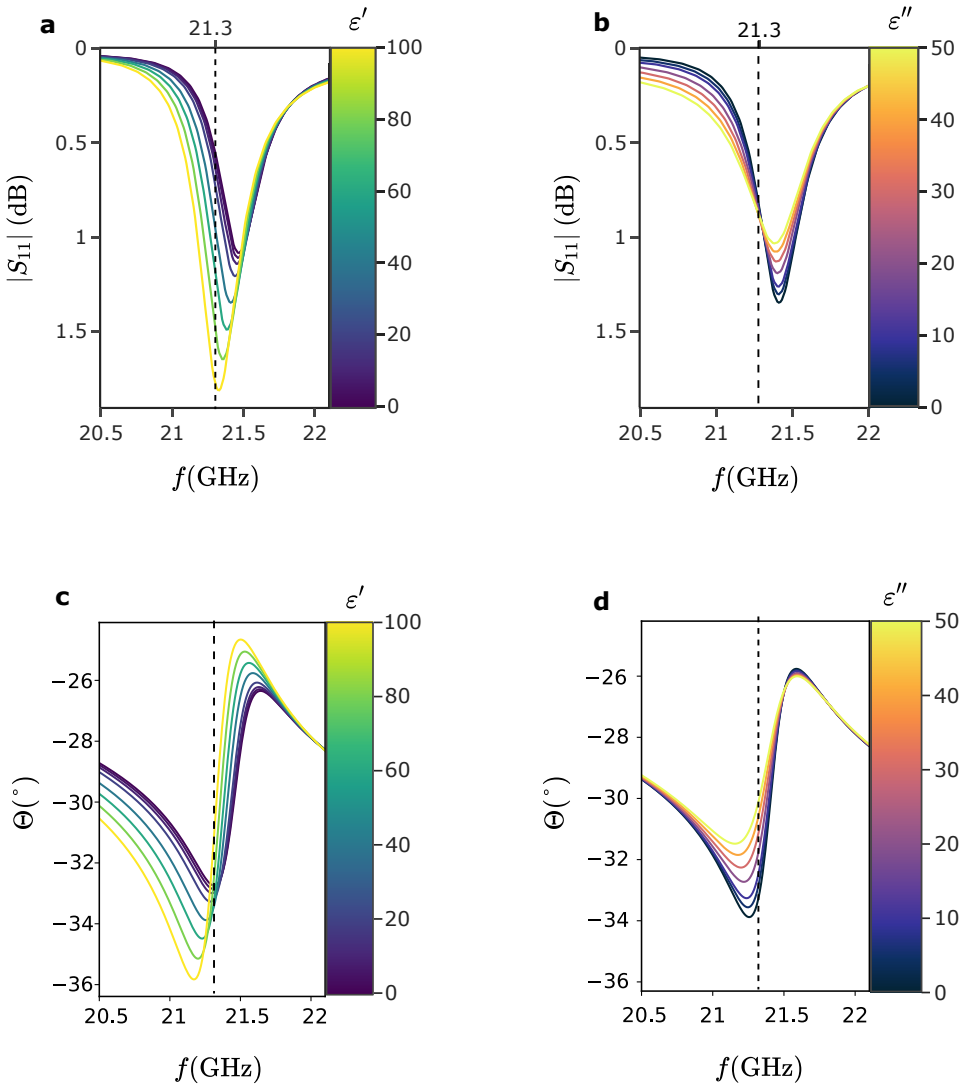

FIGURE 3.13: **Finite element method (FEM) analysis of sensor's response to complex permittivity in the sensing volume: a**, Amplitude $|S_{11}|$ and **c** Phase Θ responses as a function of real permittivity ε' ranging from 1 to 100 with imaginary permittivity ε'' held constant at 0. **b**, Amplitude $|S_{11}|$ and **d**, Phase Θ responses due to changes in imaginary permittivity ε'' from 0 to 50, with the real permittivity ε' maintained at 40. The vertical line at $f_f = 21.3$ GHz marks the most sensitive frequency, which is used for the predictive model. Graphs reproduced from my publication [1], © 2023 IEEE

Fig. 3.13 (a-b) displays the S_{11}-parameter response to changes in the complex permittivity of the sensing volume. Fig. 3.13a shows the feedback to a ε' sweep, while ε'' is fixed at 0. An increased real permittivity value leads to a rise of the S_{11}-amplitude at resonance. It is a consequence of an increased coupling capacitance and, thus, a

stronger input coupling. Additionally, the capacitive load shifts the resonance peak to lower frequencies. Both effects contribute to the total change in the reflected microwave signal.

Fig. 3.13b displays an imaginary permittivity ε'' sweep, while ε' is adjusted to 40. A rise in ε'' introduces losses into the resonator, which widens the peak shape and decreases the quality factor. Reducing the quality factor also reduces the input coupling and, thereby, the resonance peak amplitude. The resonance frequency is less sensitive to changes in the imaginary permittivity in contrast to changes in the real permittivity. Instead, the imaginary permittivity mostly influences the return loss $|S_{11}|$ and Q_L.

Predictive Model

A simple predictive model for the extraction of the complex permittivity can be constructed from the change of the loaded quality factor and a change of the amplitude at the flank of the resonance curve ($f_f = 21.3$ GHz) (similar to [80, 68, 81]).

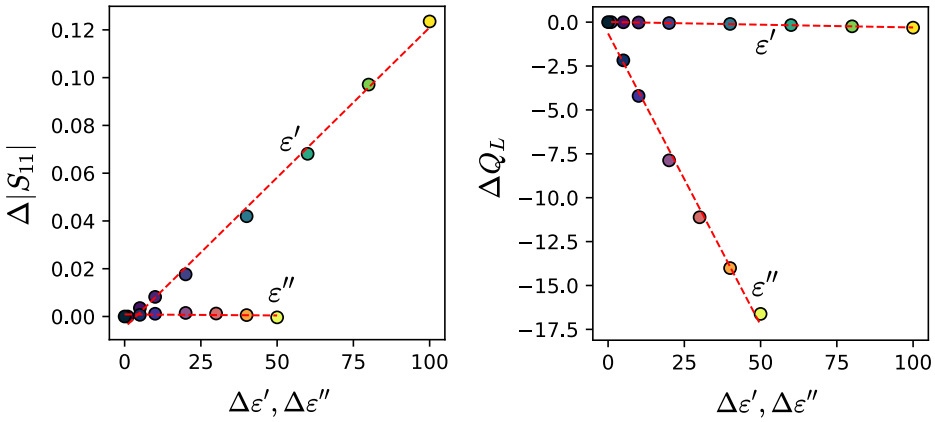

FIGURE 3.14: **Predictive model coefficients:** Through linear regression, I determine the coefficients of the predictive model Eq. 3.18. The x-axis plots the change of the real and imaginary permittivity. On the left, the graph demonstrates the amplitude shift $\Delta|S_{11}|$ at 21.2 GHz corresponding to real and imaginary permittivity changes. The graph on the right delineates the changes in the loaded quality factor ΔQ_L induced by real and imaginary permittivity changes. The values are extracted from the spectra depicted in Fig. 3.13. Graphs reproduced from my publication [1], © 2023 IEEE

$$\begin{bmatrix} \Delta|S_{11}| \\ \Delta Q_L \end{bmatrix} = \begin{bmatrix} K_1 & K_2 \\ K_3 & K_4 \end{bmatrix} \begin{bmatrix} \Delta\varepsilon' \\ \Delta\varepsilon'' \end{bmatrix} \tag{3.18}$$

where, $\Delta|S_{11}| = |S_{11}|_{\text{sample}} - |S_{11}|_{\text{ref}}$, $\Delta Q_L = Q_{L_{\text{sample}}} - Q_{L_{\text{ref}}}$, $\Delta\varepsilon' = \varepsilon'_{\text{sample}} - \varepsilon'_{\text{ref}}$ and $\Delta\varepsilon'' = \varepsilon''_{\text{sample}} - \varepsilon''_{\text{ref}}$ with the subscript (sample) for the sample and the subscribt (ref) for the reference permittivity. The reference real and imaginary permittivity is 1 and 0, respectively. The unknown coefficients K_1, K_2, K_3 and K_4 of the predictive model (Eq. 3.18) can be fitted with a least-squares method. Fig. 3.14 displays the regression fits determining the unknown coefficients. The color coding is the same as the line plots in Fig. 3.13.

The coefficients are introduced into Eq. 3.18

$$\begin{bmatrix} \Delta|S_{11}| \\ \Delta Q_L \end{bmatrix} = \begin{bmatrix} 0.0013 & -9 \cdot 10^{-6} \\ -0.0031 & -0.3322 \end{bmatrix} \begin{bmatrix} \Delta\varepsilon' \\ \Delta\varepsilon'' \end{bmatrix}. \tag{3.19}$$

By comparing the coefficients, it can be seen that the real permittivity influences the $\Delta|S_{11}|$ amplitude at f_f 139 times stronger than the imaginary permittivity. Reversely, the imaginary permittivity influences the quality factor 109 times stronger than the real permittivity. That allows to simplify the predictive model by neglecting the matrix coefficients K_2 and K_3. The complex permittivity of liquids can be determined by inverting Eq. 3.19, which leads to

$$\begin{bmatrix} \Delta\varepsilon' \\ \Delta\varepsilon'' \end{bmatrix} = \begin{bmatrix} 796.05 & 0 \\ 0 & -3.01 \end{bmatrix} \begin{bmatrix} \Delta|S_{11}| \\ \Delta Q_L \end{bmatrix}. \tag{3.20}$$

An inflow single particle detection measurement is typically conducted at a discrete frequency. A lock-in amplifier (LIA) can simultaneously measure the amplitude and phase of a reflected signal. In an ideal scenario, the amplitude and phase at the discrete frequency would only correlate to real or imaginary permittivity. In this case, a continuous flow experiment measuring at a discrete frequency could infer the real and imaginary permittivity. It would allow for a high throughput distinction of particles. As discussed, the $|S_{11}|$ amplitude at 21.3 GHz is sensitive to the real permittivity and not sensitive to the imaginary permittivity. The phase at the same frequency is linearly correlated to the imaginary permittivity (see Fig. 3.13) and non-linearly related to the real permittivity (not shown). Thus, the phase and amplitude responses are unsuitable for a linear predictive model. Nevertheless, the real permittivity dominates the amplitude response, and the imaginary permittivity dominates the phase response; thus, the amplitude and phase measurement should be sufficient to distinguish particles based on their dielectric properties.

3.8.1 Resonance Frequency Shift

Conventional TC sensors utilize a resonance frequency shift to enhance sensitivity. The resonance frequency of a TC has been described in the theory section (Eq. 2.22) as

$$f_0 = \frac{1}{2\pi} \frac{1}{\sqrt{CL}}. \tag{3.21}$$

with C and L the total capacitance and inductance of the resonant circuit, respectively. The sensing capacitance is part of the total capacitance of the resonant system. A change in the sensing capacitance alters the capacitive loading of the resonant circuit and induces a resonance peak shift. For a small capacitance change ($\Delta C \ll C$), the frequency shift can be approximated by a first-order Taylor expansion to

$$\Delta f_0 \propto \frac{\Delta C}{C}. \tag{3.22}$$

The shift is linearly related to ΔC divided by the total capacitance C. That relation holds for a conventional TC sensor and the coupling-based configuration. As a general rule, the total capacitance should be minimized to increase sensitivity due to the frequency shift.

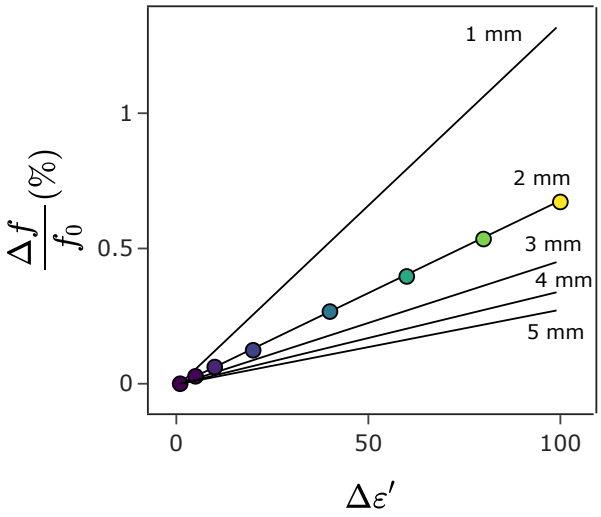

FIGURE 3.15: **Sensitivity of the frequency shift:** The colored dots plot the resonance frequencies obtained from FEM simulation displayed in Fig. 3.13a. The black lines display the theoretical values derived from numeric solutions of Eq. 2.27 for a resonator length between 1 mm - 5 mm. The numeric solutions are summarized in Tab. 3.2.

In the following, I compare the simulated peak shift with theory. Solving the transient Eq. 2.27 can determine the theoretical resonance frequency Eq. 2.27. The solution is obtained numerically with a Python script for CPW length between 1 - 5 mm. The equation is solved using the coupling capacitance values determined in section 3.2. The coupling capacitance is assumed as the sum of the parasitic capacitance with $C_p = 2.02$ fF and the sensing capacitance with $C_s = \varepsilon' \varepsilon_0 1$ µm.

Fig. 3.15 displays the relative shift of the resonance frequency $\Delta f / f_0$ plotted against a $\Delta\varepsilon'$ change. In the field of microwave complex permittivity measurements in liquids, that relation is an often used metric to define the sensitivity of a sensor. The real permittivity change is given by the sample permittivity subtracted by the permittivity of air $\Delta\varepsilon' = \varepsilon'_{\text{sample}} - \varepsilon'_{\text{air}}$.

The corresponding resonance frequency shift is calculated by the difference between an unloaded resonator (i.e., the permittivity of air) and a loaded sensor with a real permittivity of a sample $\Delta f = f_{\text{unloaded}} - f_{\text{sample}}$. The color-coded dots display simulated values from Fig. 3.13a. The black lines plot the numeric solutions of Eq. 2.27 for a CPW length between 1 - 5 mm. As discussed, a slight change in the sensing capacitance is linearly related to the peak shift $\Delta f \propto \Delta C$. The numeric solution for a resonator with a length of $l = 2$ mm fits the simulation results. The numeric solutions are summarized in Tab. 3.2.

The black lines show that reducing the resonator length increases the relative frequency shift. The CPW length of a $\lambda/4$-resonator mainly contributes to the total capacitance C. Reducing the length l changes the $\Delta C/C$ ratio, leading to a stronger resonance peak shift. The cCPW sensor utilizes a $\lambda/4$-resonator instead of a $\lambda/2$-resonator. Such a configuration cuts the electrical length by half, reducing the total capacitance. Thus, the coupling-based $\lambda/4$-resonator improves the overall sensitivity by introducing coupling and increasing the resonance frequency shift.

However, the sensitivity for detecting individual particles does not only rely on a

maximal response of the sensor to the permittivity. Another important factor is the permittivity contrast between the particle and the suspending medium. That permittivity contrast is frequency-dependent. For example, the real permittivity contrast between a cultured medium and a Chinese-Hamster-Ovary cell reduces from approximately 6 to 1 for a frequency increase from 10 GHz to 40 GHz [82]. At 20 GHz, the real permittivity contrast is approximately three, and the imaginary permittivity contrast is maximal with 5. Other studies of protein suspensions also demonstrated a similar trend of the real permittivity contrast from low to high frequencies and a maximal imaginary permittivity contrast at around 20 GHz [20]. A resonator at 20 GHz is a good trade-off between an increased relative frequency shift for high frequencies and reducing the permittivity contrast at frequencies above 20 GHz.

TABLE 3.2: **Sensitivity for varying resonator length:** Numeric solutions of the Eq. 2.27 for the resonance frequency f_0. The solutions are obtained for resonator length l between 1 mm and 5 mm and a real permittivity of $\varepsilon'_{\text{sample}} = 100$. These values are also illustrated in Fig. 3.15.

resonator length l (mm)	resonance frequency f_0 (GHz)	relative frequency shift $\frac{\Delta f}{f_0}$(%) for $\varepsilon'_{\text{sample}} = 100$
1	47.58	1.32
2	24.16	0.67
3	16.19	0.45
4	12.18	0.34
5	9.77	0.27

3.8.2 Sensitivity

The novel cCPW sensor improves sensitivity in two ways: by increasing the conventional frequency shift and by introducing an additional coupling-based component. Both contributions have been discussed in section 3.8.1 & 3.4.1. For the FEM simulation, the relative contributions of the coupling-based and frequency shift-based response can be isolated by assuming a constant input coupling (constant peak height) and no frequency shift, respectively. In this case, the peak shift contributes 45% and the coupling 55% to the total signal change, which means that the coupling approach significantly improves the overall sensitivity. These relative contributions of coupling-induced and peak shift-induced $\Delta|S_{11}|$ change strongly depend on the coupling parameters (e.g., input coupling, resonance frequency, quality factor).

Several sensitivity metrics have already been established in the field of microwave complex permittivity liquid sensors. Mostly, a permittivity normalized version of the relative resonance frequency shift ($\Delta f / f_0 \Delta\varepsilon$) is used as a sensitivity metric [83]. In the field of microwave particle sensing, comparable metrics have not yet been established. In this field, the sensor mostly operates in a continuous flow experiment at a discrete frequency. An exception is the phase lock loop tracking of the resonance frequency [72, 84]. The S-parameter measures the intensity and phase response to permittivity variations. It is the main observable used for microwave particle sensing. Therefore, the S-parameter should be part of the figure of merit (FOM), which defines the performance of a nanoparticle sensor. Moreover, in particle sensing, the

TABLE 3.3: **Sensor performance comparison:** A side-by-side assessment of our sensor's specifications with those reported in the literature. Table reproduced from my publication [1], © 2023 IEEE

sensor	f_m (GHz)	ΔS [a]	$\Delta\varepsilon$	V_{eff} (nl) [b]	FOM (nl^{-1})
[25]	0.17	0.11	79	0.1	0.014
[68]	18	0.035	10 [c]	0.29	0.012
[70]	2.2	0.019	0.6	1.6	0.020
[63]	0.18	0.04	79	0.0005	1.1
[24] (previous work)	1.1	0.055	79	$8 \cdot 10^{-6}$	87
this work	21.3	0.0013	1	$1 \cdot 10^{-6}$	1300

[a] The ΔS value can relate to the $|S_{11}|$- or $|S_{21}|$- parameter. The values are estimated from the published graphs.
[b] The effective volume is calculated from the published channel dimensions. In the case of CPW sensor configuration, the width of the sensing volume is estimated as the width of the signal line plus both signal-to-ground distances.
[c] The value corresponds to a change in ε'' as the sensor is only sensitive to the imaginary permittivity.

size of the sensing volume is particularly small, and thus, the performance needs to be evaluated for a given size of the effective sensing volume. Typically, a smaller sensing volume corresponds to a reduced S-parameter response. I propose a FOM defined as the S-parameter response normalized by the permittivity and effective sensing volume V_{eff}

$$\text{FOM} = \frac{\Delta|S|}{\Delta\epsilon V_{eff}}. \tag{3.23}$$

The effective sensing volume V_{eff} is the liquid volume with high electric fields that mainly constitutes the sensing capacitance.

The amplitude response for a real permittivity change (i.e., $\Delta|S_{11}|/\Delta\varepsilon'$) was already calculated by the predictive model with the parameter K_1. The optimized sensor has a FOM of 1300 nl^{-1} for a 1 μm^3 sensing volume. Table 3.3 compares the proposed sensor with the literature. Our previous TC-based sensor detected 500 nm particles with an FOM of 87. In contrast, the novel sensor has a FOM of 1300. Due to the high FOM, I expect to detect particles well below 100 nm. The increased sensitivity at small sensing volumes paves the way for ultra-fast sensing of individual virions or proteins based on their dielectric properties.

Chapter 4

Fabrication

The initial cell and particle detection sensor, upon which my sensor is built, was originally outlined in Paul Gwozdz's thesis [85]. A critical part of this sensor is the electrode-channel interface. In Gwozdz's design, the channel was a microscopic pore embedded in a glass substrate manufactured with an ArF-based excimer laser. In contrast, our new chip design transitions from a microscopic pore to a planar fluidic channel. This shift allows both the electrical and fluidic components to be fabricated entirely through lithographic techniques. This lithographic approach offers multiple benefits. First, lithography is a well-established method in both the semiconductor industry and academic research, supported by an extensive body of literature. Furthermore, lithographic processes can achieve exceptional resolution. For example, electron beam lithography can manufacture electrical and fluidic structures with a resolution of < 20 nm. Precise alignment between the fluidic channel and the sensing electrodes, which posed challenges in the original laser-based fabrication method, can now be attained with sub-20 nm accuracy using electron beam lithography.

Although the final chip presented in this thesis was not manufactured by electron beam lithography, seamless integration with the current chip is straightforward. In the future, this enables the incorporation of nano-electrodes for sensing proteins or single DNA.

Additionally, a planar configuration enables advanced fluidic channel and electrode designs, e.g., several channels for hydrodynamic focusing, several electrodes for sequential sensing, or funnel structures for controlled DNA unfolding. Finally, a planar configuration allows simultaneous electrical sensing and optical monitoring with a microscope. Details on integrating this chip with fluorescence microscopy, high-frequency circuits, and a specialized fluidic chip holder will be discussed in the following chapter 5.1.

4.1 Sensor Manufacturing

The chip design and fabrication process were carefully selected to enable wafer-level manufacturing. As displayed in the appendix Fig. A.2, a 2-inch wafer accommodates 16 individual chips. This wafer-level approach provides the flexibility to incorporate multiple electrode-channel interface designs on the same wafer.

Each chip features electrodes spaced at varying distances, tailored for different sensing applications. The electrode distances are set at 8 µm for cell sensing and at 2 µm and 1 µm, corresponding to sensing volume channel widths of 12 µm, 4 µm, and

2 µm, respectively. However, it should be noted that the chips with 1 µm spaced electrodes exhibited defects, rendering them unsuitable for measurements.

An additional design was introduced to address the challenge of clogging experienced with 1.75 µm polystyrene beads in a 4 µm channel width. This design pairs a 12 µm channel width with an electrode distance of 2 µm.

The layout of an individual chip is illustrated in Fig. A.3. The chip dimensions have been optimized to a compact size of 12 mm x 8 mm, only restricted by the spacing of the fluidic inlets.

4.1.1 Metal Structures

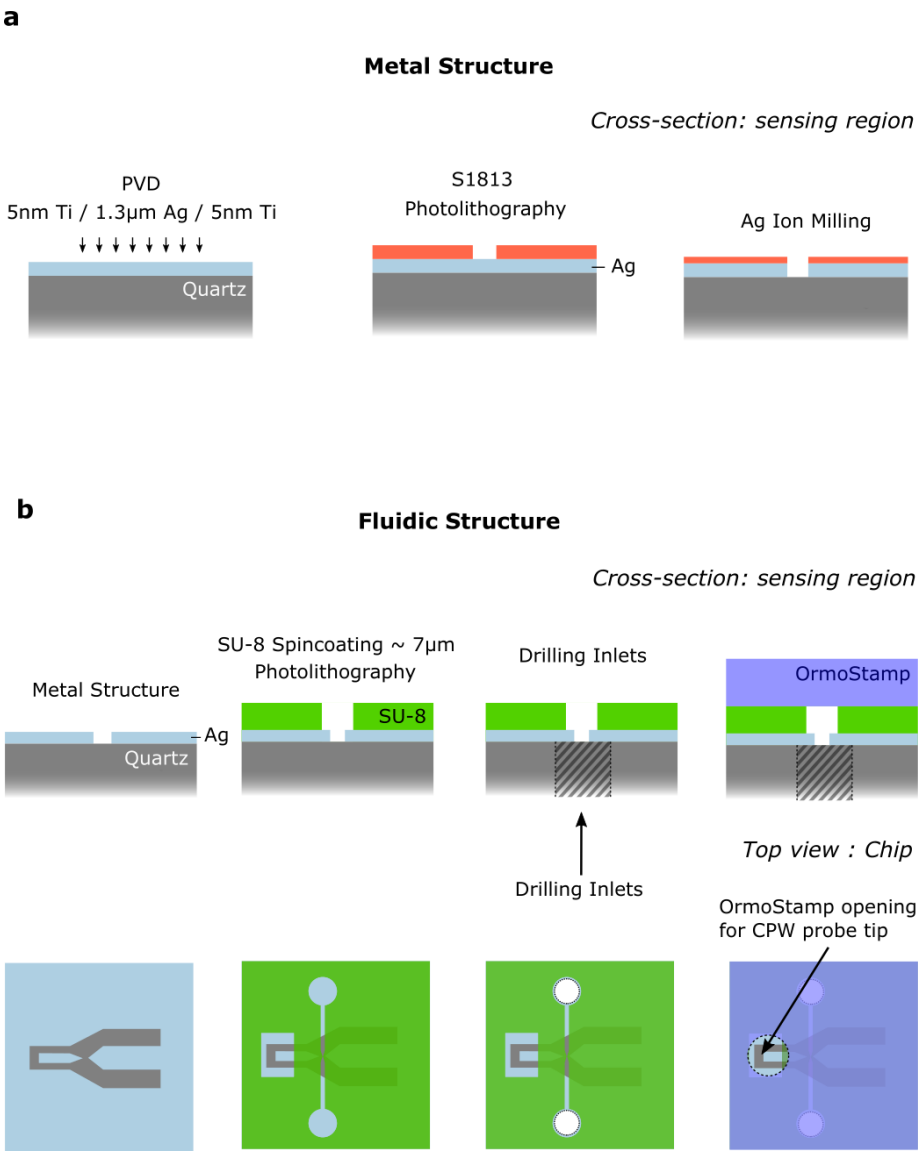

FIGURE 4.1: **Manufacturing process of metal and fluidic structures:** **a**, Cross-sectional view of the sensing region (tip region) detailing the metal structure fabrication steps. **b**, Cross-sectional and top views illustrating the fluidic channel fabrication. Illustration reproduced from my publication [1], © 2023 IEEE

Fig. 4.1a displays the manufacturing steps of the metal structures. A 500 µm thick quartz wafer is used as a substrate. Quartz glass has a dielectric constant of $\epsilon = 3.86$ and an exceptionally small loss tangent of $\delta = 0.0002$ [64, 41, 42]. The low dielectric losses enable a high quality factor of the resonator. Moreover, quartz glass is transparent, allowing the etch processes to be monitored optically.

Step 1: Metal Layer Deposition

The first step in the metal structure fabrication is physical vapor deposition (PVD) of 5 nm Ti adhesive layer, followed by the main ≈ 1 µm Ag layer and encapsulated with a 5 nm Ti layer (Fig. 4.1a) to prevent oxidation. The resistance of the metal layer is a major source of loss strongly influencing the quality factor of the resonator. Bulk silver has an exceptionally high conductivity of $\sigma_{\mathrm{Ag}} = 6.21 \cdot 10^7\ \mathrm{S\,m^{-1}}$, which is 40% higher compared to gold and more cost-effective. The conductivity of the manufactured metal layer is around $\sigma_m = 5.65 \cdot 10^7\ \mathrm{S\,m^{-1}}$. It was determined for each wafer by the van der Pauw theorem for isotropic thin films of arbitrary shape [86]. At that conductivity and 20 GHz, the skin depth is 482 nm. The thickness of 1 µm already represents 88% of the bulk conductivity. Only marginal increases in conductivity can be expected from any further thickening.

Step 2: Photoresist and Etching

In the second step, a positive photoresist (S1813, *Microposit*) is spin-coated at 1000 rpm for 1 min for a layer thickness of 1.3 µm. The resist is backed at 115°C for 1 min and exposed to UV light for 13 s with a power density of 13 $\mathrm{mW/cm^2}$. Further, the resist is developed in MF 319 for 1 min. The resulting structures are transferred into the underlying metal layer by physical etching with argon-ions. A custom-made ion etching machine is used. The etch rate of silver is more than twice as fast as the photoresist; thus, the resist works as an etch mask. The etching process is finished once the etching window (see Fig. A.2) becomes transparent. Alternatively, a lift-off technique could have been used. However, lifting off metal layers becomes increasingly challenging with the metal layer thickness, and the physical etching creates vertical metal walls, which are beneficial for a homogeneous electric field distribution between the electrode trips. After etching, the leftover S1813 resist is cleaned with acetone and rinsed with water. In some cases of ion etching, the substrate was heated to the point where the S1813 resist was crosslinked beyond the acetone's removal capacity. In that case, the wafer was cleaned by the Microposit Remover 1165 at 75°C. The final metal structure consists of the CPW resonator, mask aligner marks, chip label, wafer saw cutting and drilling marks, and the macroscopic wafer alignment marks (see appendix Fig. A.2 & A.3). The quality of the final structures is assessed by determining the thickness of the metal layer with a profilometer (Bruker Dektak, XT) and by characterization of the resonator's scattering parameters with a vector network analyzer (VNA) (N5222A, *Keysight / Agilent*).

Fig. 4.2 displays a scanning electron microscope (SEM) image of exemplary electrode tips manufactured with physical ion etching. The tips are separated by 2.5 µm, close to the nominal value of 2 µm. The tip geometry exhibits a slight distortion as it is supposed to be two 2 µm wide parallel planes. The distortion results from the resolution limit of our current photo-lithographic system, causing variability in final tip structures across samples. The edges are close to vertical, which is difficult to achieve by conventional lift-off techniques and advantageous for particle sensing.

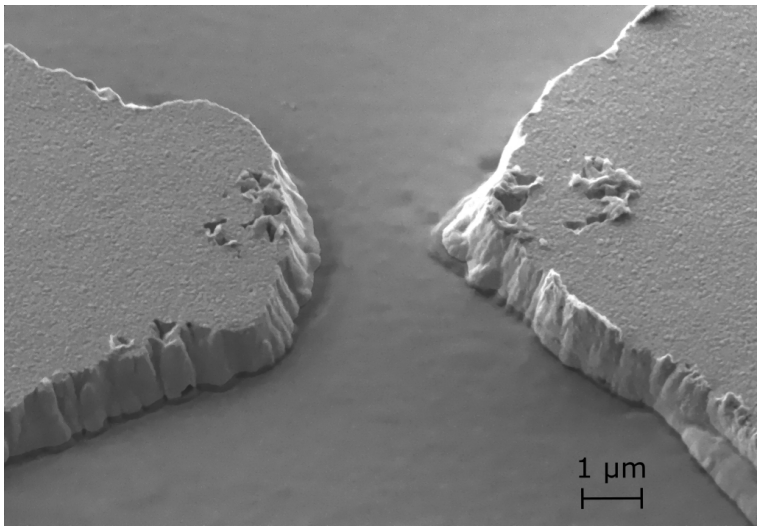

FIGURE 4.2: **Electrode tip:** SEM image of electrode tips, taken at a 37° tilt, fabricated using physical argon ion etching. The tips are spaced 2.5 µm apart, showcasing vertical walls.

4.1.2 Fluidic Structures

Fig. 4.1b displays the manufacturing steps for the fluidic channel in the cross-section and top view, respectively.

Step 1: Fluidic Channel

SU-8 GM1060 negative photoresist is used for the fluidic channels. The resist is spin-coated for 1 min at 4000 rpms for a 7 µm thickness. Before exposure, the resist is prebaked for 2 min at 65°C and then for 5 min at 95°C. The spin-coating of thick photoresists creates an edge/corner bead that prevents good contact between the Cr mask and the wafer in the mask aligner. The bead is gently removed with a cotton bud soaked with acetone. Alignment marks enable the alignment of the fluidic structures to the electrodes with a precision of approximately 1 µm. The exposure is performed with the i-line for 15 s. After exposure, the resist is post-baked at 95°C for 5 min, which selectively crosslinks the exposed area of the film. The final development step is performed with PGMEA for 1 min, followed by a rinse with isopropanol and drying with nitrogen gas flow. The SU-8 layer is characterized by determining its thickness with a profilometer and measuring the resonator's scattering parameters with a VNA.

Step 2: Drilling and Dicing

The wafer is spin-coated with old S1813 resist as a protection layer, and it is cut with a wafer saw along the wafer saw cutting marks (see appendix Fig. A.3). Further, 1 mm diameter inlets are drilled with a 1 mm diamond drill bit (see appendix Fig. A.3). Subsequently, the wafer is cleaned with acetone, followed by an isopropanol rinse, and dried with nitrogen gas flow. Fig. 4.3 illustrates a 2-inch wafer at that point of fabrication.

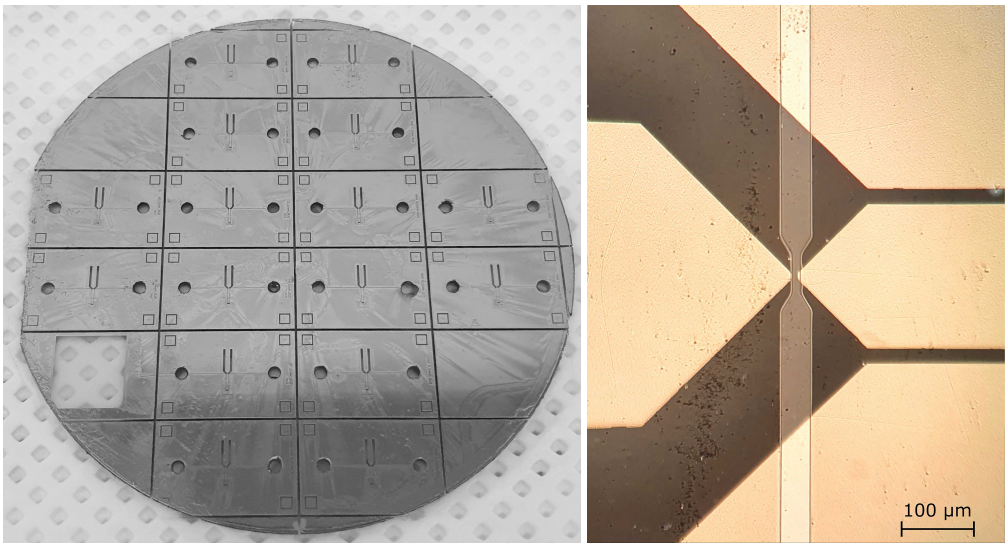

FIGURE 4.3: **Wafer and sensing region:** On the left, the wafer post-drilling and dicing. The detailed wafer layout and individual chip layout are depicted in Fig. A.2 and Fig. A.3 in the appendix. On the right, the tip region of the final chip is sealed with OrmoStamp cover foil. This chip features an 8 µm tip-to-tip distance and a 12 µm wide sensing region channel. Parts of that image reproduced from my publication [1], © 2023 IEEE

Step 3: Sealing

In the final step, the individual chips are sealed with OrmoStamp foil. OrmoStamp is highly transparent for UV and visible light and has good adhesion to SU-8. The foil is fabricated with the aid of two microscope slides. One slide is placed on the hotplate at 60°C. A small drop of OrmoStamp resist is placed on the center of the slide and sandwiched with a second slide. The resist spreads between the slides. Once interference patterns occur, the glass slides are quickly removed from the hotplate, and they are cured by exposure to UV light for 100 s. A flexible OrmoStamp foil is peeled off the microscope slides. The foil is around 15 µm thick. However, the process is poorly controlled, which leads to significant variations in the foil's thickness. A hole is punctured into the foil to create an opening for the CPW probe tips. The foil and the chip are exposed to UV ozone to activate the surface and improve the bonding. Quickly after exposure, the foil is placed on top of the chip. The bonding between the SU-8 and Ormostamp is further improved by placing the chip at 60°C on a hotplate for 5 min. The chip sealing withstands a pressure of 200 - 400 mbar.

Manufacturing Characterized with S-Parameters

Fig. 4.4 displays the scattering parameter characterization during each fabrication step. The black trace shows the bare silver structure. The resonator had an internal quality factor of 107. This serves as our reference point for subsequent changes.

After adding the SU-8 layer (green), which incorporates the fluidic structures, the quality factor reduces to 81. The effective permittivity of the CPW increases, which reduces resonance frequency by 290 MHz (described in section 2.2.2). Moreover, the baseline likely drops due to the SU-8 coating of the CPW feedline, resulting in higher broadband attenuation.

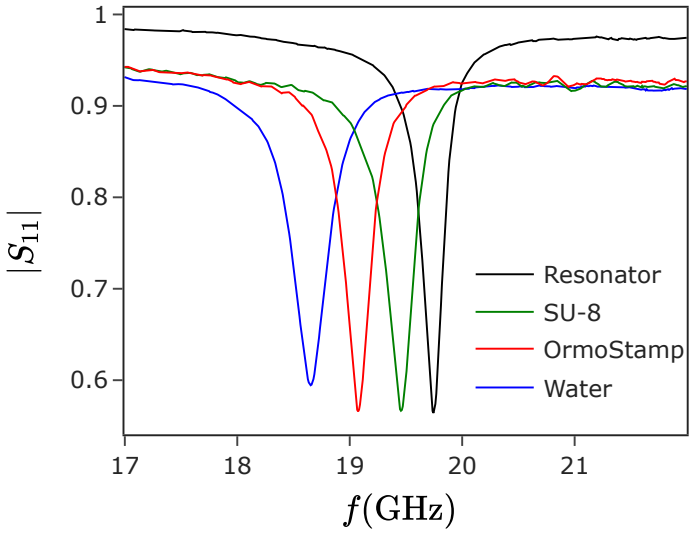

FIGURE 4.4: **Sensor response to manufacturing steps and water loading**: The influence of the fluidic material system and water loading on the resonance frequency and quality of the resonator. The $|S_{11}|$-parameter is measured during various manufacturing steps of the sensor, starting with the bare silver resonator shown in black. The addition of the SU-8 layer, which forms the microfluidic structures, is represented in green. The sealing of the chip with the OrmoStamp lid is illustrated in red. Lastly, the chip is loaded with water, as depicted in blue. Each subsequent step causes a shift in the resonance peak towards lower frequencies.

The red trace corresponds to the sealing with OrmoStamp. The incorporation of OrmoStamp further raises the effective permittivity of the CPW, causing the resonance frequency to decrease by 385 MHz. The internal quality factor is 84, which is higher by three than the sensor without OrmoStamp. The increase in quality factor is surprising, but it can be concluded that Ormostamp has good microwave properties with little losses.

Finally, water is introduced into the channel, represented by the blue trace. The resonance frequency reduces by 424 MHz due to capacitive loading of the resonator. The internal quality factor reduces to 62. Such a reduction in the Q-factor can be explained by the introduction of losses by water due to its high imaginary permittivity of 35 at 20 GHz [78].

In the future, the fluidic structures are intended to be fabricated without SU-8. Also, the sensing volume is intended to be significantly smaller. Together, these two optimizations should retain the high Q-factor of the initial bare resonator.

4.2 Fabrication Outlook

The current fabrication approach has several drawbacks. Firstly, the SU-8 resist layer degrades the resonator's quality factor, reducing the sensor's sensitivity. Furthermore, a 7 µm thick SU-8 layer was used for the microfluidic channel. The height of the microfluidic channel is seven times higher than the thickness of the electrodes, which creates a dead volume above the sensing volume. In such a configuration, the translocating particles are not focused between the electrodes, and the sensor's

response strongly depends on the particle's position in the channel. A thinner SU-8 layer could not be applied, as for thin layers, the metal structures created shadow effects during spin-coating, which made the SU-8 layer not flat enough for sealing with OrmoStamp foil.

Moreover, SU-8 is a photoresist with an inherent resolution limit set by optical lithography. In our case, the resolution was around 1 µm. Such a resolution is insufficient as, in the future, the fluidics should be capable of guiding single DNA to the sensing volume, which requires nanoscopic features. Consequently, alternative manufacturing protocols for nanofluidic channels need to be explored.

Electron Beam Lithography

In the following, I showcase that the fabrication of nanoscopic sensing electrodes embedded into a fluidic channel is feasible by electron beam lithography (EBL). The fabrication protocol is based on two EBL processes followed by reactive ion etching (RIE) steps, physical vapor deposition, and a lift-off process. The fabrication steps are schematized in Fig. 4.5a. A silicon substrate is coated with a 90 nm thick resist layer of Polymethyl methacrylate (PMMA 950-A4 polymer, *MicroChem. Corp.*) with 6000 rpm for 1 min and baked at 160°C for 2 min. In the first EBL step, the electrodes and alignment structures are patterned using electron beam lithography (EBL) (Voyager, Raith GmbH). After lithography, a cold development with MIBK:IPA at the ratio of 3:1 at -14 °C is performed to enhance the resolution [87]. This process is stopped using isopropanol. The structures are then etched into silicon for 110 seconds to the depth of 110 nm using RIE (ICP-RIE SI 500, *SENTECH Instruments GmbH*) with a gas mixture of 10 sccm SF_6 and 22 sccm C_4F_8 at 150 W ICP power, 10 W radio frequency power, 0.5 Pa pressure, at 0°C. The sample is then transferred into a PVD machine for evaporation in a high vacuum. A 2 nm Cr layer is the adhesion layer, and then 110 nm gold is evaporated. After the lift-off process in an ultrasonic bath, the electrode tips fabrication process is finished. The second EBL process is aligning

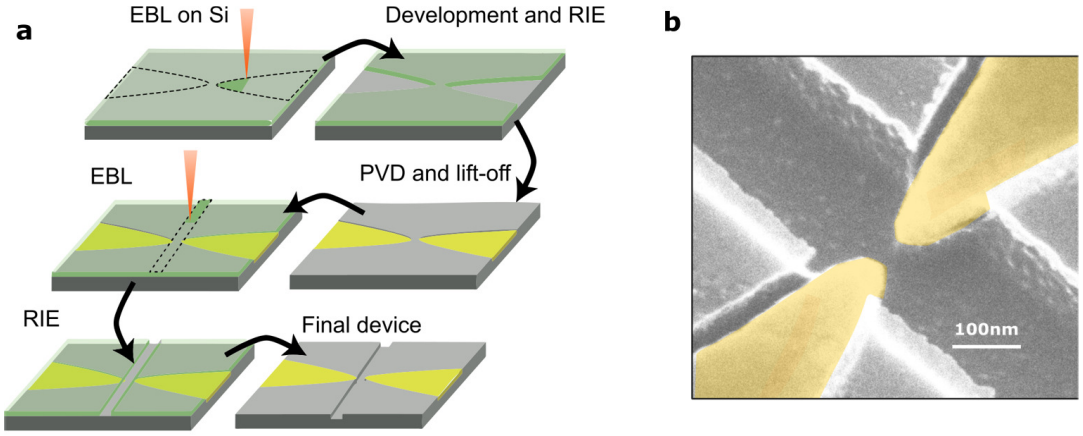

FIGURE 4.5: **Fabrication nanoscopic sensing volume: a**, Fabrication steps for nano-electrodes integrated into a nanochannel. **b**, SEM image of electrode tips separated by 30 nm and integrated into a 200 nm wide channel, highlighting the high-resolution capabilities of e-beam lithography.

the nanochannel to the tips of electrodes. The alignment is performed on alignment marks, enabling an alignment precision below 20 nm. This ensures that the electrodes can be positioned inside a fluidic channel. The nanochannel is supposed to

be located between the electrode gap. The pre-processing of spin coating and heating up remains the same as for the electrodes. After lithography of the nanochannel and cold development, the channel is etched using RIE for 70 seconds to achieve a depth of 70 nm. Then, the rest of the resist is dissolved in acetone, rinsed with isopropanol, and dried with nitrogen.

Fig. 4.5b displays the high-resolution electrode-channel interface. The electrodes are separated by 30 nm (significantly smaller than the potentially needed 75 nm) and embedded into a fluidic channel with a width of 200 nm.

While this fabrication protocol has demonstrated a tiny sensing region, it has challenges. A primary concern is the sealing of the fluidic channels. Simply placing a flat layer of Ormostamp or PDMS on top of the channel for sealing is not feasible because the resonator structures are not flush with the chip; they protrude by approximately a micrometer from the fluidic channel. Additionally, achieving precise control over the etching depth and the metal deposition thickness for the electrodes is challenging. The electrodes must be level with the substrate to ensure an adequate seal at the electrode-channel interface.

These sealing challenges motivated me to investigate sacrificial layer fluidics (SLF) for integrating a small fluidic channel between electrodes.

Sacrificial Layer Fluidics

We suggest a fabrication method for the next chip iteration based on removing a sacrificial layer. Such a fabrication method is called sacrificial layer fluidics (SLF). It has the potential of wafer-scale fabrication, with nanometer channel resolution and reliable fluidic sealing [88, 89]. For the interested reader, I recommend an older review from 2006 by Peeni et al., which summarizes fabrication methods with a particular emphasis on the sacrificial materials [90]. In the case of our chip, SLF allows to confine the channel in-between the electrodes without a dead volume above the sensing volume [91, 92]. Moreover, SLF approaches are possible with silicon oxide or silicon nitride capping layers which have excellent dielectric properties for microwave electric circuits [93, 91, 94, 95, 96, 97, 98].

The sacrificial layer is commonly removed by wet chemical etching with a solvent. In confined spaces, such a process is diffusion-limited. During etching, at the solvent-solid interface, the solvent is saturated with solute molecules of the sacrificial layer. These molecules diffuse away from the interface through the solvent defined by the diffusion constant D. The time-depended position of the dissolution front can be described with [99]

$$\delta(t) = \sqrt{\frac{2D(C_s - C_b)}{\rho}t}, \tag{4.1}$$

with C_s the saturation concentration of the solute in the solvent at the solvent-solid interface. C_b is the concentration of the solute in the bulk solvent outside of the channel, and ρ is the density of the solute in the sacrificial layer. The dissolution front is proportional to the square root of time ($\delta \propto t^{-\frac{1}{2}}$) [99], which makes the removal of long channels time-consuming. An alternative approach is based on thermally decomposable polymers. These polymers decompose into volatile gases, which diffuse through the encapsulation material like silicon oxide or silicon nitride. That diffusion process fundamentally differs from diffusion through the channel because the

diffusion length l does not change. Such a process can be described by [100]:

$$\delta(t) = \frac{2D(C_s - C_b)}{\rho l} t, \tag{4.2}$$

with l the encapsulation layer thickness and δ the removed sacrifical layer thickness. The dissolution front is linearly related to time ($\delta \propto t$). This leads to a sacrificial layer removal time unrelated to the channel design. The most established sacrificial material for thermal decomposition is polynorbornene [97, 98, 96, 91, 94, 101, 92, 102]. Unfortunately, that resist is commercially not available anymore. Alternatively, we propose polycarbonate (PC) as the sacrificial layer. PC is thermally decomposable and was already applied to manufacturing SLF ([100, 103, 104]). Also, it can be used as a negative-tone resist for electron-beam lithography [105]. To my knowledge, these two qualities of PC were never combined to manufacture nanoscopic channels.

4.2.1 Polycarbonate as a Negative-tone Resist for Electron-Beam Lithography

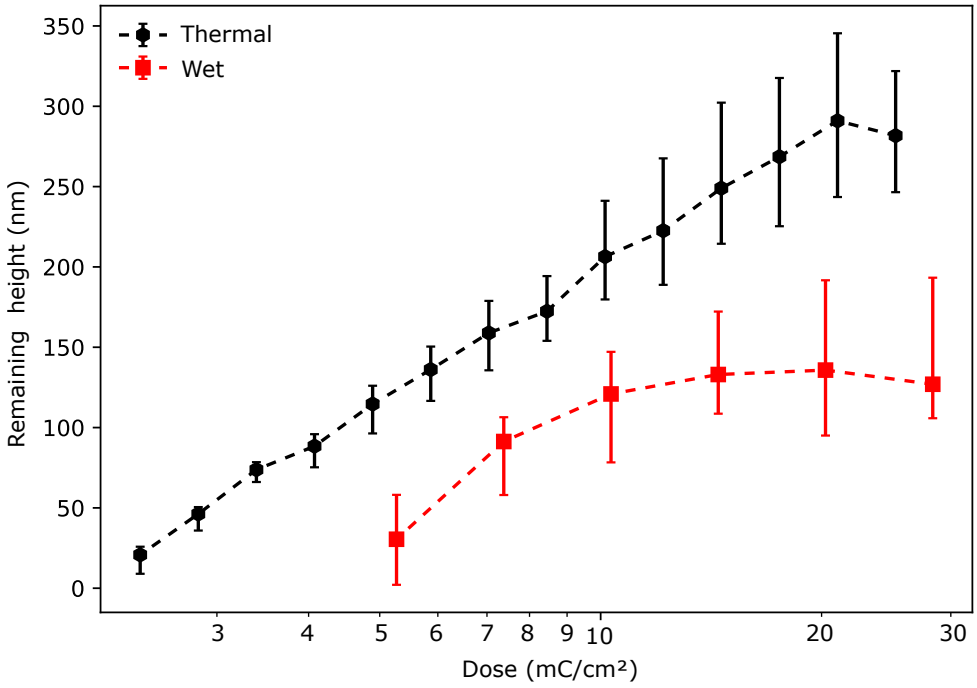

FIGURE 4.6: **Electron-beam lithography contrast curves for polycarbonate resist:** A polycarbonate layer was spin-coated on a silicon wafer, resulting in a thickness of 1.1 µm. Red and blue dotted lines represent the electron beam dose curves for wet and thermal development, respectively. Thermal development involved a 3-minute treatment on a 300°C hotplate, while the wet development spanned 120 seconds using cyclohexanone at ambient temperature. The height-to-dose relationship is derived from a line scan across the dose structures shown in Fig. 4.7.

Allresist GmbH provided an experimental resist sample of polycarbonate (PC) dissolved in N-Methyl-2-pyrrolidone (NMP). This solution was spin-coated onto a silicon substrate to achieve a thickness of 1.1 µm. Subsequently, the coated substrate

underwent a soft bake at 170°C for 1 minute. Electron beam lithography was employed to inscribe dose patterns, utilizing an acceleration voltage of 50 kV.

Upon exposure, a fraction of the PC undergoes crosslinking, reducing its solubility to a developer and its susceptibility to decomposition at elevated temperatures. This characteristic facilitates either wet chemical or thermal development of the resist. NMP and cyclohexanone were evaluated as potential wet developers. Cyclohexanone yielded the most favorable outcomes. Notably, a fraction of the resist decomposes during e-beam exposure, even before the development phase.

Another part of the exposed PC crosslinks and becomes more resistant to solvents and less decomposable at higher temperatures. That allows for a wet chemical or thermal development of the resist. NMP and cyclohexanone worked as wet developers. The best results were obtained with cyclohexanone. During exposure, depending on the dose, a fraction of the resist already decomposes before development. Fig. 4.6 displays contrast curves for a wet and thermally development in a logarithmic scale. For wet development (red), the resist was dipped into cyclohexanone for 120 s, followed by a water bath to stop the development. The thermal development (black) was performed on a hotplate for 3 min at 300°C. The dose structures were 20 µm wide stripes. The height was measured with a profilometer (DektakXT stylus, *Bruker*) by averaging over an area of 5 µm left and right from the highest position of the structure. The error bars indicate the highest and lowest values in that area. The significant error comes from a tip-like feature in the center of the structures. A line scan over the dose structures with the tip-like features is displayed in Fig. 4.7. The origin of that undesirable feature is not yet known. For smaller structures, it disappears, and for wet development, it changes to a sharp spike. At a dose of 2000 µC/cm^2, the thermally developed structures appear, and the wet developed structures appear at 5000 µC/cm^2. Both development methods achieve the maximal height around 20 mC/cm^2. For the thermal development, the maximal thickness reduces to 1/4 of the original height of the undeveloped layer, and the wet development reduces to 1/8 of the original layer thickness. The height-dose dependence enables gray-scale lithography for 3D structures, e.g., funnel-like structures that connect microchannels with nanochannels. The lateral resolution was better for the wet development than the thermal development. The smallest structure was 250 nm wide and developed with NMP. The resolution of the cyclohexanone-developed structures appeared to be comparable or superior. The resolution limit has yet to be determined with SEM.

4.2.2 Polycarbonate Thermal Decomposition

To demonstrate the thermal decomposition of PC, we heat the thermally developed dose structures without a capping layer. The previous section described the dose-height relation (summarized in Fig. 4.6). The thermal development was performed on a hotplate at 300°C for 3 min. After thermal development, the sample was placed on a hotplate with increasing temperature for 5 - 15 min. The temperature was increased from 310°C to 550°C. Fig. 4.7 displays the height profile over the dose structures measured after each heating step. After the last heating step of 15 min at 550°C, the structures are no longer visible, and we assume that all the PC is thermally decomposed.

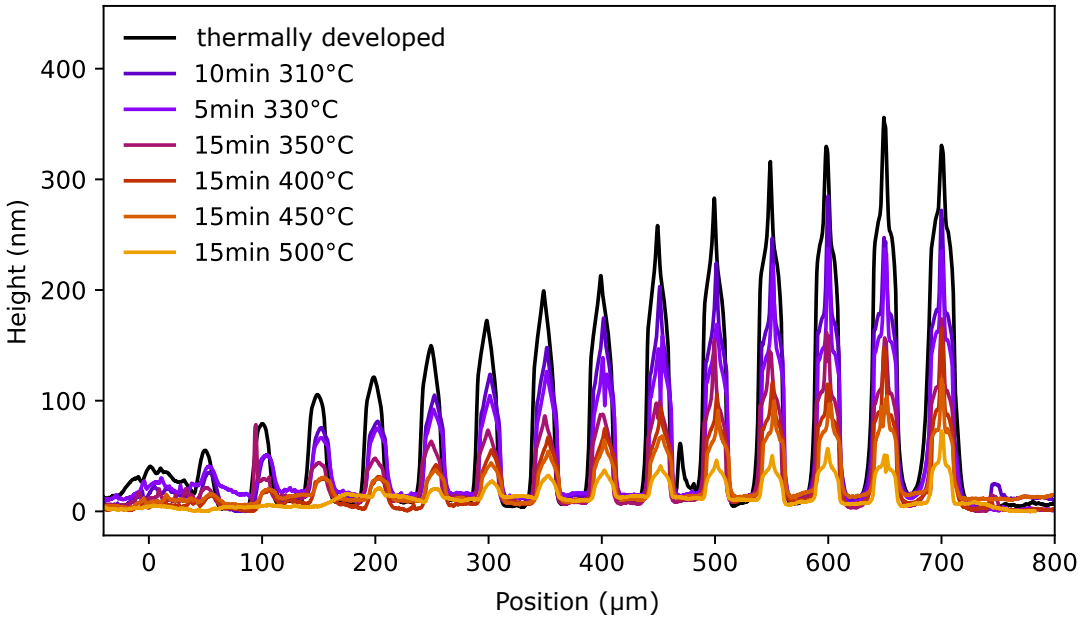

FIGURE 4.7: **Thermal decomposition of polycarbonate electron-beam dose structures:** A sample with dose structures, developed thermally on a 300°C hotplate for 3 minutes, undergoes subsequent heating from 310°C to 550°C. After each heating interval, a height profile of the dose structures is captured. After the final 15-minute exposure at 550°C, all the resist had decomposed, and no line profile could be recorded.

4.2.3 Sacrificial Layer Channel

As a proof of concept, sacrificial layer fluidic channels were manufactured, and the flow was tested. Polycarbonate resist was spin-coated at a thickness of 1.1 µm and soft baked at 170°C for 1 min. Several sets of four parallel channels separated by 20 µm were written with electron beam lithography at 17 mC/cm^2. Each set had channels with a width of 5 µm, 1 µm, 500 nm, and 200 nm. After wet chemical development with cyclohexanone for 120 s, the sample was placed into a water bath and dried with a nitrogen stream. Due to the low operating temperature, sputter deposition was used to deposit an 800 nm capping layer of SiO_2 on top of the channels. The sacrificial layer removal was performed in a furnace with a nitrogen stream. The temperature was increased fast to 300°C, followed by a slow ramp to 600°C with a ramp rate of 3°C/minute. The final temperature is held for 1 hour, followed by the same cooling rate of 3°C/minute to 300°C. Faster ramp rates lead to cracking of the encapsulation layers. At temperatures above 550°C, the sacrificial layer decomposes, diffuses through the capping layer, and leaves hollow channels. The flow through the channels was tested with isopropanol. The channels were opened by scratching with a diamond cutter at the end and beginning of the channel. A droplet of isopropanol was placed on one opening. The capillary forces suck the liquid into the hollow channels and initiate flow. The flow was monitored with a microscope. Fig. 4.8 displays a time series of three parallel 1 µm wide channels with the flow of isopropanol. Similar results were observable for the 5 µm wide channels. For the 500 nm and 200 nm channels, the resolution of the microscope or the contrast was insufficient to observe the flow. In the future, the experiment should be repeated with a fluorescent dye, and a focused ion beam-prepared cross-section of the smaller channels should be imaged with an SEM to confirm that the channels

are hollow.

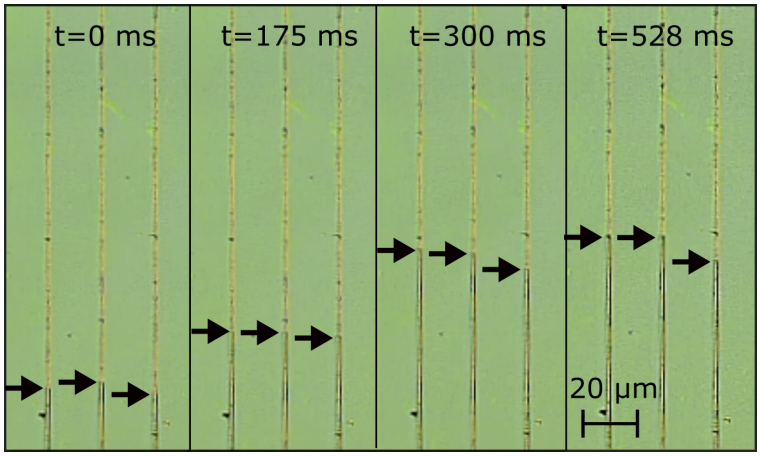

FIGURE 4.8: **Sacrificial layer fluidics (SLF) manufactured by thermal decomposition:** A time-lapse sequence of four images showcases isopropanol flowing through three parallel channels, each 1 µm wide. Arrows highlight the progression of the isopropanol-air boundary.

4.2.4 Outlook

In the previous section, we could demonstrate SLF made of E-beam structured polycarbonate. Based on these developments, I suggest two fabrication protocols using SLF to manufacture a sensor for single particle detection. Both protocols allow for wafer-scale production. The first protocol is displayed in the appendix Fig. A.4. The starting point is a quartz wafer with silver resonator structures manufactured like the currently used sensor. The wafer is spin-coated with PC, and the micro- and nanochannels are written with E-Beam lithography. During wet or thermal development, the height of the sacrificial layer reduces below the thickness of the silver electrodes. In this way, the final fluidic channel is confined between the electrodes. After development, a physical mask is aligned so that the area with the sacrificial PC is accessible for the deposition of an encapsulation layer, and the CPW probe tip contacts are covered. Low-temperature plasma-enhanced chemical vapor deposition (PECVD) or sputter deposition of 2 µm of SiO_2 is performed, leading to an encapsulation of the sacrificial layer. Inlets are drilled with a diamond drill bid, and the wafer is cut into chips. Finally, the sacrificial layer is removed in a furnace at a temperature of 600°C, removing the sacrificial layer and leaving hollow channels. The heating should be performed under a nitrogen stream. During heating, the Ti/Ag/Ti metal layers undergo self-encapsulation, providing an Ag surface protection layer and an interfacial adhesion layer between the silicon dioxide and the silver [106]. The drilled inlet holes are sealed by OrmoStamp foil.

For better sealing and no labor-intensive drilling and wafer cutting, we propose an alternative manufacturing protocol depicted in the appendix Fig. A.5. A high-resistivity silicon wafer is used as a substrate. The metal resonator structures and fluidic sacrificial PC layer are manufactured in the same way as previously described. The design of the coupled resonator has to be updated because the permittivity of the substrate significantly changes the resonance frequency, characteristic impedance, and coupling capacitance. As a coating layer, instead of SiO_2, a silicon

nitride layer is deposited. In the next step, the top side is spin-coated with a designated resist to protect against KOH etching. The bottom side of the wafer is spin-coated with a KOH stable photoresist (SX AR-PC 5000/41, *Allresist*). The inlets and the dicing lines are photo-lithographically transferred into the resist. Subsequently, a deep silicon etching is performed with KOH. Silicon nitride is not etched by KOH [107], which leads to open inlets while the silicon nitride encapsulation layer is protected. The silicon nitride seals the fluidic channel. Additionally, the KOH-etching dices the wafer into individual chips. In the final step, the sacrificial layer is removed in the furnace by heating to 600°C with a nitrogen stream.

Implementing one of the two fabrication processes is intended for the future. The new chip design would circumvent the main drawbacks of the current design. The fluidic channel would not extend over the electrodes. This configuration leads to a homogeneous electric field in the channel, and thus, there would be no position dependence between the particles in the channel and the detected signal. Also, the encapsulation layer is SiO_2 or Si_3N_4 with small dielectric losses, which would lead to an insignificant reduction of the quality factor. These benefits could be obtained even though a wafer-level fabrication would still be possible.

This page has been intentionally left blank.

Chapter 5

Setup

The setup chapter is separated into two sections. First, the interfacing between the chip and the macroscopic fluidic tubing, high-frequency circuitry, and fluorescence microscope are described. That interface enables the simultaneous measurement of the sensor's high-frequency response, control of the pump pressure (i.e., liquid flow), and monitoring of particle flow with the microscope. In the second section, I discuss the high-frequency circuit in detail. This circuit combines the new coupling-based cCPW sensor with an interferometer. This combination improves the setup sensitivity by several orders of magnitude compared to the previous sensor iterations [24, 85].

5.1 Interfacing

The setup aims to establish a platform capable of detecting single nanoparticles in flow at GHz frequencies. A challenging engineering aspect was the simultaneous optical and electrical monitoring of particles inflow, with a chip of minimal size, a chip-to-setup interface that does not degrade the quality of the sensor. The detection

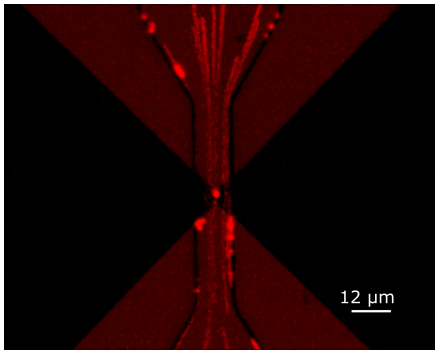

FIGURE 5.1: **Validation of particle flow by fluorescent microscopy:** The image captures 1.75 µm fluorescent polystyrene beads moving between the sensing electrodes. The image overlays selected frames where translocation events occurred during a 4-second video. The chip features electrodes spaced 2 µm apart and a 12 µm wide channel.

of nanoscopic particles inflow is best established with a fluorescence microscope. Therefore, the central component of the setup is a fluorescence microscope (Eclipse LV100, *Nikon*) which monitors particle flow. Fig. 5.1 shows an example image of 1.75 µm fluorescent polystyrene beads inflow, detected with a long working distance 100X objective (100X Plan Apo NIR Infinity Corrected Objective, *Mitutoyo*). The electrodes are separated by 2 µm, and the channel is 12 µm wide. The image summarizes a 4 s video collected at a slow flow rate. The available camera (DS-Fi1c, *Nikon*)

is limited to 23 frames per second, which necessitates conducting the experiment at a slower flow rate. The video frames with translocation events are overlayed for illustrational purposes. The bright dots correspond to trapped polystyrene beads.

Fig. 5.2 shows the experimental setup. It consists of a fluorescence microscope extended by several custom-made components. These components provide interfaces between the sensor chip, the fluidic tubing, and the electrical circuitry. This setup allows the simultaneous optical monitoring of fluorescent particles and high-frequency reflectometric measurements while controlling the sample flow rate. A custom microscope stage incorporates two micromanipulators with CPW probes. In this way, the stage, chip, and CPW probes form a unit that moves independently of the objective. Consequently, the objective can be moved during a flow experiment without detaching the probe.

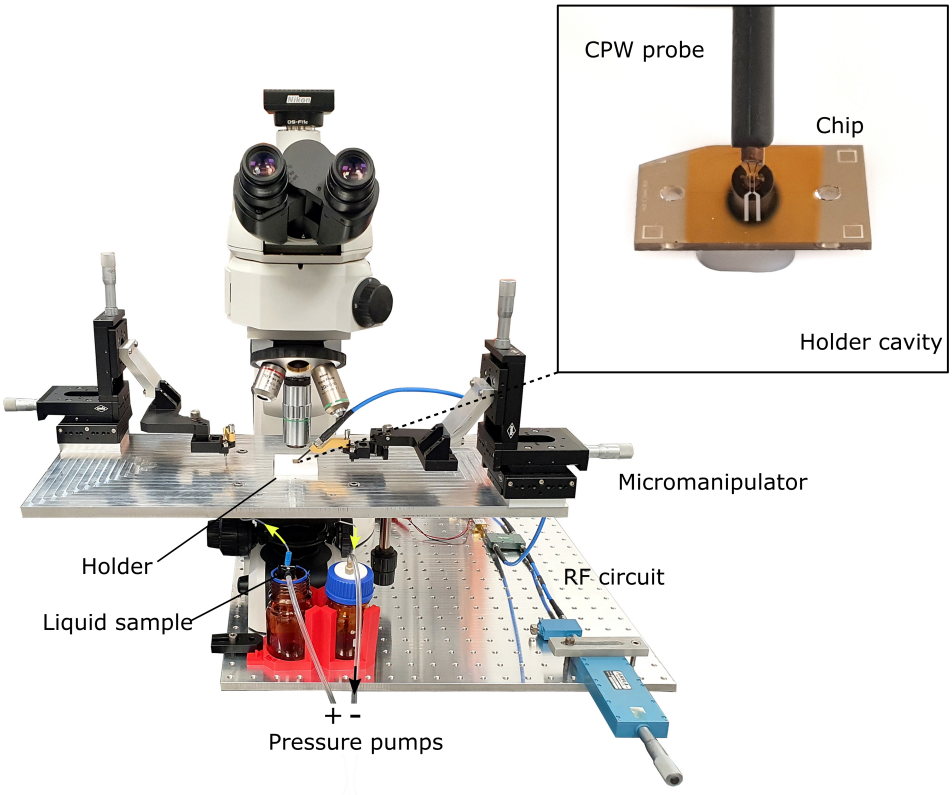

FIGURE 5.2: **Experimental setup:** A fluorescent microscope (Eclipse LV100, *Nikon*) paired with a custom-designed stage featuring a Polytetrafluoroethylene (PTFE) chip holder and micromanipulators for the CPW probe tip control. The holder grants excess for tubing from the bottom of the stage. Pressure pumps control the inlet and outlet pressure. A 50 Ω CPW probe tip connects the chip with the RF circuit. A cavity beneath the chip decouples the resonator from the holder material. Image adapted from my publication [1], © 2023 IEEE

A CPW probe tip (Cascade Microtech FPC-GSG-250) is attached to the top of the chip (inset Fig. 5.2). This CPW probe can be connected either to a microwave circuit for time-resolved particle detection measurements or to a VNA for S-parameter sensor characterization. In a previous iteration of the setup, as designed by Paul Gwozdz [24, 85], this connection between the sensor and the RF sensing circuitry was made by soldering the sensor to a circuit board. This poorly controlled connection varied with each solder joint, resulting in impedance mismatches with reflected

and standing waves. In contrast, the CPW probe tip used in this setup is a reversible and reproducible connection. It has a standard characteristic impedance of 50 Ω, which matches the characteristic impedance of the sensor feedline of 50 Ω (determined by conformal mapping Eq. 2.46 with a center line width of 200 µm and a signal-to-ground distance of 21 µm). In this way, no microwaves are reflected at the interface.

In addition, the CPW probe tips allow the calibration of the VNA by shifting the reference plane to the CPW probe tip. As a result, the VNA measures only the sensor, and the scattering parameters obtained are comparable to simulations. Calibration is performed using the short-open-load-thru (SOLT) calibration method on an MPI AC-2 calibration substrate. In the previous setup, the S-parameter response was measured for the sensor, including the PCB. In this way, the S-parameters of the sensor could not be de-embedded from the PCB, and the S-parameters could not be compared with simulations. The S-parameter response had many peaks, and the origin of each peak could not be traced back.

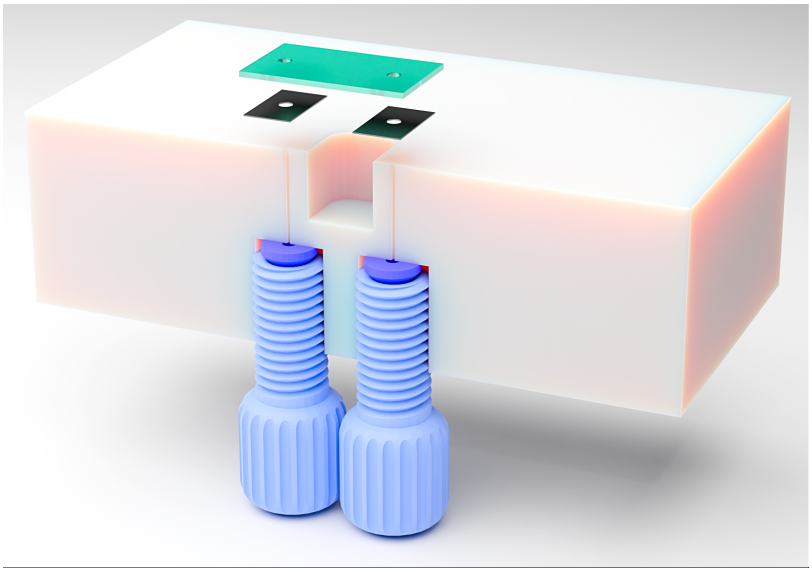

FIGURE 5.3: **PTFE holder cross-section:** This holder establishes the chip's connection to fluidic tubing. A section of the PTFE holder is cut away to reveal the 300 µm diameter holes, aligning the chip with flat-bottom fittings. These fittings at the base ensure a secure, pressure-tight seal to the external tubing. A cavity below the resonator decouples from the sensor from the holder material. The chip is attached to the holder using double-sided M3 VHB 4926 tape (black), providing a pressure seal of over 500 mbar. Illustration reproduced from my publication [1], © 2023 IEEE

One of the primary design challenges was accommodating a compact chip size of only 12 mm x 8 mm, which is critical for wafer-scale fabrication. This size constraint had to be balanced with the need for simultaneous accessibility by both a CPW probe tip and a 100X microscope objective, the latter having a working distance of 12 mm. To address this, an innovative chip holder design was developed. Fig. 5.3 shows a cross-section of the holder containing fluidic holes and a cavity inside the holder. The holes, each have a diameter of 300 µm, connect the top of the chip to the flat bottom fittings. More about the cavity the cavity will be discussed later. The chip is attached to the top of the holder with double-sided tape (M3 VHB 4926). Each

tape strip has a hole punched through the center allowing fluid to flow into the chip. The tape seal withstands pressures in excess of 500 mbar and is easy to install and remove. The channel is sealed from the top with approximately 15 µm thick transparent Ormostamp foil (see fabrication section 4.1).

The custom holder fits into the custom microscope stage, and a hole in the stage allows for tubing (1/16" OD) from the bottom. A flat-bottom fitting at the bottom of the holder provides a pressure-tight seal rated up to 138 bar. This configuration allows a positive pressure at the inlet, suction at the outlet, and pressure reversal to unclog the channel. Also, it enables high-pressure gradients across the inlet and outlet, resulting in fast particle translocation events of down to 25 µs. In the current design, the diameter of the flat-bottom mounting screws and the size of the resonator limit the chip size to approximately 12 mm x 8 mm.

The CPW ground-to-ground distance of the resonator has a width of 800 µm. While this width is not substantial compared to the 12 mm width of the chip, the electric field extends beneath the chip, interacting with the material of the holder. This phenomenon is shown in Fig. 5.4, which displays the S-parameters of the sensor for different backing materials. With no holder and backside is air, the resonator's qual-

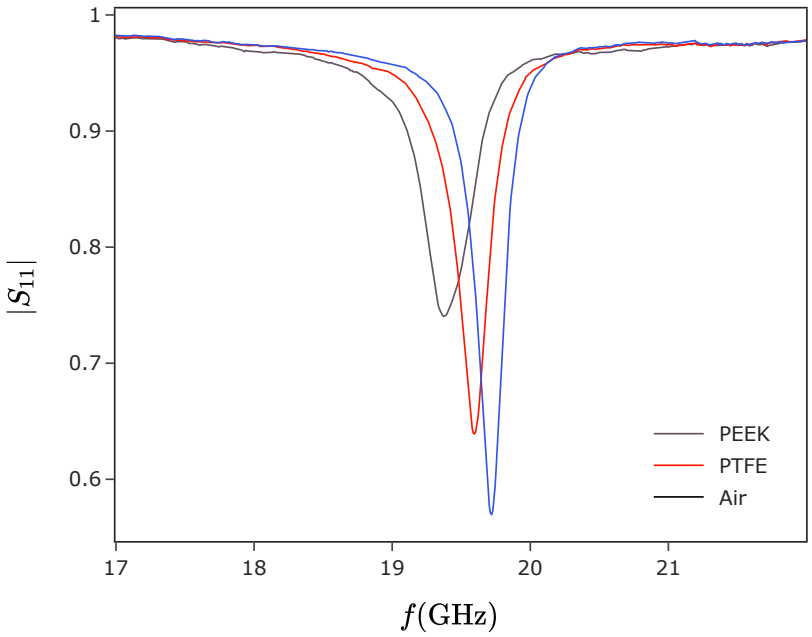

FIGURE 5.4: **S-Parameter response of various holder materials:** The influence of the holder materials (PEEK, PTFE, and air) on the resonator's resonance frequency and quality factor is assessed by attaching them to the chip's backside. A sensor devoid of the SU-8 fluidic layer, featuring only metal structures, was utilized for this evaluation.

ity factor is 108. With a polytetrafluoroethylene (PTFE) holder, this value drops to 82. With a polyetheretherketone (PEEK) holder, it drops even further to 52. PTFE has a real permittivity of 2.05 and a low dielectric loss (about $2 \cdot 10^{-4}$). PEEK's real permittivity is 3.1, and its dielectric loss is about $3 \cdot 10^{-4}$ [108, 109]. These properties affect the performance of the resonator. Higher real permittivity reduces the resonant frequency, which is consistent with the theory described by Eq. 3.8. As the dielectric loss increases, the quality factor of the resonator decreases. In order to minimize the influence of the holder material on the resonator quality, two changes were made. Firstly, the holder material was selected as PTFE because of the low dielectric loss

value. Secondly, a cavity was fabricated beneath the resonator. These changes made the resonator performance virtually identical with and without the holder material.

5.2 Microwave Circuit

This section begins with a brief literature review of reflectometric circuit architectures that have been applied to high-frequency single-particle sensing. The measurement circuit is divided into three sections: sensor, signal generation & detection, and impedance matching. I will omit the discussion of the various sensor architectures since they have already been discussed in detail in section 3.3. In the second part of this section, I will present the advanced microwave circuit developed in this thesis.

Review: Microwave Circuits for Inflow Particle Sensing

Reflectometry-based setups for single particle detection date back to Wood et al.'s work in 2005 [25]. For *signal generation and detection*, he used the most straightforward approach, a VNA. VNAs generate and detect high-frequency signals and they can be used in a steady-state configuration, collecting a spectrum before and after a particle attaches to the sensor [69, 110, 111], or in a time-resolved configuration, collecting time traces as individual particles pass through the sensor [112, 72, 63]). However, VNAs are less optimal for time-resolved applications due to bandwidth, noise, and sampling rate limitations. As alternatives, digital storage oscilloscopes and LIAs are employed, requiring separate high-frequency signal generation sources [25, 26, 24, 52, 67, 113, 85]. The operating frequency of these detectors is typically in the MHz range, so the signal must be downconverted from GHz to the MHz range for high-frequency detection. Custom phase-locked-loop configurations have recently been used to track the resonant frequency [114, 72]. The phase-locked-loop systems also use a dedicated RF source, and the RF signal was down-converted.

Impedance matching plays a crucial role in efficiently coupling the power into the sensor, thereby minimizing signal reflection between the source and the sensor. An impedance match sensor results in a higher contrast for small signal changes and the sensitivity to load impedance changes are increased [53]. Furthermore, higher source powers can be used without saturating the detection electronics. A common impedance matching approach is a TC. At the resonance frequency, the power is efficiently coupled to the sensor. However, adjusting the impedance match of a TC can be challenging, in particular when temperature fluctuations affect the stability of the impedance match. Active impedance matching circuits have been developed to overcome these problems. A notable advancement in this area is the integration of a shunt varactor with the TC, allowing active impedance matching of the sensor by tuning the capacitance of a varactor diode. This innovation has allowed short-term impedance matching of up to -100 dB, often exceeding -40 dB [26, 24]. However, in this configuration, the capacitance of the varactor diode is part of the sensor tank circuit, which increases the total capacitance of the resonant circuit. This makes the sensor less sensitive to variations in the sensing capacitance.

An alternative method for impedance matching is interferometry. Interferometry is based on the destructive interference of a reference signal with a measurement signal. It can be realized by a three-port power splitter, mixer, and hybrid couplers. To my knowledge, for inflow particle detection, only mixers had been used for interferometric impedance-matching [114, 72, 52, 67]. In that configuration, the sensing

signal is split into a part that interacts with the sensor and a second part connected to a mixer. Mixing a signal with the same frequencies down-converts the signal to a DC value. The phase shift between both signals can be adjusted to reduce the signal to zero. Unfortunately, such an interferometric configuration can either measure the signal's in-phase or out-of-phase component. The total information of the amplitude and phase is lost. An improved version of this technique employs a hybrid coupler-based interferometer. Such a configuration has yet to be applied to inflow particle sensing. This endeavor will be discussed in the subsequent sections.

5.2.1 Circuit

The developed microwave circuit is shown in Fig. 5.5. For the discussion it is divided into three parts: **(i) sensor, (ii) signal generation & detection, and (iii) impedance matching circuit.** The sensor has already been described in great detail in chapter 3 and will therefore be omitted in the following discussion.

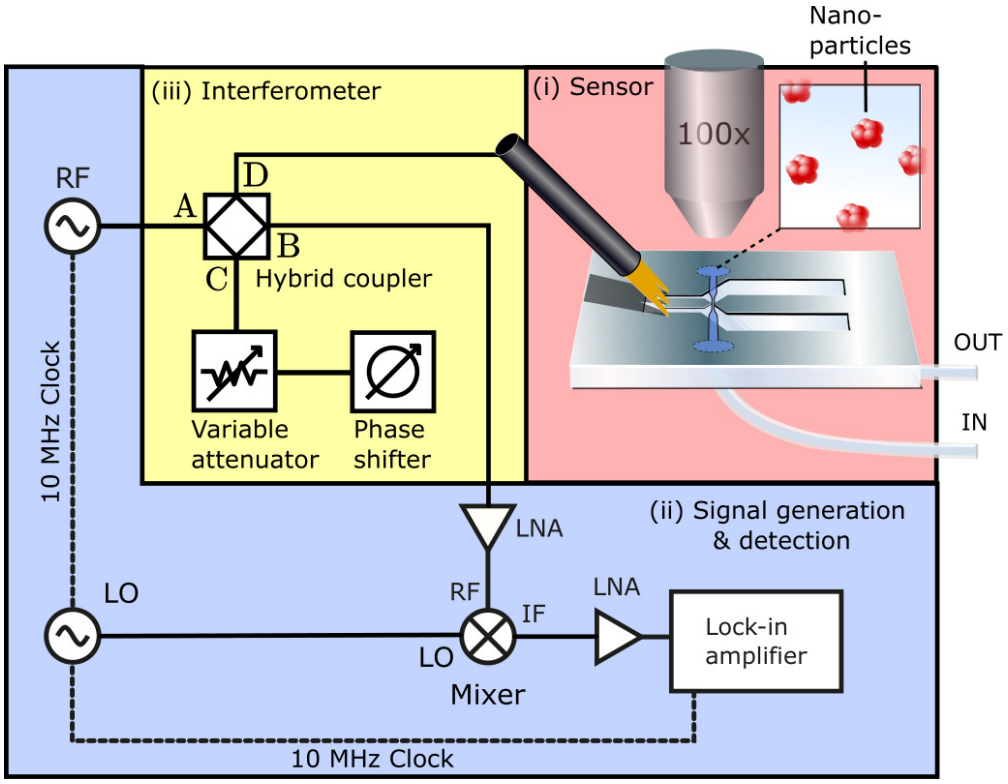

FIGURE 5.5: **Microwave circuit for time-resolved single particle sensing:** The circuit is divided into three sections: (i) Sensor: comprising of coupling-based $\lambda/4$-resonator (red); (ii) Signal generation and detection, which involves radio frequency (RF) and local oscillator (LO) sources, signal amplification using low-noise amplifiers (LNAs), down-conversion to the MHz range via a mixer, and detection with a lock-in amplifier (LIA) (blue); and (iii) Interferometer for impedance matching of the sensor (yellow). Illustration reproduced from my publication [1], © 2023 IEEE

Signal Generation & Detection

The circuit consists of two high-frequency sources (E8257D 250 kHz - 50 GHz, PSG Analog Signal Generator, Agilent Technologies), the radio frequency (RF) (i.e., sensing signal) and the local oscillator (LO) signals. The RF signal is connected to an interferometer connected to the sensor. The resulting signal is amplified by a low noise amplifier (ZX60-06203ALN+ Mini circuits) with a gain of +18 dB and connected to a mixer (ZX05-24MH-S+).

The mixer serves to down-convert the sensing signal to a frequency that can be measured with a commercially available lock-in amplifier. The setup uses a double-balanced mixer (ZX05-24MH-S+ Mini circuits). The mixer has three ports: the radio frequency (RF), local oscillator (LO), and intermediate frequency (IF) ports. An RF signal with the frequency of f_{RF} enters the RF port and is mixed with the LO signal with the frequency of f_{LO}. The LO power is +16 dBm. The resulting mixed signal at the IF port is the sum and difference of RF and LO signals $f_1 = f_{\mathrm{RF}} + f_{\mathrm{LO}}$ and $f_2 = f_{\mathrm{RF}} - f_{\mathrm{LO}}$. These signals are called upper or lower sidebands. For our application, we are interested in the down-converted, lower sideband. The upper sideband is around 40 GHz, which exceeds the transmitted BW of the LNA and LIA. A double-balanced mixer removes the initial RF and LO signals. The RF signal is adjusted to the left flank of the sensor's resonance frequency curve at approximately 20 GHz. The LO frequency is chosen between 2 - 100 MHz below that frequency. This results in an IF frequency of 2 - 100 MHz, which can be measured with a lock-in amplifier. An amplitude modulation in the RF signal translates into an amplitude modulation of the IF signal with an 8 dB down-conversion loss. The phase modulation of the RF signal is conserved in the down-converted signal.

The LO frequency can be chosen either above or below the RF frequency. Note that both RF signals $f_{\mathrm{LO}} \pm f_{\mathrm{IF}}$ are down-converted to the same f_{IF}, and the BW around both frequencies contribute to noise. The unwanted frequency band is called image frequency. In a future setup, a band-pass filter connected in front of the mixer and adjusted to the measurement frequency could reject the noise from the image frequency.

The down-converted lower sideband is amplified by +22 dB gain with an LNA (ZX60-3018G-S+) and measured by the lock-in amplifier. Fig. 5.6 displays the measurement principle of a LIA. At the input, we assume a time-depended sinusoidal input signal $V_s(t) = \frac{R}{\sqrt{2}} \sin(\omega_s t + \Theta)$ with R the root mean squared amplitude, ω the angular frequency and Θ is the phase at $t = 0$. The demodulation process can be described mathematically by translating the input signal into its complex representation:

$$\begin{aligned} V_s(t) &= \frac{R}{\sqrt{2}} \sin(\omega_s t + \Theta) \\ &= \frac{R}{\sqrt{2}} (\mathrm{e}^{j\omega_s t + \Theta} + \mathrm{e}^{-j\omega_s t + \Theta}) \end{aligned} \tag{5.1}$$

An internal reference signal $V_r(t)$ is obtained from the LIA. The complex reference signal is given by

$$V_r(t) = \sqrt{2} \mathrm{e}^{-j\omega_r t}. \tag{5.2}$$

The working principle of a mixer had already been described previously. Mathematically, the dual-phase down-mixing can be calculated by a multiplication of the

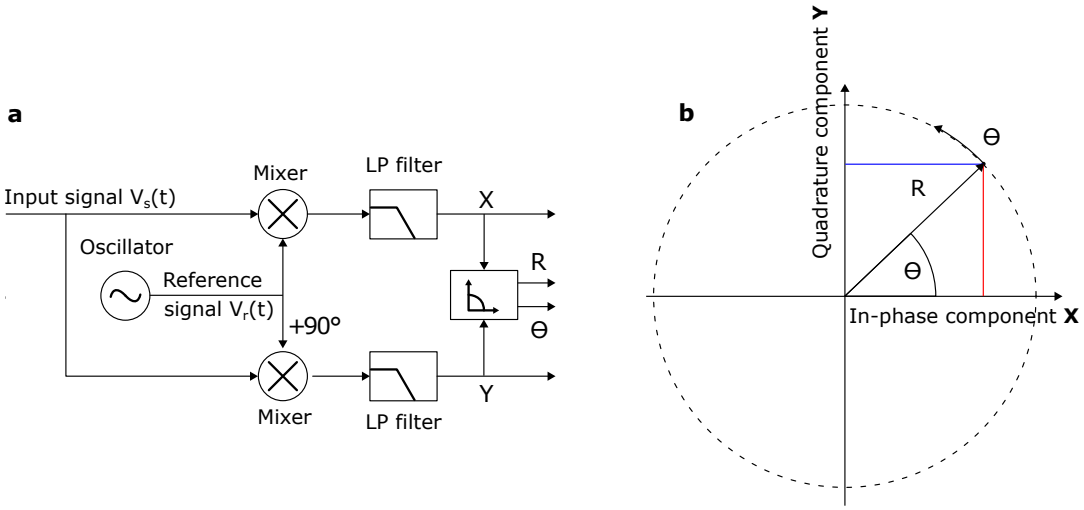

FIGURE 5.6: **Lock-in amplifier: a**, Schematic representation of a lock-in amplifier. The input signal $V_s(t)$ is mixed with a reference signal $V_r(t)$ and its 90° phase-shifted counterpart. Both signals are low-pass filtered, resulting in the in-phase X and quadrature component Y. These components can be translated to polar coordinates as amplitude R and phase Θ. The image was taken from reference [115] and modified. **b**, In-phase and quadrature (IQ) diagram of a signal with amplitude R and phase Θ.

input signal with the reference signal

$$\begin{aligned} Z(t) &= V_s(t) \cdot V_r(t) \\ &= \mathrm{X}(t) + j\mathrm{Y}(t) \\ &= R(\mathrm{e}^{j(\omega_s-\omega_r)t+\Theta} + \mathrm{e}^{-j(\omega_s+\omega_r)t+\Theta}). \end{aligned} \tag{5.3}$$

The resulting signals (i.e., upper and lower sidebands) appear at the difference of both frequencies ($\omega_s - \omega_r$) and the sum of both frequencies ($\omega_s + \omega_r$). The subsequent low-pass filter removes the unwanted upper sideband in the measurement. If the reference signal is identical to the source signal, Eq. 5.3 reduces to the time-independent DC offset

$$V_r = R\mathrm{e}^{i\Theta}. \tag{5.4}$$

The real $\mathrm{X} = \mathrm{Re}(Z) = R\cos(\Theta)$ (i.e, in-phase) and imaginary $\mathrm{Y} = \mathrm{Im}(Z) = R\sin(\Theta)$ (i.e, quadrature) components of Eq. 5.4 are the main output of the LIA. R is the root mean square amplitude of the source signal, and Θ is the phase difference between the source signal and reference signal.

The LIA (UHFLI 600 MHz, *Zurich Instruments*) has a low voltage noise of $4\,\mathrm{nV}/\sqrt{\mathrm{Hz}}$ and a demodulation bandwidth of up to 5 MHz. That BW constraint is the bottleneck of the entire setup and, therefore, responsible for the measurement speed limit of the setup.

Interferometer

An interferometric circuit establishes impedance matching. The circuit has been inspired by a publication from S. Tuca et al. [116], which stems from a related research field, the field of scanning near-field microwave microscopy. That publication demonstrated a 2-7-fold S/N performance enhancement for an interferometric matching approach compared to a classical shunt impedance matching (i.e., TC matching).

The coupling-based sensor developed in this thesis has an impedance match (at resonance) of approximately 6 dB. At this impedance match value, the sensor is optimized for maximum coupling sensitivity. This match results in 50% of the RF signal being reflected from the sensor, leading to saturation of the LIA detector at low power levels. The interferometer removes this part of the reflected signal by destructive interference. Compared to TC-based impedance matching, the interferometer can match any frequency. These unconstrained matching capabilities are crucial because the sensitivity to real and imaginary permittivity variations in the sensing volume changes over the resonance curve (as shown in section 3.8). An interferometer allows the measurement frequency to be freely chosen on this curve.

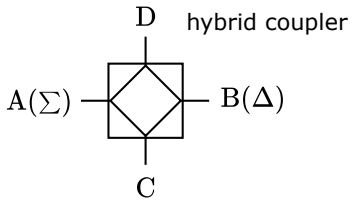

FIGURE 5.7: **90° hybrid coupler as used for the interferometry setup:** A 4-port device where the RF signal enters at port A(∑), splits equally with a 90° phase delay between ports D & C. Port D links to the sensor, while C connects to the reference arm. Port B (Δ) is the output port where signals from D & C undergo destructive interference.

The yellow section in Fig. 5.5 shows the interferometer configuration. A 90° hybrid coupler (model: 2375-9 Spectrum Control Inc.) is used for the interferometer. An ideal hybrid coupler attenuates the induced difference signal by 3 dB. As shown in Fig. 5.7, it is a 4-port device with a sum port A(∑), a difference port B(Δ), and a D & C port. The RF signal is connected to port A. It is split into equal parts to ports D & C with a 90° phase delay on one port. Port D is connected to the sensor, and port C is connected to a reference arm. This arm consists of a phase shifter (3428B ARRA Inc.) and a variable attenuator (AR 3665 ARRA Inc.). The signal from port D can be matched by adjusting the phase and attenuation. Port B (Δ) is the difference port, where the signal from port C & D interferes destructively. During the time-resolved measurement, the impedance is matched manually by changing the phase and attenuation. In practice, impedance matching is an iterative process. At the beginning of impedance matching, the source power is low. After the first impedance matching cycle, the source power is increased, followed by the next impedance matching cycle. The final source power was between -15 dBm and +19 dBm, depending on the particle under test. At the beginning of each measurement, the setup was impedance matched to the signal detected by the LIA between 0.1 mV and 1 mV. An impedance match between -99 dB and -79 dB could be achieved for the source power of +5 dBm. The impedance match drifted during the measurement and had to be readjusted before each measurement.

This page has been intentionally left blank.

Chapter 6

Interferometer & Data Analysis

This chapter discusses utilizing an interferometer to impedance-match a microwave resonator for the inflow detection of particles. To my knowledge, this measurement technique has not yet been applied in this context before. The investigation outlines the difference between the impedance-matched sensor and the standalone sensor. The aim is to find the relation between the physical properties of the sensing volume and the amplitude and phase data collected with the LIA. In the second part of this chapter, I examine a peak processing algorithm for analyzing time-dependent VNA or LIA data. Conventional reflectometric single particle detection setups collect time traces of the S-parameters (VNA) or the amplitude R and phase Θ (LIA) data. During the translocation of a particle through the sensing volume, these time traces are modulated, resulting in peaks in the traces. Each peak can be characterized by its height or width. In the case of a poor impedance match relative to the size of detected peaks, additional challenges arise. To the best of my knowledge, these effects had been overlooked in similar scientific approaches [26, 24, 25, 112, 85, 72].

6.1 Interferometeric Transformations

An interferometer impedance matches the sensor, which reduces noise and allows for a high contrast measurement [117, 118]. Additionally, the sensitivity to changes in the load impedance is increased [53]. The interferometer transforms the initial sensor response into a new signal, and it is essential to analyze these transformations in detail. Importantly, the transformation is not just a scaling of an amplitude and phase signal or subtraction of a baseline. It is worth noting that similar transformations also occur in other impedance-matching circuits, like TC matching with a varactor diode.

In the following, the aforementioned transformation is investigated by simulating two separate circuit models (with and without an interferometer). The simulations are performed with *QucsStudio* software [119]. Fig. 6.1a displays the circuit model for the sensor, and Fig. 6.1b depicts the circuit model of the sensor with an interferometer. The sensor's TL is modeled by a CPW ($w = 400$ µm, $s = 200$ µm, $l = 2.2$ mm) with the same parameters as the sensor in chapter 3.6. The sensing region is modeled with a parallel circuit composed of a capacitance and a resistance. The capacitance consists of a coupling capacitance of 7.5 fF, which leads to an optimal input coupling with a reflection coefficient of $\Gamma = 0.5$. ΔC modulates that capacitance. It models the variations of the real permittivity ε' in the sensing volume. The total resistance is given by the sum of a fixed 20 kΩ resistance and a variable resistive change, ΔR. This ΔR models the variations in the imaginary permittivity, ε'', within the sensing volume. Using this straightforward circuit, we can simulate the sensor's response to particle-induced permittivity changes in the sensing volume.

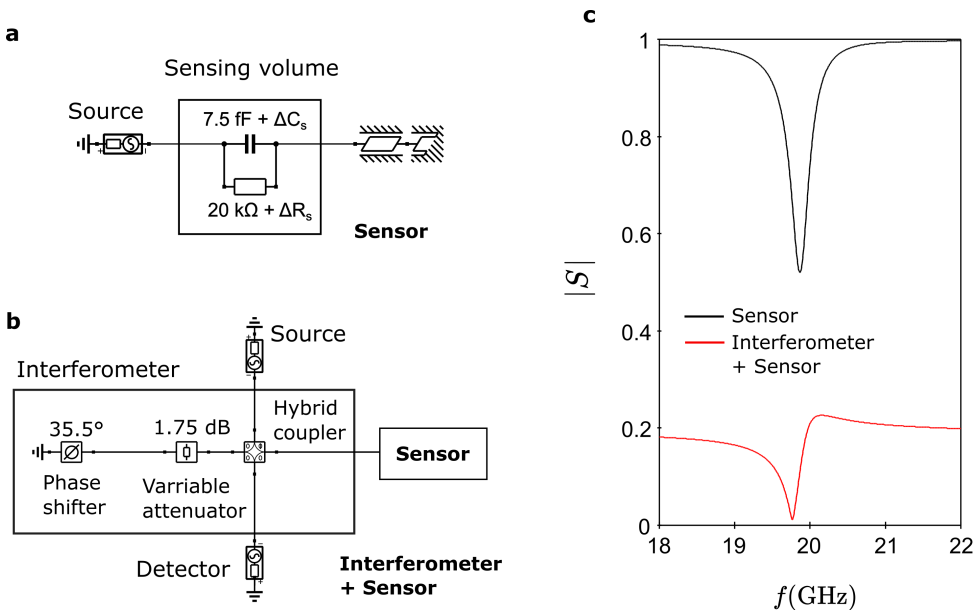

FIGURE 6.1: **Circuit model analysis of the cCPW sensor with and without an interferometer: a**, The circuit model of the coupling-based cCPW sensor. b, The interferometrically impedance-matched version of the sensor. The sensor is modeled by CPW terminated by a CPW ground. The sensing volume is depicted as a parallel circuit with capacitance C and resistance R. The capacitance C is sensitive to the real permittivity ε'), while the resistance R models the imaginary permittivity ε'') in the sensing volume. **c**, The $|S|$-Parameter response compares the original sensor (black) with its impedance-matched version (blue). The interferometer is adjusted to a phase shift of 35.5° and an attenuation of 1.75 dB, ensuring optimal impedance matching at 19.76 GHz on the left flank of the resonance curve.

The interferometer is composed of a 90° hybrid coupler, a variable attenuator, and a phase shifter. It is adjusted to a phase shift of 35.5° and an attenuation of 1.75 dB for an impedance match of -39dB at the left flank of the sensor at a frequency of 19.76 GHz. These values were chosen to approximate the experimentally achieved impedance match. Fig. 6.1c displays the $|S|$-parameter response for both circuits. The black curve depicts the $|S_{11}|$-parameter for the sensor, and the red curve shows the $|S_{21}|$-parameter for the sensor with the interferometer. As expected, the interferometer impedance matches the left flank of the sensor at 19.76 GHz.

Fig. 6.2a displays the IQ diagrams of both circuits. As discussed in the section 5.2.1, the IQ diagram visualizes the in-phase and quadrature components measured with an LIA. It provides an alternative representation of the S-parameters, which allows for a detailed analysis of the transformation. The IQ diagram represents the S-Parameters from Fig. 6.1c as circles. In the IQ plane, the signal transformation due to an interferometer reduces the circle's radius by half, rotates the circle by 90°, and shifts the circle into the origin of the diagram.

In a time-dependent measurement, a signal is measured at a discrete impedance-matched frequency of 19.76 GHz. Fig. 6.2b displays the sensor's capacitive and resistive response at that frequency. The capacitance ΔC_s (magenta) is varied from -0.2 fF to 0.2 fF, and the resistance ΔR_s (green) is changed from - 7 kΩ to + 7 kΩ. In the IQ plane, the interferometer transforms the capacitive and resistive response

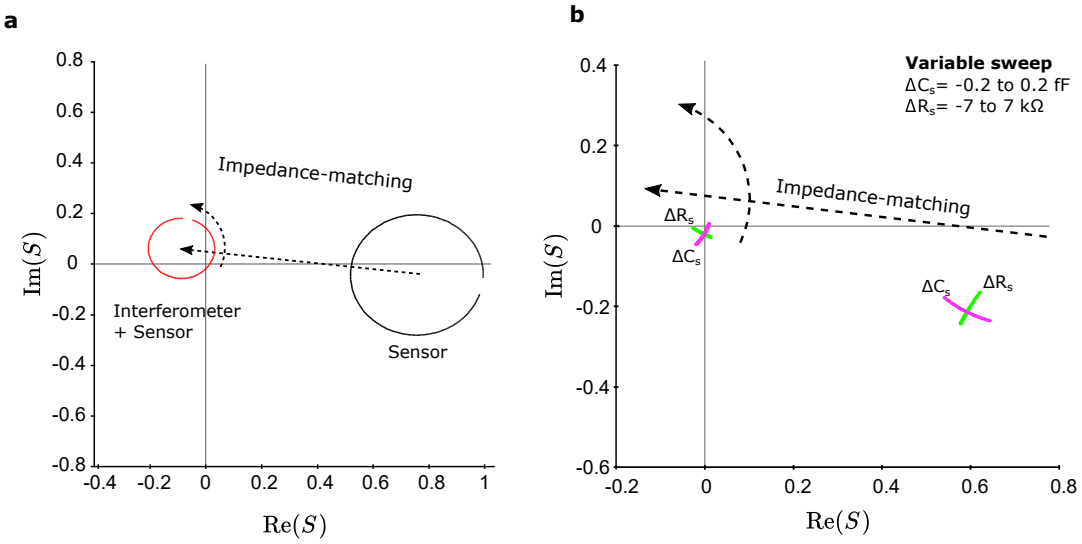

FIGURE 6.2: **IQ-diagram depicting the impact of interferometric impedance matching:** The simulation results from the circuits depicted in Fig. 6.1 are displayed in an IQ-diagram. **a**, The diagram compares the interferometrically impedance-matched sensor (red) with the standalone sensor (black) across the 18 to 22 GHz frequency range. Impedance-matching shifts the circle into the origin of the diagram reduces the radius by half and rotates by 90°. **b**, The diagram illustrates the capacitance and resistance response at 19.76 GHz, simulating a particle within the sensing volume. Capacitance variation ΔC_s (magenta) spans from -0.2 fF to +0.2 fF, and resistance ΔR_s (green) varies between -7 kΩ and +7 kΩ. The response reduces by half and rotates by 90°, matching the effects induced by interferometric impedance matching observed in **a**.

in the same way as the transformation of the circles. The response is shifted to the origin of the IQ plane, reduced by half, and rotated by 90°.

The transformation is less evident in the amplitude and phase space as the amplitude and phase are measured from the origin of the IQ-coordinate system. In the case of a perfect impedance match (transformation into the origin of the diagram), the amplitude and phase of the transformed signal are both strongly influenced by ΔC_s and ΔR_s. In comparison, the amplitude response of the initial sensor is insensitive to ΔR_s, and the phase is insensitive to ΔC_s.

Therefore, it is crucial to recognize that the amplitude and phase responses of the impedance-matched sensor do not directly correlate with those of the original sensor. Given this complexity, a mathematical explanation of the transformation process is provided in the subsequent section for clearer understanding.

6.1.1 Transformation: Mathematical Description

In the previous section, I demonstrated by circuit model simulations that the impedance-matching by an interferometer complicates the amplitude and phase response, and it is not simply a matter of subtracting a baseline amplitude or phase. Complex numbers can be used to mathematical describe the interferometric impedance-matching process. In this representation, the signal detected by the

LIA without an interferometer can be written as

$$V_{\text{sen}} = R\text{e}^{j\Theta}, \tag{6.1}$$

with R the amplitude and Θ the phase of the signal.

In the following section, I will derive the interferometrically transformed signal V_{T} and compare it to the sensor signal V_{sen}. I will examine the amplitude and phase modulation of V_{T} in relation to the modulation of V_{sen}.

The main component of the interferometer is the hybrid coupler. It splits the source signal into the reference and sensing arms connected to the sensor. The signal from the sensing arm V'_{sen} has half the amplitude and a 90° phase in comparison to the initial sensor signal V_{sen} with

$$V'_{\text{sen}} = \frac{R}{2}\text{e}^{j(\Theta+90^\circ)}. \tag{6.2}$$

At the difference port B of the hybrid coupler, the sensing signal V'_{sen} and reference signal V_r interfere destructively and combine to form V_{T}. The destructive interference can be described using complex numbers as the difference between both signals. For a perfectly impedance-matched signal, the reference signal is equal to the sensing signal, and the difference becomes zero $V_{\text{inter}} = V'_{\text{sen}} - V_r = 0$. However, if the sensing signal is modulated, the difference signal becomes non-zero and can be detected by the LIA. I will investigate the transformation for two modulation cases in the following section.

In the first case, an amplitude modulation ΔR is induced. The following calculations make use of the mathematical relationship $\text{e}^{j(\Theta+90^\circ)} = j\text{e}^{j\Theta}$. The difference signal V_{T} for an amplitude modulated signal becomes

$$\begin{aligned} V_{\text{T}}(\Delta R) =& V'_{\text{sen}} - V_r \\ &= \frac{R+\Delta R}{2}\text{e}^{j(\Theta+90^\circ)} - \frac{R}{2}\text{e}^{j(\Theta+90^\circ)} \\ &= \frac{\Delta R}{2}\text{e}^{j(\Theta+90^\circ)}. \end{aligned} \tag{6.3}$$

The transformed signal is reduced by half, and the phase rotates by 90°.

In the second case, the phase of the initial signal is modulated by $\Delta\Theta$. It is clear from a theoretical perspective that a perfectly impedance-matched signal has no amplitude or phase. Therefore, a change in this signal cannot be analyzed in terms of a phase change. Instead, the signal will be analyzed in terms of its phase and amplitude rather than a phase shift. To calculate V_{T}, a Taylor series expansion around $\Delta\Theta = 0$ is used:

$$\text{e}^{j(\Theta+\Delta\Theta)} - \text{e}^{j\Theta} = -j\Delta\Theta\text{e}^{j\Theta} + O(\Delta\Theta^2). \tag{6.4}$$

Using this expansion, the difference signal V_{T} becomes:

$$\begin{aligned} V_{\text{T}}(\Delta\Theta) &= V'_{\text{sen}} - V_r \\ &= \frac{jR}{2}(\text{e}^{j(\Theta+\Delta\Theta)} - \text{e}^{j\Theta}) \\ &= \frac{R\Delta\Theta}{2}\text{e}^{j\Theta} \end{aligned} \tag{6.5}$$

From that equation, we see that the initial phase modulated signal V_{sen} transforms into a signal $V_T(\Delta\Theta)$ that is amplitude modulated. By comparing Eq. 6.3 & 6.5, we also conclude that the transformed amplitude and phase responses are shifted by 90° with respect to each other. Note that the Taylor series terms of $O(\Delta\Theta^2)$ were neglected so that the approximation is only valid for small modulations.

Finally, we calculate transformed amplitude ΔR_T and phase Θ_T detected by the LIA as a function of the initial modulations (ΔR & $\Delta\Theta$). For the rest of the thesis, I use an amplitude and phase notation with subscript (T) to indicate that the transformed amplitude and phase differ from the initial one.

The amplitude can be calculated by the vector sum of both signals $V_T(\Delta\Theta)$ and $V_T(\Delta R)$ and the phase in respect to the original sensor phase change $\Delta\Theta$ can be calculated by the angle between the signals $V_T(\Delta\Theta)$ and $V_T(\Delta R)$. With the condition that both signals are shifted by 90° in respect to each other, we get:

$$\boxed{\begin{aligned} \Delta R_T &= |V_T(\Delta R) + V_T(\Delta\Theta)| = \frac{\sqrt{(R\Delta\Theta)^2 + (\Delta R)^2}}{2} \\ \Theta_T &= \angle(V_T(\Delta R), V_T(\Delta\Theta)) = \arctan 2\left(\frac{\Delta R}{R\Delta\Theta}\right) \end{aligned}} \tag{6.6}$$

The equations show that the phase and amplitude response of the impedance-matched sensor is a complex function of the initial amplitude and phase modulation and not just a baseline subtraction. The transformed amplitude has an enhanced sensitivity as it is now the sum of the initial amplitude response with an added component from the initial phase. The transformed phase parameter, Θ_T, is of particular interest because it is a function of the ratio between the amplitude change and the phase change (i.e., $\Theta_T(\Delta R/\Delta\Theta)$). That ratio can be related to the material properties of the particles in the sensing volume, which will be described next.

Previous circuit model simulations and the FEM simulation in section 3.8 have shown that the amplitude and phase of the standalone sensor respond to the dielectric properties of the sensing volume. However, this change in the dielectric properties of the sensing volume, which I will refer to as the permittivity contrast, depends not only on the permittivity of the particle and suspending medium permittivity but also on the particle size and its position in the channel (i.e., the electric field strength). These dependencies complicate the correlation of measurement data with particle permittivity.

To circumvent these complications, I want to discuss a particular parameter, namely, the ratio between the effective real and imaginary part of the complex permittivity ($\varepsilon'/\varepsilon''$). Dividing these two variables cancels out the size and electric field dependence because they both affect the variables in the same way. As a result, that ratio becomes independent of particle size and electric field strength (i.e., particle position in the sensing volume).

Previous simulations of the standalone sensor demonstrated that the ε_r (capacitance) of the sensing volume mainly affects the sensor's amplitude. In contrast, the ε'' (resistance) mainly changes the phase. Furthermore, I demonstrated in Eq. 6.6 that the transformed phase Θ_T is related to the ratio between the sensor's initial amplitude and phase response. Consequently, Θ_T is related to the ratio between the effective real and imaginary part of the complex permittivity and becomes independent of the particle size and its translocation position in the fluidic channel. It is expected

that the relative phase should be the same for particles made of identical material, making Θ_T a suitable observable for determining the material properties of particles in a fluidic channel.

6.2 Data Analysis

In this section, I describe the algorithms used to detect peaks in the data obtained with the LIA. Contrary to what we assumed in the previous section, the interferometer never perfectly impedance-matched the sensor. Consequently, the collected data must be pre-processed to resemble the previously discussed transformed amplitude and phase variables accurately—additionally, a not reproducible impedance match results in not reproducible data. To the best of my knowledge, this effect had been overlooked in similar scientific approaches [26, 24, 25, 112, 85, 72]. The challenges related to the impedance match will be schematically illustrated. The schematic illustrations are based on circuit model simulations (see appendix A.6), which are not discussed in detail.

6.2.1 Preprocessing for Reproducibility

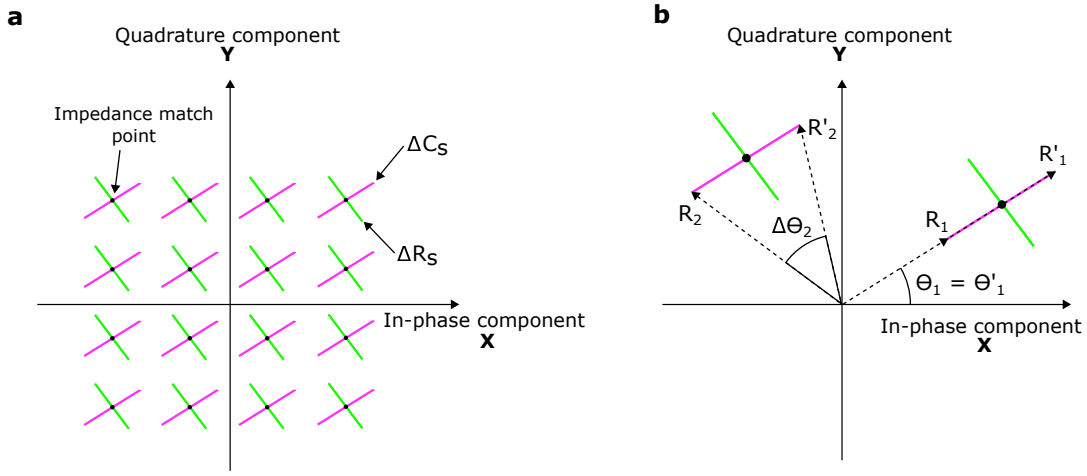

FIGURE 6.3: **Reproducibility challenges in amplitude and phase measurements resulting from impedance-matching:** A schematic representation in an in-phase and quadrature (IQ) diagram. **a**, The variable attenuator and phase shifter displace the measurement point on the diagram. During impedance matching, that point is not controlled and is located somewhere close to the origin of the IQ diagram. The black dots indicate exemplary impedance match points. The magenta and green lines show the sensor's response to variations of losses ΔR_s and capacitance ΔC_s in the sensing volume. **b**, Depicts the amplitude $\Delta R_i = |R_i - R_i'|$ and phase response $\Delta\Theta_i = |\Theta_i - \Theta_i'|$ for the same capacitance change at different impedance matching points. The amplitude and phase responses are different for both impedance matching points $\Delta R_1 \neq \Delta R_2$ and $\Delta\Theta_1 \neq \Delta\Theta_2$.

The process of adjusting the impedance match by an interferometer can be represented in the in-phase and quadrature diagram shown in Figure 6.3a. The variable attenuator and phase-shifter impedance match the sensor. In the IQ diagram, the impedance-matching shifts the measurement point closer to the origin. However, in

the real world, the match is not perfect, and the measurement point can be located in any quadrant around the origin.

The sensor's responses to capacitance and dielectric loss variations in the sensing volume are illustrated as magenta and green lines, respectively. Fig. 6.3b displays a close-up of two different impedance-match points and the corresponding amplitude $\Delta R = |R - R'|$ response, and phase Θ and phase change $\Delta\Theta = |\Theta - \Theta'|$ for the same capacitance variation. It is clear that neither the amplitude response $\Delta R_1 \neq \Delta R_2$ nor the phase $\Theta_1 \neq \Theta_2$ or phase change $\Delta\Theta_1 \neq \Delta\Theta_2$ are comparable for both impedance matching points. As a consequence, it can be concluded that the characteristic peak properties are not comparable for varying impedance match points in the amplitude and phase space. This is because the amplitude and phase are calculated in relation to the origin of the IQ diagram.

To solve this issue, either the coordinate system can be transformed into the origin of the IQ plane or the time traces of the in-phase ΔX and quadrature component ΔY can be analyzed directly. The second option has been found to yield better results, and it will be discussed in detail. The relative amplitude and phase responses are approximately the same for all impedance matching points around the origin of the IQ diagram. That has been confirmed by *QucsStudio* circuit simulations (see appendix Fig. A.6) [119]. The relative amplitude and phase are equal to a perfectly impedance-matched sensor. They can, therefore, be used in place of the transformed amplitude and phase variables.

The phase is dependent on the reference phase provided by the LIA. Moreover, the phase changes with the measurement frequencies (i.e., position on the resonance curve) and resonator properties. Up to now, the fabrication of the chip has yet to be controlled well enough to ensure the same resonance frequency and quality factor. Mainly, the OrmoStamp layer's thickness and the fluidic channel's alignment to the sensing electrodes vary from chip to chip. As a consequence, the phase cannot be compared between different chips.

6.2.2 Peak Parameters

Building on the previously discussed (ΔX, ΔY)- approach, two peak analysis algorithms have been developed and are demonstrated using an exemplary 15 s time-trace containing peaks corresponding to 1.75 µm sized polystyrene beads (Flouresbrite Carboxy 17687) (see Fig. 6.4a). The LIA collects the in-phase X and quadrature Y components. The RF signal frequency was set to the flank of the resonance curve at 18.326 GHz with 8.8 dBm power, and the demodulation bandwidth was adjusted to 10 kHz and recorded at a rate of 54.93 ksamples/s. Fig. 6.4b shows a zoomed view of a random X and Y peak in the time traces at 5.2166 s. The peak amplitudes (ΔX, ΔY) and peak width w_p at full half width maximum (FWHM) are calculated using two Python algorithms. The first algorithm (*algorithm 1*) uses the SciPy *signal.find_peaks* function. Peak detection is applied to both X and Y time traces, and the trace with the most detected peaks at a given threshold is selected as the primary trace. The peak amplitude, width, and left and right base positions (i.e., the positions where the peak starts and ends) are obtained for the primary trace. A custom script selects the secondary trace's left and right base positions and calculates a linear baseline between them. The peak height in the secondary trace is then obtained by calculating the difference between the baseline value and the trace value at the peak position of the primary trace. This algorithm produces a ΔX and ΔY value for each peak

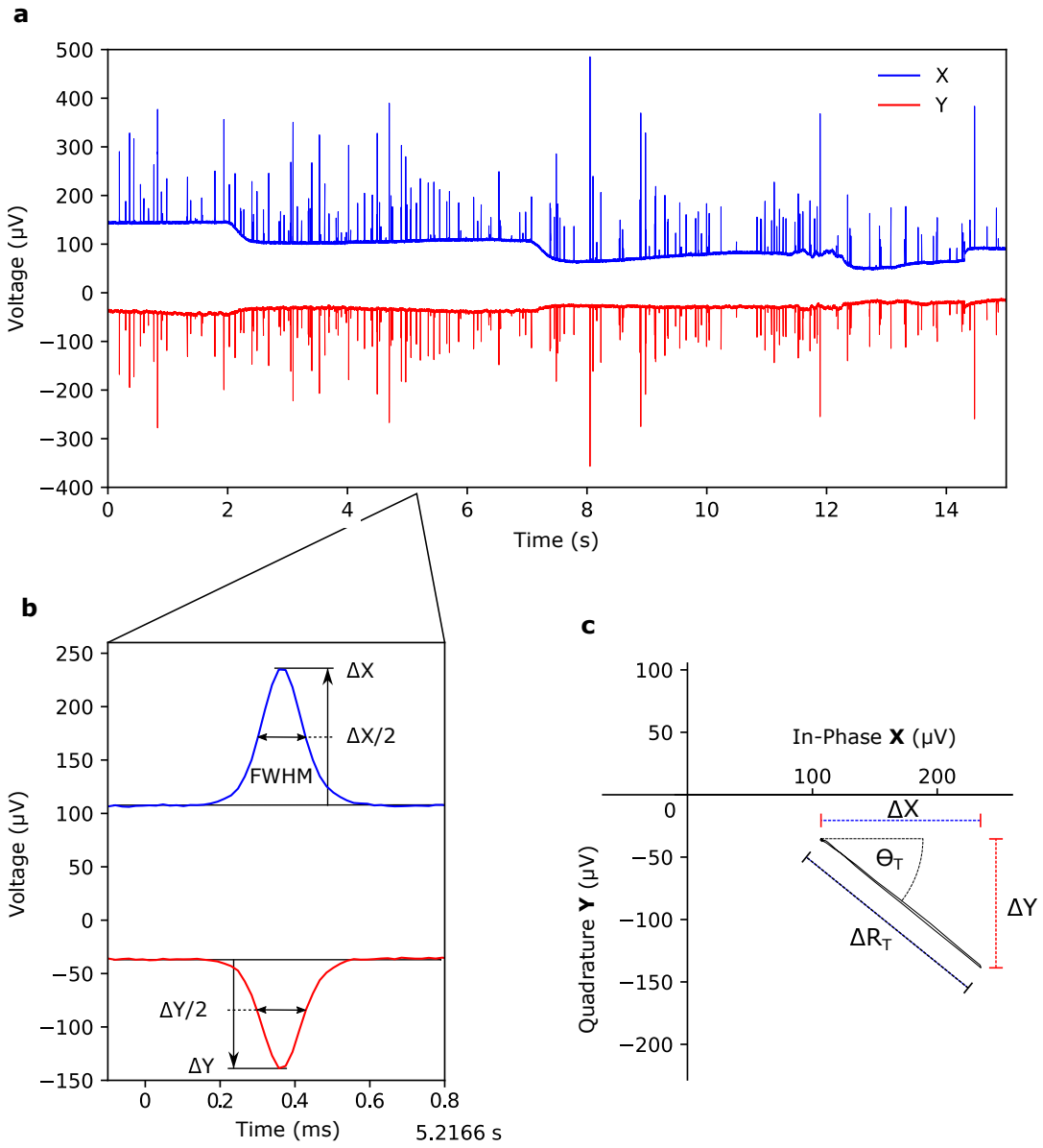

FIGURE 6.4: **Analysis of peak parameters:** **a**, Time-traces of in-phase X (blue) and quadrature Y (red) component during the flow of 1.75 µm polystyrene beads (Carboxy 17687, *Flouresbrite*). **b**, Peak heights (ΔX, ΔY) are calculated separately for the X and Y trace. The peak width w_p is based on the full-width half maximum (FWHM). Two Python algorithms evaluate height and FWHM: *algorithm 1* employs SciPy's *signal.find_peaks*, while *algorithm 2* utilizes *optimize.curve_fit* [120]. **c**, IQ-diagram representation of the X, Y-peaks with the relative amplitude ΔR_T and phase Θ_T}.

and a corresponding peak width w_p. From the ΔX and ΔY components, a relative amplitude and phase can be calculated via a polar transformation with:

$$\begin{aligned} \Delta R_\mathrm{T} &= \sqrt{\Delta X^2 + \Delta Y^2}, \\ \Theta_\mathrm{T} &= \arctan 2(\Delta X, \Delta Y). \end{aligned} \tag{6.7}$$

Note that the equation for ΔR_T is similar to Eq. 6.6 for ΔR_T. In fact, for a correct reference phase of the LIA, the ΔX and ΔY can be directly related to $R\Delta\Theta/\sqrt{2}$, and

$\Delta R/\sqrt{2}$.

The second algorithm (*algorithm 2*) finds the peaks using the SciPy *signal.find_peaks* function. As before, the primary time trace is selected based on the number of detected peaks at a given threshold. The detected peak positions are then used to run a peak fitting algorithm (SciPy *optimize.curve_fit*) for both (X, Y) time traces. A Gaussian shape with

$$f(t) = A\mathrm{e}^{\frac{-(t-t_0)^2}{2\sigma^2}} + D \tag{6.8}$$

is used to fit the peak, where A is the peak amplitude, and the peak width w_p at FWHM is given by $2.334 \cdot \sigma$. The Gaussian function was chosen because it provided a good fit for most of the peaks. The fitted amplitudes correspond to the Δ X and Δ Y values, which are then transformed into ΔR_T and Θ_T via Eq. 6.7.

These two algorithms performed differently on different datasets. The peak fitting (*algorithm 2*) performed better for small peaks and noisy data. Reversely, a brought distribution of peak widths could be better analyzed by *algorithm 1* (*signal.find_peaks*) such as peaks generated by water droplets in an oil suspension. These droplets were partially larger than the sensing volume, which resulted in a brought peak width distribution. Droplets bigger than the sensing volume deviated from the Gaussian peak shape, and the peak fitting algorithm performed poorly.

6.2.3 Phase Correction

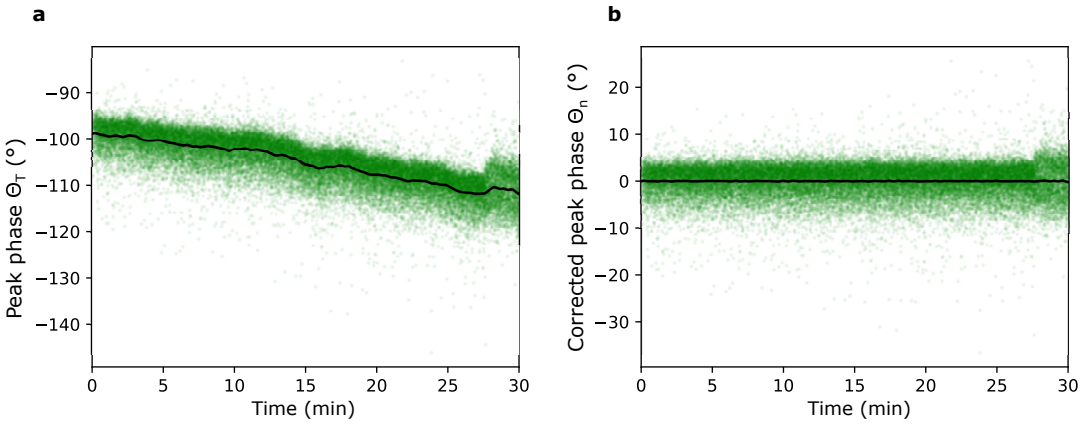

FIGURE 6.5: **Correction of a drifting peak phase: a**, Time-depended drift of the peak phase Θ_T and **b**, corrected peak phase Θ_n of the events displayed in Fig. 7.1. The black line displays the moving average.

A drift of the peak phase parameter Θ_T was commonly observed. To illustrate that drift, I present the time-dependent peak phase data of 1.75 µm-sized polystyrene beads detected over 30 min (analyzed in detail in section 7.1.2). Fig. 6.5a displays the evolution of the peak phase, Θ_T, over the time course of the experiment. The average phase value shifts by 13.1° throughout the experiment. The origin of that drift is not yet understood. However, a plausible cause is attributed to temperature fluctuations. These fluctuations alter the permittivity of the substrate, subsequently affecting the effective permittivity of the TL. Such a permittivity drift results in a corresponding drift in the resonance frequency, leading to the observed phase drift. To correct this drift, we subtract a moving average value plotted as a solid black line from the phase value Θ_T. The resulting corrected phase, Θ_n, is plotted in Fig. 6.5b.

As anticipated, this corrected phase consistently maintains a moving average of 0. From now on, in this thesis, I will only present and discuss the corrected peak phase parameter Θ_n.

Chapter 7

High Frequency Particle Detection

This chapter presents the results of single particle detection using the innovative sensor conceptualized and developed in this thesis, which operates at approximately 20 GHz. Current AC-based measurement setups still lack sensitivity, with the most advanced setups detecting particles as small as 200 nm at a frequency of 1.1 MHz and a maximum signal-to-noise ratio (S/N) of $\approx$ 6 [16]. The smallest detected particles within the GHz frequency range have been 500 nm polystyrene beads at 1 GHz, as reported by Bhat et al. [24]. The primary objective of the developed sensor is to increase the sensitivity to detect particles in the sub-100 nm regime eventually. Such a detection capability has numerous biomedical applications, like detecting and characterizing virions, proteins, or DNA. Various particle systems were investigated to characterize the sensor's capabilities, including polystyrene beads of different sizes, cells, droplets, and vesicles. Specifically, 1.75 µm polystyrene beads, significantly larger than the detection threshold, facilitated the examination of variables such as pump pressure and source power, thereby deepening our comprehension of the sensor's behavior.

7.1 Polystyrene Beads

For this measurement, polystyrene beads (Fluoresbrite Carboxy 17687) with a 1.75 µm diameter were suspended in Milli-Q water. The suspension was degassed for 30 minutes, which reduces bubble formation [121].

The sample was introduced into the chip by gradually increasing the inlet pressure to 40 mbar and applying a negative pressure at the outlet of up to -200 mbar. The chip's filling process was continuously monitored using both a microscope and S-parameter scans conducted with a VNA (see Fig. 5.1 and 4.4). The water shift in the S-parameter measurement is discussed in section 4.1.2. Once the channel was filled, the pressures were turned off, and the CPW probe was detached from the VNA and connected to the RF circuit.

The chip features sensing electrodes separated by 2 µm and a 12 µm fluidic channel wider than most channel designs. This prevents potential clogging by the 1.75 µm particles. The RF measurement frequency was adjusted to 18.326 GHz, the left flank of the resonance curve, and a power of 10.15 dBm. Before the LIA, the RF frequency was down-mixed to an IF frequency of 10 MHz. The flow was initiated by increasing the suction pressure at the outlet to -200 mbar. The particle flow was verified with a fluorescent microscope.

The LIA measured the Y and X time traces at a sampling rate of 84000 samples per second and a 5 kHz demodulation BW. Three parameters were obtained for each

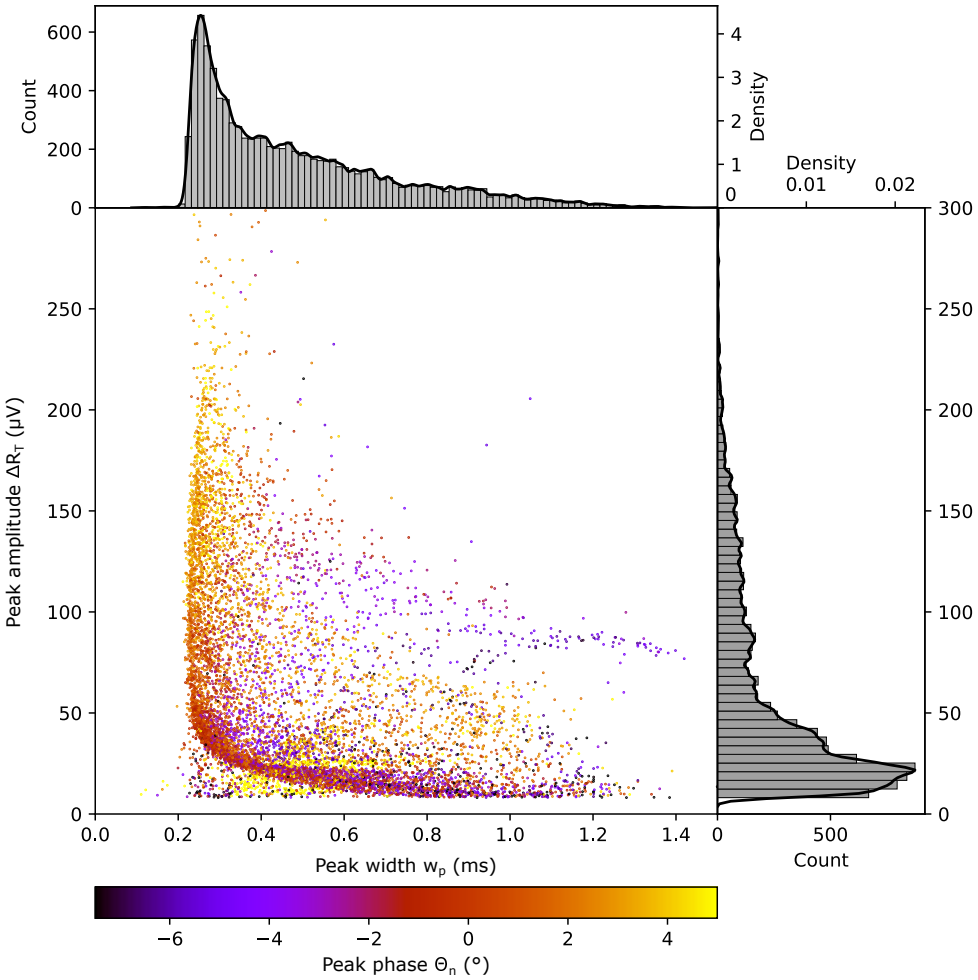

FIGURE 7.1: **Peak amplitude and width analysis of 1.75 µm polystyrene beads:** Scatter plot of peak amplitude ΔR_T against peak width w_p detected at 18.326 GHz. Every point represents an individual translocation event. Histograms and kernel density estimation are located above and to the right of the scatter plot. The color encodes the corrected peak phase Θ_n .

particle using *algorithm 1*: the peak amplitude ΔR_T, corrected phase Θ_n, and peak width w_p. The peak detection algorithm was applied with a threshold of 8 µV, which is well above the noise floor ($\sigma_{noise} = 0.50$ µV). As a result, 9974 peaks were detected during 150 seconds. The noise level is quantified by the standard deviation of the amplitude trace R, based on 600 data points without any peaks.

7.1.1 Peak Parameter: Amplitude and Width

Figure 7.1 shows a typical L-shaped scatter plot of peak amplitude ΔR_T versus peak width w_p. A similar peak width vs. amplitude dependence was reported by M. Nikolic-Jaric et al. [52]. Histograms and kernel density estimation can be found to the right and above the scatter plot. Each data point on the scatter plot is color-coded based on the corrected phase. The corrected phase was discussed in section 6.2.3.

The amplitude's broad range, spanning several orders of magnitude, is attributed to the non-uniform electric field within the sensing volume. The electrodes have a

thickness of approximately one µm, and the channel extends 7 µm above the electrodes. Above the electrodes, the electric field strength reduces strongly towards the top channel wall. The relationship between the electric field intensity and signal amplitude is described by Eq. 2.62. The same-sized particle induces a smaller capacitive change as the electric field reduces. Consequently, particles that translocate further away from the electrodes result in smaller peaks. For subsequent sensor designs, the goal is to limit the sensing volume exclusively to the region between the electrodes.

In the scatter plot, particles moving through that volume correspond to peaks with the highest amplitude ΔR_T. A conservative estimate of the S/N in that region is estimated by assuming that the S/N should be higher than the highest 1-percentile of detected peaks, resulting in $\mathrm{S/N}_{1\%} = 199.9\,\mu\mathrm{V}/0.5\,\mu\mathrm{V} = 399.8$. The S/N is calculated using the following formula:

$$\mathrm{S/N} = \frac{\Delta R_\mathrm{T}}{\sigma_\mathrm{noise}}. \tag{7.1}$$

The detected particles exhibit peak widths ranging from 0.2 ms to roughly 1.4 ms. Two phenomena can explain this range. First, particles that translocate further away from the electrodes experience a smaller electric field gradient (i.e., the electric field is less confined), which results in a broader peak width. Second, within the microfluidic channel, particle flow velocity is not uniform. The flow is established by applying a pressure difference between the inlet and outlet of the fluidic chip. This kind of pressure-driven, steady-state flow in a microfluidic channel is called Poiseuille flow. In rectangular channels, Poiseuille flow has a velocity field that is maximal in the center and reduces towards the walls of the channel.

The combined effects of the electric field distribution and the flow velocity profile within the channel give rise to the L-shaped scatter plot. Each translocation position in the sensing volume can be mapped to a point in the scatter plot. The peak amplitude encodes the particle's distance from the electrodes. In contrast, the peak width at the corresponding amplitude represents the distance from the channel walls. Therefore, the scatter plot can be understood as a transformed representation of the particle's translocation position in the sensing volume.

In the following, I will briefly describe the phase-changing patterns in Fig. 7.1. A comprehensive phase analysis is reserved for the subsequent section, introducing a dataset with more data points. These points allow a deeper exploration of phase dependencies, particularly at the rare translocation positions situated to the right of the L-shape.

Two trends in the phase are observable. The phase reduces with peak amplitude and peak width from 5° to -5°. As a result of the interferometric transformation, the phase should be insensitive to the size or position of translocating particles and solely sensitive to the material properties (permittivity contrast). Consequently, all polystyrene particle peaks should have the same phase, which is not the case. That contradiction will be discussed in the next chapter. Furthermore, a cluster of yellow dots with a phase above 5° is observed around a width of 0.5 ms and an amplitude of 25 µV. These data points do not fit into the L-shape and correspond to double peaks. For these peaks, the phase and amplitude can not be determined correctly because the superposition of two peaks influences the amplitude and phase-determining algorithm.

7.1.2 Peak Parameter: Phase

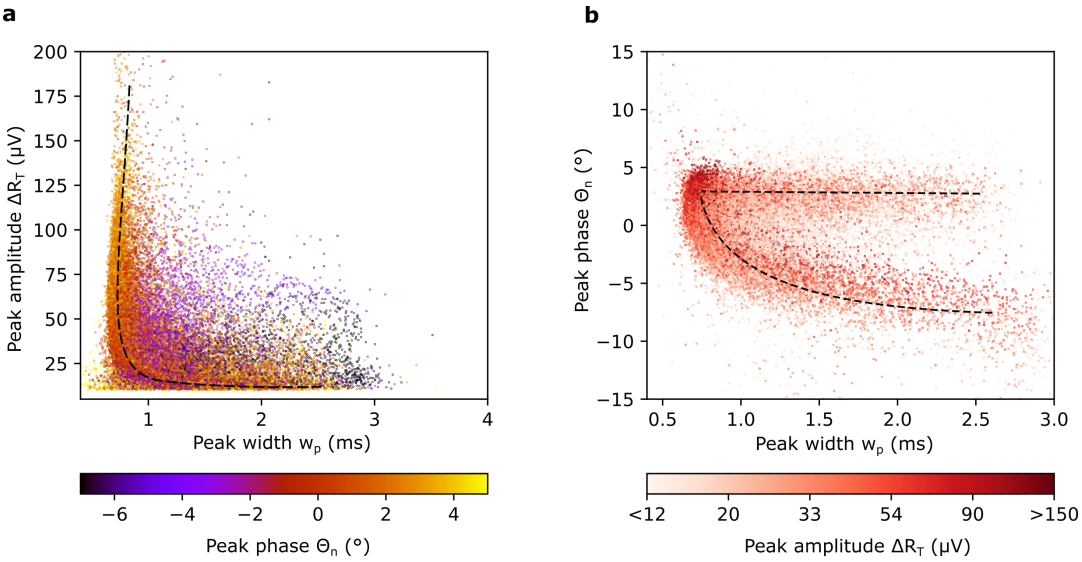

FIGURE 7.2: **Analysis of the corrected peak phase of 1.75 µm polystyrene beads:** Large data set recorded over a time period of 30 min at 18.326 GHz. In total, 43971 translocation events were captured. **a**, Amplitude ΔR_T against peak width w_p: The color coding represents the phase Θ_n of the detected particles. **b**, Phase Θ_n against peak width w_p: The color encodes the peak amplitude ΔR_T. The dotted lines indicate trends in the data.

In Fig. 7.2, I present an additional data set of the same experiment recorded over a longer time span of 30 min and a lower suction pressure of -70 mbar. In total, a large number of 43971 peaks were detected. The last data set was great for showing the L-shaped scatter distribution and discussing the dependence between peak amplitude, peak width, and the translocation position. This data set has more data points. Thus, more points are located right of the L-shape, which allows us to analyze the phase dependency at these rare translocation positions.

As discussed earlier (section 6.1.1), the interferometer transforms the phase into a variable that is sensitive to the material properties (dielectric contrast) and not to the size or the position of the particle in the fluidic channel. As a result, all polystyrene particle peaks should have the same phase. However, this is not the case. Instead, several phase-changing patterns can be identified in Fig 7.2a. The color shifts from violet to yellow as the peak amplitude increases, representing an increase in phase from -5° to 5°. This pattern is a positive phase change towards the channel's top. A less clear phase dependence is present towards a higher peak width. That effect is further studied in Fig. 7.2b, which displays the peak phase Θ_n vs. peak width w_p scatter plot with the peak amplitude color-coded with a red gradient. Dotted black lines serve as guides to the eye, indicating trends in the data set.

With increasing peak width, the peak phase splits into high or low phase values. That splitting is independent of the peak amplitude (i.e., translocation height). A possible cause for that splitting might be an influence of the particle's horizontal translocation position on the phase. For example, the phase might change from the channel center towards the walls or from the left channel wall to the right channel. This dependency would also explain the increased phase splitting with higher peak width, as the peak width increases towards the sides of the channel walls.

A possible explanation for the changing phase might be a temperature gradient inside the channel. As discussed in section 2.3, water's dielectric properties are highly sensitive to temperature changes, particularly near the relaxation frequency of water, where our experiment is conducted [50]. A particle of the same size in water at different temperatures produces a different permittivity contrast. The sensing signal heats the chip, and the chip heats the fluid through the channel walls, which could lead to a temperature gradient inside the channel. This temperature gradient could cause the observed variations in the phase of the detected particles. Further investigations would be worth conducting to confirm this hypothesis and understand the exact mechanism behind the observed phenomenon.

7.1.3 Outlet Pressure

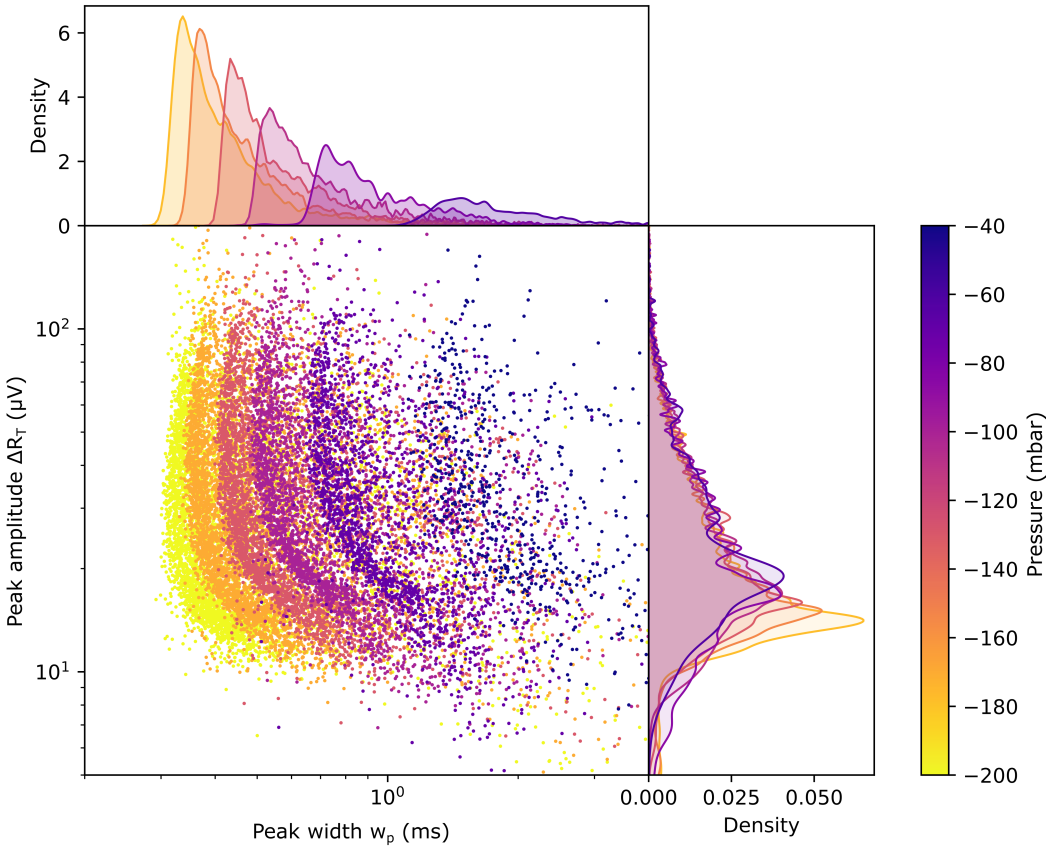

FIGURE 7.3: **Influence of the outlet pressure on peak parameters:** The scatter plot shows the relationship between the outlet pressure and the amplitude (ΔR_T) and peak width (w_p) of 1.75 µm polystyrene beads detected at 18.326 GHz. Each point represents a single translocation event. The pressure varied from -40 to -200 mbar, with the color indicating the different pressure values. The experiments were conducted for 60 seconds. Kernel density estimates are located above and to the right of the scatter plot.

In this section, we investigate the effect of increasing outlet suction pressure. The measurement setup and particle suspension are identical to the previous chapter. The inlet pressure is turned off while the suction pressure varies from -40 to -200 mbar. For each pressure, the measurement is conducted for 60 seconds. Fig. 7.3

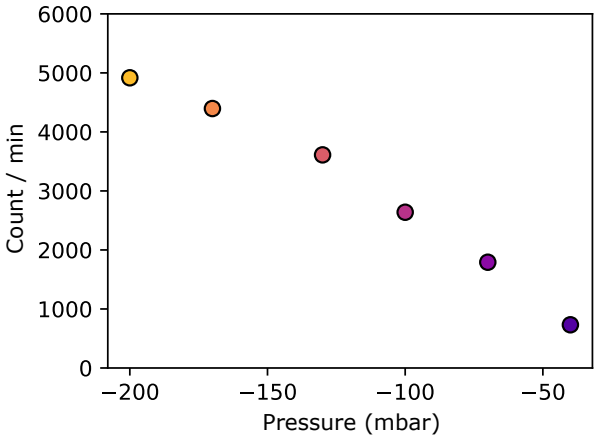

FIGURE 7.4: **Number of translocation events at various outlet pressure:** In a flow experiment with 1.75 µm polystyrene beads, the outlet pressure was adjusted between -40 and -200 mbar. The number of translocation events is counted at each pressure over 60 seconds. The number corresponds to the cumulative sum of the events displayed in Fig. 7.3.

displays the scatter plot and kernel density estimations of translocation events color-coded by the pressure value. As suction pressure increases, the characteristic L-shaped scatter plot of ΔR_T vs. w_p shifts to narrower peak widths. The smallest peak width shifts from 0.3 ms to 1 ms. That is expected as the higher pressure results in faster particle translocation with reduced peak width. The kernel density plot above the scatter plot confirms the shift in peak width. Additionally, the density plot on the right displays the peak amplitude distribution. As previously mentioned, the peak amplitude is related to the particle's position in the sensing volume. Notably, the distribution indicates a systematic increase in the number of peaks at amplitudes between 10-20 µV. These small amplitudes correspond to particles further away from the electrodes, suggesting that with increasing pressure, some particles translocate further away from the electrodes. This effect may be explained by the higher inertial lift force that particles experience at higher flow velocities, as reported in [122]. In Poiseuille flow, due to the curvature of the fluid velocity profile and its interaction with particles, the shear gradient lift force directs particles away from the channel center.

Fig. 7.4 illustrates the number of particles detected within 60 seconds at various pressure values. This number is calculated as the cumulative total of all events plotted in Fig. 7.3. As expected, the number of detected events increases with stronger suction. The initial increase in suction results in an approximately linear increase in detected particles, while at higher pressures, the linear relationship becomes less pronounced.

7.1.4 Source Power

The influence of source power on the signal amplitude is investigated. Identical to the previous sections, the translocation of 1.75 µm polystyrene beads is investigated. The input and output pressure, as well as the duration of the experiment, were not the same for each source power. However, this did not affect the peak amplitude. Fig. 7.5a displays the scattering plots with the typical L-shape distribution that shifts to higher values as the amplitude increases. Fig. 7.5b shows the mean amplitude for all detected peaks for each source voltage. A linear relationship between source

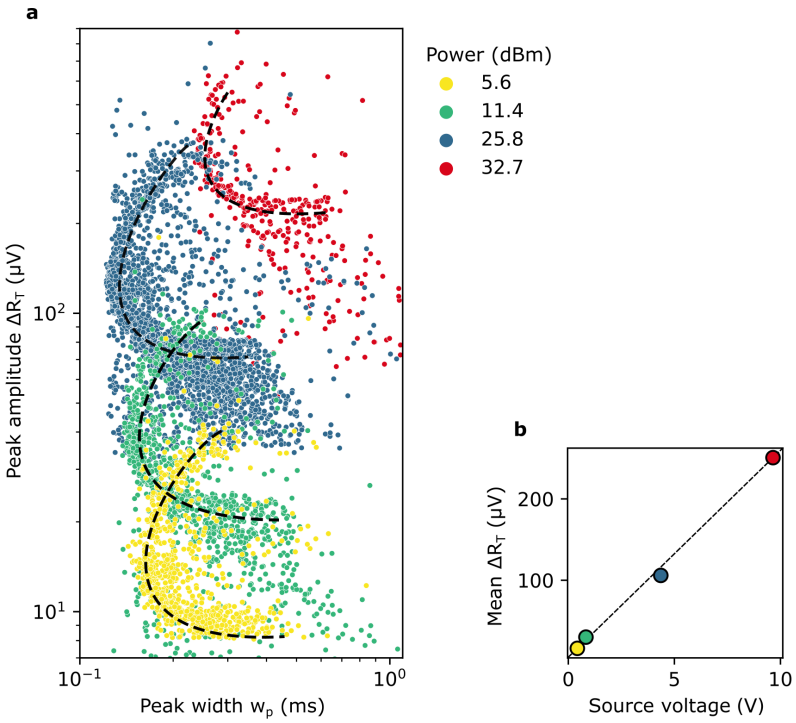

FIGURE 7.5: **Source power: a**, Scatter plot illustrating the relationship between peak amplitude (ΔR_T) and peak width (w_p) for various source powers. Dotted lines indicate the characteristic L-shape at different power levels. A difference in the input and output pressure at the highest power level is responsible for the shift in peak width. That shift is independent of the source power. The color coding represents the power level. **b**, The mean amplitude value for each power level (source voltage). A dotted line is a visual aid indicating the expected linear correlation.

voltage and mean amplitude is expected if no non-linear effects, such as heating or shunts, exist. The plot includes a dotted straight line indicating this linear dependency. The mean values follow the expected linear relation.

The variation of suction pressure and source power resulted in a shift of the scatter distribution along the peak width and amplitude axis. During these experiments, the L-shaped distribution remained consistent, substantiating that this distribution is not coincidental and represents the flow profile within the nanochannel.

7.1.5 Polystyrene Beads with a Diameter of 200 nm

In this section, I evaluated the sensitivity of our detection system using polystyrene beads (Polybead Dyed Yellow 15707) with a diameter of 200 nm. To the best of my knowledge, the size of these beads is among the smallest detected using AC signals. The beads were suspended in milliQ water, and the suspension was degassed for 30 minutes to reduce bubble formation in the microchannels.

The sample flow was monitored using a fluorescent microscope, and the chip used in the experiment featured sensing electrode tips separated by 3 µm and a fluidic channel width at the sensing region of 4 µm. The RF measurement frequency was adjusted to the left flank of the resonance curve at 18.77 GHz at a source power of -4.8 dBm. The RF frequency was mixed down to an IF frequency of 10 MHz.

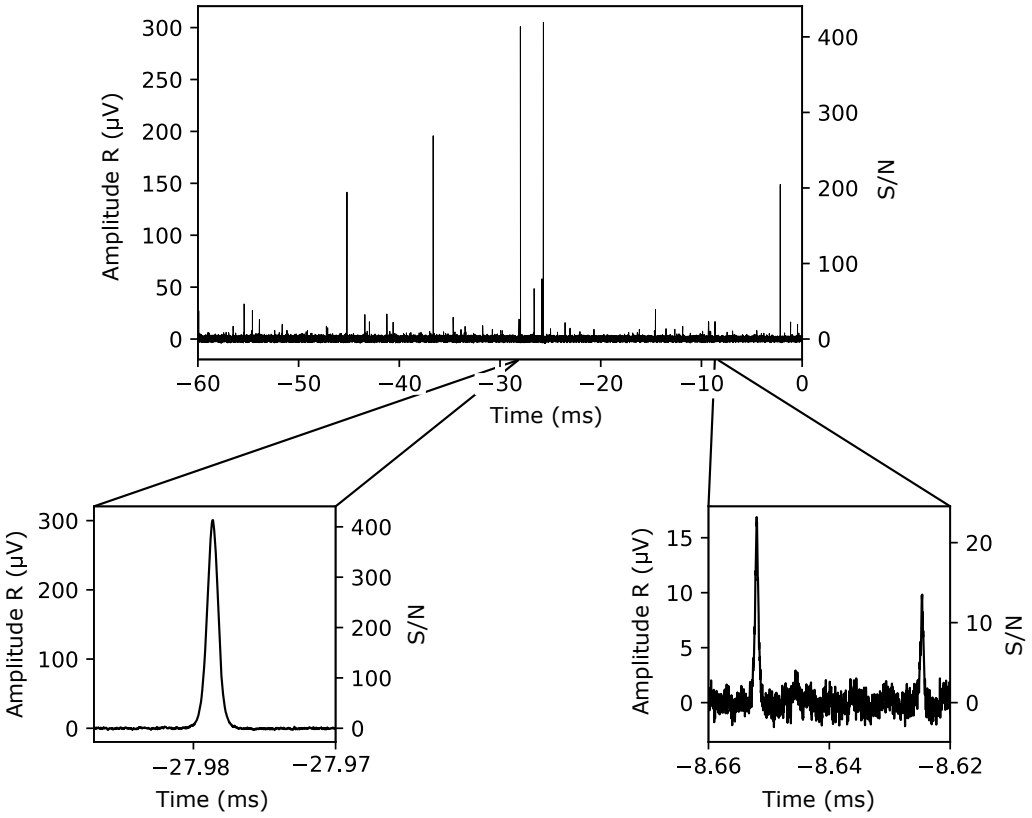

FIGURE 7.6: **Detection of 200 nm polystyrene beads:** The amplitude R signal, measured at a 5 kHz bandwidth, is presented. A 1 Hz high-pass filter is applied to remove the DC offset. The right axis shows the signal-to-noise ratio (S/N) for the corresponding peak height, with a noise level of $\sigma_{\text{noise}} = 0.73$ µV, calculated using the standard deviation of 600 data points. Beneath the primary graph, a detailed view of three distinct peaks highlights the variability in peak amplitudes.
Figure reproduced from my publication [1], © 2023 IEEE

During this measurement, a strong phase noise component at 27.3 Hz was observed, negatively affecting the quality of the X and Y-traces compared to the raw amplitude R trace. The source of this phase noise is currently unknown. As a result of the degradation of the X and Y-traces caused by the phase noise, the standard peak analysis routine was not suitable. Instead, the non-corrected raw amplitude R trace was analyzed. In this specific measurement, the peak change ΔR_{T} was observed to point in a similar direction as the raw signal R, which allowed for the evaluation of the raw amplitude signal with only minimal distortions.

Fig. 7.6 displays the amplitude R trace after a 1 Hz highpass filter was applied to remove the baseline offset. The data was recorded with a rate of 50k samples per second and a 5 kHz demodulation BW. The right axis displays a S/N ratio for a given peak amplitude. The noise level, calculated as the standard deviation of the amplitude trace R based on 600 data points without any peaks, is $\sigma_{\text{noise}} = 0.73$ µV.

The peak detection algorithm was applied with a threshold of 7 µV, which is well above the noise floor. In the 60-second time trace, 77 peaks were detected with a S/N ratio above the value of 6.9. Two peaks are depicted at the bottom of Fig. 7.6. The highest peak has a S/N ratio of 417. To the best of our knowledge, this represents a significant 69-fold improvement of the signal-to-noise ratio compared to previously

reported studies of 200 nm polystyrene beads, currently considered the smallest AC-based detected particles [16].

7.1.6 From Peaks to Flow Profiles

In section 7.1, the data of 9974 translocation events was discussed. The large number of detected peaks encodes information on flow velocities in various positions within the channel. A transformation is performed to reveal the velocity profiles. The peak amplitude ΔR_T and peak width w_p are transformed to channel height h and flow velocity v_p, respectively. This transformation results in a height profile of particle flow velocities. However, it should be noted that it is a first attempt based on several approximations and, thus, likely to have significant errors. Its purpose is solely to establish a proof of concept.

Peak Amplitude to Translocation Height

In section 3.8, I derived that the change in sensor signal $|\Delta S_{11}|$ (i.e., ΔR) at the left flank of the resonance frequency is linearly related to the change in real permittivity $\Delta\varepsilon'$ within the sensing volume, with $|\Delta S_{11}| \propto \Delta\varepsilon'$. Assuming $\Delta\varepsilon'' = 0$, the peak amplitude ΔR_T detected by the LIA described by Eq. 6.6 simplifies to:

$$\Delta R_\mathrm{T} = \frac{|\Delta S_{11}|}{2}, \quad \text{for } \Delta\varepsilon'' = 0. \tag{7.2}$$

This equation indicates that the signal detected by the LIA is approximately linearly related to the real permittivity change ($\Delta R_\mathrm{T} \propto \Delta\varepsilon'$).

Next, we derived the relationship between the real permittivity and the change in capacitance, described by the Clausius-Mossotti factor K_CM (see Eq. 2.63). The influence of the imaginary permittivity is neglected, and for cases where $\varepsilon'_p \ll \varepsilon'_l$, such as the real permittivity of water and polystyrene beads with $\varepsilon'_l = 40$ and $\varepsilon'_p = 2.5$ [50, 123], the Clausius-Mossotti factor K_CM can be simplified to:

$$K_\mathrm{CM} = \frac{\Delta\varepsilon'}{2\varepsilon'_l}, \quad \text{for } \varepsilon'_p \ll \varepsilon'_l$$

where $\Delta\varepsilon' = |\varepsilon'_p - \varepsilon'_l|$. From Eq. 2.62 with the modified Clausius-Mossotti factor, follows a linear dependency between the change in capacitance and the change in real permittivity ($\Delta C \propto \Delta\varepsilon'$). Furthermore, Eq. 2.62 also states that the capacitance change is proportional to the electric field squared ($\Delta C \propto |E^2_\mathrm{rms}|$). The previously discussed relations can be combined to:

$$\Delta R_\mathrm{T} \propto \Delta|S_{11}| \propto \Delta\varepsilon' \propto \Delta C \propto |E^2_\mathrm{rms}| \tag{7.3}$$

In the following, I discuss the electric field strength to height dependency. For a first approximation, I assumed that dependency is $|\vec{E}| \propto 1/h$. This dependency has a smaller gradient than that of a point charge ($\propto 1/h^2$) and a stronger gradient than that of two parallel plates (constant value). However, this approximation needs to be refined in the future through FEM simulation of the electric field or by using analytical solutions such as the conformal mapping approach presented in reference [124].

The resulting transformation between the peak amplitude and height is given by:

$$h = \alpha_1 \cdot \frac{1}{\sqrt{\Delta R_T}}, \tag{7.4}$$

where α_1 is a proportionality factor.

From Peak Width to Flow Velocity

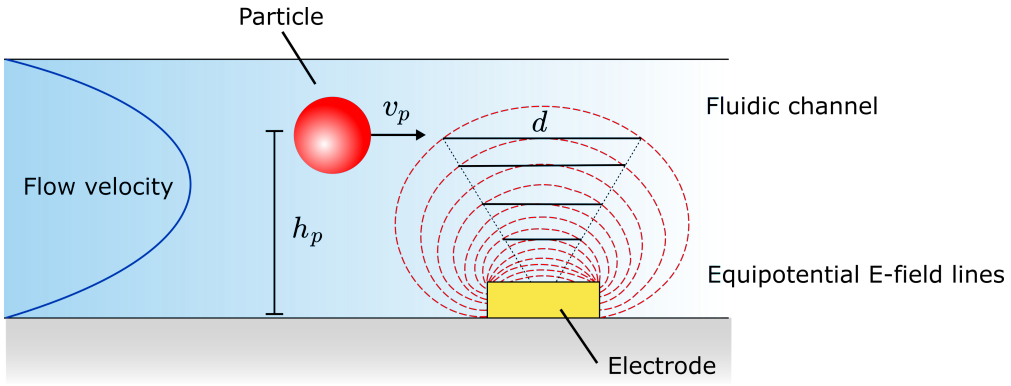

FIGURE 7.7: **Dependence between translocation height and peak width:** This cross-sectional sketch of a fluidic channel highlights the translocation of a polystyrene bead close to the electrodes. The blue line depicts the Poiseuille flow, while the red lines illustrate the electrode fringing fields represented by equipotential electric field lines. The horizontal lines d above the electrode illustrate the increasing distance a particle must travel to cross an equipotential line. That distance represents the detected peak width w_p, and with increasing height h_p, the peak width w_p increases.

In the following, I propose a second transformation between the peak width w_p and the particle velocity v_p. The sketch in Fig. 7.7 illustrates a cross-section view along the fluidic channel, with the electrodes facing in and out of the view plane. This illustration highlights the complexity behind the transformation, which is not just the inverse of the peak width.

A particle at a height h_p translocates through the channel at velocity v_p. The red lines indicate equipotential electric field lines resulting from the fringing fields of the sensing capacitance. The horizontal lines above the electrode illustrate the distance d a particle needs to travel to cross an equipotential electric field line. The distance required to cross an equipotential line increases as the height increases. Each translocating particle has an equipotential line that corresponds to the detected peak width w_p at FWHM. This equipotential line is higher for increasing translocation height h_p. As a result, the corresponding distance d increases with increasing height.

The factor at which the distance d increases with height h_p can be deduced from geometrical considerations. We assume that the distance d increases as illustrated by the dotted line. The relation between the distance and height can be calculated with trigonometric identities as

$$d = 2h_p \tan(\phi), \tag{7.5}$$

with ϕ being the angle between the dotted and vertical lines. That distance d value will be subsequently used to normalize the peak width w_p. After normalization, the

resulting value is inversely proportional to the peak velocity. Together with Eq. 7.4, the transformation from peak width w_p to particle velocity v_p becomes

$$\begin{aligned} v_p &\propto \left(\frac{d}{w_p}\right) \\ \Rightarrow v_p &\propto \left(\frac{2h_p \tan(\alpha)}{w_p}\right) \\ \Rightarrow v_p &= \alpha_2 \left(\frac{1}{w_p\sqrt{\Delta R_\mathrm{T}}}\right), \end{aligned} \tag{7.6}$$

where α_2 is a proportionality factor.

Poiseuille Flow Profile

The velocity field in a Poiseuille flow is a solution of the Navier-Stokes equations. For a rectangular channel with a cross-section of height h, width w, and a channel length L, the velocity field is given by [125]:

$$v_x(y,z) = \frac{4h^2\Delta p}{\pi^3\eta L}\sum_{n,odd}^{\infty}\frac{1}{n^3}\left[1-\frac{\cosh(n\pi\frac{y}{h})}{\cosh(n\pi\frac{w}{2h})}\right]\sin\left(n\pi\frac{z}{h}\right). \tag{7.7}$$

Δp is the pressure difference, η is the viscosity of the medium, and x,y, and z are the coordinate axes along the channel length, width, and height, respectively.

The Hagen-Poiseuille law, given by

$$\Delta p = R_\mathrm{hyd} Q, \tag{7.8}$$

allows for the calculation of the pressure difference across a channel using the hydraulic resistance R_hyd and the flow rate Q. The fluidic chip can be divided into three microchannels: the inlet, outlet, and sensing channels, which are connected in series. These three channels form the total hydraulic resistance of the chip, with $R_\mathrm{hyd,tot} = R_\mathrm{hyd,1} + R_\mathrm{hyd,2} + R_\mathrm{hyd,3}$. The inlet and outlet channels have a length of $L_{1,2} = 3.5$ mm, a width of $w_{1,2} = 40$ µm, and a height of $h_{1,2} = 7$ µm. The sensing channel has a length of $L_3 = 50$ µm, a width of $w_{1,2} = 12$ µm, and a height of $h_{1,2} = 7$ µm. The hydraulic resistance for such a rectangular channel is given by [125]

$$R_\mathrm{hyd,rec} = \frac{12\eta L}{1-0.63(h/w)}\frac{1}{h^3 w} \tag{7.9}$$

By using Eqs. 7.8 and 7.9 with a pressure difference of 240 mbar, the flow rate is calculated to be $Q = 3.4\cdot 10^{-12}$ m^3/s. The pressure difference across the sensing channel is 7.78 mbar.

Finally, in Fig. 7.8 the flow velocities of polystyrene beads analyzed in section 7.1 are compared to the theoretical water flow velocity profile. Double peaks separated by less than 2.4 ms have been removed from the data set. A scattering plot is generated using the transformed peak amplitude, which corresponds to the translocation

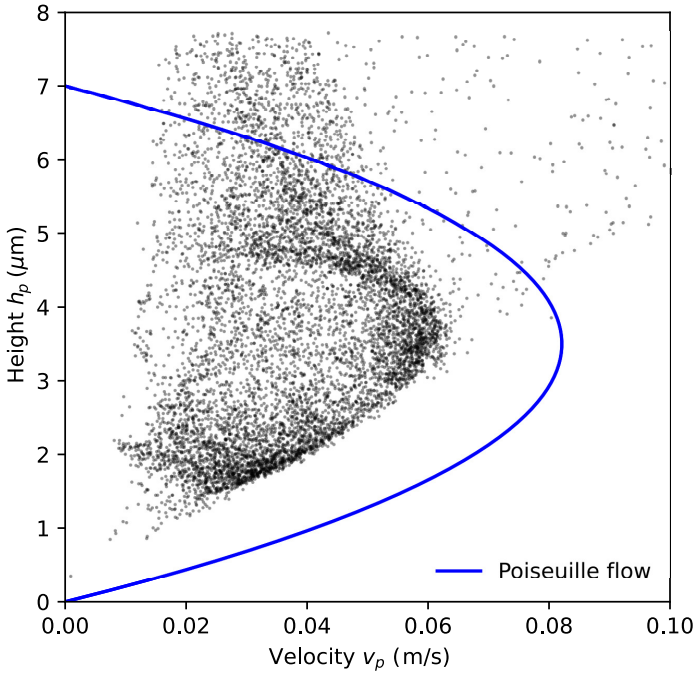

FIGURE 7.8: **Particle flow velocity profile:**. The data for 1.75 µm polystyrene beads from Fig. 7.1 is transformed from peak amplitude to translocation height h_p, and from peak width to flow velocity v_p using Eq. 7.4 & 7.4, respectively. The normalization factors are set to $\alpha_1 = 22$ and $\alpha_2 = 1 \cdot 10^{-4}$. The blue line represents the theoretical water velocity profile (Eq. 7.7) for a Poiseuille flow in a rectangular channel measuring 12 µm in width and 7 µm in height under a pressure drop of 7.78 mbar. The similarities between both flow profiles suggest the efficacy of the sensor and transformation method in assessing flow profiles within microfluidic channels.

height h_p, and the peak width, which corresponds to the flow velocity v_p, as determined by Eq. 7.4 and 7.6 respectively. The normalization factors α_1 and α_2 were adjusted to 22 and 10^{-4} respectively. A blue line shows the theoretical Poiseuille flow of a rectangular channel with a width of 12 µm, a height of 7 µm, and a pressure drop of 7.78 mbar. The densest areas in the scatter plot reveal a parabolic distribution. That parabolic distribution is narrower and bends stronger towards the middle of the channel compared to the water velocity profile. A similar particle velocity profile has been previously described in the literature [126]. However, some events above 4 µm appear to be faster than the maximum water velocity, which is impossible. This discrepancy is likely due to inaccuracies in the transformation model at high particle translocation distances. Additionally, the parabolic distribution appears to have a shadow towards higher heights, which may be caused by particles translocating further to the sides of the 12 µm channel and experiencing lower electric fields, an effect that is not accounted for in the peak amplitude to translocation height transformation.

In Fig. 7.9, the previously discussed transformations are applied (with the same normalization factors) to the data obtained for 1.75 µm polystyrene beads at various outlet pressures (see section 7.1.3). The scatter plot displays the translocation height h and flow velocity v_p for each translocation event. The color encodes the outlet pressures between -40 mbar and -200 mbar. The distribution of the translocation events reveals a parabolic flow velocity profile for each pressure. With increasing suction,

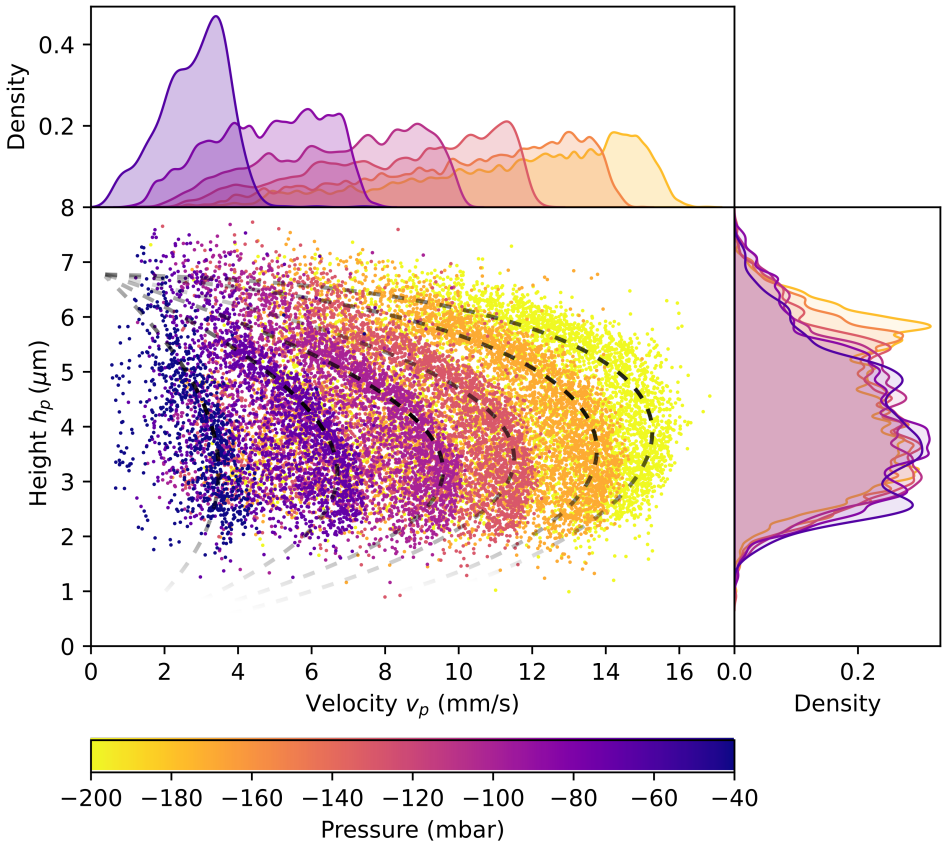

FIGURE 7.9: **Particle flow velocity profile for various pressures:**. The data for 1.75 µm polystyrene beads and various outlet pressures from Fig. 7.3 is transformed from peak amplitude to translocation height h_p, and from peak width to flow velocity v_p using Eq. 7.4 & 7.4, respectively. The normalization factors are set to $\alpha_1 = 22$ and $\alpha_2 = 1 \cdot 10^{-4}$. The dotted black lines are guides to the eye indicating parabolic event distributions. Kernel density estimates are located above and to the right of the scatter plot.

the profile shifts to higher velocities. That phenomenon is also evident in the kernel density estimation above the scatter plot. In contrast to the data presented in Fig. 7.8, the parabolic distribution is discontinued at a height below 2.5 µm. An explanation for that feature could be the attachment of polystyrene beads to the electrodes, which block the translocation volume close to the electrodes. That blockage could result in a lack of translocation events below 2.5 µm. After the flow experiments, the electrode tips were inspected with light microscopy, which revealed that they were covered with beads. Hence, the developed technique might help determine electrode particle contamination. A kernel density estimate is located to the right of the scatter plot. That plot describes the translocation height distribution. With increasing pressure, some particles translocate further away from the electrodes. This effect may be explained by the higher inertial lift force that particles experience at higher flow velocities, as reported in [122]. In Poiseuille flow, due to the curvature of the fluid velocity profile and its interaction with particles, the shear gradient lift force directs particles away from the channel center.

In conclusion, the present study has shown that it is possible to transform the peak data from the LIA into particle flow profiles. The transformation models used in this

study were based on rough approximations, and further research is needed to develop more accurate models. The dependence between the electric field and channel height could be improved through FEM simulations or by using a conformal mapping approach as presented in reference [124]. Additionally, the particle velocity data could be improved by introducing a second pair of electrodes and evaluating the time between both translocation events. Overall, this study has provided proof of concept for transforming peak data into particle flow profiles.

7.2 Cells

Recently, the GHz-regime (γ-dispersion) of cells has garnered increasing scientific attention. One reason for this is that the unique intracellular properties of cells become accessible only at frequencies exceeding 10 MHz, a phenomenon attributed to the shorting of the membrane capacitance[15]. Numerous studies indicate that cell measurements at these high frequencies can effectively differentiate between diverse cell types and states, including the identification of cancerous cells[19, 20, 21, 22].

The novel sensor combined with an interferometric setup gives rise to detection sensitivities, which allow for the simultaneous detection of cells and cell debris. This detection capabilities are showcased for cells derived from human induced pluripotent stem cells (iPSCs) and their cell debris in PBS. IPSCs enable the study of human cells without restrictions in cell availability and without the ethical and political controversies related to the more commonly used embryonic stem cells [127].

For cell detection, the channel dimensions of the sensing area are designed to be 12 µm wide and 7 µm high, with electrodes separated by 8 µm (see image displayed in Fig. 4.3). This design allows cells to squeeze through the microfluidic channel and fill the sensing area. However, because most cells have a diameter larger than 7 µm, they often become stuck or burst in the entrance region of the chip. The narrow channel design, which causes cells to get stuck or burst in the entrance region of the chip, is utilized as an advantage to demonstrate the detection capabilities of the proposed sensor, detecting both intact cells and smaller cell debris.

The particle loading procedure is the same as the polystyrene beads experiment previously described. S-parameters are continuously recorded while the channel fills with the sample until the water shift is detected. The CPW probe tip is connected to the RF circuit. A positive pressure is applied at the inlet, and negative pressure at the outlet. High input and output pressures (up to 200 mbar and -300 mbar) were used to prevent cells from clogging the microfluidic channel. The flow of the cells was confirmed with a microscope. The measurement frequency was set to 18.72 GHz on the left flank of the resonance curve, with a power of -0.4 dBm. A measurement BW of 10 kHz with a sampling rate of 54k samples per second was selected.

Fig. 7.10 shows the raw amplitude R time trace collected over 5 minutes. Peaks above 1.5 mV correspond to whole cells; peaks below that value represent cell debris. A microscope observation confirms that the prominent peaks correspond to intact cells. Due to the blockage of the channel, the particle flow is not continuous. That can be seen by a burst of cell peaks around -50 seconds and the absence of peaks between -300 and -250 seconds.

Algorithm 2 detected 297 peaks with a detection threshold above 10 µV. Out of these, 47 were whole cells, and 250 were cell debris. Fig. 7.11 presents the peak amplitude,

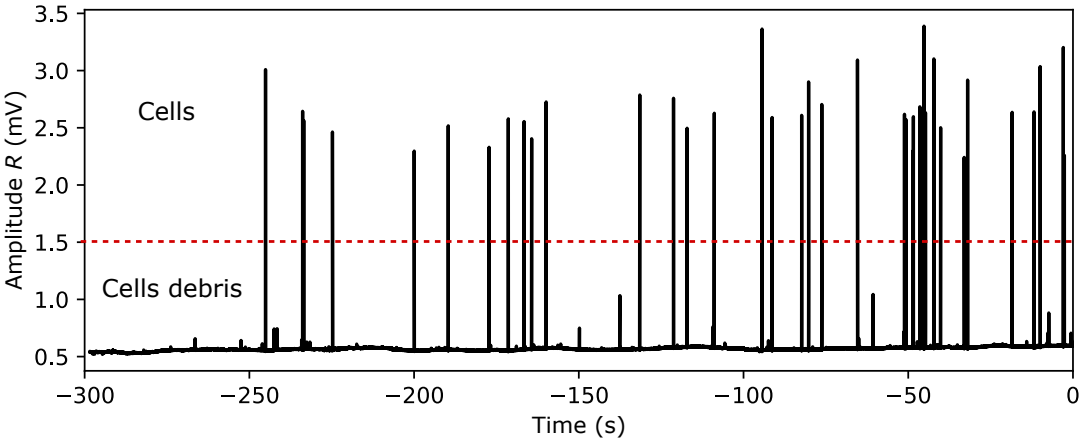

FIGURE 7.10: **Detection of pluripotent stem cells:** Time-trace amplitude R showcasing the differentiation between human induced pluripotent stem cells and cell debris in a PBS buffer solution. Peaks exceeding 1.5 mV are attributed to cells, while those below are identified as cell debris.

width, and phase data in scatter plots. Histograms and kernel density estimations are plotted above each scatter plot.

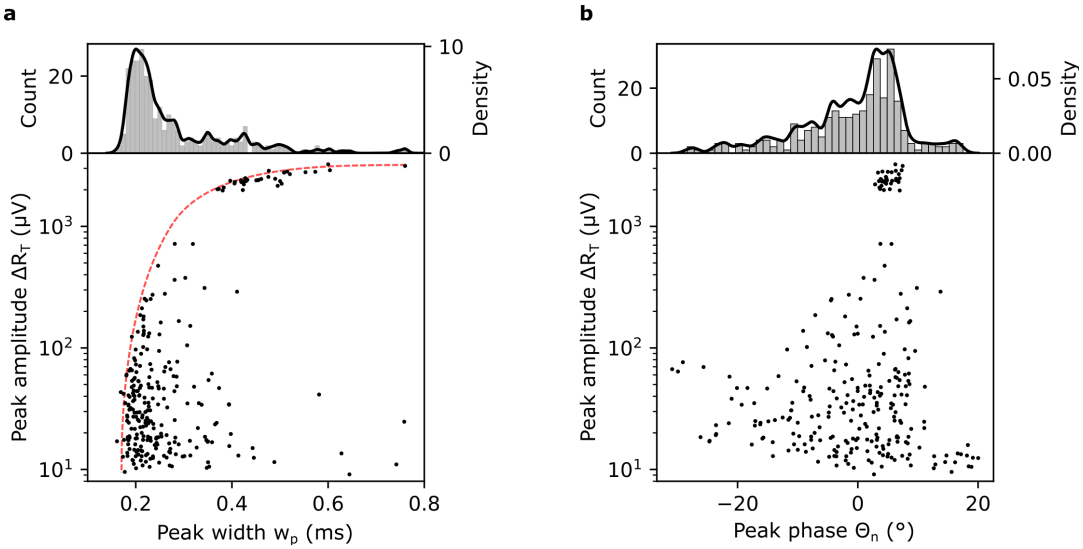

FIGURE 7.11: **Cell peak parameters:** Scatter plots representing flow experiments with human induced pluripotent stem cells and cell debris. **a**, Peak amplitude ΔR_T against the peak width w_p, and **b**, peak amplitude against the peak phase Θ_n. A histogram and a kernel density estimation are located above each scatter plot. The red dotted line serves as a visual guide, highlighting an observable trend.

Fig. 7.11a presents the peak amplitude ΔR_T versus the peak width w_p. Despite the logarithmic scale, the cell peaks above 1.5 mV are still distinct from the cell debris peaks. The peak amplitudes span nearly three orders of magnitude, from 10 µV to 3.119 mV. The noise level, calculated as the standard deviation of the amplitude trace R based on 100 data points without any peaks, is $\sigma_\mathrm{noise} = 0.83$ µV. The highest cell peak has a signal-to-noise (S/N) ratio of 3760.

The red dashed line indicates the narrowest peak widths at a given peak amplitude.

This line shifts towards broader peaks as the peak amplitude increases. That effect probably originates from the dependence between the particle's translocation height, electric field gradient, and the flow velocity profile. The previous chapters have discussed these effects in detail (see section 7.1.6). Additionally, the size of cells and cell debris varies significantly in this experiment, with larger particles having a lower flow velocity [126]. Also, with increasing size, particles induce a higher peak amplitude. Both effects lead to a peak width that increases with peak amplitude. That effect intensifies for cells as they need to squeeze through the sensing channel. The bigger the cell, the slower it moves through the sensing volume. That phenomenon can be seen in the scatter plot as the cell peak width strongly increases for higher cell peak amplitudes.

Unfortunately, as previously mentioned, the channel is susceptible to clogging, significantly reducing the flow velocity. This clogging may cause some broader peaks at small peak amplitudes.

Fig. 7.11b displays the peak amplitude ΔR_T vs. the corrected peak phase Θ_n. The cell peaks are above 1.5 mV in amplitude and have a phase concentrated between 4° and 8°. In contrast, cell debris peaks have a broader phase distribution (-30° to 20°), possibly due to different permittivity values among the debris components. However, the influence of translocation position on phase, seen in the previous polystyrene bead experiment, may also play a role. The phase of the identical particles varied from -15° to 15° depending on the translocation position. Thus, both effects, the particle's permittivity, and the translocation position, likely influence the phase. Further investigation is required to determine the contribution of each effect.

7.3 Droplets

Droplet-based microfluidic systems offer numerous advantages due to their ability to precisely control the chemical or biological condition in a tiny volume (i.e., droplet). Droplets allow for the measurement of individual molecules and cells [128]. Additionally, minimal diffusion of analytes and dilution within the droplets leads to a stable microenvironment. Such droplet-based systems have been used for long-term monitoring of cell cultures [129]. The high-throughput generation and detection of droplets facilitate large-scale screening of samples and reaction conditions, including directed evolution [130] and drug discovery [131]. Furthermore, droplets can be manipulated by merging, splitting, and sorting, which allows for multi-step reactions. The enhanced mass and heat transfer in droplets also accelerate reaction kinetics for chemical synthesis [132]. Droplet-based microfluidic systems are also cost-effective, as a single device can generate millions of droplets.

Most commonly, droplets are monitored by optical means with fluorescent imaging or absorption spectroscopy [133]. Alternatively, electrical sensing can be used for the label-free detection of droplets. For example, droplets with agglutinated red blood cells were detected at 50 kHz to 2 MHz frequencies with an inflow sampling rate of 135 Hz [134]. Furthermore, Kubra Isgor et al. demonstrated an inexpensive droplet capacitive detection system [135]. They quantified ethanol concentrations inside nano-liter droplets at 32 kHz frequency and a sampling rate of 50 Hz.

In the following, the detection of droplets with the sensor developed in this thesis is presented. Water droplets are generated in a fluorinated oil (FluoSurf High-Performance oil, *Darwin Microfluidics*) with a surfactant HFE 7500 (Novec 7500) concentration of 2 w/w %. The droplets are generated with a droplet-generating chip (Fluidic 947, *microfluidic-ChipShop*) with a droplet diameter of 15 µm. The measurement frequency is adjusted to 18.720 GHz with a power of -8 dBm, a BW of 100 kHz, and the sampling rate is 55 kHz. The measurement speed is up to three orders of magnitude faster than the previously reported electrical sensing of droplets [134, 135].

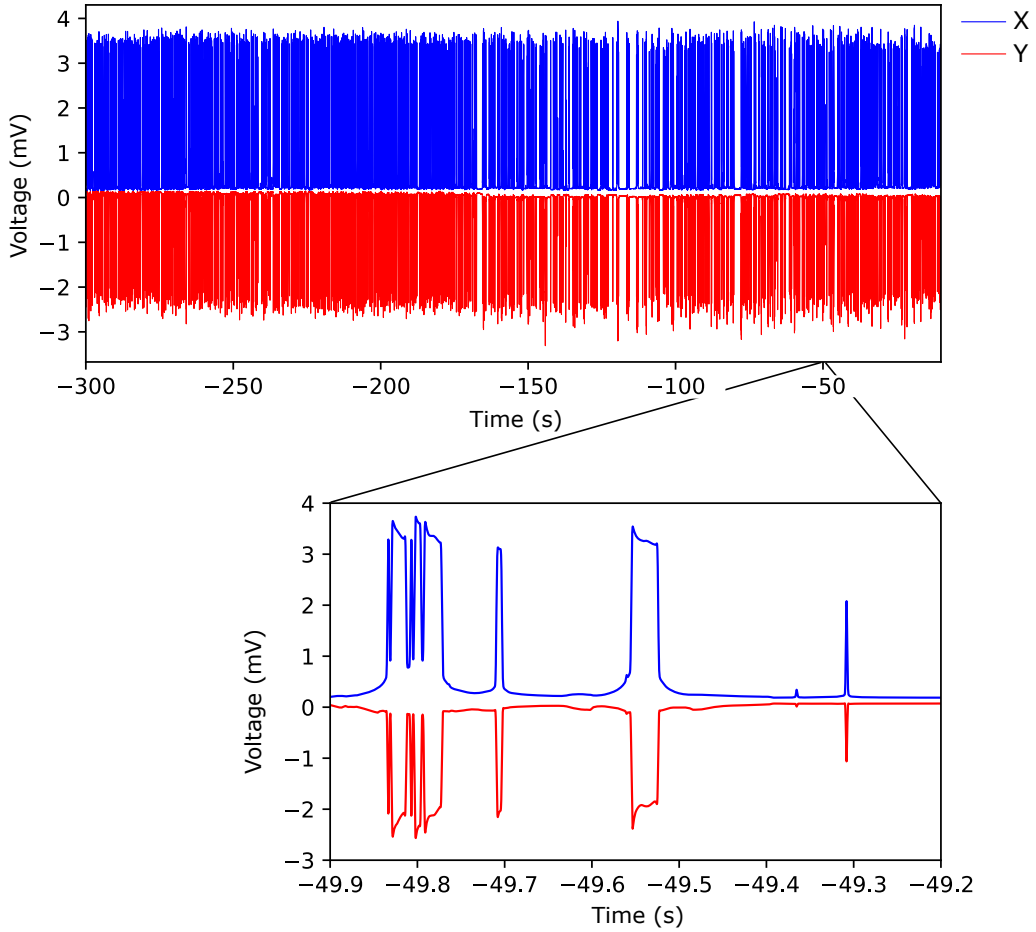

FIGURE 7.12: **Detection of water droplets in oil:** Top graph shows time-traces of the raw in-phase (X) and quadrature (Y) components during droplet translocation over 290 s. The measurement frequency is 18.720 GHz with a power of -8 dBm. The bottom graph provides a magnified view, displaying various peak types corresponding to different droplet sizes.

Until now, we have discussed the detection of cells, cell debris, and polystyrene beads. The droplet experiment was designed as a simpler system, where a droplet, composed of a single liquid, occupies the entire sensing volume. Such droplets should result in a constant amplitude and phase response. Notably, the droplets had a diameter of 15 µm, which is larger than the channel dimensions of the sensing area, which measures 12 µm in width and 7 µm in height, with electrodes spaced 8 µm apart. As such, these droplets should occupy the entire sensing volume. However, these droplets proved unstable within the chip's microfluidic channel, leading

to instances of merging and bursting. This instability persisted despite the use of surfactants during droplet generation. As a result, droplets of varying sizes passed through the sensing area.

Fig. 7.12 displays the time traces of the raw in-phase (X) and quadrature (Y) components during the translocation of droplets over a time period of 290 s. The LIA recorded the (X, Y) components in blue and red, respectively. These traces feature peaks with heights of up to X≈ 3.5 mV and Y≈ 2.5 mV. The Y-component time-trace behaves like the inverted X-trace. Each peak represents the translocation event of a water droplet. At the bottom of the figure, a zoomed view of a time period of 0.7 s is depicted. During that time, several distinct peak types are presented. The first peak type is composed of a brought peak with several sharp negative features. The origin of these negative features is not known yet. This peak type might result from several connected but not merged droplets translocating simultaneously through the sensing area.

Alternatively, large water droplets must squeeze from the 40 µm wide inlet channel into the smaller 12 µm wide sensing channel. During that process, the oil between the channel walls and the water droplet might get trapped inside the water droplet. The trapped oil would form tiny oil droplets inside the water droplet. The sharp negative peaks might correspond to these oil droplets. Further investigations are needed to understand the negative features.

The second and third peaks have similar heights (X≈3 mV) with varying peak widths. These peaks probably correspond to droplets of different sizes that fully fill out the sensing region. There is a fourth barely visible peak around -49.35 s with a height of X = 0.2 mV and a fifth more prominent peak at -49.3 s with a height of X = 2.1 mV. These peaks are shorter than the previous peaks, and as their X-component is below 3 mV, they probably correspond to droplets smaller than the sensing volume.

The peak detection *algorithm 1* detected 1042 peaks over the threshold of 100 µV. The peak width is calculated at a 10% height of the peak amplitude. In this way, the negative features do not interfere with the peak detection algorithm. The noise level, calculated as the standard deviation of the in-phase (X) trace based on 500 data points without any peaks, is $\sigma_{\text{noise}} = 2.68$ µV.

Fig. 7.13a displays scattering plots of the detected peak amplitudes ΔR_{T} versus the width w_p. It shows a rapid rise of the peak amplitude at a peak width of 2 ms, indicated by a vertical dotted red line. That rise is assigned to two phenomena. Firstly, there is an increase in droplet size, while the sensing volume is not entirely filled with the droplet. Secondly, there is a reduction in the droplet's translocation height. Both effects increase the peak amplitude without an extreme change in width. That rapid rise stops at an amplitude of 3.7 mV and gradually increases to 4.4 mV, indicated by a second red dotted line. That gradual rise with increasing peak width is assigned to an increasing droplet size while the sensing volume is completely filled with the droplet. At the intersection point of both lines, the droplet size equals the sensing volume size.

Fig. 7.13b shows the peak amplitude ΔR_{T} against the corrected phase Θ_n. The droplets that fill out the sensing volume have an amplitude above 3.7 mV and a corrected phase around 0°. With decreasing amplitude (i.e., droplet size), the corrected phase linearly reduces to -10°, as indicated by the dotted red line. That amplitude phase dependence was not expected as the same material, even at different droplet sizes, should lead to a constant phase value (discussed in section 6.1.1). Additional

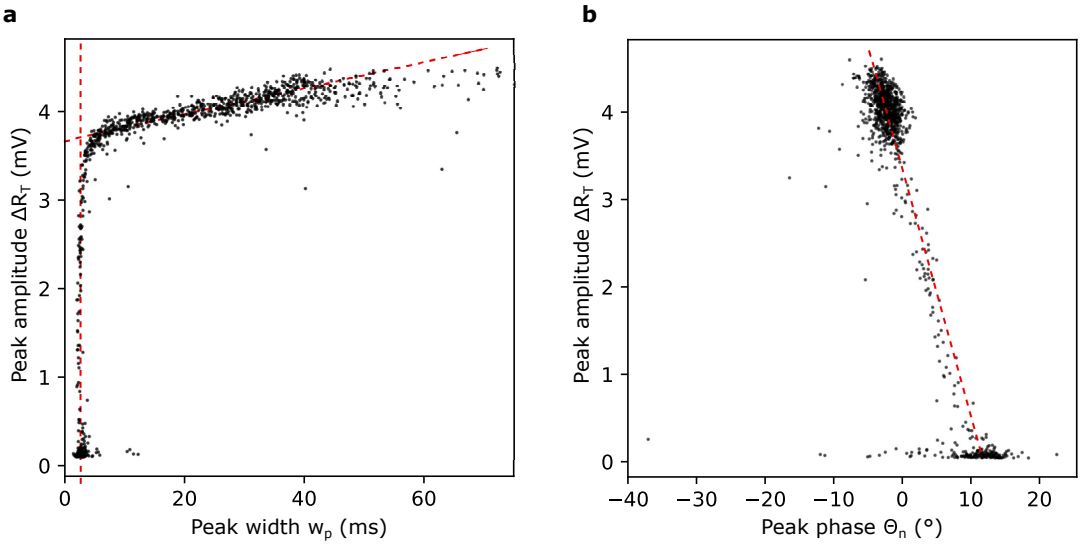

FIGURE 7.13: **Droplet peak parameter:** Scatter plots depicting the peak parameter of water droplets in oil, showing **a** the relationship between peak amplitude ΔR_T and peak width w_p, and **b** the relationship between peak amplitude and peak phase Θ_n. Red dotted lines indicate trends, providing visual guidance.

experiments with higher powers did not affect the -10 ° phase shift, but a change of the measurement frequency to 19 GHz increased the phase shift to around -20 °. Consequently, I expect that the measurement frequency in that experiment was not set to the correct spot on the left flank of the resonator. A deviation of the measurement frequency from the left flank results in a non-linear response of the $|S_{11}|$-parameter and phase with respect to the real and imaginary permittivity of the sensing volume (see section 3.8).

7.4 Liposomes

The global outbreak of the coronavirus disease in 2020, caused by the Severe Acute Respiratory Syndrome Coronavirus 2 (SARS-CoV-2), placed unprecedented strain on public health systems and ignited a worldwide economic crisis. Fast and widespread testing concepts were crucial for controlling the Covid-19 pandemic outbreak. The real-time reverse transcription-polymerase chain reaction (RT-PCR) assay is the gold standard for identifying a SARS-CoV-2 infection [136]. It is a nucleic-acid-based method that takes hours to perform and requires specialized reagents, equipment, and the development of detection assays [137]. These requirements need considerable lead-up time until RT-PCR assays enter the market. Hence, novel universal viral detection concepts are of significant interest for controlling a pandemic outbreak in its early stages. The sensor presented in this thesis stands out as the up-to-date, most sensitive dielectric inflow single-particle detection system reported in the literature. Its increased sensitivity could pave the way for the dielectric characterization of virions.

Moreover, the viral load of SARS-CoV-2 in patients, a measure for infectiousness, spans over a range of $10^2 - 10^{12}$ virions per mL of sputum or per entire swab sample [138]. Consequently, determining infectiousness requires novel detection concepts

that can measure extremely high dynamic ranges in viral load. Single particle detection solutions require ultra-fast particle sensing to achieve such a high dynamic range. Unlike conventional EIFC setups, reflectometric setups, as used in this thesis, are independent of TIAs and are not limited by f^2-noise, as seen in the Coulter principle, allowing for measurement bandwidths over 100 MHz [24]. Consequently, your measurement architecture has the potential to detect extremely high dynamic ranges of particle concentrations. Such bandwidth makes determining viral loads (indicating infectiousness) plausible in a single measurement.

Liposomes exhibit structural parallels with virions, characterized by an aqueous core surrounded by a lipid bilayer. Such liposomes can be created in various sizes and incorporate different liquids and lipids. As such, they are ideal model systems to mimic viruses. Furthermore, liposomes are used as drug delivery systems by encapsulating drugs within the aqueous core or integrating them into the lipid bilayer of liposomes. For example, the anti-SARS-CoV-2 vaccines developed by Pfizer/BioNTech are based on the mRNA encapsulated in a nanoparticle liposome [139]. In the subsequent sections, the focus will be on evaluating the sensor's capacity to detect liposomes, shedding light on its potential for virion detection or the quality control of liposome-based drug delivery systems.

7.4.1 Preparation

Two distinct liposome size distributions were prepared through extrusion using an Avanti mini extruder (610000, Avanti Polar Lipids). The lipid, 1,2-diphytanoyl-sn-glycero-3-phosphocholine (4ME-PC, catalog #850356, Avanti Polar Lipids), was dissolved in chloroform and subsequently dried under a stream of dry nitrogen. When re-suspended in water, the lipids spontaneously form multilamellar liposomes. These liposomes were extruded (i.e., forced through a porous polycarbonate filter) ten times in each direction, resulting in a suspension of uniformly sized unilamellar liposomes [140]. Small-sized liposomes were generated using a 100 nm polycarbonate filter. In contrast, larger-sized liposomes inadvertently resulted from a damaged polycarbonate filter.

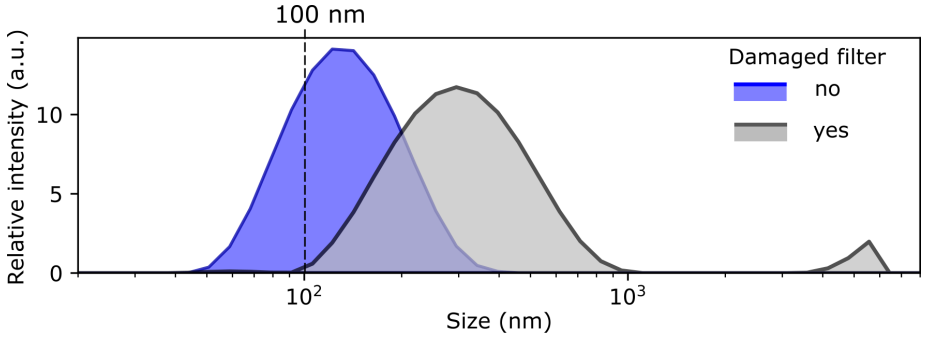

FIGURE 7.14: **Hydrodynamic diameter of liposome solutions:** Using dynamic light scattering (DLS), we determined the hydrodynamic diameter of liposomes. The black curve illustrates the size distribution of liposomes processed through an accidentally ruptured 100 nm polycarbonate filter. In contrast, the blue curve depicts those extruded through an intact 100 nm polycarbonate filter.

The hydrodynamic radius distribution of the liposomes was assessed using dynamic light scattering (DLS) on a Zetasizer Nano ZS (Malvern Instruments, UK). This instrument features a 4 mW helium/neon laser emitting at a wavelength of 633 nm

and evaluates particle suspensions via non-invasive light scattering at a 173° detection angle. Data analysis was performed with the Zetasizer Software version 7.13.

Fig. 7.14 illustrates the hydrodynamic diameter of the larger-sized liposome solution (extruded through a damaged polycarbonate filter) in grey and the smaller-sized liposome solution (extruded through a 100 nm filter) in blue. The respective average hydrodynamic diameters measure 332 nm and 139 nm. The larger-sized liposomes feature a primary peak around 300 nm, with a secondary, less prominent peak around 5-6 µm. The second peak is at the DLS system's detection limit, potentially extending over 10 µm. The presence of oversized liposomes, exceeding one micrometer in diameter, was further validated using light microscopy.

Interestingly, the size distribution of the smaller liposomes closely aligns with the dimensions of a coronavirion (80 nm - 120 nm) [141], rendering these suspensions an ideal reference system for detecting the coronavirus.

Both liposome suspensions were subsequently analyzed with the sensor developed in this thesis.

7.4.2 Time-Resolved Single Liposome Detection

The experimental setup described in chapter 5 was utilized to measure time-resolved signals of smaller and larger liposome solutions. Each solution was analyzed using a separate chip. Both chips featured electrode tips separated by 3 µm and a fluidic channel measuring 4 µm in width and 7 µm in height at the sensing region. The larger-sized liposomes were measured at an RF frequency of 18.70 GHz, while the smaller-sized liposomes were detected at 18.657 GHz. Both frequencies correspond to the left flank of the resonance curve, with a source power set at -5 dBm. The RF frequency was downmixed to an IF frequency of 2 MHz.

Before loading, both solutions were degassed for 30 minutes. After loading, a flow was initiated using an inlet pressure of 115 mbar and an outlet suction pressure of 435 mbar for the larger-sized liposome solution and 500 mbar for the smaller-sized liposomes.

Fig. 7.15a displays the amplitude R time-trace for the larger-sized liposome solution with an average diameter of 332 nm in black, and Fig. 7.15b shows the smaller-sized liposomes averaging 139 nm in diameter (depicted in blue). A 1 Hz highpass filter was applied to remove the X and Y DC offsets, and a lowpass filter of 27 kHz removed high-frequency noise for the larger-sized liposome measurement and a 63 kHz lowpass filter for the smaller-sized liposomes. The noise level, calculated as the standard deviation of the amplitude trace R based on 600 data points without any peaks, is $\sigma_{\text{noise}} = 5.27$ µV for the large liposome solution and $\sigma_{\text{noise}} = 3.05$ µV for the smaller liposome solution. Over the course of 10 minutes, 26,734 larger-sized liposomes above the threshold of 35 µV and 2,547 smaller-sized liposomes above the threshold of 30 µV were detected, which is well above the noise levels.

Analysis of Larger-Sized Liposomes

Fig. 7.16 analyses the peak parameters associated with larger-sized liposome solutions, explicitly focusing on width w_p, amplitude ΔR_{T}, and the corrected phase Θ_n. The scatter plot in Fig. 7.16a displays the liposome peak amplitude against the peak width. The events are color-coded based on the corrected phase Θ_n. A rapid amplitude rise is evident at approximately 50 µs peak width. That rise is attributed

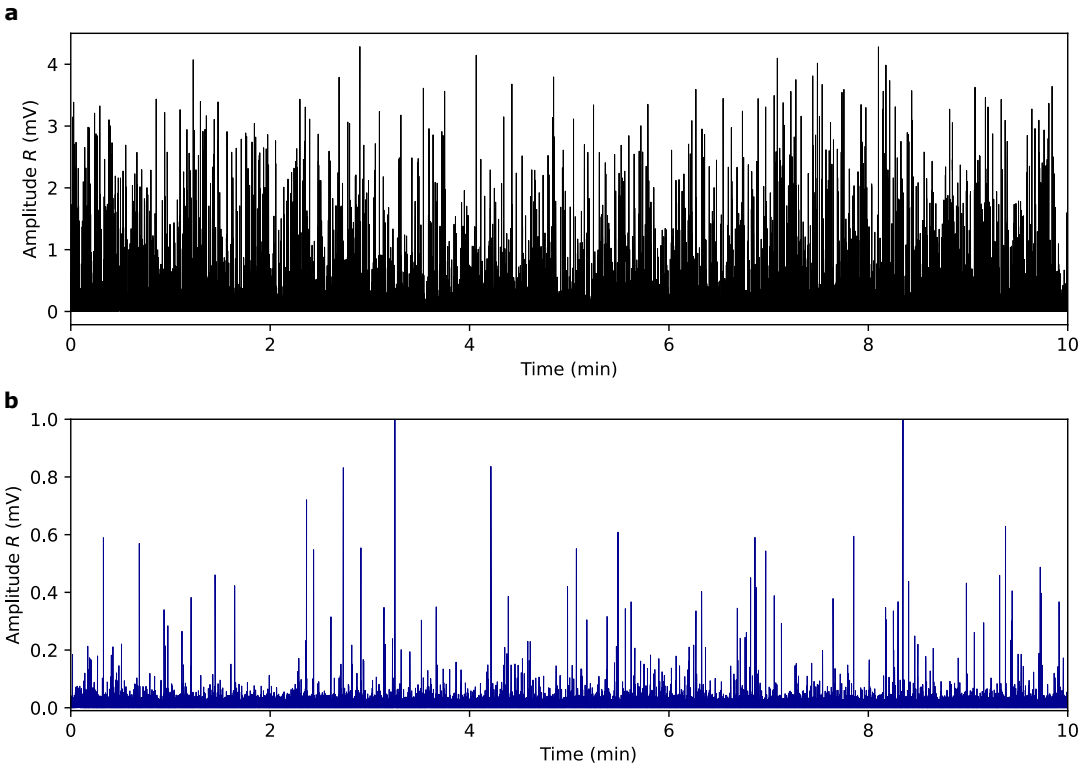

FIGURE 7.15: **Liposome detection**: Continuous amplitude R traces, recorded over a span of 10 minutes for **a** liposomes with an average diameter of 332 nm, and **b** liposomes with an average diameter of 139 nm. A size distribution of these liposomes is depicted in Fig. 7.14. In total, 26,734 peaks above the threshold of 35 µV were detected for the larger liposomes, and 2,547 peaks over the threshold of 30 µV were detected for the smaller liposomes.

to the reduction of translocation height of the liposome and increasing liposome size. Above the 1 mV peak amplitude, the rate of amplitude growth slows down. These events are assigned to liposomes with a size larger than the sensing volume. These liposomes must squeeze through the sensing volume, drastically increasing the peak width. DLS measurements and light microscopy confirmed the presence of over-sized liposomes, which are larger than the sensing volume.

An L-shaped distribution is absent in the liposome data, as observed for 1.75 µm polystyrene beads. Nevertheless, a slight increase in peak width at the smallest amplitudes is observable, suggesting the non-detection of liposomes further from the electrodes due to sensitivity constraints.

The color-coded phase in Fig. 7.16a predominantly shows events with a phase of 0°, with a smaller subset of events with a phase of around 20°. These subsets are also observed in Fig. 7.16b, which displays the relationship between amplitude ΔR_T and phase Θ_n. The prominent peak at 0° shows little dependence between the phase and amplitude, indicated by the vertical red dotted line. As discussed, amplitude is a proxy for particle translocation height and size. The phase is expected to be independent of the translocation height and particle size, translating to the observed independence between peak phase and amplitude. Instead, the phase should relate to the material properties, as theoretically derived in section 6.1.1. Consequently, the two subsets of phases could relate to different liposome types, for example, uni- and

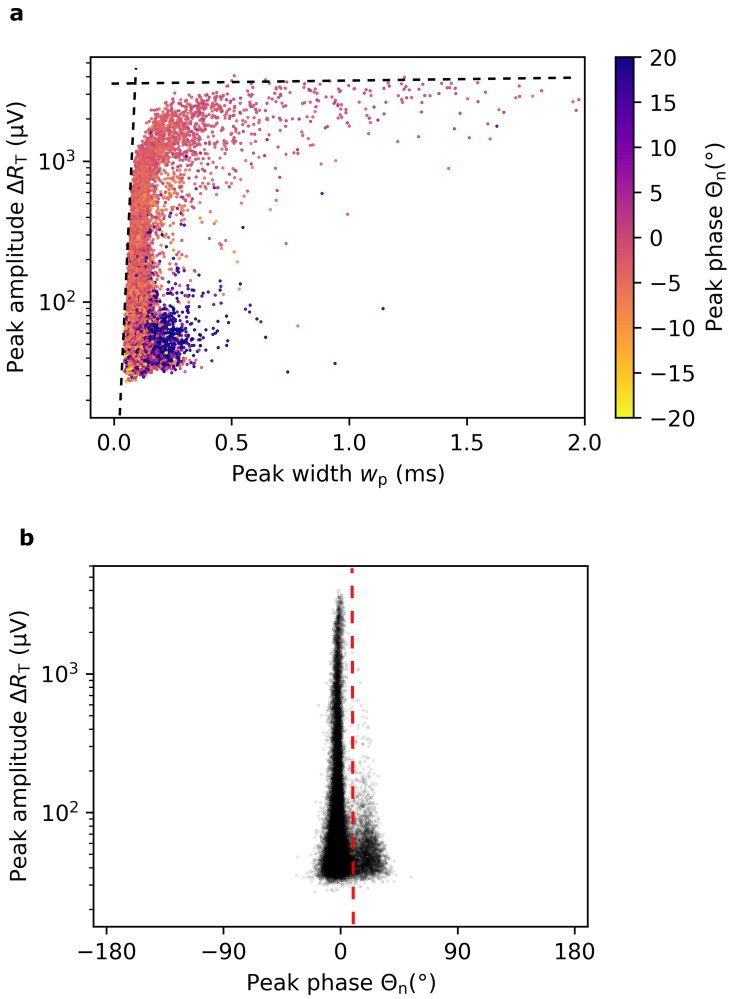

FIGURE 7.16: **Peak parameters of larger-sized liposomes:** Measurements taken at 18.70 GHz captured 26,734 translocation events over 10 minutes. **a**, Plots amplitude ΔR_T against peak width w_p, with colors representing the phase Θ_n. **b**, Shows the correlation between ΔR_T and phase Θ_n.

multilamellar liposomes.

Interestingly, the subset at 20° has a peak width above 0.1 ms, higher than the 0° subset. Given that there is no rationale for such peak width discrepancies for uni- or multilamellar liposomes, the phase subsets at 20° might also stem from a different origin. Further research with particles composed of various permittivities might offer greater clarity. In the future, we intend to encapsulate various mediums into liposomes. As a result, we could investigate if the normalized phase is an adequate parameter to distinguish the particle's material proprieties. A great candidate for creating a set of liposomes with different permittivity values would be the encapsulation of various glycerin-water mixtures [142]. For example, introducing 10% glycerin into water reduces the real permittivity of water by 25% and the imaginary permittivity by 16%.

An alternative explanation for the distinct phases is specific translocation positions in the sensing volume obtained by inertial focusing. Inertial focusing is affected by channel dimensions, aspect ratio, particle diameter, and flow rate. In the present

experiment, a higher pressure gradient of 550 mbar across the in- and outlet was applied, which is higher than the maximal suction pressure of 200 mbar in the previous experiment, indicating inertial focusing (section 7.1.3). Additionally, this experiment featured narrow channel dimensions, which likely increased the effects of inertial focusing. However, the exact source of these phase subsets remains unidentified and necessitates further research.

Analysis of Smaller-Sized Liposomes

Consistent with the previous investigation of the larger-sized liposome peaks, an analysis of smaller-sized liposomes is conducted, highlighting the differences between both solutions.

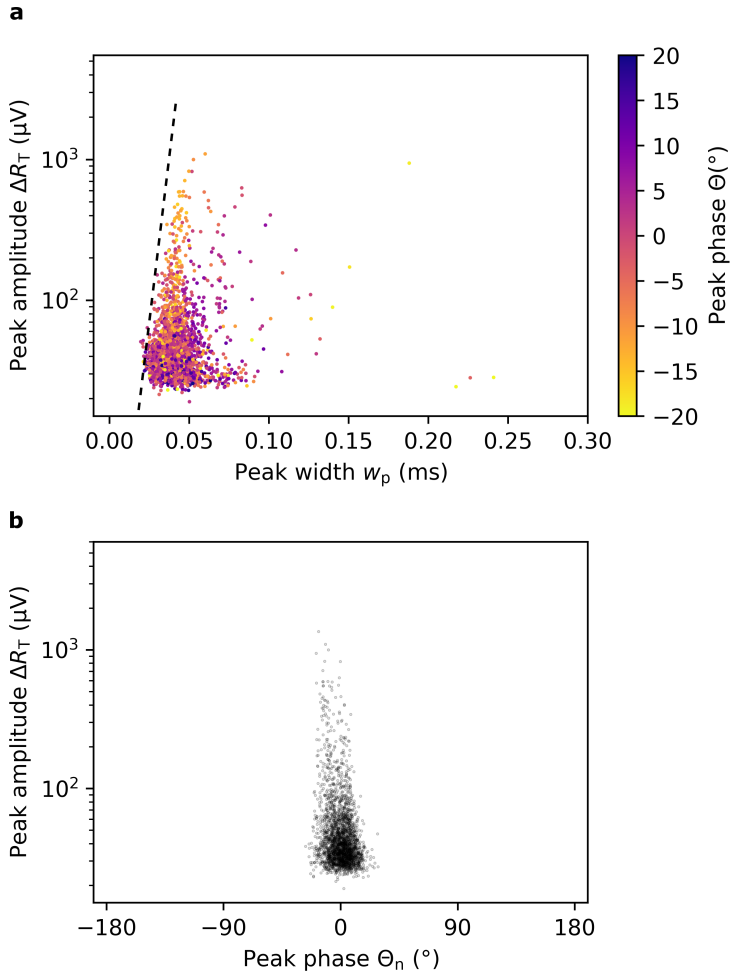

FIGURE 7.17: **Peak parameters of smaller-sized liposomes:** Measurements taken at 18.657 GHz captured 2,547 translocation events over 10 minutes. **a**, Amplitude ΔR_T against peak width w_p, with color representing the phase Θ_n. **b**, Correlation between amplitude ΔR_T and phase Θ_n.

Fig. 7.17a plots the peak amplitude ΔR_T against peak width w_p. The colors encode the corrected phase Θ_n. Akin to the larger-sized liposomes, a rapid amplitude rise is evident at approximately 20 µs peak width, as indicated by a dotted black line. Again, this phenomenon can be attributed to two main factors: the reduction in translocation height of the liposome towards the sensing electrodes and the increase

in liposome size. As previously established, particles transiting through the region between the electrodes correlate to peaks with the highest amplitude ΔR_T. Unlike the prior measurement, the present solution lacks liposomes exceeding a size of 400 nm. Consequently, liposomes do not squeeze through the sensing volume, and no significant reduction in peak width at high amplitudes can be observed.

The liposome size distribution ranges from 50 nm to 400 nm, with an average diameter of 139 nm. The events with the highest signal likely correspond to one of the larger-sized liposomes, which happen to translocate close to the electrodes. A conservative estimate of the S/N in that region is estimated by assuming that the S/N should be higher than the highest 1-percentile of detected peaks, resulting in $S/N_{1\%} = 433.5\,\mu V/3.05\,\mu V = 142$. Given that the detectable amplitude spans over two orders of magnitude, it is highly probable that liposomes with sizes below 100 nm were also detected. Further experiments with monodisperse size distributions are necessary to determine the liposome size detection limit. Nevertheless, the preliminary results suggest that the developed sensor can detect virions, such as the coronavirus, which exhibit sizes within the 80 -120 nm range.

The color-coded phase in Fig. 7.17a indicates a subtitle decrease in phase with increasing peak amplitudes. This dependency is less evident in Fig. 7.17b, which plots the peak amplitude against the peak phase. It is possible that both phase subsets, which were present in the larger-sized liposomes, are also observable in this measurement. However, this interpretation is speculative as both subsets overlap and are not easily distinguishable. As mentioned before, further analysis of the sensor's feedback to variation of the complex permittivity in the sensing volume is needed. For example, characterizing a mixture of liposomes encapsulating different liquids would provide additional insights.

This page has been intentionally left blank.

Chapter 8

Conclusion

8.1 Summary

The research in this thesis details the comprehensive development of a novel coupling-based coplanar waveguide (cCPW) sensor, introduces an ultra-fast measurement setup operating at GHz frequencies, and evaluates the sensor's performance across various particle systems with unprecedented sensitivity.

The primary objective was to overcome the existing sensitivity constraints, thereby facilitating the detection of individual nanoparticles. To achieve this, a unique coupling-based sensing concept has been developed, and the theory has been derived and compared to the conventional TC approach. The innovation in our sensor design lies in utilizing the sensing volume as the input coupling capacitance to the TC. TL Theory, FEM simulations, and empirical results worked together to develop, optimize, and validate the coupling-based sensor concept. FEM simulations guided the geometrical optimization process, enhancing the coupling-related sensitivity. Moreover, simulations were conducted to understand the sensor's response to variations in permittivity within the sensing volume. Remarkably, our sensor achieved a figure-of-merit (FOM) of 1300, representing a 15-fold improvement over our preceding TC-based design, which was already state of the art in detecting particles at GHz frequencies, able to detect polystyrene beads with a diameter of 500 nm [24].

The novel sensor was integrated into a reflectometric measurement concept as first introduced by Schoelkopf et al. to enable the detection at GHz frequencies [23]. In comparison, conventional EIFCs operate within the MHz range [17], typically limited by the trans-impedance amplifier (TIA). The highest reported measurement frequency for such configurations is 450 MHz [18]. No conventional EIFC has achieved sensing at GHz frequencies to date. In contrast, the reflectometric measurement architectures do not require TIAs. They are not subject to f^2-noise limitations, as seen in the Coulter principle, which enables it to measure GHz frequencies with a BW exceeding 100 MHz.

The reflectometric setup was extended with an interferometric impedance-matching technique. To my knowledge, this is a pioneering effort in its application for single-particle sensing in a fluidic system. The design was adopted from Tuca et al.'s work [116], which exhibited a 2-7-fold enhancement in S/N ratio performance using an interferometric matching approach, in contrast to the classical shunt impedance matching. The integrated interferometer counteracts the reflected signal through destructive interference and enables multi-frequency impedance-matching capabilities along the resonance curve. This stands in contrast to the TC-based impedance

matching circuit, which is optimized solely for the resonance frequency. The interferometer allowed for an impedance match of up to -99 dB. An added advantage of the interferometric approach is the absence of an additional capacitance to the sensing/resonating part of the circuit, ensuring no compromise in the sensor's responsiveness.

However, introducing an interferometer poses challenges as it transforms the sensor's amplitude and phase response. That transformation has been described in detail in section 6.1.1. It enables an interpretation of the peak amplitude and phase data with respect to the particle's dielectric properties. Interestingly, the transformed phase parameter becomes a metric related to the ratio between the effective real and imaginary part of the complex permittivity. In other words, it is related to the ratio between the stored and dissipated energy the particle induces. In theory, that ratio cancels out the size and electric field dependence, and as a result, the detected phase becomes independent of the particle size and position in the fluidic channel. It is expected that the relative phase should be an excellent metric for distinguishing particles based on their material proprieties. Such a metric might reduce the constraints for the optimal focusing of particles in a microfluidic channel and for a homogeneous electric field in the sensing volume.

A noteworthy challenge arises in the case of a poor impedance match relative to the amplitude of detected peaks. That case is especially prominent when detecting ultra-small signals. To the best of my knowledge, these effects had been overlooked in similar scientific approaches [26, 24, 25, 112, 85, 72], and solutions have not yet been proposed in literate. We address this challenge by calculating the relative peak amplitude and phase. Those metrics remain consistent regardless of the impedance match quality, which ensures reproducible measurements.

The last chapter combines the previously described developments, including the cCPW sensor, interferometric setup, and signal analysis algorithm to a sensing platform and showcases its performance on various particle systems, including polystyrene beads, cells, droplets, and liposomes, each illustrating a unique application. The detection of 200 nm polystyrene beads demonstrates a 69-fold improvement in the S/N ratio compared to the smallest particles previously reported in the literature. The increased sensitivity paves the way for ultra-fast characterization of individual nanoparticles based on their dielectric properties, an unexplored domain. The extraordinary sensitivity also allows for the simultaneous detection of cells and cell debris.

Furthermore, the peak analysis algorithm and the high sensitivity allowed for the label-free measuring of polystyrene bead flow velocity profiles in sub-10 micrometer fluidic channels. In addition, I detected droplets of varying sizes at a 100 kHz bandwidth, which paves the way for applications such as high-throughput screening in drug discovery.

Finally, liposomes with an average diameter of 139 nm were detected, which further showcases the sensitivity of the novel sensing platform. The relevance of this capability extends to the quality control of drug delivery systems, like the anti-SARS-CoV-2 vaccines developed by Pfizer/BioNTech, which is based on the mRNA encapsulated in a nanoparticle liposome [139]. Furthermore, liposomes share structural similarities with virions. The detected liposomes are comparable in size to the coronavirus, which is between 80 and 120 nm, indicating the sensor is capable of

detecting individual virions. The reflectometric concept enables ultra-fast measurements, thus offering the potential for high dynamic range detection of viral loads in a single measurement. In the future, this capability could increase the speed and efficiency of testing viral infectiousness. In summary, this sensing platform holds great promise for a wide range of applications in biomedical, academic, and industrial settings.

8.2 Outlook

The outlook can be separated into two main areas: Sensor **characterization** and **optimization**.

Characterization

A systematic study of the phase parameter is crucial to evaluate the sensor's abilities. In particular, two aspects need confirmation: Differentiating particles based on their material composition and validating the independence of the phase parameter from the electric field distribution inside the sensing area and particle size. These aspects could be studied with liposomes encapsulating glycerin-water mixtures with different permittivity values [142]. A phase parameter independent of the electric field distribution would reduce the constraint of focusing particles inside the fluidic channel or diminish the necessity for a perfectly homogeneous electric field within the sensing area.

Finally, the clinical and scientific relevance of the GHz regime for small biological objects like bacteria or virions needs to be evaluated by investigating whether the sensor can discriminate their types or states.

Optimization

The sensor optimization largely relies on the refinement of the sensing region. Two goals are set for the subsequent sensor designs. The first goal is to limit the sensing volume exclusively to the region between the electrodes. Such volume would result in a homogeneous electric field and less variance in the signal amplitudes. The second goal is to reduce the size of the sensing volume by reducing the size of the electrode tips and bringing them closer together. That configuration has several benefits. We retain a high Q-factor because the losses introduced by the water are reduced. Furthermore, the capacitance per unit volume increases, as described by Eq. 2.64, leading to higher signals. In the following, I will estimate the limit of detection (LOD) in terms of particle size if we bring the sensing electrodes closer together.

We have achieved an S/N of 417 for polystyrene beads with a diameter of 200 nm. Assuming a linear relation between the detected signal and the capacitive change (as observed in section 3.8), and a relation between the capacitive response and the particle radius a of $\Delta C \propto a^3$ (as described by Eq. 2.64), we can estimate a LOD of about 60 nm for polystyrene beads at an S/N of 10. Note that this LOD corresponds to the current electrode distance of 3 µm. By reducing the electrode distance, we can reduce the LOD. If we assume that the electrode spacing is reduced in proportion to the decrease in particle size, then the LOD is reduced to 5 nm for an electrode spacing of 75 nm and an S/N of 10. Consider an uncoiled DNA double strand within the sensing volume created by electrodes spaced 75 nm apart. Since the width of the

DNA is approximately 2nm, the DNA can be visualized as occupying a cylindrical volume with a diameter of 2nm and a length of 75nm. This volume is larger than that of a 5 nm bead. Suppose the permittivity contrast for DNA is similar to that of a polystyrene bead. In this case, a strand of DNA may be detectable with our current sensor configuration with a reduced sensing volume. Therefore, developing fabrication protocols capable of producing nanoscopic electrode-channel interfaces should be a major focus in the future.

In the section on fabrication outlook (4.2), preliminary work towards this goal has already been presented. The feasibility of creating a nanoscopic sensing volume using EBL was demonstrated. One significant challenge encountered was sealing the electrode-channel interface. This challenge led to the exploration of the potential of sacrificial layer fluidics to integrate a fluidic channel between electrodes with polycarbonate (PC) as a sacrificial layer. Previous studies have demonstrated that PC is thermally decomposable and can be utilized in the fabrication of sacrificial layer fluidics [100, 103, 104]. Additionally, PC has the potential to serve as a negative-tone resist for electron-beam lithography, enabling the creation of high-resolution structures [105, 87]. By merging these two distinctive qualities of PC, we created nanoscopic fluidic channels by combining sacrificial layer fluidics with e-beam lithography, as detailed in section 4.2. The next step is to integrate electrodes into the SLF fabrication approach. I proposed two SLF-based fabrication processes, as depicted in the appendix A.4.

In summary, our proposed sensing platform with unprecedented sensitivity and ultra-fast sensing capabilities paves the way for the detection and characterization of single nano-scale entities, including bacteria, virions, vaccines, proteins, and DNA, within microfluidic systems. Unlike traditional Coulter counter-based or mass spectrometer methods, which primarily focus on particle size or weight, high-frequency sensing informs on the dielectric properties of these particles. This dielectric characterization provides insights into the composition of a particle that cannot be inferred solely from its dimensions or mass. The significance of such measurements is underscored by their proven efficacy in differentiating cancerous cells. I believe that single nanoparticle dielectric characterization holds vast diagnostic and scientific promise, as high-frequency characterization remains an underexplored domain, and the detection of sub-100 nm particles has not yet been demonstrated. I anticipate that the proposed sensing platform can illuminate this uncharted domain.

Appendix A

Supplementary Images

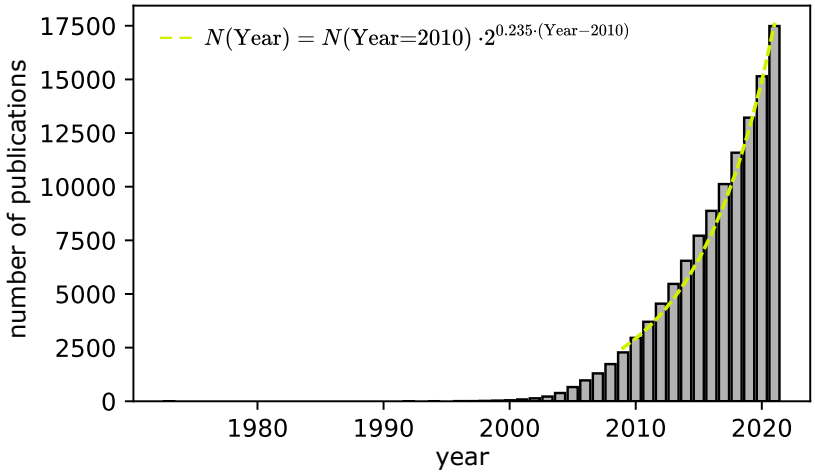

FIGURE A.1: **Popularity of resistive pulse sensing (RPS):** Total number of entries in PubMed for the keywords *nanopore, resistive pulse sensing* and *Coulter counter*. The gray bars display the sum of all publications until that year and the yellow line is a exponential fit. The number of publications doubles every 4.26 years since 2010.

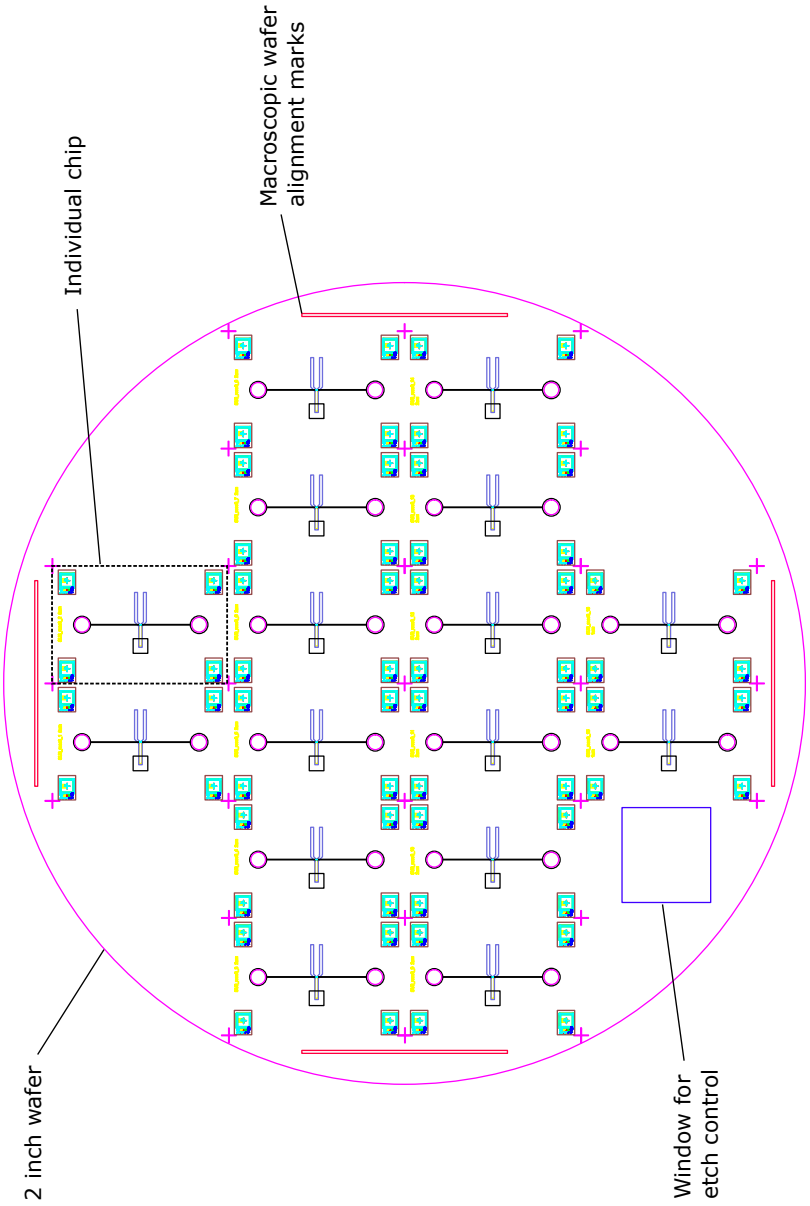

FIGURE A.2: **Wafer layout with 16 chips:** The manufacturing protocol has been optimized to facilitate wafer-scale production, accommodating 16 individual chips, each measuring 8 mm x 12 mm, on a 2-inch wafer.

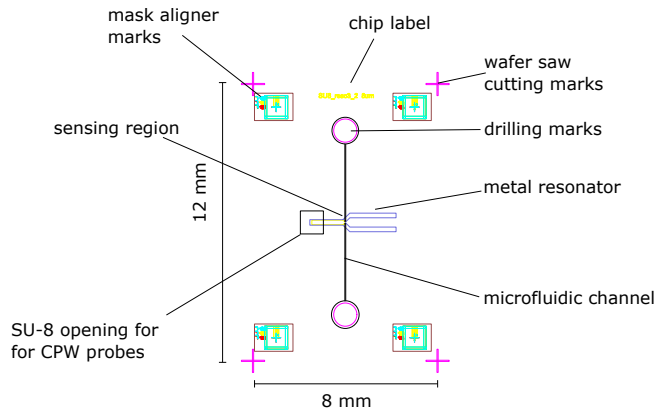

FIGURE A.3: **Layout of an individual chip:** Illustrates various components, including microfluidic and microwave elements.

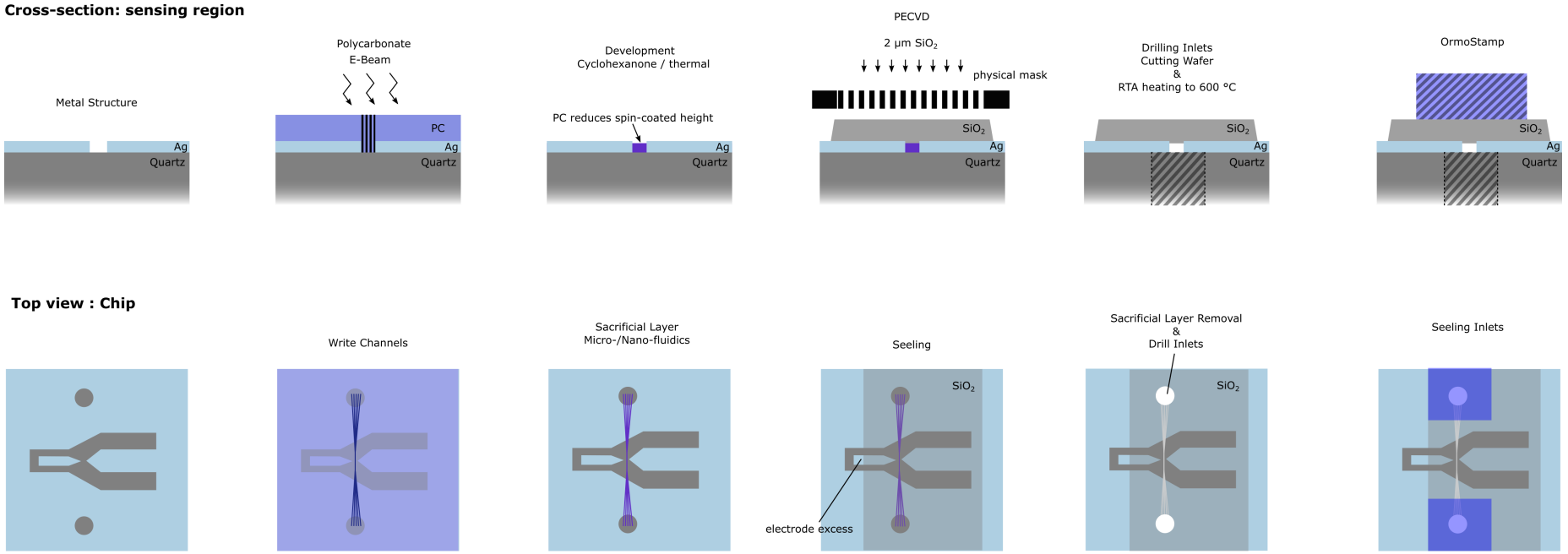

FIGURE A.4: **Fabrication process one of the SLF-based sensor:** A quartz wafer with Ag resonator structures is spin-coating with polycarbonate (PC) resist and e-beam lithography is used to write micro- and nanochannels. Wet or thermal development creates the sacrificial structures. Due to the reduction of the sacrificial layer height upon development, its height is below the thickness of the electrodes. A physical mask is employed to shield the CPW probe tip contacts while exposing the sacrificial PC area. This is followed by the encapsulation of the sacrificial layer with a 2 µm SiO_2 layer via PECVD. Inlets are then created by drilling, and the wafer is segmented into individual chips. The wafer is heated to 600°C to eliminate the sacrificial layer, forming hollow channels and facilitating the self-encapsulation of the Ti/Ag/Ti metal layers. Finally, the inlet holes are sealed with OrmoStamp foil. Cross-sectional and top views are provided for each step.

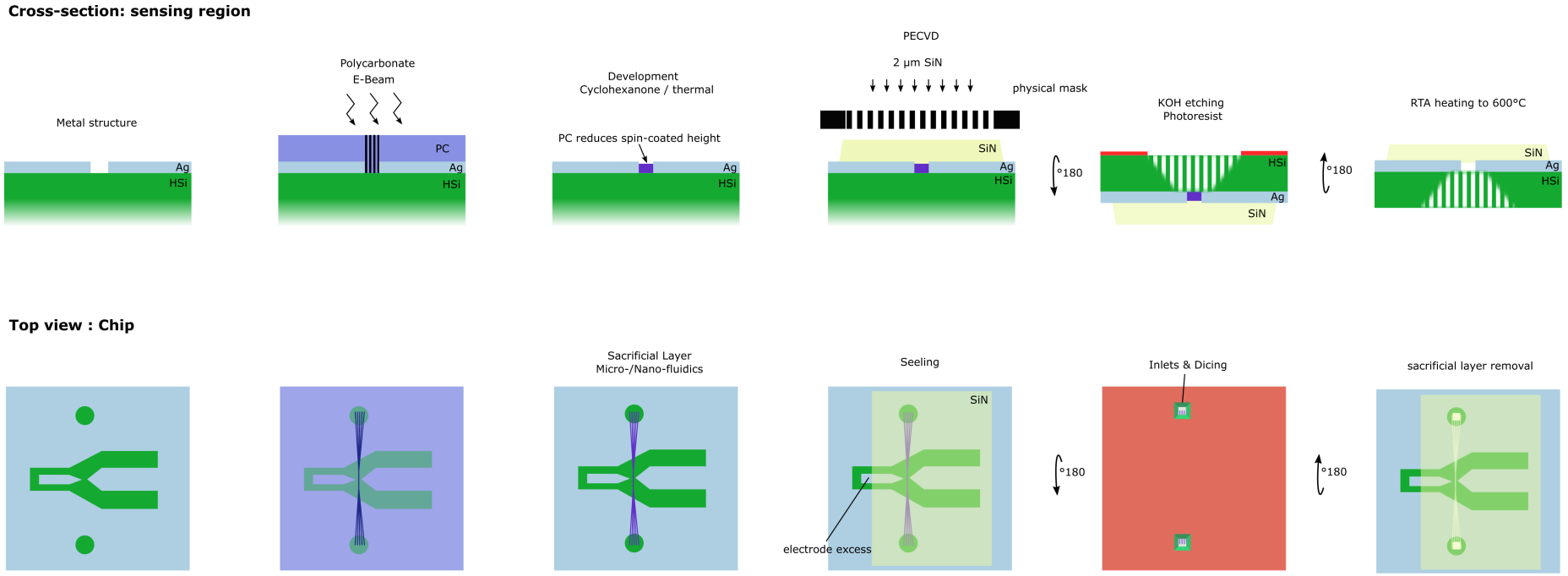

FIGURE A.5: **Fabrication process two for the SLF-based sensor with enhanced sealing:** A high-resistivity silicon wafer is utilized as the substrate. The Ag resonator structures are fabricated identical to the sensor presented in this thesis. The wafer, with metal structures, is spin-coating with polycarbonate (PC) resist. E-beam lithography is then employed to pattern micro- and nanochannels. Wet or thermal development forms the sacrificial structures. Due to the reduction of the sacrificial layer height upon development, its height can be below the thickness of the electrodes. A physical mask is employed to shield the CPW probe tip contacts while exposing the sacrificial PC area. This is followed by the encapsulation of the sacrificial layer with a 2 µm SiN layer via PECVD. The wafer's top side is then coated with a KOH-protective resist, while its bottom side is spin-coated with a KOH-stable photo-resist (e.g., SX AR-PC 5000/41, *Allresist*). Photolithography is used to define the inlets and dicing lines on the resist. The wafer undergoes deep silicon etching using KOH, but the silicon nitride remains intact due to its KOH resistance [107]. This process yields open inlets and resist that is sealed by the silicon nitride and simultaneously separates the wafer into individual chips. In the final step, the sacrificial layer is removed by heating the wafer to 600°C under a nitrogen flow.

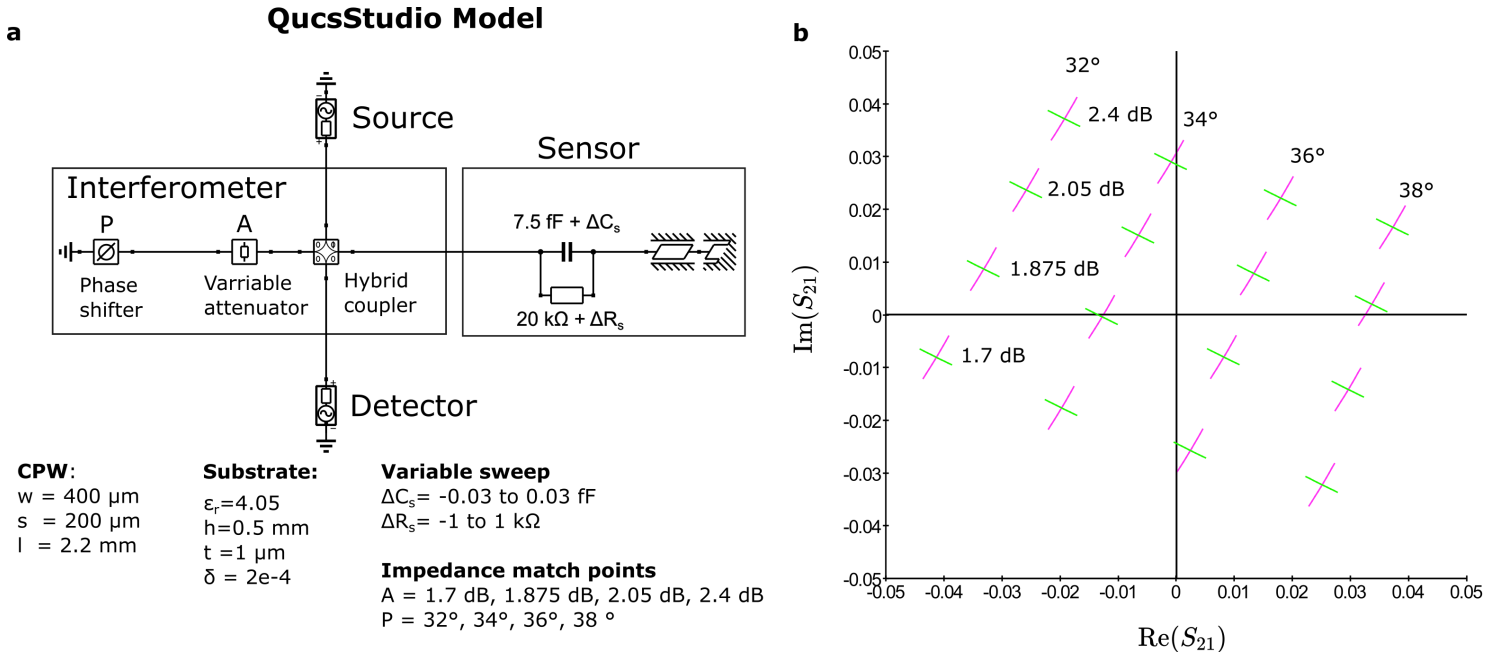

FIGURE A.6: **Simulation of interferometerically impedance-matched sensor using QucsStudio 2.5.7: a**, Model of an interferometer combined with a coupling-based sensor. The interferometer consists of a hybrid coupler, variable attenuator, and phase-shifter. Adjusting the attenuator and phase-shifter to four distinct values yields 16 impedance-match points. The coupling-based sensor's resonator is formed by a CPW and a CPW ground termination. Lumped components, including a capacitance and resistance, account for the coupling capacitance and dielectric losses in the sensing volume. A coupling capacitance of 7.5 fF leads to an optimal input-coupling with a reflection coefficient of $\Gamma = 0.5$. The sensor's capacitive and dielectric loss response is explored by varying the coupling capacitance between -0.03 fF and +0.03 fF and adjusting the resistance between -1 kΩ to + 1 kΩ. **b**, The IQ-diagram displays the simulation results. The position of the impedance-matching points are located in all quadrants of the IQ-diagram. The capacitance (magenta) and loss (green) responses have the same amplitude and also point in the same direction for all impedance-matching points. These results validate the relative amplitude and phase approach as detailed in section 6.2.

Bibliography

[1] Lucjan Grzegorzewski, Robert Zierold, and Robert H. Blick. "Coupling-Based Sensing with a Microwave Resonator for Single Nanoscale Particles Detection". In: *IEEE Sensors Journal* (2023), pp. 1–1. DOI: 10.1109/JSEN.2023.3312517.

[2] John J. Kasianowicz et al. "Characterization of individual polynucleotide molecules using a membrane channel". In: *Proceedings of the National Academy of Sciences of the United States of America*. Vol. 93. 24. Nov. 1996, pp. 13770–13773. DOI: 10.1073/pnas.93.24.13770. URL: https://www.pnas.org.

[3] W. H. Coulter. "Means for counting particles suspended in a fluid". Pat. 2656508. Oct. 20, 2053. URL: https://patents.google.com/patent/US2656508A.

[4] Kidan Lee et al. "Recent Progress in Solid-State Nanopores". In: *Advanced Materials* 30 (42 Oct. 2018), p. 1704680. ISSN: 1521-4095. DOI: 10.1002/ADMA.201704680. URL: https://onlinelibrary.wiley.com/doi/full/10.1002/adma.201704680.

[5] Yanxiao Feng et al. "Nanopore-based Fourth-generation DNA Sequencing Technology". In: *Genomics, Proteomics and Bioinformatics* 13.1 (2015), pp. 4–16. ISSN: 1672-0229. DOI: https://doi.org/10.1016/j.gpb.2015.01.009. URL: http://www.sciencedirect.com/science/article/pii/S1672022915000133.

[6] James M. Heather and Benjamin Chain. "The sequence of sequencers: The history of sequencing DNA". In: *Genomics* 107 (1 Jan. 2016), p. 1. ISSN: 10898646. DOI: 10.1016/J.YGENO.2015.11.003. URL: https://www.ncbi.nlm.nih.gov/pmc/articles/PMC4727787/.

[7] Andreas J.W. Hartel et al. "High bandwidth approaches in nanopore and ion channel recordings - A tutorial review". In: *Analytica Chimica Acta* 1061 (2019), pp. 13–27. ISSN: 0003-2670. DOI: https://doi.org/10.1016/j.aca.2019.01.034. URL: https://www.sciencedirect.com/science/article/pii/S0003267019301035.

[8] R. W. DeBlois and C. P. Bean. "Counting and Sizing of Submicron Particles by the Resistive Pulse Technique". In: *Review of Scientific Instruments* 41 (7 Feb. 1970), p. 909. ISSN: 0034-6748. DOI: 10.1063/1.1684724. URL: https://aip.scitation.org/doi/abs/10.1063/1.1684724.

[9] Hagan Bayley and Charles R. Martin. "Resistive-pulse sensing - from microbes to molecules". In: *Chemical Reviews* 100 (7 July 2000), pp. 2575–2594. ISSN: 00092665. DOI: 10.1021/CR980099G/ASSET/CR980099G.FP.PNG_V03. URL: https://pubs.acs.org/doi/abs/10.1021/cr980099g.

[10] Xue Sun et al. "Nanopore sequencing and its clinical applications". In: vol. 2204. 2020. DOI: 10.1007/978-1-0716-0904-0_2.

[11] Adrian Balan et al. "Improving Signal-to-Noise Performance for DNA Translocation in Solid-State Nanopores at MHz Bandwidths". In: *Nano Letters* 14.12 (2014). PMID: 25418589, pp. 7215–7220. DOI: 10.1021/nl504345y.

eprint: https://doi.org/10.1021/nl504345y. URL: https://doi.org/10.1021/nl504345y.

[12] Alessio Fragasso, Sonja Schmid, and Cees Dekker. "Comparing Current Noise in Biological and Solid-State Nanopores". In: *ACS Nano* 14 (2 Feb. 2020), pp. 1338–1349. ISSN: 1936086X. DOI: 10.1021/ACSNANO.9B09353/ASSET/IMAGES/LARGE/NN9B09353_0005.JPEG. URL: https://pubs.acs.org/doi/full/10.1021/acsnano.9b09353.

[13] H. Edward Ayliffe, A. Bruno Frazier, and R. D. Rabbitt. "Electric impedance spectroscopy using microchannels with integrated metal electrodes". In: *Journal of Microelectromechanical Systems* 8 (1 Mar. 1999), pp. 50–56. ISSN: 10577157. DOI: 10.1109/84.749402.

[14] Gerard H. Markx and Christopher L. Davey. "The dielectric properties of biological cells at radiofrequencies: applications in biotechnology". In: *Enzyme and Microbial Technology* 25.3 (1999), pp. 161–171. ISSN: 0141-0229. DOI: https://doi.org/10.1016/S0141-0229(99)00008-3. URL: https://www.sciencedirect.com/science/article/pii/S0141022999000083.

[15] Ronald Pethig. "Dielectric Properties of Biological Materials: Biophysical and Medical Applications". In: *IEEE Transactions on Electrical Insulation* EI-19.5 (1984), pp. 453–474. DOI: 10.1109/TEI.1984.298769.

[16] Xinwu Xie et al. "Optimization of an electrical impedance flow cytometry system and analysis of submicron particles and bacteria". In: *Sensors and Actuators B: Chemical* 360 (June 2022), p. 131432. ISSN: 0925-4005. DOI: 10.1016/J.SNB.2022.131432.

[17] Chayakorn Petchakup, King Ho Holden Li, and Han Wei Hou. "Advances in Single Cell Impedance Cytometry for Biomedical Applications". In: *Micromachines* 8.3 (2017). ISSN: 2072-666X. DOI: 10.3390/mi8030087. URL: https://www.mdpi.com/2072-666X/8/3/87.

[18] Niels Haandbæk et al. "Development of a microfluidic GHz impedance cytometer". In: *Technisches Messen* 80 (12 2013). ISSN: 01718096. DOI: 10.1515/teme.2013.0053.

[19] Nora Meyne et al. "Broadband dielectric characterization of CHO-K1 cells using miniaturized transmission-line sensor". In: *2015 IEEE Topical Conference on Biomedical Wireless Technologies, Networks, and Sensing Systems (BioWireleSS)*. 2015, pp. 1–3. DOI: 10.1109/BIOWIRELESS.2015.7152127.

[20] Nora Meyne née Haase et al. "Miniaturized Transmission-Line Sensor for Broadband Dielectric Characterization of Biological Liquids and Cell Suspensions". In: *IEEE Transactions on Microwave Theory and Techniques* 63.10 (2015), pp. 3026–3033. DOI: 10.1109/TMTT.2015.2472009.

[21] Amel Zedek, David Dubuc, and Katia Grenier. "Microwave permittivity extraction of individual biological cells submitted to different stimuli". In: *2017 IEEE MTT-S International Microwave Symposium (IMS)*. 2017, pp. 865–868. DOI: 10.1109/MWSYM.2017.8058718.

[22] Mousa Hussein et al. "Breast cancer cells exhibits specific dielectric signature in vitro using the open-ended coaxial probe technique from 200 MHz to 13.6 GHz". In: *Scientific Reports* 9 (1 2019). ISSN: 20452322. DOI: 10.1038/s41598-019-41124-1.

[23] R. J. Schoelkopf et al. "The Radio-Frequency Single-Electron Transistor (RF-SET): A Fast and Ultrasensitive Electrometer". In: *Science* 280 (5367 May 1998), pp. 1238–1242. ISSN: 00368075. DOI: 10.1126/SCIENCE.280.5367.1238. URL: https://www.science.org/doi/abs/10.1126/science.280.5367.1238.

[24] Abhishek Bhat et al. "Tank Circuit for Ultrafast Single-Particle Detection in Micropores". In: *Physical Review Letters* 121 (7 Aug. 2018). ISSN: 10797114. DOI: 10.1103/PhysRevLett.121.078102.

[25] D. K. Wood et al. "High-bandwidth radio frequency Coulter counter". In: *Applied Physics Letters* 87 (18 2005). ISSN: 00036951. DOI: 10.1063/1.2125111.

[26] D. K. Wood, M. V. Requa, and A. N. Cleland. "Microfabricated high-throughput electronic particle detector". In: *Review of Scientific Instruments* 78.10 (2007), p. 104301. DOI: 10.1063/1.2794230. eprint: https://doi.org/10.1063/1.2794230. URL: https://doi.org/10.1063/1.2794230.

[27] David M. Pozar. *Microwave Engineering, 4th Edition*. John Wiley & Sons, Inc, 2011. ISBN: 978-1-118-21363-6.

[28] R.N. Simons. *Coplanar Waveguide Circuits, Components, and Systems*. Wiley Series in Microwave and Optical Engineering. Wiley, 2004. ISBN: 978-0-471-46393-1.

[29] C.P. Wen. "Coplanar Waveguide: A Surface Strip Transmission Line Suitable for Nonreciprocal Gyromagnetic Device Applications". In: *IEEE Transactions on Microwave Theory and Techniques* 17.12 (1969), pp. 1087–1090. DOI: 10.1109/TMTT.1969.1127105.

[30] C. VEYRES and V. FOUAD HANNA. "Extension of the application of conformal mapping techniques to coplanar lines with finite dimensions". In: *International Journal of Electronics* 48.1 (1980), pp. 47–56. DOI: 10.1080/00207218008901066. eprint: https://doi.org/10.1080/00207218008901066. URL: https://doi.org/10.1080/00207218008901066.

[31] K Gupta, R Garg, and I Bahl. *Microstrip Lines and Slotlines 3rd ed.* 3rd ed. Norwood, MA: Artech House, 2013. ISBN: 1608075354.

[32] W. Hilberg. "From Approximations to Exact Relations for Characteristic Impedances". In: *IEEE Transactions on Microwave Theory and Techniques* 17.5 (1969), pp. 259–265. DOI: 10.1109/TMTT.1969.1126946.

[33] Koki Watanabe et al. "Kinetic Inductance of Superconducting Coplanar Waveguides". In: *Japanese Journal of Applied Physics* 33.Part 1, No. 10 (Oct. 1994), pp. 5708–5712. DOI: 10.1143/jjap.33.5708. URL: https://doi.org/10.1143/jjap.33.5708.

[34] "Attenuation Characteristics of Conventional, Micromachined, and Superconducting Coplanar Waveguides". In: *Coplanar Waveguide Circuits, Components, and Systems*. John Wiley & Sons, Ltd, 2001. Chap. 8, pp. 203–236. ISBN: 9780471224754. DOI: https://doi.org/10.1002/0471224758.ch8. eprint: https://onlinelibrary.wiley.com/doi/pdf/10.1002/0471224758.ch8. URL: https://onlinelibrary.wiley.com/doi/abs/10.1002/0471224758.ch8.

[35] Robert E. Collin. "Appendix III: Conformal Mapping Techniques". In: *Foundations for Microwave Engineering*. 2001, pp. 886–910. DOI: 10.1109/9780470544662.app3.

[36] Christopher L. Holloway and Edward F. Kuester. "A Quasi-Closed Form Expression for the Conductor Loss of CPW Lines, with an Investigation of Edge Shape Effects". In: *IEEE Transactions on Microwave Theory and Techniques* 43 (12 1995). ISSN: 15579670. DOI: 10.1109/22.477846.

[37] Wolfgang Heinrich. "Quasi-TEM description of MMIC coplanar lines including conductor-loss effects". In: *IEEE Transactions on Microwave Theory and Techniques* 41 (1 1993). ISSN: 15579670. DOI: 10.1109/22.210228.

[38] George E. Ponchak, Mehran Matloubian, and Linda P.B. Katehi. "A measurement-based design equation for the attenuation of MMIC-compatible coplanar waveguides". In: *IEEE Transactions on Microwave Theory and Techniques* 47 (2 1999). ISSN: 00189480. DOI: 10.1109/22.744301.

[39] K.J. Button. *Infrared and Millimeter Waves V10: Millimeter Components and Techniques, Part II*. Teil 2. Elsevier Science, 1983. ISBN: 9780323150989.

[40] Michael Y. Frankel et al. "Terahertz Attenuation and Dispersion Characteristics of Coplanar Transmission Lines". In: *IEEE Transactions on Microwave Theory and Techniques* 39 (6 1991). ISSN: 15579670. DOI: 10.1109/22.81658.

[41] Shintaro Takahashi et al. "Development of High Frequency Device Using Glass or Fused Silica with 3D Integration". In: *Proceedings - Electronic Components and Technology Conference* (Aug. 2017), pp. 758–763. ISSN: 05695503. DOI: 10.1109/ECTC.2017.124.

[42] M.D. Janezic, E.F. Kuester, and J.B. Jarvis. "Broadband complex permittivity measurements of dielectric substrates using a split-cylinder resonator". In: *2004 IEEE MTT-S International Microwave Symposium Digest (IEEE Cat. No.04CH37535)*. Vol. 3. 2004, 1817–1820 Vol.3. DOI: 10.1109/MWSYM.2004.1338956.

[43] Peter Debey. "Einige Resultate einer kinetischen Theorie der Isolatoren". In: *Physikalische Zeitschrift* 3.13 (1912), pp. 97–100.

[44] Koji Asami. "Characterization of heterogeneous systems by dielectric spectroscopy". In: *Progress in Polymer Science* 27.8 (2002), pp. 1617–1659. ISSN: 0079-6700. DOI: https://doi.org/10.1016/S0079-6700(02)00015-1. URL: https://www.sciencedirect.com/science/article/pii/S0079670002000151.

[45] Liliya Batyuk and Nataliya Kizilova. *MODELING OF DIELECTRIC PERMITTIVITY OF THE ERYTHROCYTES MEMBRANE AS A THREE-LAYER MODEL*. 2018. DOI: 10.30525/978-9934-571-31-2_2.

[46] H. Pauly and H. P. Schwan. "The Dielectric Properties of the Bovine Eye Lens". In: *IEEE Transactions on Biomedical Engineering* BME-11 (3 1964). ISSN: 15582531. DOI: 10.1109/TBME.1964.4502313.

[47] Paul Ben Ishai et al. "Electrode polarization in dielectric measurements: a review". In: *Measurement Science and Technology* 24.10 (Aug. 2013), p. 102001. DOI: 10.1088/0957-0233/24/10/102001. URL: https://doi.org/10.1088/0957-0233/24/10/102001.

[48] T. S. ENGLAND. "Dielectric Properties of the Human Body for Wave-lengths in the 1–10 cm. Range". In: *Nature* 166.4220 (Sept. 1950), pp. 480–481. ISSN: 1476-4687. DOI: 10.1038/166480b0. URL: https://doi.org/10.1038/166480b0.

[49] H. F. Cook. "The dielectric behaviour of some types of human tissues at microwave frequencies". In: *British Journal of Applied Physics* 2.10 (Oct. 1951), pp. 295–300. DOI: 10.1088/0508-3443/2/10/304. URL: https://doi.org/10.1088/0508-3443/2/10/304.

[50] W J Ellison. "Permittivity of Pure Water, at Standard Atmospheric Pressure, over the Frequency Range 0–25THz and the Temperature Range 0-100°". In: *Journal of Physical and Chemical Reference Data* 36 (1 2007), pp. 1–18. DOI: 10.1063/1.2360986.

[51] Amel Zedek, David Dubuc, and Katia Grenier. "Microwave permittivity extraction of individual biological cells submitted to different stimuli". In: 2017. DOI: 10.1109/MWSYM.2017.8058718.

[52] M. Nikolic-Jaric et al. "Microwave frequency sensor for detection of biological cells in microfluidic channels". In: *Biomicrofluidics* 3 (3 2009). ISSN: 19321058. DOI: 10.1063/1.3187149.

[53] T. Mitch Wallis and Pavel Kabos. "Extreme Impedance Measurements". In: *Measurement Techniques for Radio Frequency Nanoelectronics*. The Cambridge RF and Microwave Engineering Series. Cambridge University Press, 2017, 11–35. DOI: 10.1017/9781316343098.003.

[54] Romen Rodriguez-Trujillo et al. "Low cost micro-Coulter counter with hydrodynamic focusing". In: *Microfluidics and Nanofluidics* 3 (2 Apr. 2007), pp. 171–176. ISSN: 16134982. DOI: 10.1007/s10404-006-0113-8.

[55] Shady Gawad et al. "Dielectric spectroscopy in a micromachined flow cytometer: Theoretical and practical considerations". In: *Lab on a Chip* 4.3 (2004), pp. 241–251. ISSN: 14730197. DOI: 10.1039/b313761a.

[56] Karen Cheung, Shady Gawad, and Philippe Renaud. "Impedance spectroscopy flow cytometry: On-chip label-free cell differentiation". In: *Cytometry Part A* 65A.2 (2005), pp. 124–132. DOI: https://doi.org/10.1002/cyto.a.20141. eprint: https://onlinelibrary.wiley.com/doi/pdf/10.1002/cyto.a.20141. URL: https://onlinelibrary.wiley.com/doi/abs/10.1002/cyto.a.20141.

[57] Guillaume Mernier, Enri Duqi, and Philippe Renaud. "Characterization of a novel impedance cytometer design and its integration with lateral focusing by dielectrophoresis". In: *Lab on a Chip* 12 (21 Nov. 2012), pp. 4344–4349. ISSN: 14730189. DOI: 10.1039/c2lc40551b. URL: www.rsc.org/loc.

[58] S Gawad, L Schild, and Ph Renaud. "Micromachined impedance spectroscopy flow cytometer for cell analysis and particle sizing". In: *Lab on a Chip* 1 (1 May 2001), pp. 76–82. ISSN: 14730197. DOI: 10.1039/b103933b. URL: https://pubs.rsc.org/en/content/articlehtml/2001/lc/b103933b.

[59] Jianwei Zhong, Minhui Liang, and Ye Ai. "Submicron-precision particle characterization in microfluidic impedance cytometry with double differential electrodes". In: *Lab Chip* 21 (15 2021), pp. 2869–2880. DOI: 10.1039/D1LC00481F. URL: http://dx.doi.org/10.1039/D1LC00481F.

[60] James C. Booth et al. "Quantitative permittivity measurements of nanoliter Liquid volumes in microfluidic channels to 40 GHz". In: *IEEE Transactions on Instrumentation and Measurement* 59 (12 Dec. 2010), pp. 3279–3288. ISSN: 00189456. DOI: 10.1109/TIM.2010.2047141.

[61] Tao Sun and Hywel Morgan. *Single-cell microfluidic Impedance cytometry: A review*. Vol. 8. 4. Springer-Verlag, Apr. 2010, pp. 423–443. DOI: 10.1007/s10404-010-0580-9. URL: http://link.springer.com/10.1007/s10404-010-0580-9.

[62] Hugo Daguerre et al. "Positional dependence of particles and cells in microfluidic electrical impedance flow cytometry: Origin, challenges and opportunities". In: *Lab on a Chip* 20 (20 Oct. 2020), pp. 3665–3689. ISSN: 14730189. DOI: 10.1039/d0lc00616e. URL: https://pubs.rsc.org/en/content/articlehtml/2020/lc/d0lc00616e.

[63] Cornelius S. Bausch et al. "Ultra-fast cell counters based on microtubular waveguides". In: *Scientific Reports* (2017). ISSN: 20452322. DOI: 10.1038/srep41584.

[64] Lei Li et al. "Microwave Dielectric Properties of Fused Silica Prepared by Different Approaches". In: *International Journal of Applied Ceramic Technology* 11 (1 2014), pp. 193–199. DOI: 10.1111/j.1744-7402.2012.02846.x.

[65] Dean A. Frickey. "Conversions Between S, Z, Y, h, ABCD, and T Parameters which are Valid for Complex Source and Load Impedances". In: *IEEE Transactions on Microwave Theory and Techniques* 42 (2 1994). ISSN: 15579670. DOI: 10.1109/22.275248.

[66] Abhishek Bhat et al. "Radio Frequency Tank Circuit for Probing Planar Lipid Bilayers". In: *Soft Nanoscience Letters* 03 (04 2013), pp. 87–92. ISSN: 2160-0600. DOI: 10.4236/snl.2013.34016.

[67] Graham A. Ferrier et al. "A microwave interferometric system for simultaneous actuation and detection of single biological cells". In: *Lab Chip* 9 (23 2009), pp. 3406–3412. DOI: 10.1039/B908974H. URL: http://dx.doi.org/10.1039/B908974H.

[68] Thomas Chretiennot, David Dubuc, and Katia Grenier. "A Microwave and microfluidic planar resonator for efficient and accurate complex permittivity characterization of aqueous solutions". In: *IEEE Transactions on Microwave Theory and Techniques* 61 (2 2013), pp. 972–978. ISSN: 00189480. DOI: 10.1109/TMTT.2012.2231877.

[69] J. Leroy et al. "Microfluidic biosensors for microwave dielectric spectroscopy". In: *Sensors and Actuators, A: Physical* 229 (June 2015), pp. 172–181. ISSN: 09244247. DOI: 10.1016/j.sna.2015.04.002.

[70] A.M. Watson et al. "High-Q on-chip microwave resonator for sensitive permittivity detection in nanoliter volumes". In: *2015 Transducers - 2015 18th International Conference on Solid-State Sensors, Actuators and Microsystems (TRANSDUCERS)*. 2015, pp. 1665–1668. DOI: 10.1109/TRANSDUCERS.2015.7181262.

[71] Chia Feng Liu, Min Haw Wang, and Ling Sheng Jang. "Microfluidics-based hairpin resonator biosensor for biological cell detection". In: *Sensors and Actuators, B: Chemical* 263 (June 2018), pp. 129–136. ISSN: 09254005. DOI: 10.1016/j.snb.2018.01.234.

[72] Tzung Tsuen Tsai et al. "High throughput and label-free particle sensor based on microwave resonators". In: *Sensors and Actuators, A: Physical* 285 (2019). ISSN: 09244247. DOI: 10.1016/j.sna.2018.12.008.

[73] Niels Haandbæk et al. "Resonance-enhanced microfluidic impedance cytometer for detection of single bacteria". In: *Lab on a Chip* 14 (17 Sept. 2014), pp. 3313–3324. ISSN: 14730189. DOI: 10.1039/C4LC00576G.

[74] Rammah Ali Alahnomi et al. "Review of Recent Microwave Planar Resonator-Based Sensors: Techniques of Complex Permittivity Extraction, Applications, Open Challenges and Future Research Directions". In: *Sensors* 21.7 (2021). ISSN: 1424-8220. DOI: 10.3390/s21072267. URL: https://www.mdpi.com/1424-8220/21/7/2267.

[75] J. R. Bray and L. Roy. "Measuring the unloaded, loaded, and external quality factors of one- and two-port resonators using scattering-parameter magnitudes at fractional power levels". In: *IEE Proceedings: Microwaves, Antennas and Propagation* 151 (4 Aug. 2004), pp. 345–350. ISSN: 13502417. DOI: 10.1049/IP-MAP:20040521.

[76] M. Göppl et al. "Coplanar waveguide resonators for circuit quantum electrodynamics". In: *Journal of Applied Physics* 104 (11 2008). ISSN: 00218979. DOI: 10.1063/1.3010859.

[77] K. Beilenhoff et al. "Open and short circuits in coplanar MMIC's". In: *IEEE Transactions on Microwave Theory and Techniques* 41.9 (1993), pp. 1534–1537. DOI: 10.1109/22.245673.

[78] Maxim Zhadobov et al. "Complex permittivity of representative biological solutions in the 2-67GHz range". In: *Bioelectromagnetics* (2012). ISSN: 01978462. DOI: 10.1002/bem.20713.

[79] Ting Chen, Glenn Hefter, and Richard Buchner. "Dielectric Spectroscopy of Aqueous Solutions of KCl and CsCl". In: *The Journal of Physical Chemistry A* 107 (20 2003), pp. 4025–4031. DOI: 10.1021/jp026429p.

[80] Jialu Ma et al. "Complex permittivity characterization of liquid samples based on a split ring resonator (Srr)". In: *Sensors* 21 (10 2021). ISSN: 14248220. DOI: 10.3390/s21103385.

[81] Amir Ebrahimi et al. "High-Sensitivity Metamaterial-Inspired Sensor for Microfluidic Dielectric Characterization". In: *IEEE Sensors Journal* 14.5 (2014), pp. 1345–1351. DOI: 10.1109/JSEN.2013.2295312.

[82] Aleksandar Savic et al. "A Capacitive Microwave Sensor With Guard Electrode for Single-Cell Characterization". In: *IEEE Journal of Electromagnetics, RF and Microwaves in Medicine and Biology* 6 (2 2022). ISSN: 24697249. DOI: 10.1109/JERM.2021.3078850.

[83] Larbi Benkhaoua et al. "Miniaturized Quasi-Lumped Resonator for Dielectric Characterization of Liquid Mixtures". In: *IEEE Sensors Journal* 16.6 (2016), pp. 1603–1610. DOI: 10.1109/JSEN.2015.2504601.

[84] M. V. Requa et al. "Nanoscale radiofrequency impedance sensors with unconditionally stable tuning". In: *Journal of Applied Physics* 106 (7 2009). ISSN: 00218979. DOI: 10.1063/1.3243315.

[85] Paul V Gwozdz. "Label-Free Electrical Sensing of Single Cells Translocating through Micropores at Gigahertz Frequencies". PhD thesis. Staats-und Universitätsbibliothek Hamburg Carl von Ossietzky, 2019.

[86] L. J. van der PAUW. "A METHOD OF MEASURING SPECIFIC RESISTIVITY AND HALL EFFECT OF DISCS OF ARBITRARY SHAPE". In: *Semiconductor Devices: Pioneering Papers*, pp. 174–182. DOI: 10.1142/9789814503464_0017. eprint: https://www.worldscientific.com/doi/pdf/10.1142/9789814503464_0017. URL: https://www.worldscientific.com/doi/abs/10.1142/9789814503464_0017.

[87] Bryan Cord, Jodie Lutkenhaus, and Karl K. Berggren. "Optimal temperature for development of poly(methylmethacrylate)". In: *Journal of Vacuum Science & Technology B: Microelectronics and Nanometer Structures* 25 (6 2007). ISSN: 10711023. DOI: 10.1116/1.2799978.

[88] Chao Wang et al. "Wafer-scale integration of sacrificial nanofluidic chips for detecting and manipulating single DNA molecules". In: *Nature Communications* 8 (2017). ISSN: 20411723. DOI: 10.1038/ncomms14243.

[89] Chuanhua Duan, Wei Wang, and Quan Xie. "Review article: Fabrication of nanofluidic devices". In: *Biomicrofluidics* 7.2 (2013), p. 026501. DOI: 10.1063/1.4794973. eprint: https://doi.org/10.1063/1.4794973. URL: https://doi.org/10.1063/1.4794973.

[90] Bridget Peeni et al. "Sacrificial Layer Microfluidic Device Fabrication Methods". In: *ELECTROPHORESIS* 27 (Dec. 2006), pp. 4888 –4895. DOI: 10.1002/elps.200600399.

[91] D. Bhusari et al. "Fabrication of air-channel structures for microfluidic, microelectromechanical, and microelectronic applications". In: *Journal of Microelectromechanical Systems* 10.3 (2001), pp. 400–408. DOI: 10.1109/84.946793.

[92] P.A. Kohl et al. "Air-gaps in 0.3 μm electrical interconnections". In: *IEEE Electron Device Letters* 21.12 (2000), pp. 557–559. DOI: 10.1109/55.887464.

[93] Mathieu Foquet et al. “DNA Fragment Sizing by Single Molecule Detection in Submicrometer-Sized Closed Fluidic Channels”. In: *Analytical Chemistry* 74.6 (2002). PMID: 11922312, pp. 1415–1422. DOI: 10.1021/ac011076w. eprint: https://doi.org/10.1021/ac011076w. URL: https://doi.org/10.1021/ac011076w.

[94] Jose Luis Salas-Vernis et al. “Hydrophobic/hydrophilic surface modification within buried air channels”. In: *Journal of Vacuum Science & Technology B: Microelectronics and Nanometer Structures Processing, Measurement, and Phenomena* 22.3 (2004), pp. 953–960. DOI: 10.1116/1.1715084. eprint: https://avs.scitation.org/doi/pdf/10.1116/1.1715084. URL: https://avs.scitation.org/doi/abs/10.1116/1.1715084.

[95] Sung-Min Kang et al. “Fabrication of on-chip nanofluidic channels by using sacrificial photoresist templated SiO2 sputter deposition”. In: *Journal of the Korean Physical Society* 48.5 (2006), p. 883.

[96] Kipp Schoenwald and Todd Sulchek. “Microfluidic to Nanofluidic Interface via a Thermally Decomposable Sacrificial Polymer”. In: *Journal of Microelectromechanical Systems* 24 (June 2015), pp. 1–1. DOI: 10.1109/JMEMS.2015.2434815.

[97] Nicole Devlin, Devin Brown, and Paul Kohl. “Patterning decomposable polynorbornene with electron beam lithography to create nanochannels”. In: *Journal of Vacuum Science & Technology B: Microelectronics and Nanometer Structures* 27 (Dec. 2009), pp. 2508 –2511. DOI: 10.1116/1.3264658.

[98] Nicole R. Devlin and Devin K. Brown. “Fabricating millimeter to nanometer sized cavities concurrently for nanofluidic devices”. In: *Journal of Vacuum Science & Technology B* 28.6 (2010), pp. C6I7–C6I10. DOI: 10.1116/1.3517701. eprint: https://doi.org/10.1116/1.3517701. URL: https://doi.org/10.1116/1.3517701.

[99] K. Walsh, J. Norville, and Yu-Chong Tai. “Photoresist as a sacrificial layer by dissolution in acetone”. In: *Technical Digest. MEMS 2001. 14th IEEE International Conference on Micro Electro Mechanical Systems (Cat. No.01CH37090)*. 2001, pp. 114–117. DOI: 10.1109/MEMSYS.2001.906492.

[100] S. Metz et al. “Polyimide and SU-8 microfluidic devices manufactured by heat-depolymerizable sacrificial material technique”. In: *Lab Chip* 4 (2 2004), pp. 114–120. DOI: 10.1039/B310866J. URL: http://dx.doi.org/10.1039/B310866J.

[101] Wanli Li et al. “Sacrificial polymers for nanofluidic channels in biological applications”. In: *Nanotechnology* 14.6 (Apr. 2003), pp. 578–583. DOI: 10.1088/0957-4484/14/6/302. URL: https://doi.org/10.1088/0957-4484/14/6/302.

[102] C. K. Harnett, G. W. Coates, and H. G. Craighead. “Heat-depolymerizable polycarbonates as electron beam patternable sacrificial layers for nanofluidics”. In: *Journal of Vacuum Science & Technology B: Microelectronics and Nanometer Structures Processing, Measurement, and Phenomena* 19.6 (2001), pp. 2842–2845. DOI: 10.1116/1.1409383. eprint: https://avs.scitation.org/doi/pdf/10.1116/1.1409383. URL: https://avs.scitation.org/doi/abs/10.1116/1.1409383.

[103] Hollie A Reed et al. “Fabrication of microchannels using polycarbonates as sacrificial materials”. In: *Journal of Micromechanics and Microengineering* 11.6 (Oct. 2001), pp. 733–737. DOI: 10.1088/0960-1317/11/6/317. URL: https://doi.org/10.1088/0960-1317/11/6/317.

[104] J.P. Jayachandran et al. "Air-channel fabrication for microelectromechanical systems via sacrificial photosensitive polycarbonates". In: *Journal of Microelectromechanical Systems* 12.2 (2003), pp. 147–159. DOI: 10.1109/JMEMS.2003.809963.

[105] Nan Zheng et al. "Polycarbonate as a negative-tone resist for electron-beam lithography". In: *Journal of Vacuum Science & Technology B* 36.2 (2018), p. 021603. DOI: 10.1116/1.5012028. eprint: https://doi.org/10.1116/1.5012028. URL: https://doi.org/10.1116/1.5012028.

[106] Daniel Adams and T.L. Alford. "Encapsulated silver for integrated circuit metallization". In: *Materials Science and Engineering: R: Reports* 40.6 (2003), pp. 207–250. ISSN: 0927-796X. DOI: https://doi.org/10.1016/S0927-796X(03)00025-1. URL: https://www.sciencedirect.com/science/article/pii/S0927796X03000251.

[107] K.R. Williams, K. Gupta, and M. Wasilik. "Etch rates for micromachining processing-Part II". In: *Journal of Microelectromechanical Systems* 12.6 (2003), pp. 761–778. DOI: 10.1109/JMEMS.2003.820936.

[108] Bradley Givot et al. "Accurate Measurements of Permittivity and Dielectric Loss Tangent of Low Loss Dielectrics at Frequency Range 100 MHz - 20 GHz". In: *2006 International Conference on Microwaves, Radar & Wireless Communications*. 2006, pp. 232–235. DOI: 10.1109/MIKON.2006.4345157.

[109] Nicolás Reyes et al. "Complex Dielectric Permittivity of Engineering and 3D-Printing Polymers at Q-Band". In: *Journal of Infrared, Millimeter, and Terahertz Waves* 39 (11 2018). ISSN: 18666906. DOI: 10.1007/s10762-018-0528-9.

[110] Yang Yang et al. "Distinguishing the viability of a single yeast cell with an ultra-sensitive radio frequency sensor". In: *Lab Chip* 10 (5 2010), pp. 553–555. DOI: 10.1039/B921502F. URL: http://dx.doi.org/10.1039/B921502F.

[111] C. Dalmay et al. "Ultra sensitive biosensor based on impedance spectroscopy at microwave frequencies for cell scale analysis". In: *Sensors and Actuators A: Physical* 162.2 (2010). Eurosensors XXIII, 2009, pp. 189–197. ISSN: 0924-4247. DOI: https://doi.org/10.1016/j.sna.2010.04.023. URL: https://www.sciencedirect.com/science/article/pii/S0924424710001998.

[112] Clare Watts et al. "Microwave Dielectric Sensing of Free-Flowing, Single, Living Cells in Aqueous Suspension". In: *IEEE Journal of Electromagnetics, RF and Microwaves in Medicine and Biology* 4.2 (2020), pp. 97–108. DOI: 10.1109/JERM.2019.2932569.

[113] G. A. Ferrier et al. "Microfluidic electromanipulation with capacitive detection for the mechanical analysis of cells". In: *Biomicrofluidics* 2.4 (2008), p. 044102. DOI: 10.1063/1.2992127. eprint: https://doi.org/10.1063/1.2992127. URL: https://doi.org/10.1063/1.2992127.

[114] Mehmet Kelleci et al. "Towards microwave imaging of cells". In: *Lab Chip* 18 (3 2018), pp. 463–472. DOI: 10.1039/C7LC01251A. URL: http://dx.doi.org/10.1039/C7LC01251A.

[115] Zurich Instruments. *Principles of lock-in detection and the state of the art*. Nov. 2016. URL: https://www.zhinst.com/sites/default/files/li_primer/zi_whitepaper_principles_of_lock-in_detection.pdf.

[116] Silviu Sorin Tuca et al. "Interferometer Scanning Microwave Microscopy: Performance Evaluation". In: *IEEE Transactions on Nanotechnology* 16 (6 2017). ISSN: 1536125X. DOI: 10.1109/TNANO.2017.2725383.

[117] Faisal Ali Mubarak et al. "Noise Behavior and Implementation of Interferometer-Based Broadband VNA". In: *IEEE Transactions on Microwave*

Theory and Techniques 67.1 (2019), pp. 249–260. DOI: 10.1109/TMTT.2018.2874667.

[118] Yan Cui and Pingshan Wang. "The Design and Operation of Ultra-Sensitive and Tunable Radio-Frequency Interferometers". In: *IEEE Transactions on Microwave Theory and Techniques* 62.12 (2014), pp. 3172–3182. DOI: 10.1109/TMTT.2014.2366134.

[119] Michael Margraf. *QucsStudio – A Free and Powerful Circuit Simulator*. URL: http://qucsstudio.de.

[120] Pauli Virtanen et al. "SciPy 1.0: Fundamental Algorithms for Scientific Computing in Python". In: *Nature Methods* 17 (2020), pp. 261–272. DOI: 10.1038/s41592-019-0686-2.

[121] Iago Pereiro et al. "Nip the bubble in the bud: a guide to avoid gas nucleation in microfluidics". In: *Lab Chip* 19 (14 2019), pp. 2296–2314. DOI: 10.1039/C9LC00211A. URL: http://dx.doi.org/10.1039/C9LC00211A.

[122] Yue Ying and Ying Lin. "Inertial Focusing and Separation of Particles in Similar Curved Channels". In: *Scientific Reports* 9 (1 2019). ISSN: 20452322. DOI: 10.1038/s41598-019-52983-z.

[123] Jerzy Krupka. "Measurements of the Complex Permittivity of Low Loss Polymers at Frequency Range From 5 GHz to 50 GHz". In: *IEEE Microwave and Wireless Components Letters* 26.6 (2016), pp. 464–466. ISSN: 1558-1764. DOI: 10.1109/LMWC.2016.2562640.

[124] Xu Chen et al. "Fringing Effect Analysis of Parallel Plate Capacitors for Capacitive Power Transfer Application". In: *2019 IEEE 4th International Future Energy Electronics Conference (IFEEC)*. 2019, pp. 1–5. DOI: 10.1109/IFEEC47410.2019.9015111.

[125] Henrik Bruus. "Lecture Notes Theoretical microfluidics". In: *Physics* 18 (33235 2008). ISSN: 15746968.

[126] Michelle E. Staben and Robert H. Davis. "Particle transport in Poiseuille flow in narrow channels". In: *International Journal of Multiphase Flow* 31 (5 2005). ISSN: 03019322. DOI: 10.1016/j.ijmultiphaseflow.2004.12.004.

[127] Rosalinda Madonna. "Human-Induced pluripotent stem cells: In quest of clinical applications". In: *Molecular Biotechnology* 52 (2 2012). ISSN: 10736085. DOI: 10.1007/s12033-012-9504-0.

[128] Karen Ven et al. "Target Confinement in Small Reaction Volumes Using Microfluidic Technologies: A Smart Approach for Single-Entity Detection and Analysis". In: *ACS Sensors* 3 (2 2018). ISSN: 23793694. DOI: 10.1021/acssensors.7b00873.

[129] Shi Ping Zhao et al. "Three-Dimensional Cell Culture and Drug Testing in a Microfluidic Sidewall-Attached Droplet Array". In: *Analytical Chemistry* 89 (19 2017). ISSN: 15206882. DOI: 10.1021/acs.analchem.7b02267.

[130] Richard Obexer et al. "Emergence of a catalytic tetrad during evolution of a highly active artificial aldolase". In: *Nature Chemistry* 9 (1 2017). ISSN: 17554349. DOI: 10.1038/nchem.2596.

[131] Anthony Kulesa et al. "Combinatorial drug discovery in nanoliter droplets". In: *Proceedings of the National Academy of Sciences of the United States of America* 115 (26 2018). ISSN: 10916490. DOI: 10.1073/pnas.1802233115.

[132] Liang Jun Pan et al. *Controllable synthesis of nanocrystals in droplet reactors*. 2018. DOI: 10.1039/c7lc00800g.

[133] Wen wen Liu and Ying Zhu. ""Development and application of analytical detection techniques for droplet-based microfluidics"-A review". In: *Analytica Chimica Acta* 1113 (2020), pp. 66–84. ISSN: 0003-2670. DOI: https://doi.

org/10.1016/j.aca.2020.03.011. URL: https://www.sciencedirect.com/science/article/pii/S0003267020303184.

[134] Merve Marcali and Caglar Elbuken. "Impedimetric detection and lumped element modelling of a hemagglutination assay in microdroplets". In: *Lab Chip* 16 (13 2016), pp. 2494–2503. DOI: 10.1039/C6LC00623J. URL: http://dx.doi.org/10.1039/C6LC00623J.

[135] Pelin Kubra Isgor et al. "Microfluidic droplet content detection using integrated capacitive sensors". In: *Sensors and Actuators, B: Chemical* 210 (2015). ISSN: 09254005. DOI: 10.1016/j.snb.2015.01.018.

[136] Yi-Wei Tang et al. "Laboratory Diagnosis of COVID-19: Current Issues and Challenges". In: *Journal of Clinical Microbiology* 58.6 (2020). Ed. by Alexander J. McAdam. ISSN: 0095-1137. DOI: 10.1128/JCM.00512-20.

[137] Meagan N. Esbin et al. *Overcoming the bottleneck to widespread testing: A rapid review of nucleic acid testing approaches for COVID-19 detection*. 2020. DOI: 10.1261/rna.076232.120.

[138] Terry C. Jones et al. "Estimating infectiousness throughout SARS-CoV-2 infection course". In: *Science* 373.6551 (2021), eabi5273. DOI: 10.1126/science.abi5273. eprint: https://www.science.org/doi/pdf/10.1126/science.abi5273. URL: https://www.science.org/doi/abs/10.1126/science.abi5273.

[139] Jacques Demongeot and Cécile Fougère. "mRNA COVID-19 Vaccines-Facts and Hypotheses on Fragmentation and Encapsulation". In: *Vaccines* 11.1 (2023). ISSN: 2076-393X. DOI: 10.3390/vaccines11010040. URL: https://www.mdpi.com/2076-393X/11/1/40.

[140] Barbara Mui, Laurie Chow, and Michael J. Hope. "Extrusion Technique to Generate Liposomes of Defined Size". In: *Methods in Enzymology* 367 (2003). ISSN: 00766879. DOI: 10.1016/S0076-6879(03)67001-1.

[141] Sindhoora Kaniyala Melanthota et al. "Elucidating the microscopic and computational techniques to study the structure and pathology of SARS-CoVs". In: *Microscopy Research and Technique* 83.12 (2020), pp. 1623–1638. DOI: https://doi.org/10.1002/jemt.23551. eprint: https://analyticalsciencejournals.onlinelibrary.wiley.com/doi/pdf/10.1002/jemt.23551. URL: https://analyticalsciencejournals.onlinelibrary.wiley.com/doi/abs/10.1002/jemt.23551.

[142] Paul M. Meaney et al. "Electrical Characterization of Glycerin: Water Mixtures: Implications for Use as a Coupling Medium in Microwave Tomography". In: *IEEE Transactions on Microwave Theory and Techniques* 65.5 (2017), pp. 1471–1478. DOI: 10.1109/TMTT.2016.2638423.